NATIONAL TECHNICAL UNIVERSITY OF ATHENS

SCHOOL OF CIVIL ENGINEERING

DERARTMENT OF GEOTECHNICAL ENGINEERING

DOCTORAL DISSERTATION

Development and Calibration of Constitutive Model for Sand

Panagiota Tasiopoulou

Diploma in Civil Engineering, N.T.U.A.

Master of Science in Civil Engineering, U.C. Davis

October 2015

ΕΘΝΙΚΟ ΜΕΤΣΟΒΙΟ ΠΟΛΥΤΕΧΝΕΙΟ

ΣΧΟΛΗ ΠΟΛΙΤΙΚΩΝ ΜΗΧΑΝΙΚΩΝ

ΤΟΜΕΑΣ ΓΕΩΤΕΧΝΙΚΗΣ

ΔΙΔΑΚΤΟΡΙΚΗ ΔΙΑΤΡΙΒΗ

Αναπτυξη και Βαθμονόμηση Καταστατικού Προσομοιώματος για Αμμώδη Εδάφη

Παναγιώτα Τασιοπούλου

Διπλωματούχος Πολιτικός Μηχανικός, Ε.Μ.Π.

Master of Science in Civil Engineering, U.C. Davis

Οκτώβριος 2015

NATIONAL TECHNICAL UNIVERSITY OF ATHENS
SCHOOL OF CIVIL ENGINEERING
DEPARTMENT OF GEOTECHNICAL ENGINEERING

DEVELOPMENT AND CALIBRATION OF CONSTITUTIVE MODEL FOR SAND

DOCTORAL THESIS

Panagiota A. Tasiopoulou

Diploma in Civil Engineering, N.T.U.A.,
M.Sc. University of California at Davis

The thesis is submitted to the School of Civil Engineering of the National Technical University of Athens in fulfilment of the requirements for the Degree of Doctor of Philosophy

ADVISORY COMMITTEE:

1. G. GAZETAS,
Professor N.T.U.A. (Supervisor)

2. N. GEROLYMOS,
Assistant Professor N.T.U.A.

3. P. DAKOULAS,
Professor Univ. of Thessaly (UTH)

EXAMINATION COMMITTEE:

1. G. GAZETAS,
Professor N.T.U.A. (Supervisor)

2. N. GEROLYMOS,
Assistant Professor N.T.U.A.

3. P. DAKOULAS,
Professor Univ. of Thessaly (UTH)

4. Y. DAFALIAS, Professor UC Davis.

5. G. VIGGIANI, Professor University Joseph Fourier, Grenoble

6. V. KOUMOUSIS, Professor N.T.U.A.

7. A. PAPADIMITRIOU,
Assistant Professor N.T.U.A.

Athens, October 2015

ΕΘΝΙΚΟ ΜΕΤΣΟΒΙΟ ΠΟΛΥΤΕΧΝΕΙΟ
ΣΧΟΛΗ ΠΟΛΙΤΙΚΩΝ ΜΗΧΑΝΙΚΩΝ
ΤΟΜΕΑΣ ΓΕΩΤΕΧΝΙΚΗΣ

ΑΝΑΠΤΥΞΗ ΚΑΙ ΒΑΘΜΟΝΟΜΗΣΗ ΚΑΤΑΣΤΑΤΙΚΟΥ ΠΡΟΣΟΜΟΙΩΜΑΤΟΣ ΓΙΑ ΑΜΜΩΔΗ ΕΔΑΦΗ

ΔΙΔΑΚΤΟΡΙΚΗ ΔΙΑΤΡΙΒΗ

Παναγιώτα Α. Τασιοπούλου

Διπλωματούχου Πολιτικού Μηχανικού Ε.Μ.Π.,
M.Sc. University of California at Davis

Η διατριβή υποβλήθηκε στη Σχολή Πολιτικών Μηχανικών του Εθνικού Μετσόβιου Πολυτεχνείου προς εκπλήρωση των προϋποθέσεων του τίτλου Διδάκτορος Μηχανικού

ΣΥΜΒΟΥΛΕΥΤΙΚΗ ΕΠΙΤΡΟΠΗ:

1. Γ. ΓΚΑΖΕΤΑΣ,
Καθηγητής Ε.Μ.Π. (Επιβλέπων)

2. Ν. ΓΕΡΟΛΥΜΟΣ,
Επίκουρος Καθηγητής Ε.Μ.Π.

3. Π. ΝΤΑΚΟΥΛΑΣ,
Καθηγητής Πανεπ. Θεσσαλίας (Π.Θ.)

ΕΞΕΤΑΣΤΙΚΗ ΕΠΙΤΡΟΠΗ:

1. Γ. ΓΚΑΖΕΤΑΣ,
Καθηγητής Ε.Μ.Π. (Επιβλέπων)

2. . Ν. ΓΕΡΟΛΥΜΟΣ,
Επίκουρος Καθηγητής Ε.Μ.Π.

3. Π. ΝΤΑΚΟΥΛΑΣ,
Καθηγητής Πανεπ. Θεσσαλίας (Π.Θ.)

4. Ι. ΔΑΦΑΛΙΑΣ, Καθηγητής UC Davis.

5. G. VIGGIANI, Καθηγητής University Joseph Fourier, Grenoble

6. Β. ΚΟΥΜΟΥΣΗΣ, Καθηγητής Ε.Μ.Π.

7. Α. ΠΑΠΑΔΗΜΗΤΡΙΟΥ,
Επίκουρος Καθηγητής Ε.Μ.Π.

Αθήνα, Οκτώβριος 2015

Στους γονείς μου,

Φωτεινή και Ανδρέα

Προλεγόμενα

Ξεκινώντας, θα ήθελα να ευχαριστήσω τον Καθηγητή μου, Γιώργο Γκαζέτα, για την συνεχή υποστήριξη του και την εμπιστοσύνη που μου έδειξε. Με ενθάρρυνε πάντα να ασχοληθώ με την έρευνα που μου άρεσε και μου χάρισε απλόχερα ευκαιρίες να ανοίξω τους ερευνητικούς μου ορίζοντες μέσα από ταξίδια, συμμετοχές σε συνέδρια και κυρίως, το μοίρασμα των εμπειριών και των γνώσεών του. Θα είμαι πάντα ευγνώμων.

Στην συνέχεια, θα ήθελα να σταθώ στην συνεργασία μου με τον Νίκο Γερόλυμο, τον οποίο πλέον ασθάνομαι σαν οικογένεια. Νιώθω ότι ό,τι και αν γράψω θα είναι λίγο... Τον ευχαριστώ που μοιράστηκε μαζί μου την άστειρευτη γνώση του, το ευρευνητικό όραμά του και που διέθεσε απεριόριστο χρόνο για να μου μεταδώσει όχι μόνον τον αναλυτικό τρόπο σκέψης του, αλλά και ηθικές αρχές και αξίες.

Επίσης, ευχαριστώ τον Καθηγητή, Ιωάννη Δαφαλιά, ως τον πρώτο άνθρωπο που μου δίδαξε το αντικείμενο με το οποίο ασχολήθηκα στην Διατριβή μου, την θεωρία της πλαστικότητας. Υπήρξε πηγή έμπνευσης.

Στο σημείο αυτό, θα ήθελα να ευχαριστήσω και τα υπόλοιπα μέλη της εξεταστικής μου επιτροπής για την συνεισφορά τους στην ολοκλήρωση της παρούσας Διατριβής: κ. Παναγιώτη Ντακούλα, κ. Βλάση Κουμούση, κ. Αχιλλέα Παπαδημητρίου και κ. Gioacchino Viggiani.

Προχωρώντας, θα ήθελα να αναφερθώ στους φίλους και συναδέλφους με τούς οποίους μοιράστηκαμε αγωνίες, άγχη, χαρές και το ίδιο γραφείο, όλα αυτά τα χρόνια. Δεν είναι άλλοι από τους: Σπύρο Γιαννακό, Μαριάννα Λώλη και Θανάση Ζαφειράκο. Το ταξίδι αυτό δεν θα ήταν το ίδιο πλούσιο σε εμπειρίες χωρίς αυτούς.

Σε αυτήν την πορεία των πέντε ετών, δημιούργησα καλούς φίλους, οι οποίοι, ο καθένας με τον τρόπο του, συνέβαλαν στην πραγματοποίηση αυτής της Διατριβής, είτε μέσω της ηθικής υποστήριξης, είτε μέσω της ανταλλαγής απόψεων επί του επιστημονικού. Θα ήθελα να ξεκινήσω με την Κατερίνα Λεοντάρη, τον Γιάννη Χαλούλο, τον Βασίλη Δρόσο, την Κική Δημητριάδη και την Βασιλική Καρδούτσου. Τους ευχαριστώ ειλικρινά για την ανιδιοτελή φιλία τους. Αμέσως μετά, θα ήθελα να αναφέρω ονομαστικά τους συναδέλφους μου στον τομέα Γεωτεχνικής και να τους ευχαριστήσω που υπήρξαν συνοδοιπόροι σε αυτό το ταξίδι: Κωνσταντίνο Κασσά, Κωνσταντίνο Τζιβάκο, Παναγιώτη Σιταρένιο, Αλέξανδρο Καλό, Δημήτρη Λίτσα, Παύλο Αστερίου, Φίλιππο Χόρτη, Γιάννη

Τσιάπα, Κωνσταντίνο Μπαζαίο, Άγγελο Τσάτση, Γεωργία Αγαπουλάκη και Ανθή Ραχμάνη.

Θα ήταν μεγάλη παράλειψη να μην ευχαριστήσω εκ βάθους καρδίας τους κοντινούς μου ανθρώπους και πιο θερμούς υποστηρικτές μου: Έλσα Κόκοτα, Κατερίνα Ζιωτοπούλου, Αντωνία Μάκρα, Μαριλία Μπαλάση, Αλεξία Στεργίου, Λένια Μόκα, Νικόλα Παπαηλίου, Μαρίνα Τζωρτζακάκη και Νίκο Καλαθά.

Κλείνοντας, ευχαριστώ τους γονείς μου, Φωτεινή και Ανδρέα, τους πιο σημαντικούς ανθρώπους στη ζωή μου.

NATIONAL TECHNICAL UNIVERSITY OF ATHENS
SCHOOL OF CIVIL ENGINEERING
DEPARTMENT OF GEOTECHNICAL ENGINEERING

"Development and Calibration of Constitutive Model for Sand"

DOCTORAL DISSERTATION

Panagiota Tasiopoulou

ABSTRACT

The behavior of granular materials has been extensively studied in literature. After numerous experimental observations, it has become common knowledge that sand tends to undergo shear-induced volume change until a critical state is reached, upon which shearing occurs with no volumetric change. Whether shearing tends to develop positive (contraction) or negative (dilation) volume change depends on the initial state of the material relative to the critical state which is a function of the relative density and the confining pressure. In case of undrained loading, the tendency for contraction (loose sand) is translated into a decrease of mean effective stress, whereas tendency for dilation (dense sand) results in increase of mean effective stress. Besides the elimination of volume change upon shearing, another characteristic of critical state is the occurrence of a residual friction angle, equivalent to the critical state line in triaxial space, being unique for all initial states.

While the above behavior can be clearly identified under monotonic loading, cyclic response of sand is quite complex and contradictive with respect to the critical state concept. Critical state, as it is strictly defined in void ratio versus mean effective stress plane, is never reached. In particular, drained cyclic loading results in positive cumulative volumetric change either in case of dense or loose sand (densification). On the other hand, if unlimited, undrained cyclic loading would lead to continuous decrease of mean

effective stress, p, until zero (liquefaction). However, after a large number of loading cycles, the critical stress ratio is reached under both drained and undrained conditions. For example, in case of liquefaction it has been experimentally observed that cyclic loading moves the stress paths towards the critical state line which coincides with the so-called failure envelope at p = 0.

Apart from the dependency of their behavior on initial and critical states, granular materials exhibit variations in their response, attributed to intrinsic and stress-induced anisotropy. Intrinsic anisotropy is related with differences on their particle shape, size and packing, known as fabric effects. Stress-induced anisotropy is associated with the loading direction relative to the bedding plane, including principal stress rotation and intermediate stress effects.

The behavioral diversity of sand for different loading conditions (drained/undrained, monotonic/cyclic, direction), and different initial state and fabric, render its modeling a difficult and challenging task. The suitability of the used constitutive model is evaluated by its capability to capture at least the trends across all these conditions without recalibration of its parameters for each specific case. Simplicity is needless to say a desirable attribute. Too many parameters might increase the versatility of the model at the risk, however, of losing its physical appeal.

A novel constitutive model for sand is developed as an alternative plasticity formulation that exhibits critical state consistency for both monotonic and cyclic loading and uniqueness of its parameters for a given type of sand, irrespective of loading conditions. The model, designated as Ta-Ger sand model (Tasiopoulou and Gerolymos, 2012, 2014), is based on a reformulation of perfect elastoplasticity by introducing a hardening law inspired from Bouc-Wen hysteresis. The latter is a smooth hysteresis model originally proposed by Bouc (1971), extended by Wen (1976), and used in random vibration studies of inelastic systems. Since then, modified or extended versions of this model have been extensively used in numerous structural (e.g. Sivaselvan and Reinhorn, 2000; Triantafyllou and Koumousis, 2012) and geotechnical applications (e.g. Pires et al., 1989; Gerolymos and Gazetas, 2005). The developed constitutive formulation can be

regarded as a bounding single-surface model with vanished elastic region and the distinguished characteristic of a non-explicitly defined plastic modulus.

The goal is to provide a simpler but equally efficient scheme of high versatility. The explicitly formulated plastic matrix, **H**, plays a triple role: (i) it offers a gradual and smooth ("hardening-type") transition from the elastic to perfectly plastic response in order to capture pre-failure nonlinearity and the coupling between elastic and plastic counterparts composing the total strain increment, (ii) it provides an appropriate loading/unloading/reloading mapping rule by tracking the distance from the ultimate perfectly plastic state as defined by the failure surface, which herein, serves as a bounding surface, and (iii) its terms attain values that are strictly bounded within the range of [0,1].

Salient features of the proposed plasticity approach are: (i) a new plastic flow rule based on a revision of Rowe dilatancy theory (1962), accounting for anisotropic distribution of dilatancy to the normal plastic strain increments, as well as densification due to cyclic loading, (ii) a mapping rule and load reversal criterion based on the first order work, inspired from Bouc-Wen hysteresis, and (iii) a new formulation for the evolution of the bounding and phase transformation surfaces as a function of the cumulative deviatoric strain increment, ensuring critical state consistency not only for monotonic but also for cyclic loading.

An extensive calibration methodology is then developed aiming at: (i) increasing model predictability and (ii) minimizing the number of internal model parameters. Initially, constitutive formulation was adjusted to Bolton's (1986) empirical correlations for dilatancy, given as a function of relative dilatancy index, I_r; the latter works as a state parameter in the constitutive framework. This step reduces the number of unknown model parameters to three, besides the ones related directly to measurable physical properties, such as critical state friction angle and elastic modulus. At this stage, the remaining three unknown parameters are expressed as functions of the initial state (relative density and pressure), while inherent fabric effects (such as particle shape, size and packing) on the calibration process are considered. At last, stress-induced anisotropy

is dealt with introducing a scalar-valued variable in the model, a function of principal stress rotation angle, α, and the intermediate stress parameter, b, without affecting the number of unknown model parameters. Validation against experimental data was performed in every step for various drained and undrained loading paths in a wide range of α, b values, as well as initial states, for three different types of sand (Toyoura, Fontainebleau, Sacramento–River). Comparison with experiments reveals the capability of the model to describe complex patterns of sand behavior, as well as its versatility to reproduce liquefaction due to cyclic loading at very large strains (e.g. $\gamma > 8\%$) without exhibiting shear locking.

ΕΘΝΙΚΟ ΜΕΤΣΟΒΙΟ ΠΟΛΥΤΕΧΝΕΙΟ
ΣΧΟΛΗ ΠΟΛΙΤΙΚΩΝ ΜΗΧΑΝΙΚΩΝ
ΤΟΜΕΑΣ ΓΕΩΤΕΧΝΙΚΗΣ

"Ανάπτυξη και Βαθμονόμηση Καταστατικού Προσομοιώματος για Αμμώδη Εδάφη"

ΔΙΔΑΚΤΟΡΙΚΗ ΔΙΑΤΡΙΒΗ

Παναγιώτα Τασιοπούλου

ΠΕΡΙΛΗΨΗ

Η συμπεριφορά κοκκωδών εδαφών έχει μελετηθεί επισταμένως στην βιβλιογραφία. Μετά από επανειλημμένες πειραματικές παρατηρήσεις, είναι πλέον κοινώς γνωστό πως η άμμος υφίσταται ογκομετρικές παραμορφώσεις υπό διάτμηση, έως ότου φτάσει μία *κρίσιμη κατάσταση*, πέραν της οποίας καμία περαιτέρω ογκομετρική αλλαγή δεν πραγματοποιείται παρά τη συνέχιση της διατμητικής φόρτισης. Το αν η άμμος, υπό διάτμηση και πήρως στραγγιζόμενες συνθήκες, τείνει να αναπτύξει θετικές (συσταλτική συμπεριφορά) ή αρνητικές (διασταλτική συμπεριφορά) ογκομετρικές παραμορφώσεις εξαρτάται από την αρχική της κατάσταση σε σχέση με την κρίσιμη, η οποία καθορίζεται από την σχετική της πυκνότητα και την μέση ενεργό τάση. Υπό αστράγγιστες συνθήκες, η τάση για συσταλτικότητα (χαλαρή κατάσταση) εκδηλώνεται μέσω μείωσης της μέση ενεργού τάσης έως και την στατική ρευστοποίηση, ενώ η τάση για διασταλτικότητα οδηγεί τελικά σε αύξηση της μέσης ενεργού τάσης. Στην κρίσιμη κατάσταση, πέρα απο το γεγονός ότι η άμμος υφίσταται διατμητικές παραμορφώσεις υπό σταθερό όγκο, η διατμητική τάση αποκτά τιμές που καθορίζονται από μία χαρακτηριστική γωνία τριβής κρίσιμης καταστασης, η οποία αντιστοιχεί στην γραμμή κρίσιμης κατάστασης στο χώρο διεκτροπικής τάσης, q, και μέσης ενεργού τάσης, p, και είναι μοναδική για όλα τις αρχικές καταστάσεις (χαλαρή ή πυκνή άμμος).

Παρόλου που η προαναφερθείσα συμπεριφορά μπορεί να αναγνωρισθεί με ευκολία σε συνθήκες μονοτονικής φόρτισης, η ανακυκλική απόκριση της άμμου είναι πιο περίπλοκη και ενδεχομένως αντιφατική σε σχέση με την θεωρία κρίσιμης κατάστασης. Η κρίσιμη κατάσταση, όπως ορίζεται αυστηρά σε όρους λόγου κενών και μέσης ενεργού τάσης, δεν επιτυγχάνεται ποτέ σε συνθήκες ανακυκλικής φόρτισης. Συγκεκριμένα, η ανακυκλική φόρτιση υπό πλήρως στραγγιζόμενες συνθήκες προκαλεί εν γένει την συσσώρευση θετικών ογκομετρικών αλλαγων (συμπύκνωση) τόσο σε περίπτωση χαλαρής όσο και πυκνής άμμου. Αντίστοιχα, ανακυκλική φόρτιση υπό αστράγγιστες συνθήκες, οδηγεί σε συνεχή μείωση της μέσης ενεργού τάσης, δυνητικώς έως και στο μηδενισμό της (ρευστοποίηση). Όμως, μετά από ικανό αριθμό κύκλων φόρτισης, η κρίσιμη κατάσταση μπορεί τελικά να επιτευχθεί, αλλά μόνον σε όρους αντοχής, δηλαδή μέσω της γωνία τριβής κρίσιμης καταστασης. Για παράδειγμα, στην περίπτωση ρευστοποίησης, έχει διαπιστωθεί πειραματικά πως η ανακυκλική φόρτιση κινεί την τασική οδευση προς την γραμμή κρίσιμης κατάστασης, ή αλλιώς περιβάλλουσα αστοχίας για p = 0.

Πέρα από την εξάρτηση της συμπεριφοράς τους από την αρχική και κρίσιμη κατάσταση, τα κοκκώδη υλικά παρουσιάζουν διαφοροποιήσεις στην απόκριση τους που αποδίδονται σε φαινόμενα εγγενούς ανισοτροπίας ή/και ανισοτροπία λόγω κατεύθυνσης φόρτισης. Η εγγενής ανισοτροπία οφείλεται στις διαφορές στο σχήμα, το μέγεθος, την διάταξη, την διαβάθμιση κλπ. των κόκκων, δηλαδή σε φαινόμενα δομής. Η ανισοτροπία λόγω κατεύθυνσης φόρτισης σχετίζεται με την κατεύθυνση της επιβαλλόμενης φόρτισης ως προς το επίπεδο απόθεσης ή διαστρωμάτωσης, την στροφή των κύριων αξόνων και την επίδραση της ενδιάμεσης κύριας τάσης.

Η εξάρτηση της συμπεριφοράς της άμμου από τις συνθήκες φόρτισης (στραγγιζόμενη/αστράγγιστη, μονοτονική/ανακυκλική, κατεύθυνση), την αρχική και κρίσιμη κατάσταση (χαλαρή/πυκνή) και τη δομή, καθιστά την προσομοίωση δύσκολη και απαιτητική. Η καταλληλότητα ενός καταστατικού προσομοιώματος αποτιμάται από την ικανότητά του να αναπαράγει ποιοτικά τουλάχιστον τις προαναφερθείσες τάσεις υπό όλες τις συνθήκες, χωρίς να χρειάζεται εκ νέου βαθμονόμηση για κάθε συνθήκη

ξεχωριστά. Η εισαγωγή πρόσθετων παραμέτρων αυξάνει την ευελιξία του προσομοιώματος με κόστος, όμως, την ευχρηστία του και προβλεψιμότητά του.

Ένα νέο καταστατικό προσομοίωμα για αμμώδη εδάφη αναπτύχθηκε (Ta-Ger sand model) ως μία εναλλακτική διατύπωση της θεωρία πλαστικότητας (Tasiopoulou and Gerolymos, 2012, 2014). Το προσομοίωμα είναι συνεπές με τη θεωρία κρίσιμης κατάστασης τόσο για μονοτονική όσο και για ανακυκλική φόρτιση, ενώ χαρακτηρίζεται από μοναδικότητα των τιμών των παραμέτρων του για δεδομένο τύπο άμμου ανεξάρτητα από τις συνθήκες φόρτισης. Ουσιαστικά, το προσομοίωμα αποτελεί μία επαναδιατύπωση της θεωρίας τέλειας ελαστοπλαστικότητας εισάγοντας έναν νόμο κράτυνσης εμπνευσμένο από το προσομοίωμα ομαλής υστέρησης, Bouc-Wen. Το προσομοίωμα αυτό αρχικά προτάθηκε απο τον Bouc (1971) και στην συνέχεια επεκτάθηκε από τον Wen (1976) και χρησιμοποιήθηκε για μελέτες απόκρισης ανελαστικών συστημάτων σε τυχαίες ταλαντώσεις. Από τότε, τροποποιημένες εκδοχές του προσομομοιώματος χρησιμοποιήθηκαν σε διάφορες δομοστατικές (e.g. Sivaselvan and Reinhorn, 2000; Triantafyllou and Koumousis, 2012) και γεωτεχνικές εφαρμογές (e.g. Pires et al., 1989; Gerolymos and Gazetas, 2005). Το ανεπτυγμένο καταστατικό προσομοίωμα της παρούσας εργασίας επίσης περιλαμβάνει μία μοναδική περιβάλλουσα επιφάνεια οριακής αντοχής με μηδενική ελαστική περιοχή, καθώς και ένα μη σαφώς ορισμένο μέτρο πλαστικότητας, όπως υπαγορεύει η κλασική θεωρία πλαστικότητας, αλλά αντί αυτού ένα σαφώς ορισμένο πλαστικό μητρώο, **H**.

Στόχος είναι η πρόταση μίας απλουστευμένης αλλά ευέλικτης διατύπωσης του τέλειου ελαστοπλαστικού μητρώου μέσω της εισαγωγής του πλαστικού μητρώου, **H**. Το πλαστικό μητρώο, **H**, έχει έναν τριπλό ρόλο: (α) προσφέρει μία σταδιακή και ομαλή μετάβαση (κράτυνση) από την ελαστική στην πλήρως πλαστική απόκριση αναπαράγοντας επιτυχώς την μη-γραμμικότητα πριν την αστοχία και την σύζευξη ελαστικών και πλαστικών επαυξητικών παραμορφώσεων, (β) παρέχει ένα κατάλληλο νόμο προβολής φόρτισης/αποφόρτισης/επαναφόρτισης καταγράφοντας την τρεχουσα τασική κατάσταση από την επιφάνεια αστοχίας, που λειτουργεί σαν περιβάλλουσα οριακής αντοχής, και (γ) οι όροι του δέχονται τιμές φραγμένες στο διάστημα [0,1].

Άλλα βασικά χαρακτηριστικά του προτεινόμενου προσομοιώματος είναι: (α) ένας νέος νόμος πλαστικής ροής βασισμένος στη θεωρία διασταλτικότητας του Rowe (1962), που επιτρέπει ανισότροπη κατανομή της διασταλτικότητας στις ορθές επαυξητικές παραμορφώσεις, (β) ένα νόμο προβολής συνδυασμένο με ένα κριτήριο αντιστροφής φόρτισης που βασίζεται στο έργο πρώτης τάξης, και (γ) εξάρτηση του ρυθμού εξέλιξης της περιβάλλουσας επιφάνειας οριακής αντοχής και της επιφάνειας αλλαγής φάσης ή διασταλτικότητας από την συσσωρευτική διεκτροπική παραμόρφωση, εξασφαλίζοντας επίτευξη της κρίσιμης κατάστασης τόσο για μονοτονικές όσο και ανακυκλικές συνθήκες φόρτισης.

Μία εκτενής μεθοδολογία βαθμονόμησης αναπτύχθηκε με σκοπό: (α) την αύξηση της ικανότητας πρόβλεψης και (β) την μείωση του αριθμού των παραμέτρων του προσομοιώματος. Αρχικά, οι εμπειρικές συσχετίσεις διασταλτικότητας του Bolton (1986), ως συνάρτηση του σχετικού δείκτη διασταλτικότητας, I_r, ενσωματώθηκαν στο καταστατικό πλαίσιο προσομοίωσης. Σε αυτό το στάδιο, ο αριθμός των άγνωστων παραμέτρων του προσομοιώματος μειώθηκε σε τρεις, χωρίς αυτές που μπορούν να συσχετιστούν με άμεσα μετρήσιμες φυσικές ιδιότητες, όπως η γωνία τριβής κρίσιμης κατάστασης και το μέτρο ελαστικότητας. Σε επόμενο στάδιο, οι τρεις εναπομενουσες παράμετροι εκφράστηκαν συναρτήσει της αρχικής κατάστασης (αρχική σχετική πυκνότητα, αρχική μέση ενεργός τάση), ενώ η επίδραση των φαινομένων δομής (όπως, σχήμα, μέγεθος, διάταξη κλπ. κόκκων) στην βαθμονόμηση ερευνάται. Τέλος, η ανισοτροπία λόγω κατευθύνσης φόρτισης προσεγγίστηκε με την εισαγωγή μιας βαθμωτής μεταβλητής που ορίζεται ως συνάρτηση της στροφής των κύριων αξόνων, α, και της παραμέτρου για την επίδραση της ενδιάμεσης κύριας τάσης, b, χωρίς να αλλάξει ο αριθμός των παραμέτρων του προσομοιώματος. Επαλήθευση του προσομοιώματος έναντι πειραματικών δεδομένων πραγματοποιήθηκε σε κάθε βήμα της βαθμονόμησης για διάφορες οδεύσεις φόρτισης υπό συνθήκες τόσο πλήρως στραγγιζόμενες όσο και αστράγγιστες, σε ένα μεγάλο εύρος τιμών α, b, και αρχικών καταστάσεων, για τρεις τύπους άμμου (Toyoura, Fontainebleau, Sacramento–River). Η σύγκριση με πειράματα ανέδειξε την ικανότητα του προσομοιώματος στο να περιγράφει επιτυχώς σύνθετες

πτυχές της συμπεριφοράς της άμμου, όπως την αναπαραγωγη ρευστοποίησης λόγω ανακυκλικής διατμησης σε μεγάλες παραμορφώσεις (e.g. γ > 8%), χωρίς να παρουσιάζει «διατμητικό κλείδωμα» (shear locking).

TABLE OF CONTENTS

CHAPTER 1

Introduction

1.1 PROBLEM DESCRIPTION

The behavior of sand has been extensively studied in literature both experimentally and theoretically. Experimental observations provided an insight on the behavioral trends and mechanisms developed under various loading conditions. These observations constituted the basis upon which Critical State Theory by Roscoe et al. (1958) and Schofield and Wroth (1968) was formulated, aiming to accommodate and interpret the basic behavioral characteristics of sand. In the following, a review of the most characteristic aspects of sand response is held within the framework of Critical State Theory.

1.1.1 Monotonic Behavior of Sand

After numerous experimental observations, it has become common knowledge that sand tends to undergo shear-induced volume change until a critical state is reached, upon which shearing occurs with no volumetric change. Whether shearing tends to develop positive (contraction) or negative (dilation) volume change depends on the initial state of the material relative to the critical state which is a function of the relative density and the

confining pressure. The critical state is defined by a surface formed in e-p-q space, which is projected as a line (CSL) in the e-p and q-p planes; e being the void ratio, q the deviatoric stress and p being the mean effective stress. Critical state is considered to be unique for each type of sand. Figure 1.1 illustrates the critical state line (CSL) in e-p plane. Initial loose states, located at the right-hand side of CSL, exhibit contractive behavior which is reflected through reduction of: (i) void ratio, e, in case of drained p-constant loading and (ii) mean effective stress, p, in case of undrained loading, until CSL is reached. Dense states, located at the left-hand side, initially exhibit contractive response until phase transformation line (PTL) is reached. Thereafter, dilative response dominates which is interpreted as increase of: (i) void ratio, e, in case of drained p-constant loading and (ii) mean effective stress, p, in case of undrained loading, until CSL is reached.

This kind of behavior is confirmed experimentally, as shown in Figure 1.2(a). As the initial void ratio increases for a given initial confining pressure, the response tends to be more contractive. In terms of stress-strain curves, a hardening type of response is observed which becomes more intense as the initial void ratio increases. It should be noticed that the void ratio reaches practically the same residual value, known as critical void ratio, irrespectively of the initial value, as it is predicted by the Critical State Theory. It is also worth mentioning that critical state is also reached in p-q space at large strains, as shown by Figure 1.2(b). The stress ratio q/p reaches a unique residual critical stress ratio, irrespectively of the initial conditions.

Apart from the dependency of sand response on the initial void ratio (or initial relative density, D_r), Figure 1.3 demonstrates the impact of initial confining pressure, p. For a given initial relative density, the response becomes more dilative as initial confining pressure decreases. In stress-strain terms, the effect of dilatancy is exhibited by an increase in maximum obtained strength followed by strain softening.

The tendency of positive (dilatancy) or negative (contraction) volumetric change in case of drained loading conditions is expressed through increase or reduction of mean effective stress, respectively, in case of undrained loading, as characteristically shown in Figure 1.4. Experimental results of Figure 1.5 illustrate the behavioral trend under undrained conditions for various initial relative densities and confining pressures. All the evolving stress paths in p-q space converge to the critical state line, which works as a failure envelope, until the ultimate critical stress state is reached.

So far, it has been shown that the behavior of sand is dependent on the relative position of its initial state, in terms of initial density and means effective stress, to the critical state line in e-p plane. However, experimental results depicted in Figure 1.6 indicate dependency on the loading direction, for a given initial state. Despite the given constant distance between initial state and CSL in e-p space, sand exhibits contractive behavior in case of triaxial extension loading, while its response is dilative under triaxial compression loading. This behavioral diversity is attributed to stress-induced anisotropy.

1.1.2 Cyclic Behavior of Sand

Cyclic behavior of sand presents certain differentiations when compared to the monotonic response, which cannot be fully accommodated by the strictly defined Critical State framework. For example, experiments confirm that irrespectively of the initial state relative to the CSL in e-p space, sand exhibits only contractive behavior, in accumulative terms, tending to reach the densest possible configuration, defined by minimum void ratio, e_{min}, under drained conditions, or reach zero values of mean effective stress under undrained conditions, as shown in Figure 1.7. The first tendency leads to densification and increase in strength/stiffness, known as cyclic hardening, (Figures 1.8-1.10), while the latter one is associated with cyclic mobility and liquefaction effects (Figure 1.11(a)). It should be mentioned, though, that the critical state concept applies in p-q space,

where the critical stress ratio is reached at large strains, after a sufficient number of cycles, irrespectively of the drainage conditions.

In other words, the dependency of sand behavior on the initial state relative to CSL in e-p space is not reflected in the same way as in case of monotonic loading, where it determines whether the response will be dilative or contractive. In case of cyclic loading, the above mentioned dependency determines the number of loading cycles needed to achieve either: (i) $e = e_{min}$ (drained conditions) or (ii) $p = 0$ (undrained conditions). The correlation between number of cycles and initial relative density is shown in Figures 1.10 and 1.11(b).

1.2. SCOPE OF DISSERTATION

The scope of the Dissertation is to develop a unified versatile macroscopic constitutive framework that can describe all the aforementioned different aspects of sand behavior under various loading conditions. It is aimed that the proposed constitutive model can be used in practice for relevant geotechnical problems. In this line of thought, minimizing the number of model parameters is intended in order to enhance the usability and applicability of the model.

1.3 STRUCTURE OF DISSERTATION

The Dissertation is structured in three main chapters, each corresponding to an autonomous, self-contained, single paper that has either been published in a peer-reviewed journal and/or conference proceedings, or is undergoing review. However, the sequence of the chapters, as presented below, intends to propose an indicative path to the reader, with each chapter appearing motivated or closely related, in logical order, with the preceding ones.

Chapter 2

This chapter presents a new constitutive model for sand in triaxial space for drained and undrained behavior of sand under monotonic and cyclic loading conditions, with emphasis on liquefaction. The model is based on a modified elastoplasticity scheme combining features of: (a) the bounding surface plasticity, (b) the critical state concept, and (c) a hardening evolution law and unloading-reloading rule inspired by smooth hysteresis models, such as Bouc-Wen type. The model performance is demonstrated through a series of simulations in p-q space, for all combinations (4 in total) of drained and undrained loading with monotonic and cyclic loading. It is shown that the model is capable of reproducing some basic aspects of sand behavior, such as static liquefaction, strain softening, hysteretic loops and cyclic mobility.

Chapter 3

The above proposed formulation is extended in multiaxial space in Chapter 3. Thus, a complete novel constitutive model for sand is proposed as an alternative plasticity formulation that exhibits critical state consistency for both monotonic and cyclic loading and uniqueness of its parameters for a given type of sand, irrespective of loading conditions. The model, designated as Ta-Ger (Tasiopoulou – Gerolymos) sand model is based on a reformulation of perfect elastoplasticity by introducing a hardening law inspired from Bouc-Wen hysteresis. The latter is a smooth hysteresis model originally proposed by Bouc (1971), extended by Wen (1976), and used in random vibration studies of inelastic systems. Since then, modified or extended versions of this model have been extensively used in numerous structural (e.g. Sivaselvan and Reinhorn, 2000; Triantafyllou and Koumousis, 2012) and geotechnical applications (e.g. Pires et al., 1989; Gerolymos and Gazetas, 2005). The developed constitutive formulation can be regarded as a bounding single-surface model with vanished elastic region and the distinguished characteristic of an explicitly formulated plastic matrix instead of a plastic modulus.

The explicitly formulated plastic matrix plays a triple role: (i) it offers a gradual and smooth ("hardening-type") transition from the elastic to perfectly plastic response in order to capture pre-failure nonlinearity and the coupling between elastic and plastic counterparts composing the total strain increment, (ii) it provides an appropriate loading/unloading/reloading mapping rule by tracking the distance from the ultimate perfectly plastic state as defined by the failure surface, which herein, serves as a bounding surface, and (iii) its terms attain values that are strictly bounded within the range of [0,1].

Salient features of the proposed plasticity approach are: (i) a new plastic flow rule based on a revision of Rowe dilatancy theory (1962), accounting for anisotropic distribution of dilatancy to the normal plastic strain increments, as well as densification due to cyclic loading, (ii) a mapping rule and load reversal criterion based on the first order work, inspired from Bouc-Wen hysteresis, and (iii) a new formulation for the evolution of the bounding and phase transformation surfaces as a function of the cumulative deviatoric strain increment, ensuring critical state consistency not only for monotonic but also for cyclic loading.

Comparison with experiments reveals the capability of the model to describe complex patterns of sand behavior, such as densification, cyclic hardening, as well as, liquefaction due to cyclic loading at very large strains (e.g. $\gamma > 8\%$) without exhibiting shear locking.

Chapter 4

An extensive calibration methodology is developed in Chapter 4 aiming at: (i) increasing model predictability and (ii) minimizing the number of internal model parameters. Initially, constitutive formulation was adjusted to Bolton's (1986) empirical correlations for dilatancy, given as a function of relative dilatancy index, I_r; the latter works as a state parameter in the constitutive framework. This step reduces the number of unknown

model parameters to three, besides the ones related directly to measurable physical properties, such as critical state friction angle and elastic modulus. At this stage, the remaining three unknown parameters are expressed as functions of the initial state (relative density and pressure), while inherent fabric effects (such as particle shape, size and packing) on the calibration process are considered. At last, stress-induced anisotropy is dealt with introducing a scalar-valued variable in the model, a function of principal stress rotation angle, α, and the intermediate stress parameter, b, without affecting the number of unknown model parameters. Validation against experimental data was performed in every step for various drained and undrained loading paths in a wide range of α, b values, as well as initial states, for three different types of sand (Toyoura, Fontainebleau, Sacramento–River).

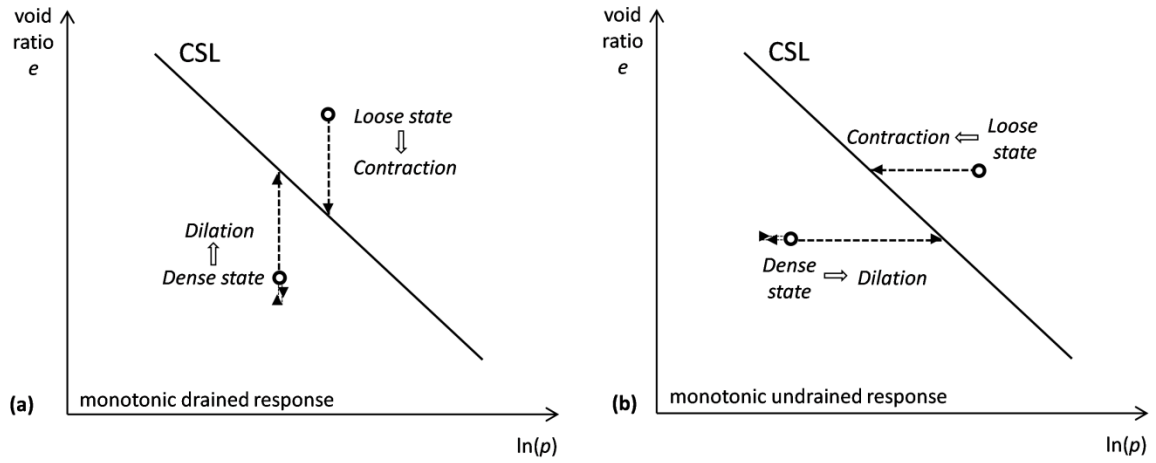

Figure 1.1. Illustration of monotonic behavior of sand in e-p space, where e is the void ratio and p is the mean effective stress: (a) drained and (b) undrained conditions.

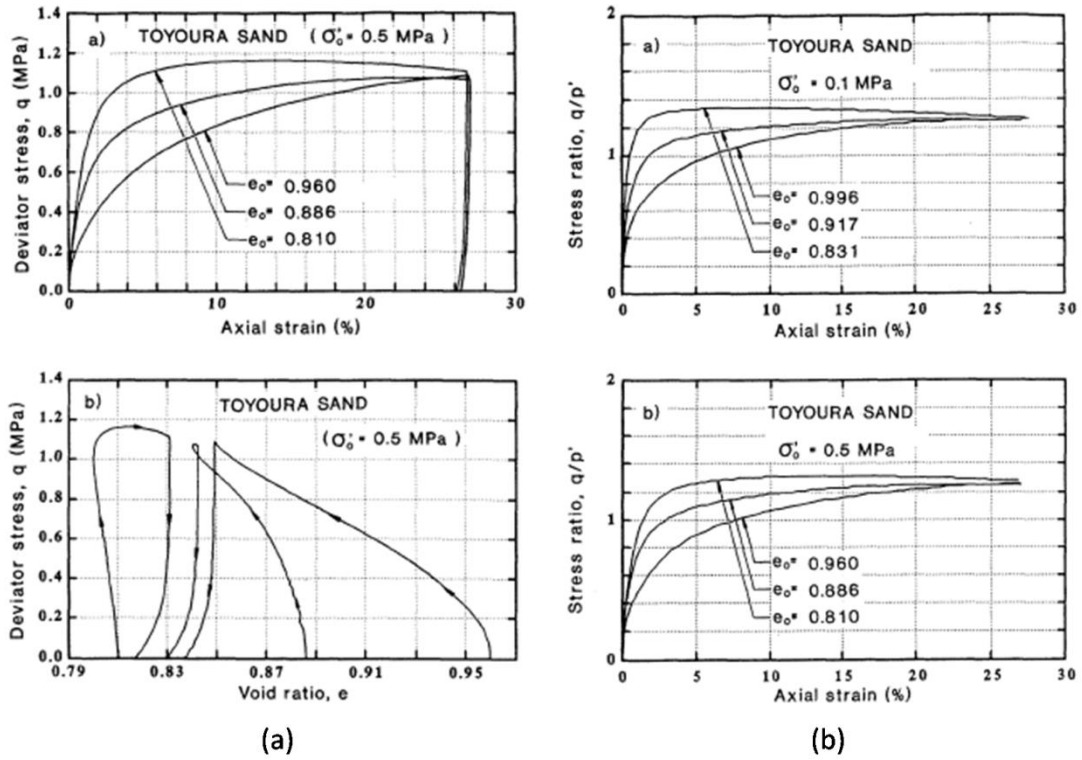

Figure 1.2. Drained triaxial tests: (a) stress-strain curves and void ratio versus deviatoric stress, (b) stress ratio versus axial strain (Verdugo and Ishihara, 1996).

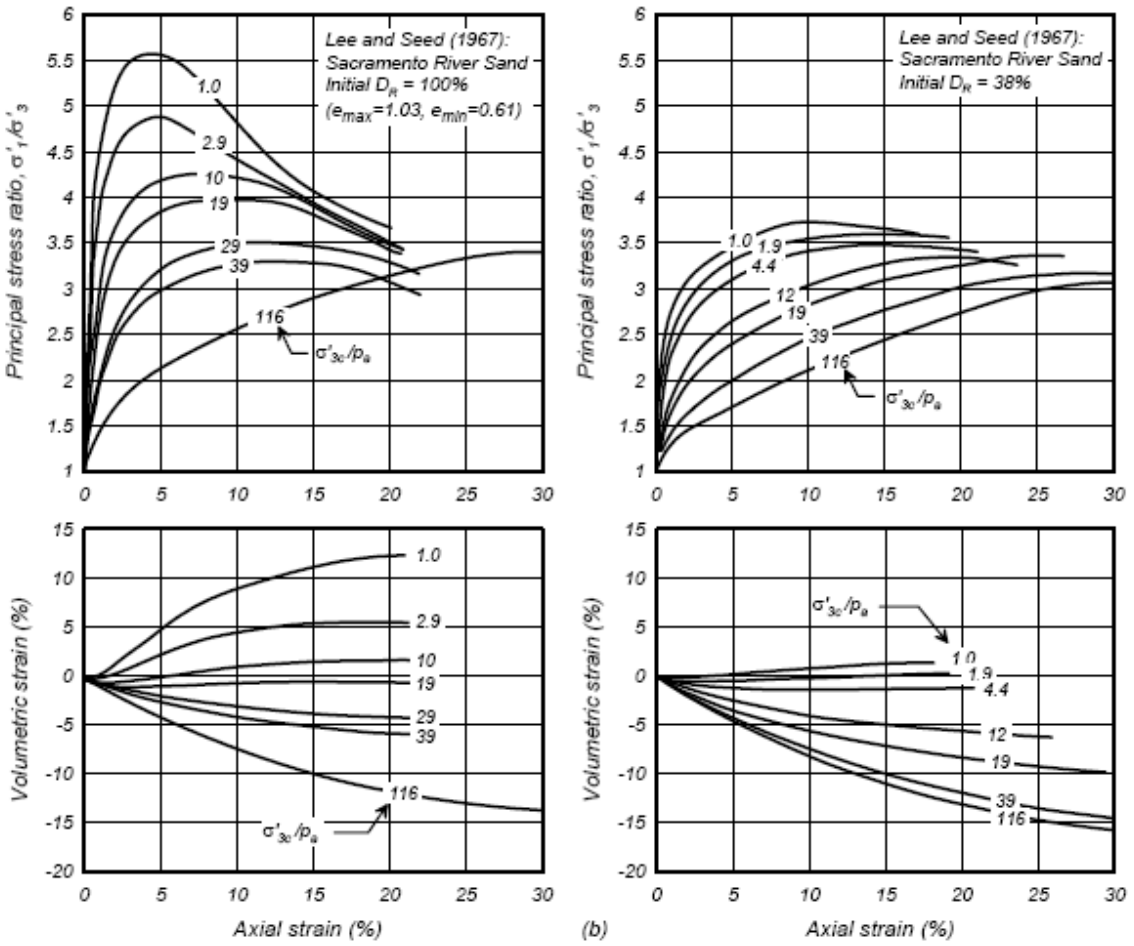

Figure 1.3. Drained triaxial compression tests on loose and dense sand specimens under a range of effective confining stresses (Lee and Seed, 1967).

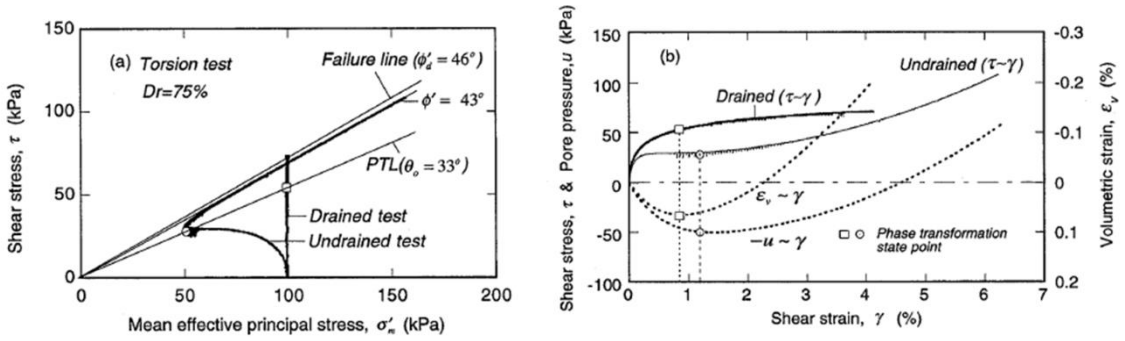

Figure 1.4. Influence of drainage conditions on sand response (Zhang et al., 1997).

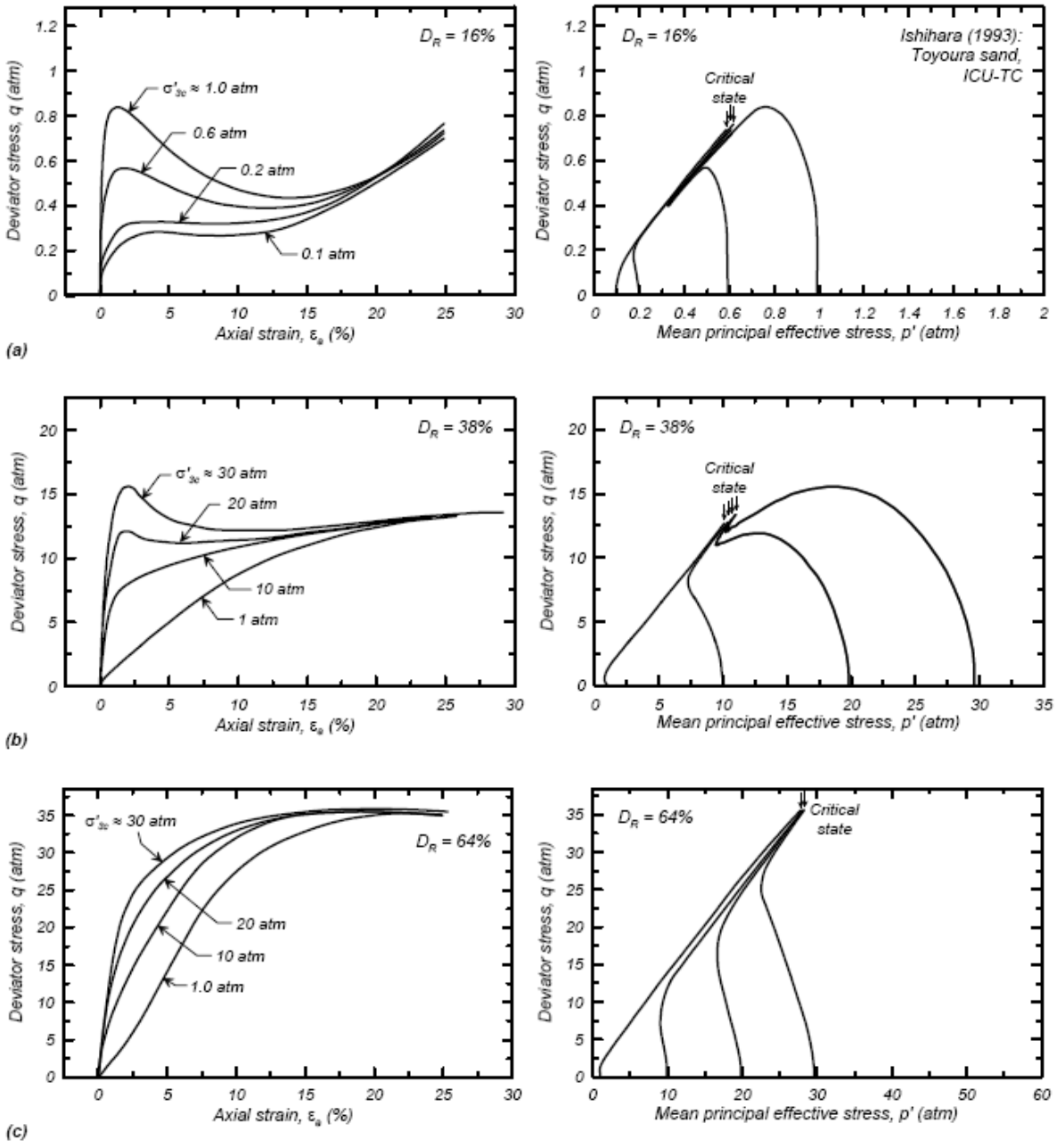

Figure 1.5. Undrained triaxial compression tests on sand specimens of various initial relative densities under a range of effective consolidation stresses (Verdugo and Ishihara, 1996).

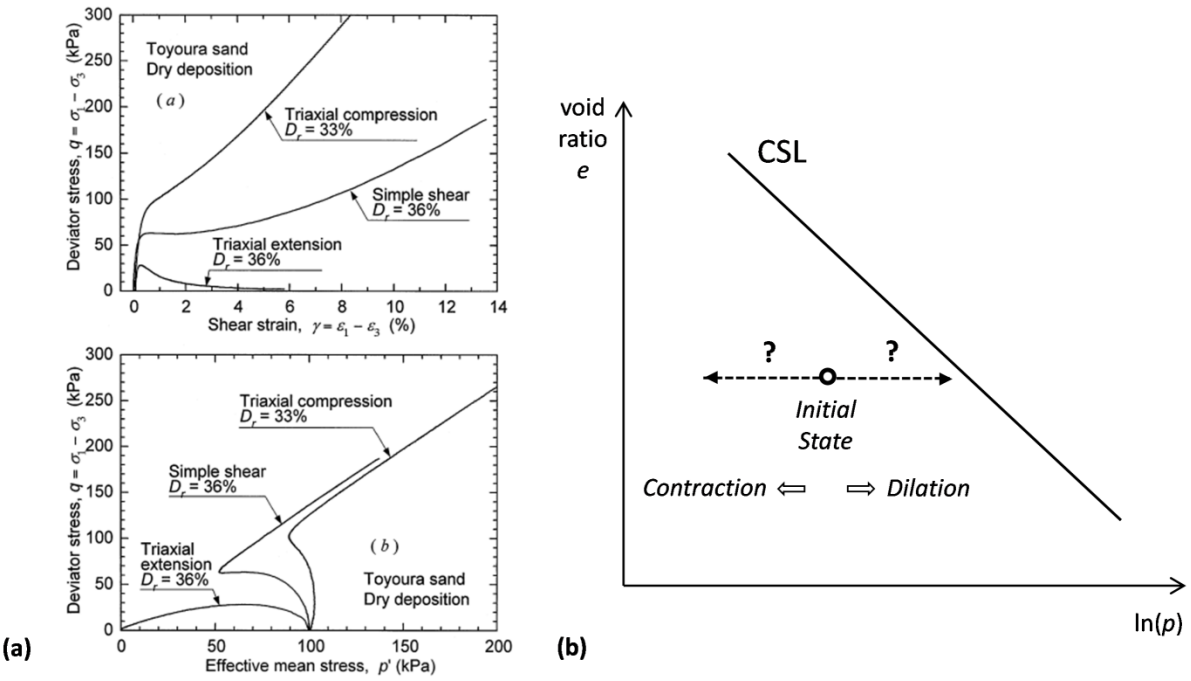

Figure 1.6. (a) Influence of loading direction on sand response (Yoshimine et al., 1998) and (b) how it can be predicted within the critical state framework.

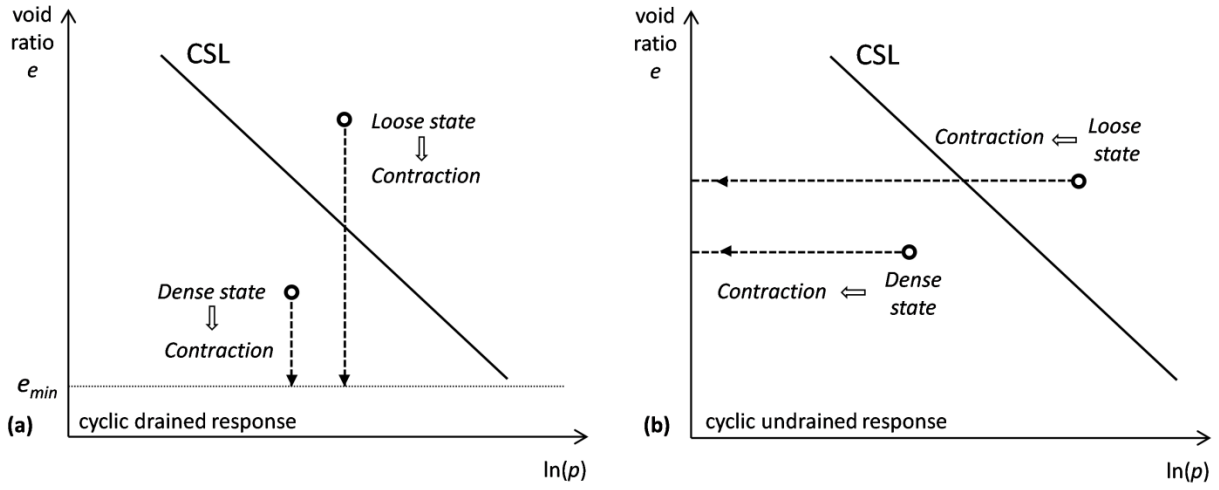

Figure 1.7. Illustration of cyclic behavior of sand in e-p space, where e is the void ratio and p is the mean effective stress: (a) drained and (b) undrained conditions.

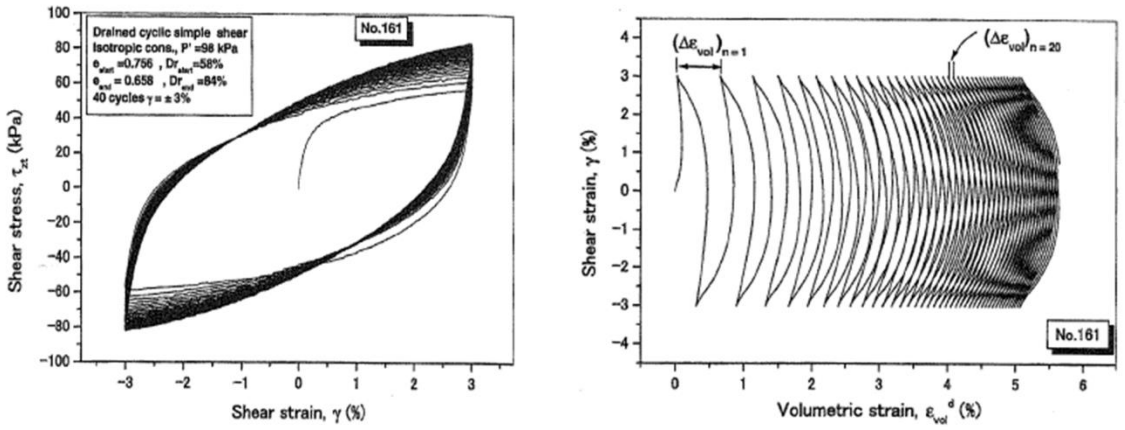

Figure 1.9. Stress-strain curves (left) and volumetric strain versus shear strain for a medium dense sand specimen subjected to drained cyclic simple shear under constant strain amplitude (Shahnazari and Towhata, 2002).

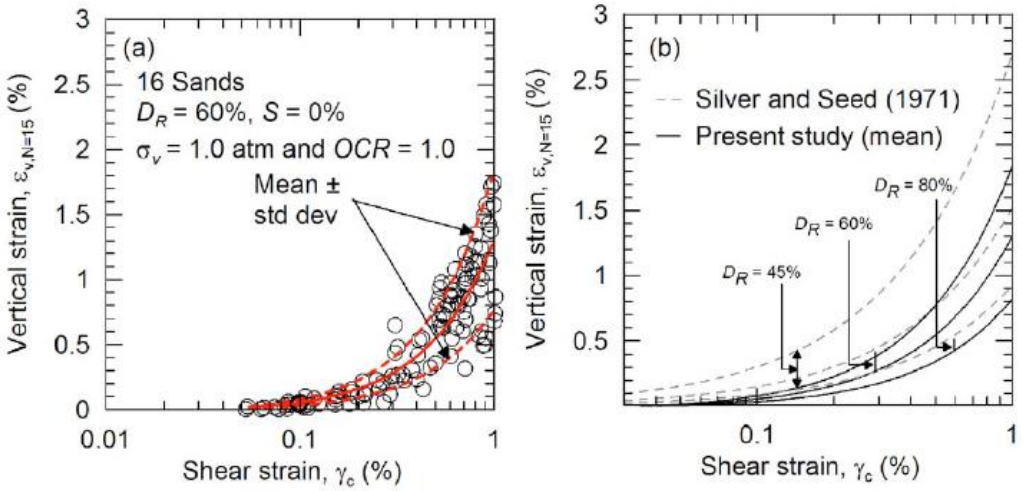

Figure 1.10. Volumetric strains in drained cyclic direct simple shear tests on clean sands (Duku et al. 2008): (a) Results from 16 sands at a relative density of about 60% with an overburden stress of 1.0 atm, and (b) Comparison of trends with earlier relationships by Silver and Seed (1971) for sands at relative densities of 45, 60, and 80%.

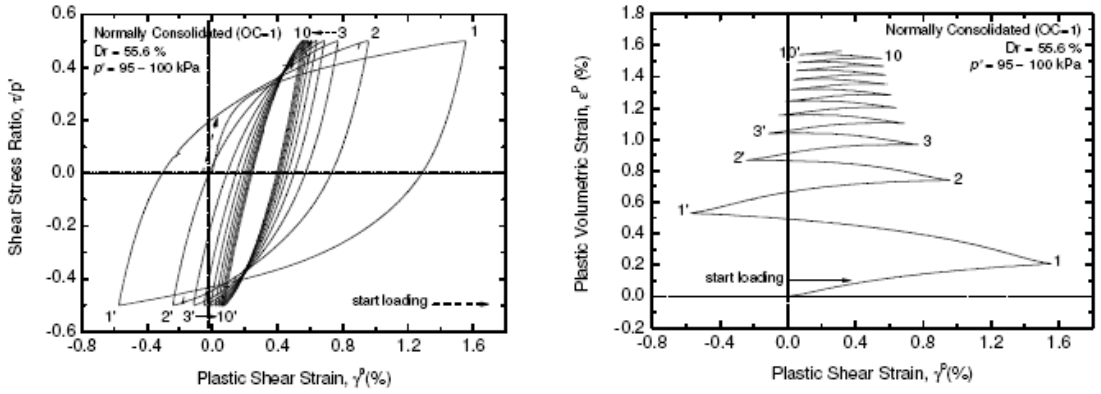

Figure 1.8. Stress-strain curves (left) and volumetric strain versus shear strain for a medium dense sand specimen subjected to drained cyclic simple shear under constant shear stress amplitude (Wahyudi et al., 2010).

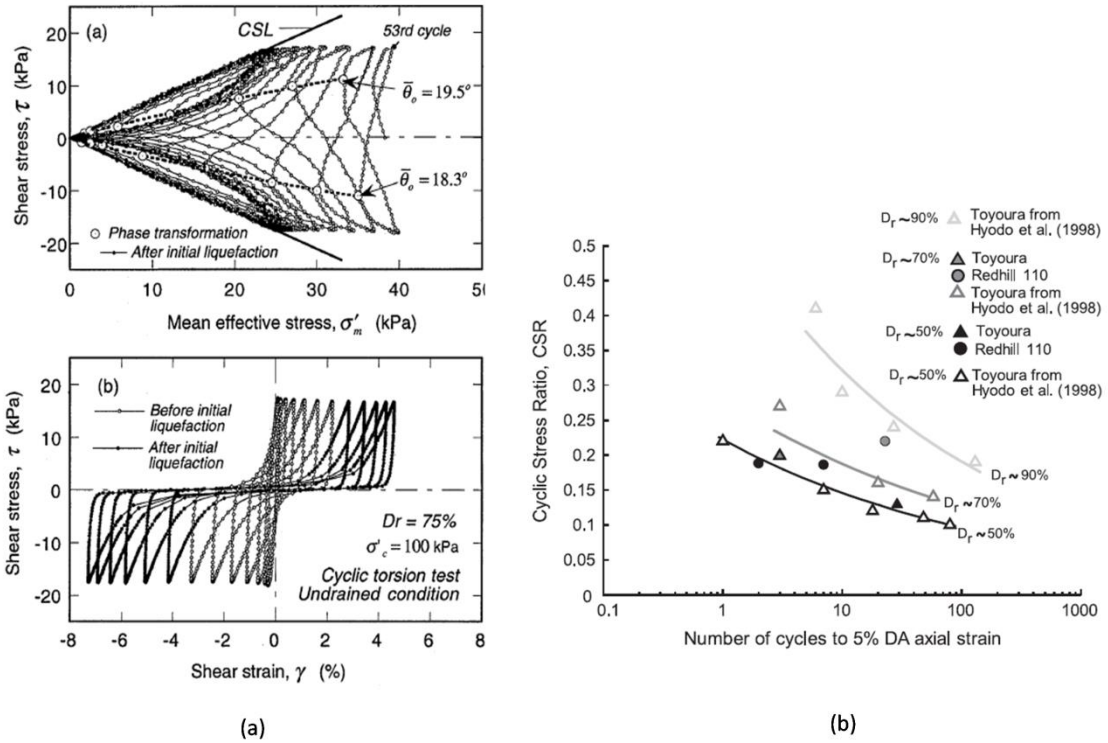

(a) (b)

Figure 1.11. (a) Effective stress path and stress-strain hysteresis observed in a cyclic undrained torsional test (Zhang et al., 1997), (b) Cyclic stress ratio versus number of cycles required to cause 5% of DA axial strain for samples with relative density, D_r of 50%, 70% and 90% (Lombardi et al., 2014).

REFERENCES

Bolton, M. D. (1986). The strength and dilatancy of sands. *Geotechinque* **36**, No. 1, 65-78.

Bouc, R. (1971). Modele mathematique d' hysteresis. *Acustica* **21**, 16-25.

Duku, P. M., Stewart, J. P., and Whang, D. H. (2008). Volumetric strains of clean sands subject to cyclic loads. *J. Geotechnical and Geoenvironmental Eng., ASCE* **134**, No. 8, 1073-1085.

Gerolymos, N. and Gazetas, G. (2005). Constitutive model for 1–D cyclic soil behavior applied to seismic analysis of layered deposits. *Soils and Foundations* **45**, No. 3, 147-159.

Lee, K.L. and Seed, H.B. (1967). Drained strength characteristics of sands. *Journal of Soil Mechanics and Foundation Division, ASCE*, **93**, SM6, 117–41.

Lombardi, D., Bhattacharya, S., Hyodo, M. & Kaneko, T. (2014). Undrained behaviour of two silica sands and practical implications for modelling SSI in liquefiable soils. *Soil Dynamics and Earthquake Engineering*, **66**, 293-304.

Roscoe, K. H., Schofield, A. N., and Wroth, C. P. (1958). On the yielding of soils, *Géotechnique*, **8**, No. 1, 22–53.

Rowe, P. W. (1962). The stress-dilatancy relation for static equilibrium of an assembly of particles in contact. *Proceedings, Royal Soc. London, Ser. A,* Vol. 269, 500–527.

Sivaselvan, M.V., Reinhorn, A. M. (2000). Hysteretic models for deteriorating inelastic structures. *J. Eng. Mech.* **126**, No 6, 633–640.

Schofield, A. N., and Wroth, C. P. (1968) *Critical state soil mechanics*, McGraw-Hill, London.

Shahnazari H. and Towhata I., (2002). Torsion shear tests on cyclic stress-dilatancy relationship of sand, *Soils and Foundations*, **42**, No. 1, 105-119

Triantafyllou, S., Koumousis, V. (2012). An hysteretic quadrilateral plane stress element. *Archive of Applied Mechanics* **82**, 1675-1687.

Verdugo, R and Ishihara, K. (1996). The steady state of sandy soils. *Soils and Foundations* **36**, No.2, 81–91.

Wahyudi S., Chiaro G., De Silva L.I.N. & Koseki J. (2010) Stress-dilatancy behavior of loose sand during cyclic torsional shear loading, *Proc. of the 12th International Summer Symposium of JSCE, Funabashi*, Japan, 183-186.

Wen, Y. K. (1976). Method for random vibration of hysteretic systems. *Journal of Engineering Mechanic, ASCE* **102**, 249-263.

Yoshimine, M., Ishihara, K., and Vargas, W. (1998). Effects of principal stress direction and intermediate principal stress on undrained shear behavior of sand. *Soils and Foundations*, **38**, No 3, 179–188.

Zhang, J. M., Shamoto, Y. and Tokimatsu, K. (1997). Moving Critical and Phase-Transformation Stress State Lines of Saturated Sand during Undrained Cyclic Shear, *Soils and Foundations* **37**, No.2, 51-59.

CHAPTER 2

Development of a Modified Elastoplasticity Model for Sand in Triaxial Space

ABSTRACT

The key prerequisite to performance based design of geotechnical structures is the reliable estimation of the induced displacements. Thus, the need for advanced yet practical constitutive modeling of soil behavior continuously becomes more profound and demanding. This chapter presents a new simple effective stress model in triaxial space for drained and undrained behavior of sand under monotonic and cyclic loading conditions, with emphasis on liquefaction. The model is formulated in the framework of classical elastoplasticity, and combines features of: (a) the bounding surface plasticity, (b) the critical state concept, and (c) a hardening evolution law and unloading-reloading rule inspired by smooth hysteresis models, such as Bouc-Wen type. The predictive capabilities of the model are demonstrated through simulations of loading tests in p-q space.

2.1 INTRODUCTION

Performance based analysis is increasingly gaining ground in daily practice against conventional pseudostatic analysis. The necessity of developing economically efficient solutions without jeopardizing safety, is the main reason for this drastic change in the way we you used to design our structures.

However, the effectiveness of a performance based design approach strongly hinges on the ability of the utilized numerical tool to realistically calculate the soil and structural displacements for a wide range of loading paths and initial conditions. Apparently, the constitutive modeling of soil behavior plays a decisive role on this. The behavioral diversity of sand for different loading (drained /undrained, monotonic/cyclic), initial stress and fabric conditions, renders its modeling a difficult and challenging task. The suitability of the used constitutive model is evaluated by its capability to capture the trends across all these conditions without recalibration of its parameters for each specific case, but also by its simplicity. Too many parameters might increase the versatility of the model at the risk, however, of losing its physical meaning.

In the last three decades, many constitutive models for sand have been proposed, each with varying degree of accuracy and applicability. The most promising ones are plasticity-based and incorporate the effective stress and critical state concepts (e.g. Ishihara and Towhata, 1980; Cubrinovski and Ishihara, 2000; Dafalias and Manzari, 2004; Park and Byrne, 2004; Boulanger et al., 2011). In this chapter, a brief mathematical description of a new constitutive model for sand in triaxial space is presented.

The model, which is motivated by the BWGG constitutive law (Gerolymos, 2002; Gerolymos and Gazetas, 2005), combines features of the bounding surface plasticity and critical state concept. Having the BWGG genes in its DNA, the proposed model can be consistent with almost any pair of shear modulus and damping curves of the literature, while at the same time the corresponding experimentally observed hysteretic soil

behavior is realistically reproduced. At this stage of development the Drucker-Prager failure envelope is used as bounding surface, but modifications can be easily implemented to account for Lode angle dependency, as it will be shown in the multiaxial formulation in Chapter 3. The combined influence of density and confining stress on the response is efficiently taken into account through the critical state approach.

The ability of the model to realistically reproduce complex patterns of monotonic and cyclic behavior such as hysteretic response, dilation, contraction, loss of strength and cyclic mobility in undrained monotonic and cyclic loading, respectively, etc. is highlighted through a series of numerical examples in p-q loading space.

2.2 CONSTITUTIVE EQUATIONS

2.2.1 Review of classical elastoplasticity

Within the framework of deformation theory of classical elastoplasticity, the incremental total deformation, $d\boldsymbol{\varepsilon}$ is decomposed into the elastic and plastic components $d\boldsymbol{\varepsilon}^e$ and $d\boldsymbol{\varepsilon}^p$ by a simple superposition:

$$d\boldsymbol{\varepsilon} = d\boldsymbol{\varepsilon}^e + d\boldsymbol{\varepsilon}^p \qquad (2.1)$$

The plastic strain increment is obtained from the flow rule:

$$d\boldsymbol{\varepsilon}^p = \langle L \rangle \frac{\partial g}{\partial \boldsymbol{\sigma}} \qquad (2.2)$$

implying normality to the plastic potential function g. L is a positive scalar of proportionality designated as the loading index.

Substituting Eq. (2.2) into Eq. (2.1) and applying elasticity theory, the following stress-strain relationship is obtained:

$$d\boldsymbol{\sigma} = \mathbf{E}^{e}\left(d\boldsymbol{\varepsilon} - \langle L\rangle \frac{\partial g}{\partial \boldsymbol{\sigma}}\right) \tag{2.3}$$

For a perfectly plastic material, the yield surface is fixed in stress space, and therefore plastic deformation occurs only when the stress path moves on the yield surface. Thus, the loading condition at failure is postulated by the following consistency equation:

$$df = 0 \Rightarrow \left(\frac{\partial f}{\partial \boldsymbol{\sigma}}\right)^{\mathrm{T}} d\boldsymbol{\sigma} = 0 \tag{2.4}$$

Combining Eqs. (2.3) and (2.4), and after some algebra, the stress-strain relationship is reformulated into:

$$d\boldsymbol{\sigma} = \mathbf{E}^{ep} d\boldsymbol{\varepsilon} \tag{2.5}$$

in which $\mathbf{E}^{ep}$ is the elasto-plastic matrix, given by:

$$\mathbf{E}^{ep} = \mathbf{E}^{e}\left[\mathbf{I} - \boldsymbol{\Phi}_{g}\left(\boldsymbol{\Phi}_{f}^{T}\mathbf{E}^{e}\boldsymbol{\Phi}_{g}\right)^{-1}\boldsymbol{\Phi}_{f}^{T}\mathbf{E}^{e}\right] \tag{2.6}$$

in which $\boldsymbol{\Phi}_f$ and $\boldsymbol{\Phi}_g$ account for the gradient to the failure surface and plastic flow rule, respectively:

$$\boldsymbol{\Phi}_{f} = \frac{\partial f}{\partial \boldsymbol{\sigma}} \quad , \quad \boldsymbol{\Phi}_{g} = \frac{\partial g}{\partial \boldsymbol{\sigma}} \tag{2.7}$$

2.2.2 Modified elastoplasticity

Hardening and Unloading-Reloading laws

Hardening and hysteretic behavior is introduced by inserting the matrices **H** and **η** into Eq. (2.6):

$$\mathbf{E}_{h}^{ep} = \mathbf{E}^{e}\left(\mathbf{I} - \mathbf{BH}\right)\boldsymbol{\eta} \tag{2.8}$$

The terms in matrix **H** are functions of the dimensionless hardening parameter ζ, which is inspired by the Bouc-Wen smooth hysteresis model Bouc (1971) and its extended versions (Wen, 1976 ; Gerolymos and Gazetas, 2005), and η (Gerolymos and Gazetas, 2005; Drosos et al., 2012) accounts for stiffness degradation by modifying the shape and size of the hysteretic loops according to the amplitude of the deviatoric strain ε_q . Finally, **B** is the abbreviation of the right-hand side term inside the parentheses of Eq. (2.6):

$$\mathbf{B} = \mathbf{\Phi}_g \left(\mathbf{\Phi}_f^T \mathbf{E}^e \mathbf{\Phi}_g \right)^{-1} \mathbf{\Phi}_f^T \mathbf{E}^e \qquad (2.9)$$

Elastic Moduli

The terms in matrix $\mathbf{E}^e$ include the shear and bulk moduli which are expressed as functions of the mean effective stress p, according to:

$$G = A_o p_\alpha \left(\frac{p}{p_\alpha} \right)^m \qquad K = \frac{2(1+v)}{3(1-2v)} G \qquad (2.10)$$

in which, A_o is a dimensionless material parameter, v is the Poisson's ratio, p_a is the atmospheric pressure, and m is a dimensionless parameter determining the rate of variation of G and K with p.

2.2.3 Formulation in p-q space

Elastic Matrix

The elastic deviatoric and volumetric strain increments, $d\varepsilon_q^e$ and $d\varepsilon_p^e$ in respect, are used to calculate deviatoric, dq , and mean effective, dp , stress increments by:

$$dp = K d\varepsilon_p^e \qquad (2.11)$$

$$dq = 3G d\varepsilon_q^e \qquad (2.12)$$

in which, G and K are the elastic shear and bulk moduli, respectively, estimated by Eqs. (2.10). Thus, the elastic matrix in triaxial space is given by:

$$\mathbf{E}^e = \begin{bmatrix} K & 0 \\ 0 & 3G \end{bmatrix} \tag{2.13}$$

Yield Function

At the current stage of development, the model incorporates the Drucker-Prager failure envelope as the bounding surface:

$$f = q - M_s p = 0 \tag{2.14}$$

in which, M_s is the ultimate strength line in q-p space.

Eq. (2.14) implies the following consistency condition at failure:

$$f = 0 \Leftrightarrow \frac{q}{M_s p} = 1 \tag{2.15}$$

Following Eq. (2.15), the hardening parameter, ζ, is defined as:

$$\zeta = \left| \frac{q}{M_s p} \right| \tag{2.16}$$

The hardening parameter, ζ, is bounded, strictly obtaining values within the range [0, 1]. At reversal points, ζ is transformed to ζ_α , according to:

$$\zeta_a = \left| \frac{\zeta - \zeta_{max}}{2} \right| \tag{2.17}$$

in which ζ_{max} is the maximum value of ζ at the previous reversal (pivot) point. Hence, hardening parameter ζ_α becomes equal to 0 at the occurrence of loading reversal, indicating elastic response at the beginning of unloading/reloading.

The hardening matrix **H**, for monotonic loading, is defined as:

$$\mathbf{H}=\begin{bmatrix}\zeta^{n} & 0\\ 0 & \zeta^{n}\end{bmatrix} \tag{2.18}$$

where *n* is an exponential parameter which "controls" the distance of the current stress state from the failure line (Gerolymos and Gazetas, 2005). For cycling loading parameter ζ_α of Eq. (2.17) is used for the formation of the plastic matrix:

$$\mathbf{H}=\begin{bmatrix}\zeta_\alpha{}^{n} & 0\\ 0 & \zeta_\alpha{}^{n}\end{bmatrix} \tag{2.19}$$

Details on the role of hardening parameter ζ and exponent n will be given in Chapter 3.

Finally, the gradient to the failure surface described by Eq. (2.14), is given by:

$$\Phi_f=\begin{bmatrix}\dfrac{\partial f}{\partial p}\\ \dfrac{\partial f}{\partial q}\end{bmatrix}=\begin{bmatrix}-M_s\\ 1\end{bmatrix} \tag{2.20}$$

Flow rule

The stress-dilatancy relationship, adopted by the model, is based on Rowe's dilatancy theory (Rowe 1962). Dilatancy, defined as the ratio of the plastic volumetric strain increment, $d\varepsilon_p{}^p$, over the plastic deviatoric strain increment, $d\varepsilon_q{}^p$ depends on the distance of the current stress ratio, $q / p = \zeta M_s$ from the phase transformation line, M_{pt}, as follows:

$$d=\frac{d\varepsilon_p{}^p}{d\varepsilon_q{}^p}=\left(M_{pt}-\left|\frac{q}{p}\right|\right)=\left(M_{pt}-\zeta M_s\right) \tag{2.21}$$

Assuming associativity only for the plastic deviatoric strain increment:

$$d\varepsilon_q{}^p=\langle L\rangle \tag{2.22}$$

the plastic volumetric strain increment is estimated, combining Eqs.(2.21) and (2.22):

$$d\varepsilon_p{}^p = \langle L \rangle \left(M_{pt} - \zeta M_s \right) \tag{2.23}$$

Eqs. (2.21) to (2.23), which imply that a non-associative plastic flow rule is used, determine the gradient to the plastic potential surface, $\mathbf{\Phi}_g$, according to:

$$\Phi_g = \begin{bmatrix} \frac{\partial g}{\partial p} \\ \frac{\partial g}{\partial q} \end{bmatrix} = \begin{bmatrix} \left(M_{pt} - \zeta M_s \right) \\ 1 \end{bmatrix} = \begin{bmatrix} d \\ 1 \end{bmatrix} \tag{2.24}$$

Modified Elastoplastic Matrix

Matrix B of Eq. (2.9) is calculated using matrices of Eqs. (2.13), (2.20) and (2.24):

$$\mathbf{B} = \mathbf{\Phi}_g \left(\mathbf{\Phi}_f^T \mathbf{E}^e \mathbf{\Phi}_g \right)^{-1} \mathbf{\Phi}_f^T \mathbf{E}^e \Leftrightarrow$$

$$\mathbf{B} = \frac{\begin{bmatrix} d \\ 1 \end{bmatrix} \begin{bmatrix} -M_s & 1 \end{bmatrix} \begin{bmatrix} K & 0 \\ 0 & 3G \end{bmatrix}}{\begin{bmatrix} -M_s & 1 \end{bmatrix} \begin{bmatrix} K & 0 \\ 0 & 3G \end{bmatrix} \begin{bmatrix} d \\ 1 \end{bmatrix}} = \frac{\begin{bmatrix} -dM_s & d \\ -M_s & 1 \end{bmatrix} \begin{bmatrix} K & 0 \\ 0 & 3G \end{bmatrix}}{\begin{bmatrix} -KM_s & 3G \end{bmatrix} \begin{bmatrix} d \\ 1 \end{bmatrix}} = \frac{\begin{bmatrix} -KM_s d & 3Gd \\ -KM_s & 3G \end{bmatrix}}{-KM_s d + 3G} \Leftrightarrow \tag{2.25}$$

$$\mathbf{B} = \begin{bmatrix} \frac{-KM_s d}{-KM_s d + 3G} & \frac{3Gd}{-KM_s d + 3G} \\ \frac{-KM_s}{-KM_s d + 3G} & \frac{3G}{-KM_s d + 3G} \end{bmatrix}$$

The modified elastoplastic matrix, $\mathbf{E}_h^{ep}$, of Eq. (2.8) is calculated by substitution with Eqs. (2.13), (2.25) and (2.18):

$$\mathbf{E}_h^{ep} = \mathbf{E}^e\left(\mathbf{I}-\mathbf{BH}\right) \Leftrightarrow$$

$$\mathbf{E}_h^{ep} = \begin{bmatrix} K & 0 \\ 0 & 3G \end{bmatrix}\left(\begin{bmatrix} 1 & 0 \\ 0 & 1 \end{bmatrix} - \begin{bmatrix} \dfrac{-KM_s d}{-KM_s d+3G} & \dfrac{3Gd}{-KM_s d+3G} \\ \dfrac{-KM_s}{-KM_s d+3G} & \dfrac{3G}{-KM_s d+3G} \end{bmatrix}\begin{bmatrix} \zeta^n & 0 \\ 0 & \zeta^n \end{bmatrix}\right) \Leftrightarrow$$

$$\mathbf{E}_h^{ep} = \begin{bmatrix} K & 0 \\ 0 & 3G \end{bmatrix}\left(\begin{bmatrix} 1 & 0 \\ 0 & 1 \end{bmatrix} - \begin{bmatrix} \dfrac{-KM_s d}{-KM_s d+3G}\zeta^n & \dfrac{3Gd}{-KM_s d+3G}\zeta^n \\ \dfrac{-KM_s}{-KM_s d+3G}\zeta^n & \dfrac{3G}{-KM_s d+3G}\zeta^n \end{bmatrix}\right) \Leftrightarrow$$

$$\mathbf{E}_h^{ep} = \begin{bmatrix} K & 0 \\ 0 & 3G \end{bmatrix}\begin{bmatrix} 1-\dfrac{-KM_s d}{-KM_s d+3G}\zeta^n & \dfrac{3Gd}{-KM_s d+3G}\zeta^n \\ \dfrac{-KM_s}{-KM_s d+3G}\zeta^n & 1-\dfrac{3G}{-KM_s d+3G}\zeta^n \end{bmatrix} \Leftrightarrow$$

$$\mathbf{E}_h^{ep} = \begin{bmatrix} K-\dfrac{-K^2M_s d}{-KM_s d+3G}\zeta^n & \dfrac{3KGd}{-KM_s d+3G}\zeta^n \\ \dfrac{-3KGM_s}{-KM_s d+3G}\zeta^n & 3G-\dfrac{9G^2}{-KM_s d+3G}\zeta^n \end{bmatrix} \qquad (2.26)$$

The only difference between the modified elastoplastic matrix, $\mathbf{E}_h^{ep}$, and the elastoplastic matrix, $\mathbf{E}^{ep}$, resulting from elastic-perfectly plastic formulation, given by the following equation:

$$\mathbf{E}^{ep} = \begin{bmatrix} K-\dfrac{-K^2M_s d}{-KM_s d+3G} & \dfrac{3KGd}{-KM_s d+3G} \\ \dfrac{-3KGM_s}{-KM_s d+3G} & 3G-\dfrac{9G^2}{-KM_s d+3G} \end{bmatrix} \qquad (2.27)$$

is attributed to the introduction of hardening parameter ζ^n, which provides a smooth hysteretic interpolation, Bouc-Wen motivated, between elastic and perfect plastic stress states. Thus, stress increments are calculated as:

$$\begin{bmatrix} dp \\ dq \end{bmatrix} = \begin{bmatrix} A & B \\ C & D \end{bmatrix} \begin{bmatrix} d\varepsilon_p \\ d\varepsilon_q \end{bmatrix} \tag{2.28}$$

where:

$$A = K - \frac{-K^2 M_s d}{-KM_s d + 3G}$$

$$B = \frac{3KGd}{-KM_s d + 3G}$$

$$C = \frac{-3KGM_s}{-KM_s d + 3G} \tag{2.29}$$

$$D = 3G - \frac{9G^2}{-KM_s d + 3G}$$

If matrix **η**, which consists of only diagonal terms:

$$\boldsymbol{\eta} = \begin{bmatrix} \eta & 0 \\ 0 & \eta \end{bmatrix} \tag{2.30}$$

is incorporated into Eq. (2.27), then the elastoplastic matrix is modified as:

$$\mathbf{E}_{h,\eta}^{ep} = \eta \begin{bmatrix} K - \dfrac{-K^2 M_s d}{-KM_s d + 3G} & \dfrac{3KGd}{-KM_s d + 3G} \\ \dfrac{-3KGM_s}{-KM_s d + 3G} & 3G - \dfrac{9G^2}{-KM_s d + 3G} \end{bmatrix} \tag{2.31}$$

2.2.4. Critical state concept

The essence of the critical state concept is that no change in volume occurs when the current stress state reaches the critical state, while the shear deformation continuously increases. In order to achieve this kind of performance upon critical state, both the phase transformation line, M_{pt} and the ultimate strength line, M_s, should evolve in p-q space converging to the critical state line, M_{cs} and producing zero plastic volumetric change

when $M_{pt} = M_s = M_{cs}$. The evolution of the ultimate strength line is expressed as a function of the cumulative total deviatoric strain, $\sum|d\varepsilon_q|$:

$$M_s = M_{cs} + \left[M_{sp} + \left(M_{s0} - M_{sp} \right) e^{-c_1 \sum |d\varepsilon_q|} - M_{cs} \right] e^{-c_2 \sum |d\varepsilon_q|} \quad (2.32)$$

where M_{s0} is an initial value of the ultimate strength, and M_{sp} is a maximum value that can be potentially reached depending on the model parameters c_1 and c_2.

The phase transformation line evolves according to following expression:

$$M_{pt} = M_{cs} + \left(M_{pt0} - M_{cs} \right) e^{-c_3 \sum |d\varepsilon_q|} \quad (2.33)$$

in which M_{pt0} is the initial value of M_{pt} , c_3 is a model parameter and $\sum|d\varepsilon_q|$ expresses the accumulation of total deviatoric strain increments.

2.3 MODEL PERFORMANCE

Simulations of drained and undrained behavior of sand under monotonic and cyclic loading have been performed in p-q space (Figures 2.1-2.8). Internal model parameter η of Eq. (2.31) is set equal to unity for subsequent numerical examples of Figures 2.1 to 2.8. Both drained and undrained simulations are strain controlled; thus, the applied deviatoric strain increment $d\varepsilon_q$ is considered known. In case of drained loading, the mean effective stress, p, is assumed constant, so that dp = 0. According to Eqs. (2.28) and (2.29), the deviatoric stess increment, dq, is calculated as:

$$dq = \left(-\frac{BC}{A} + D \right) d\varepsilon_q \quad (2.34)$$

and the volumetric strain increment, $d\varepsilon_p$, is obtained by:

$$d\varepsilon_p = -\frac{B}{A} \left| d\varepsilon_q \right| \quad (2.35)$$

In case of undrained simulations, the volumetric strain, ε_p, is assumed constant, thus, $de_p = 0$. The deviatoric stress increment, dq and the mean effective stress increment are estimated according to Eqs. (2.28) and (2.29):

$$dq = D d\varepsilon_q \tag{2.36}$$

$$dp = B\left|d\varepsilon_q\right| \tag{2.37}$$

Regarding the monotonic loading, four different relative densities were examined. Specifically for the monotonic undrained case (Figures 2.1-2.3), the evolution of phase transformation and ultimate strength lines are illustrated in Figure 2.3 as a function of deviatoric strain, in order to better demonstrate that both lines reach the critical state line at large strains. Moreover, it is worth noting that for loose sands the phase transformation line is initially located above the ultimate strength line in p-q space and vice versa for denser sands. This is attributed to the more contractive behavior which leads them directly to the critical state with no phase transformation (Yoshimine and Ishihara, 1998). The opposite behavior is observed for denser sand crossing the phase transformation line (contractive response) before "moving" towards the critical state (dilative response).

The set of model parameters, shown in Table 2.1, is common for all simulations with three exceptions: i) the peak value of ultimate strength line, M_{sp} and ii) the initial value of phase transformation line, M_{pt0} , and iii) parameter c_3 in case of cyclic loading. Readjustment of the values of M_s and M_{pt0}, for each specific initial state (loose, medium, dense etc.) is of critical significance to the model, since they determine how dilative or contractive the response will be. Lower values of parameter c_3 in case of undrained cyclic loading indicate slower evolution of phase transformation line towards critical state; thus allowing for more cycles to occur once the stress path has reached the failure envelope, close to the apex (cyclic mobility), creating the "butterfly effects" (Ishihara and Towhata, 1980). In case of cyclic drained loading, slower evolution of phase transformation line towards critical state leads to less accumulation of volumetric strain for a certain number of cycles, due to generation of greater "uplift" of the e_p-e_q curve, close to the reversal points.

Overall, it should be mentioned that critical state, M_{cs}, is achieved under monotonic, as well as cyclic loading.

Last, model validation, against experimental data under undrained simple shear loading (Yoshimine et al., 1998) for various relative densities, is demonstrated in Figure 2.8. Table 2.2 shows the calibrated model parameters offering the best fit with the experiments. It is worth noticing that almost all model parameters remain the same within the range of tested relative densities, apart from M_{pt0} and M_{sp}. In particular, as D_{r0} increases, M_{sp} increases while M_{pt0} decreases, highlighting the need to correlate the values of these with initial state (D_{r0}, p_0). Indeed, based on Eq. (2.21), decreasing M_{pt0} and increasing M_{sp} leads to negative values of dilatancy, d, indicating a more dilative response and vice versa. It is interesting to mention that the initial value of the bounding line, M_{s0}, is less than the value of M_{cs}, irrespectively of the initial relative density (an observation that will appear to be useful in calibration process described in Chapter 4.)

Finally, demonstration of the impact of parameter η of Eq. (2.31) on the response, in terms of stress-strain loops, is shown in Figure 2.9 for three different strain amplitudes. Evidently, for values of parameter η less than 1, the secant shear modulus along with the size of the loop decreases, leading to smaller hysteretic damping. On the other hand, greater values of parameter η less than 1 lead to increase of the secant shear modulus and the area of the loop producing larger hysteretic damping. Appropriate calibration of parameter η can offer consistency with any pair of shear modulus and damping curves of the literature.

2.4 CONCLUSIONS

A new constitutive model for sand in triaxial space was presented, based on a modified elastoplasticity scheme and founded on the effective stress and critical state concepts. The constitutive formulation combines features of classical elastoplasticity with a hardening law

and an unloading-reloading rule of the Bouc-Wen type. The model performance was demonstrated through a series of simulations in p-q space, for all combinations (4 in total) of drained and undrained loading with monotonic and cyclic loading. It was shown that the model is capable of reproducing the basic aspects of sand behavior, such as static liquefaction, strain softening, hysteretic loops, cyclic mobility etc.

REFERENCES

Bouc, R. (1971). Modele mathematique d' hysteresis. *Acustica* **21**, 16-25.

Boulanger, R.W., Kamai R. and Ziotopoulou, K. (2011)."Numerical modeling of liquefaction effects", Proc. of 4th IASPEI/IAEE International Symposium, August 23-26, 2011, UC, Santa Barbara.

Cubrinovski, M. and Ishihara, K. (2000). "State concept and modified elastoplasticity for sand modelling", Soils and Foundations Vol. 40, No. 5, pp. 124 – 125.

Dafalias, Y. F. and Manzari, M. T. (2004). "Simple plasticity sand model accounting for fabric change effects", Journal of Engineering Mechanics, ASCE, Vol. 130, No. 6, pp. 622 – 634.

Drosos V., Gerolymos N., Gazetas G., (2012). "Constitutive model for soil amplification of ground shaking: Parameter calibration, comparisons, validation", Soil Dynamics and Earthquake Engineering (Submitted for Publication).

Gerolymos N., (2002). "Constitutive model for static and dynamic response analysis of soil, soil-pile and soil-caisson", Ph.D. thesis, National Technical University of Athens, School of Civil Engineering (in Greek).

Gerolymos N., Gazetas G. (2005), "Constitutive model for 1–D cyclic soil behavior applied to seismic analysis of layered deposits", Soils and Foundations, 45(3), 147-159.

Ishihara, K. and Towhata, I. (1980). "One-dimensional soil response analysis during earthquakes based on effective stress method", Journal of the Faculty of Engineering, University of Tokyo (B), Vol. 35, No. 4, pp. 665 – 700.

Park, S.S. and Byrne, P.M. (2004) "Practical constitutive model for soil liquefaction", Proc. of 9th Intl Sym on Numerical Mo.dels in Geomechanics NUMOG IX.

Rowe, P. W. (1962). ‘‘The stress-dilatancy relation for static equilibrium of an assembly of particles in contact”, Proc. R. Soc. London, Ser. A, 269, 500–527.

Yoshimine, M. and Ishihara, K. (1998). “Flow potential of sand during liquefaction”, Soils and Foundations, Vol. 38, No. 3, pp. 189 – 198.

Yoshimine, M., Ishihara, K., and Vargas, W. (1998). Effects of principal stress direction and intermediate principal stress on undrained shear behavior of sand. *Soils and Foundations*, **38**, No 3, 179–188.

Wen, Y. K. (1976). Method for random vibration of hysteretic systems. *Journal of Engineering Mechanic, ASCE* **102**, 249-263.

Table 2.1. Model parameters for simulations illustrated in Figures 2.1-2.7 and 2.9.

		Monotonic Loading (Drained & Undrained)				***Drained cyclic loading***	***Unrained cyclic loading***
		Very loose sand	**Loose sand**	**Medium sand**	**Dense sand**	**Medium sand**	**Dense sand**
Elasticity	A_o	250	250	250	250	250	250
	m	0.6	0.6	0.6	0.6	0.6	0.6
	v	0.2	0.2	0.2	0.2	0.2	0.2
Ultimate strength	M_{so}	1	1	1	1	1	1
	M_{sp}	1.2	1.3	1.4	1.8	1.4	1.8
	c_1	40	40	40	40	40	40
	c_2	40	40	40	40	40	40
Phase transformation	M_{pto}	1.22	1.14	0.9	0.5	0.9	0.5
	c_3	40	40	40	40	5	5
Critical state	M_{cs}	1.2	1.2	1.2	1.2	1.2	1.2
Hardening	n	0.7	0.7	0.7	0.7	0.7	0.7

Table 2.2. Model parameters for prediction of undrained simple shear experiments by Yoshimine et al. (1998), shown in Figure 2.8.

		Relative Density						
		23%	**25%**	**29%**	**34%**	**35%**	**41%**	**44%**
Elasticity	A_o	315	315	315	315	315	315	315
	m	0.6	0.6	0.6	0.6	0.6	0.6	0.6
	v	0.15	0.15	0.15	0.15	0.15	0.15	0.15
Ultimate strength	M_{so}	1	1	1	1	1	1	1
	M_{sp}	1.18	1.201	1.215	1.22	1.225	1.235	1.3
	c_1	45	45	45	45	45	45	45
	c_2	10	10	10	10	10	10	10
Phase transformation	M_{pto}	1.28	1.174	1.145	1.1	1.06	1.01	0.83
	c_3	20	20	20	20	20	20	20
Critical state	M_{cs}	1.2	1.2	1.2	1.2	1.2	1.2	1.2
Hardening	n	0.55	0.55	0.55	0.55	0.55	0.55	0.55

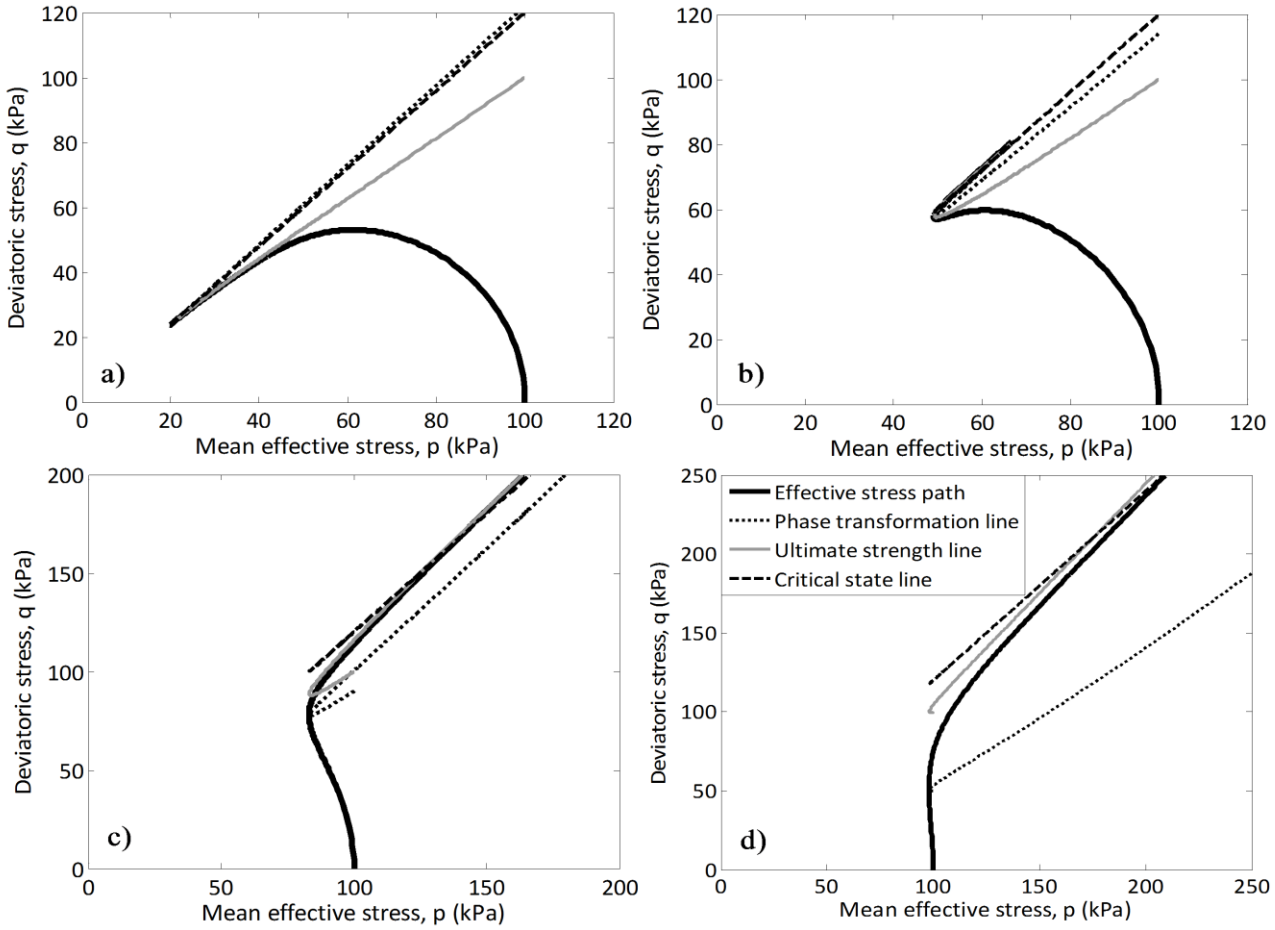

Figure 2.1. Simulation of monotonic undrained behavior of sand: a) very loose, b) loose, c) medium and d) dense sand.

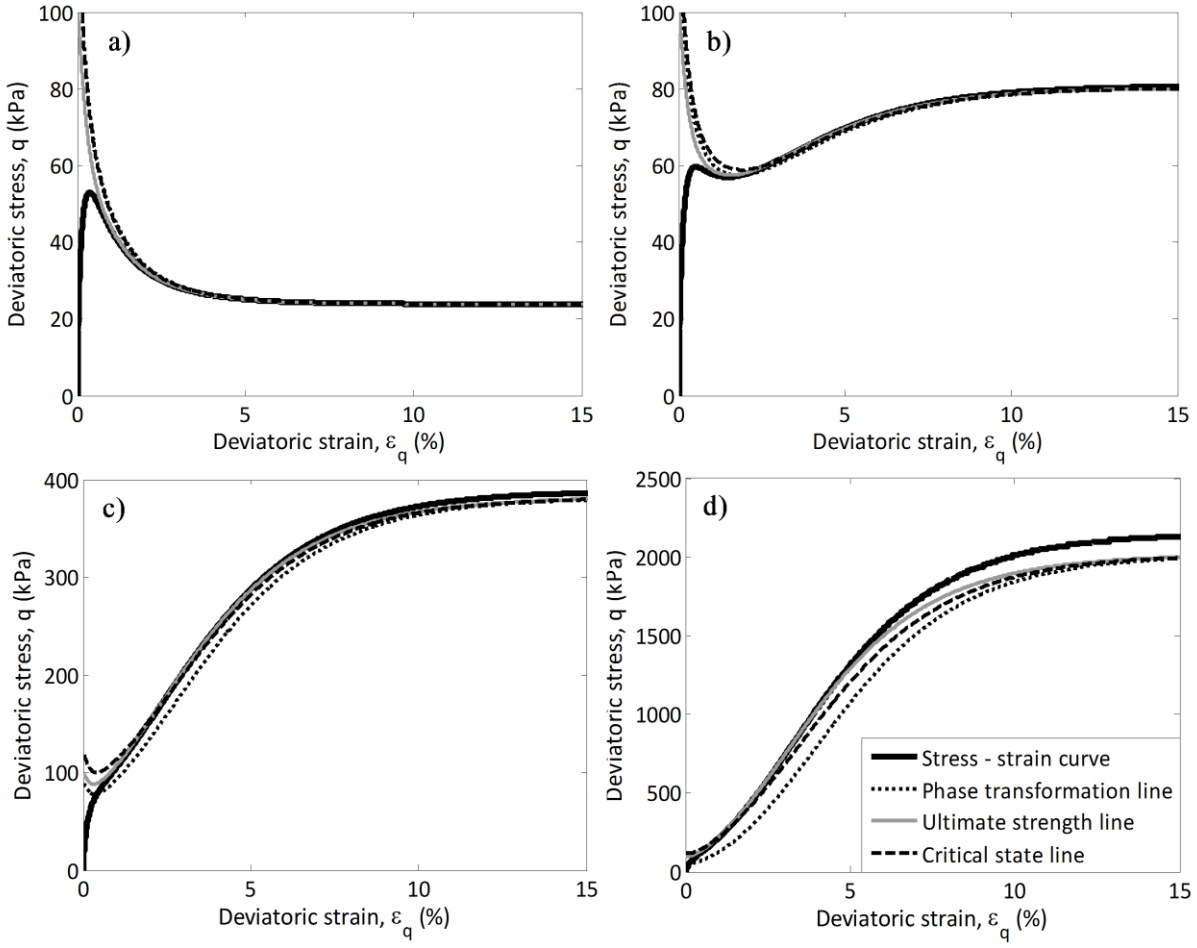

Figure 2.2. Simulation of monotonic undrained behavior of sand: a) very loose, b) loose, c) medium and d) dense sand.

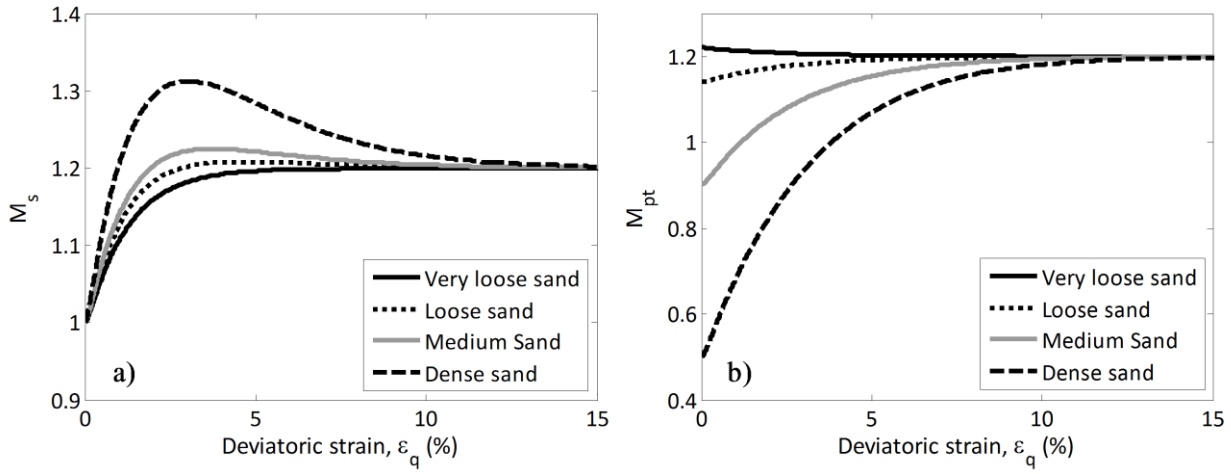

Figure 2.3. Evolution of ultimate strength, M_s and phase transformation lines, M_{pt} during simulation of monotonic undrained loading.

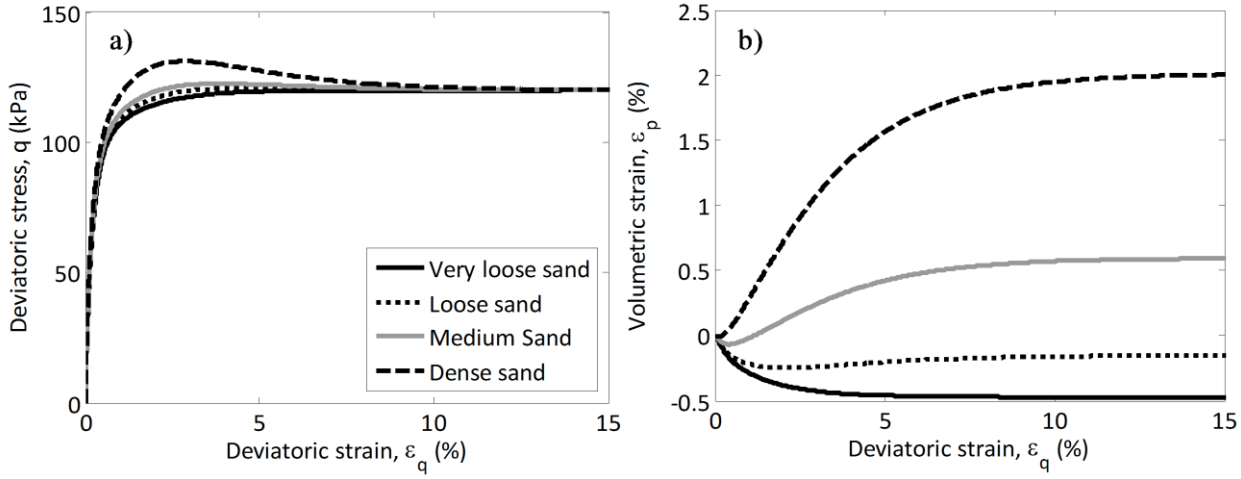

Figure 2.4. Simulation of monotonic drained behavior of sand.

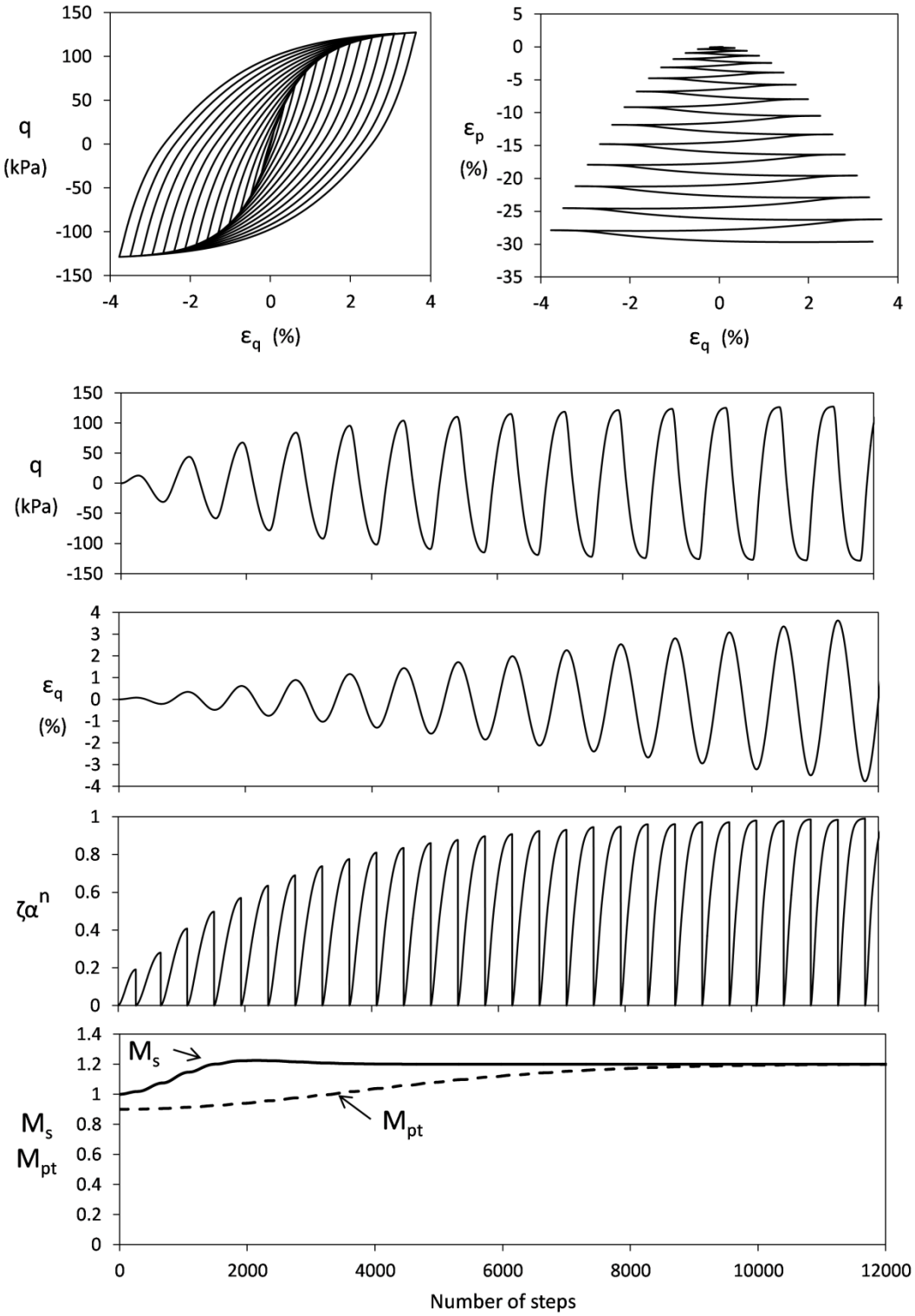

Figure 2.5. Simulation of cyclic drained behavior of sand (medium density) with increasing deviatoric strain amplitude.

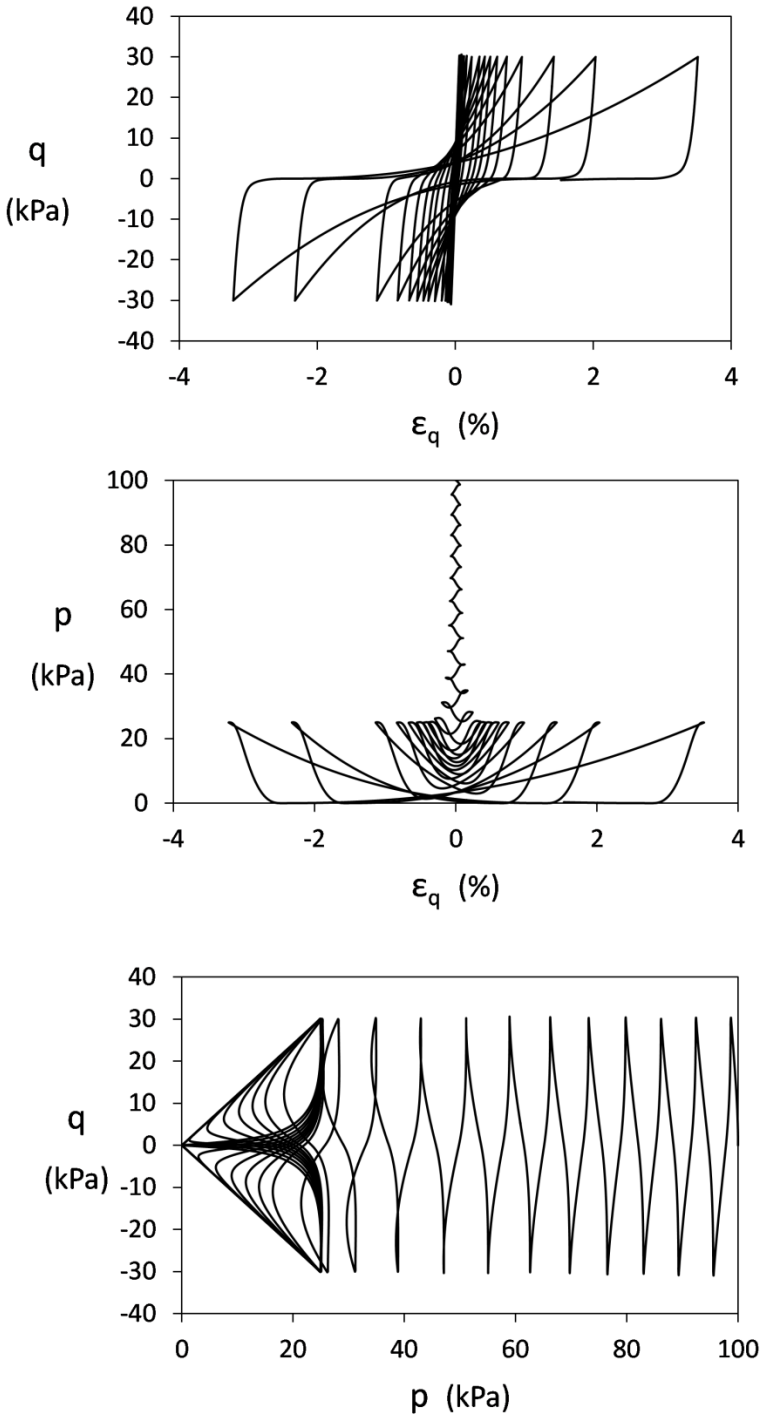

Figure 2.6. Simulation of cyclic undrained behavior of dense sand.

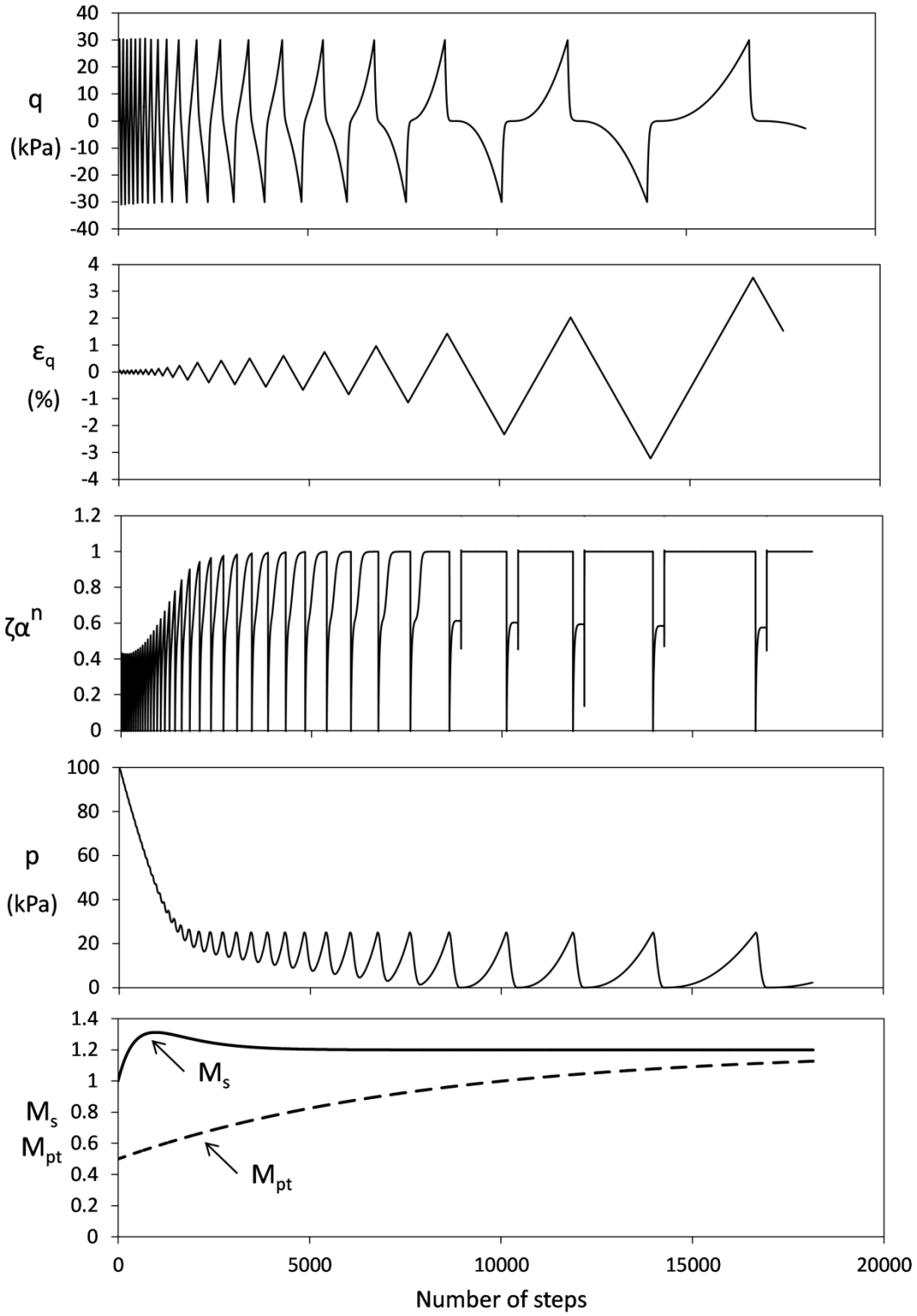

Figure 2.7. Evolution of stress and strain components, as well as internal model variables for the simulation of cyclic undrained behavior of dense sand, shown in Figure 2.6.

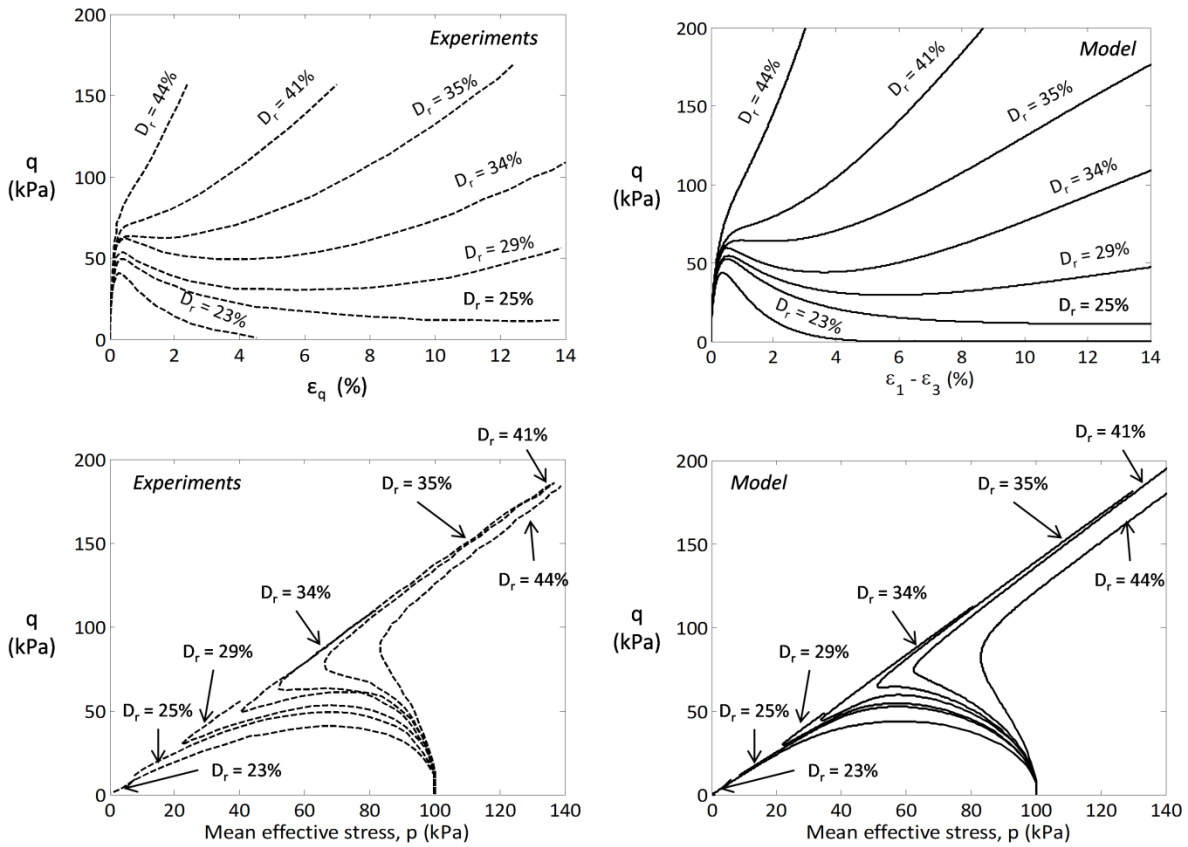

Figure 2.8. Mode predictions versus experiments (Yoshimine et al., 1998) for undrained simple shear loading. Model parameters are shown in Table 2.2.

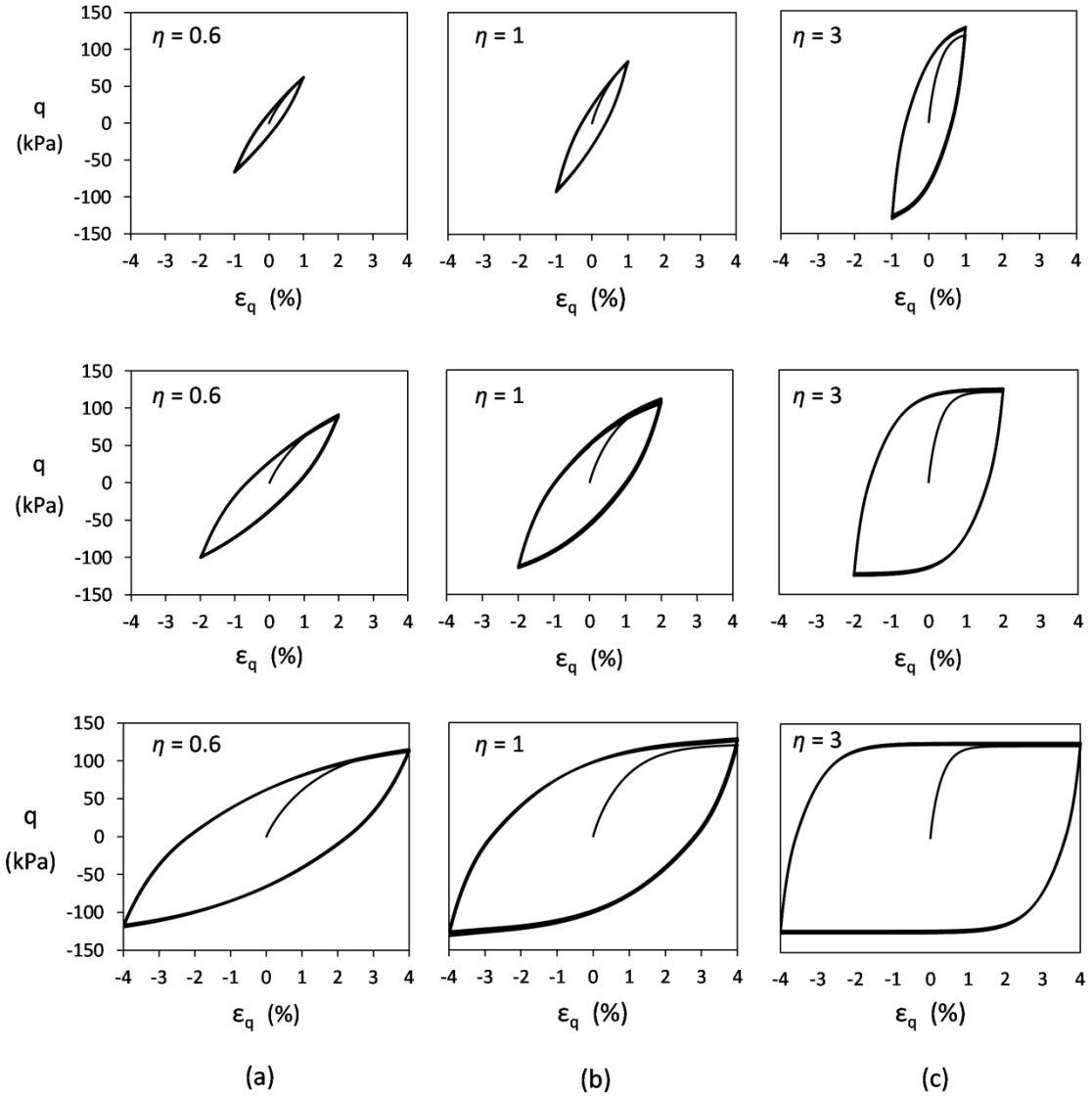

Figure 2.9. Demonstration of impact of parameter η of Eq. (2.31) on the size of stress-strain hysteretic loops for: (a) 1% , (b) 2% and (c) 4% strain amplitude.

CHAPTER 3

Constitutive Modeling for Sand in Multiaxial Space: A New Plasticity Approach

ABSTRACT

A constitutive model for sand is derived in multiaxial space based on a new theoretical framework that combines features of classical (perfect) elastoplasticity and hardening plasticity of the Bouc-Wen type. It resembles a bounding surface model with vanished elastic region, but with considerable modifications in that the plastic modulus is not explicitly defined, and the mapping rule being Bouc-Wen motivated works equally well in monotonic as well as stress-reversal loading. Among the innovations, are: (a) Critical state consistency not only for monotonic but also for cyclic loading, and (b) novel plastic flow rule accounting for anisotropic distribution of the dilatancy strain ratio, d, to the normal plastic strain increments. The capabilities of the model in capturing complex aspects of sand behavior (e.g. cyclic mobility, static liquefaction, densification) are

demonstrated through illustrative paradigms and comparisons with experimental data, emphasizing the physical meaning of each key-model parameter.

3.1 INTRODUCTION

The behavioral diversity of sand for different loading (drained/undrained, monotonic/cyclic), initial stress and fabric conditions, renders its modeling a difficult and challenging task. The suitability of the used constitutive model is evaluated by its capability to capture the trends across all these conditions without recalibration of its parameters for each specific case, but also by its simplicity. Too many parameters might increase the versatility of the model at the risk, however, of losing its physical meaning.

In the last three decades, many constitutive models for sand have been proposed, each with varying degree of accuracy and applicability. The most promising ones are plasticity-based that incorporate the effective stress and critical state concepts (e.g.: Ishihara and Towhata, 1980; Prevost 1985, Pastor et al. 1990, Manzari and Dafalias, 1997, Cubrinovski and Ishihara, 2000; Papadimitriou et al., 2001, Elgamal et al., 2002, Dafalias and Manzari, 2004; Park and Byrne, 2004; Boulanger et Ziotopoulou, 2013, Taborda et al, 2014), though recently developed hypoplastic models have shown remarkable predictability (e.g. Gudehus 1996, Kolymbas 2012). In this study, a novel constitutive model for sand is presented based on a new plasticity framework that joins together features from perfect elastoplasticity and Bouc-Wen type hardening plasticity. The motivation is to develop an alternative plasticity formulation that exhibits critical state consistency for cyclic loading and uniqueness of its parameters for a given type of sand, irrespective of loading conditions.

The model, designated as Ta-Ger sand model, is based on a reformulation of perfect elastoplasticity by introducing a hardening law inspired from Bouc-Wen hysteresis. The

latter is a smooth hysteresis model originally proposed by Bouc (1971) and subsequently extended by Wen (1976) and used in random vibration studies of inelastic systems. Since then, modified or extended versions of this model has been extensively applied in modeling structural (e.g. Sivaselvan and Reinhorn 2000, Triantafyllou and Koumousis, 2012) and soil behaviour (e.g. Gerolymos and Gazetas 2005, Gerolymos et al. 2007, Gerolymos 2010).

The developed constitutive formulation can be regarded as a bounding surface model with vanished elastic region and the distinguished characteristic of a non-explicitly defined plastic modulus. Salient features of the proposed plasticity approach are: (i) a new plastic flow rule which is based on a revision of Rowe's dilatancy theory (1962) to account for anisotropic distribution of the dilatancy to the normal plastic strain increments as well as densification due to cyclic loading, (ii) a mapping rule and load reversal criterion inspired from Bouc-Wen hysteresis, and (iii) a new formulation for the critical state concept that introduces two state parameters. The first being the cumulative incremental deviatoric strain and the second one, the relative dilatancy index, I_r, as originally proposed by Bolton (1986). The main advantage against well-established formulations using the traditional state parameter Ψ (Been and Jefferies, 1985, Manzari and Dafalias, 1997), is critical state consistency for both monotonic cyclic loading and avoidance of early shear locking in cyclic undrained response (as observed in Dafalias and Manzari, 2004).

In the following sections, a mathematical description of the proposed plasticity formulation in multiaxial stress space is attempted, emphasizing the role of the evolution equations and the physical meaning of key-variables. Finally, the model is shown to be capable of reproducing complicated experimental behavior with satisfactory engineering accuracy.

3.2 PLASTICITY CONCEPT: COMBINING PERFECT PLASTICITY WITH BOUC-WEN TYPE OF HYSTERESIS

The governing equations of a typical elastoplastic formulation with no hardening (elastic/perfectly-plastic behavior), in generalized stress space, are revisited. For reasons of simplicity and convenience, the equations are given in the form of matrices instead of tensors. The incremental total strain, $\{d\varepsilon\}$, is decomposed into its elastic and plastic counterparts $\{d\varepsilon^e\}$ and $\{d\varepsilon^p\}$ by a simple addition:

$$\{d\varepsilon\} = \{d\varepsilon^e\} + \{d\varepsilon^p\} \tag{3.1}$$

The plastic strain increment is obtained from the flow rule:

$$\{d\varepsilon^p\} = \langle L \rangle \frac{\partial g(\{\sigma\})}{\partial \{\sigma\}} \tag{3.2}$$

Eq. (3.2) applies normality of the plastic strain increment to a plastic potential function g. L is the common scalar-valued stress-dependent multiplier, designated as the loading index. Substituting Eq. (3.2) into Eq. (3.1) and applying the theory of elasticity, $\{d\sigma\} = \{E^e\}\{d\varepsilon^e\}$, $\{E^e\}$, being the linear elastic matrix, the following stress-strain relationship is obtained:

$$\{d\sigma\} = \{E^e\}\left(\{d\varepsilon\} - \langle L \rangle \frac{\partial g(\{\sigma\})}{\partial \{\sigma\}} \right) \tag{3.3}$$

For a perfectly plastic material, the yield surface, f, is fixed in stress space and thus not functionally dependent on any other state variable than stress. Plastic deformation occurs only when the stress point reaches and lies on the failure surface. This postulate is stated by the following consistency equation:

$$df\left(\{\sigma\}\right)=0\Rightarrow\left(\frac{\partial f}{\partial\{\sigma\}}\right)^{T}\{d\sigma\}=0 \qquad (3.4)$$

Combining Eqs. (3.3) and (3.4), one can obtain both the definition of scalar multiplier, L, and the elastoplastic stress strain relationship, in respect:

$$\langle L\rangle=\frac{\left(\frac{\partial f}{\partial\{\sigma\}}\right)^{T}\{E^{e}\}}{\left(\frac{\partial f}{\partial\{\sigma\}}\right)^{T}\{E^{e}\}\left(\frac{\partial g}{\partial\{\sigma\}}\right)}\{d\varepsilon\} \qquad (3.5)$$

$$\{d\sigma\}=\{E^{e}\}\left[\{I\}-\frac{\left(\frac{\partial g}{\partial\{\sigma\}}\right)\left(\frac{\partial f}{\partial\{\sigma\}}\right)^{T}\{E^{e}\}}{\left(\frac{\partial f}{\partial\{\sigma\}}\right)^{T}\{E^{e}\}\left(\frac{\partial g}{\partial\{\sigma\}}\right)}\right]\{d\varepsilon\} \qquad (3.6)$$

and the elastic-perfectly-plastic matrix is derived:

$$\{E^{ep}\}=\{E^{e}\}\left[\{I\}-\frac{\{\Phi_{g}\}\{\Phi_{f}\}^{T}\{E^{e}\}}{\{\Phi_{f}\}^{T}\{E^{e}\}\{\Phi_{g}\}}\right] \qquad (3.7)$$

where $\{\Phi_{f}\}$ and $\{\Phi_{g}\}$ account for the gradients of yield surface and plastic potential surface, respectively:

$$\{\Phi_{f}\}=\frac{\partial f}{\partial\{\sigma\}}\quad,\quad\{\Phi_{g}\}=\frac{\partial g}{\partial\{\sigma\}} \qquad (3.8)$$

Thus far, it is clear that no kind of hardening response can be accommodated by the current formulation, allowing only for elastic/perfectly-plastic predictions. Our intention is to attribute hardening/softening characteristics to the elastic-perfectly-plastic nature of

Eq. (3.7), while deviating from the classical plasticity framework which involves the introduction of a plastic modulus, K_p, in the denominator of Eq. (3.7), according to:

$$\left\{E^{ep}\right\}=\left\{E^{e}\right\}\left[\{I\}-\frac{\left\{\Phi_g\right\}\left\{\Phi_f\right\}^T\left\{E^{e}\right\}}{K_p+\left\{\Phi_f\right\}^T\left\{E^{e}\right\}\left\{\Phi_g\right\}}\right] \tag{3.9}$$

To this end, an appropriate plastic matrix $\{H\}$ is directly inserted in Eq. (3.7) by multiplying the right-hand side term inside the parentheses:

$$\left\{E_h^{ep}\right\}=\left\{E^{e}\right\}\left[\{I\}-\frac{\left\{\Phi_g\right\}\left\{\Phi_f\right\}^T\left\{E^{e}\right\}\{H\}}{\left\{\Phi_f\right\}^T\left\{E^{e}\right\}\left\{\Phi_g\right\}}\right] \tag{3.10}$$

Our goal is to provide a simpler but equally efficient scheme with higher versatility. Therefore, the role assigned to the matrix $\{H\}$ is threefold: i) it offers a gradual and smooth ("hardening-type") transition from the elastic to perfectly plastic response in order to capture pre-failure nonlinearity and the coupling between elastic and plastic counterparts composing the total strain increment, ii) it provides an appropriate loading/unloading/reloading mapping rule by tracking the distance from the ultimate perfectly plastic state as defined by the failure surface, which herein, serves as a bounding surface, and iii) the values of its terms are strictly bounded within the range of [0,1]. In this line of thought, the matrix $\{H\}$ acquires only diagonal terms as a function of a dimensionless parameter ζ, satisfying the second and third requirements, and a hardening exponent parameter, n, fulfilling the first postulate. Both of these parameters are of the Bouc-Wen type (Gerolymos and Gazetas, 2005). Matrix $\{H\}$ is given as:

$$\{H\}=\zeta^n\{I\} \tag{3.11}$$

As it has been already stated, parameter ζ needs to be dimensionless and strictly bounded within the range [0,1]. It is obvious that ζ should obtain unit value when the stress point

reaches the ultimate failure state (perfectly plastic, f=0), while all its intermediate values, from zero to unity, correspond to intermediate stress states. In order to demonstrate an appropriate function for parameter ζ compatible with a specific failure surface, let's assume a material obeying a cone-type failure criterion in triaxial space, such as Drucker-Prager:

$$f = 0 \Leftrightarrow q - Mp = 0 \qquad (3.12)$$

where q is the deviatoric stress, p is the mean effective stress and M is the bounding stress ratio representing the ultimate strength, e.g. critical state. In lieu of the abovementioned requirements, a proper definition of ζ is:

$$\zeta = \frac{\left(q/p\right)}{M} \qquad (3.13)$$

Since the stress ratio, q/p, can only obtain values within the range of [0,M], ζ is strictly bounded in the range of [0,1]. Evidently, the elastic state corresponding to ζ=0, $\{H\} = \{0\}$ and $\left\{E_h^{ep}\right\} = \left\{E^e\right\}$, is trivialized to a single point and plastic strains develop from early on, as soon as ζ becomes greater than zero. A set of loading surfaces are created upon definition of ζ, described by the following equation:

$$q - \zeta Mp = 0 \qquad (3.14)$$

Each stress state corresponds to a unique value of ζ resulting in a specific loading surface given by Eq. (3.14). Thus, each current stress point automatically lies on a surface proportional to the failure surface of Eq. (3.12) by the value of ζ, as illustratively depicted in Figure 3.1.

Conceptually, the failure surface works similarly to a surface of reference which cannot be surpassed, namely a bounding surface (Dafalias, 1986), in the sense that for any given stress state (e.g. stress ratio, q/p) there is always an "image" stress state lying on the

failure surface (e.g. stress ratio, M) so that the ratio, ζ, between the actual and "image" stress states can be measured. Specifically, for the examined case of a Drucker-Prager failure surface which forms a circle in π plane, the current stress state is equal to the radius of the current loading surface, while the "image" stress state is always equal to the radius of the failure surface (see Figure 3.1).

Clearly, parameter ζ holds the role of evolution or else mapping rule. Having defined parameter ζ in case of monotonic loading, it remains to be defined upon reversal loading and reloading. Details are given in the following section where the above described scheme is applied to sand and a generalized bounding/failure surface for all loading/unloading/reloading conditions is proposed.

In retrospect, the plastic matrix, $\{H\}$, is dependent only on the failure/bounding surface. Hence, the proposed plasticity approach is characterized as a single-surface model. The elastic area is trivialized to a single point at the beginning of loading, unloading and reloading, where elastic behavior is expected at least momentarily satisfying Masing rule. Hence, no yield surface is involved to define the elastic region, or rather, yield surface diminishes to a single line for ζ=0 (e.g. q = 0 from Eq. (3.14) for ζ = 0). Needless to say that neutral loading cannot be captured in the lack of a yield surface. This fact will prove to be advantageous upon loading reversal where potential unrealistic reversal of loading by neutral loading is automatically excluded; a weakness that is commonly encountered in the majority of elastoplasticity models, such as bounding surface (Dafalias, 1986), generalized-plasticity (Pastor et al., 1990), multisurface ones (Prevost, 1985) etc.

While parameter ζ tracks the actual distance of the current stress state from the failure state, exponent parameter n controls the rate of transition from elastic state to the perfectly plastic one, as characteristically demonstrated in Figure 3.1 for a Drucker-Prager failure surface. Exponent n is designated as the hardening parameter in the current scheme, determining the degree of coupling between concurrent elastic and plastic strain increments during loading. As the value of n increases, the response tends

to be elastic/perfectly-plastic while the elastic and plastic strain increments tend to be decoupled during loading (e.g. n = 10), with the elastic ones occurring exclusively prior to failure (plateau) and the plastic ones developing only after failure takes place. Inversely, as the value of n decreases, the coupling between the elastic and plastic components of total strain increment increases until ultimate failure is reached, resulting in a smoother transition to failure.

3.3 CONSTITUTIVE MODEL FOR SAND

The new plasticity scheme is used as a framework to develop a simple constitutive model for sand, which can capture all important aspects of sand behavior under monotonic and cyclic loading, such as critical state behavior, densification, liquefaction etc. An appropriate bounding surface is proposed, which allows a unique derivation of parameter ζ for monotonic and cyclic loading by keeping memory of the last reversal stress state, while update is achieved by a simple first-order work criterion. Additionally, a new set of functions is suggested for the evolution of bounding and phase transformation stress ratios in order to enhance the critical state concept.

3.3.1 Pre-Failure Parameters

The terms in matrix $\left\{E^e\right\}$ are functions of the shear and bulk moduli which in turn are functions of the mean effective stress p, according to:

$$G = A_o p_\alpha \frac{(2.97-e)^2}{1+e}\left(\frac{p}{p_\alpha}\right)^m, \qquad K = \frac{2(1+v)}{3(1-2v)}G \tag{3.15}$$

in which, A_o is a dimensionless material parameter, v is the Poisson's ratio, p_a is the atmospheric pressure, e is the current void ratio, and m is a dimensionless parameter determining the rate of variation of G and K with p.

3.3.2 Bounding Surface and Hardening Parameter ζ

An open-end, cone-type bounding surface is proposed as a function of the current stress state as well as the stress state at the last reversal of loading:

$$f = \left[(\mathbf{s} - \mathbf{r}_p p) : (\mathbf{s} - \mathbf{r}_p p) \right]^{1/2} - \left(\sqrt{\frac{2}{3}} M_{s,\theta} - n_p \right) p = 0 \qquad (3.16)$$

where **s** is the second order deviatoric stress tensor and $M_{s,\theta}$ is the bounding stress ratio, determining the ultimate strength, dependent on the lode angle θ. The stress ratio tensor, $\mathbf{r}_p$ is given by:

$$\mathbf{r}_p = \frac{\mathbf{s}_p}{p_p} = \frac{\boldsymbol{\sigma}_p - p_p \mathbf{I}}{p_p} \qquad (3.17)$$

where $\boldsymbol{\sigma}_p$ is equal to the stress tensor and p_p the mean effective stress at the pivot points, once reversal of loading occurs. It is noted that $\mathbf{r_p}$ is comparatively equivalent to the back-stress ratio, **α**, in a conventional bounding surface model. The scalar valued stress ratio n_p is defined as the inner product of two tensors denoting the distance of the pivot stress ratio $\mathbf{r}_p$ from the hydrostatic axis:

$$n_p = \mathbf{n} : \mathbf{r}_p \qquad (3.18)$$

in which **n** is a normalized stress ratio tensor, normal to f:

$$\mathbf{n} = \frac{\mathbf{s} - \mathbf{r}_p p}{\left[(\mathbf{s} - \mathbf{r}_p p) : (\mathbf{s} - \mathbf{r}_p p) \right]^{1/2}} \qquad (3.19)$$

The properties of tensor **n** are given by the following equations:

$$\mathrm{tr}\mathbf{n} = n_{11} + n_{22} + n_{33} = 0 \qquad (3.20)$$

$$\mathrm{tr}\mathbf{n}^2 = \mathbf{n} : \mathbf{n} = n_{11}^2 + n_{22}^2 + n_{33}^2 + 2n_{12}^2 + 2n_{23}^2 + 2n_{31}^2 = 1 \qquad (3.21)$$

Evidently, in case of monotonic loading, the bounding surface, f, returns to its common Drucker-Prager form but with Lode angle dependency:

$$F=\left[\mathbf{s}:\mathbf{s}\right]^{1/2}-\sqrt{\frac{2}{3}}M_{s,\theta}p=0 \qquad (3.22)$$

The evolution of its shape, once reversal occurs, is explained in section 3.3.4 along with the mapping rule. Parameter ζ is defined following the same concept described in section 3.2:

$$\zeta=\frac{\left[(\mathbf{r}-\mathbf{r}_p):(\mathbf{r}-\mathbf{r}_p)\right]^{1/2}}{\sqrt{\frac{2}{3}}M_{s,\theta}-n_p}=\frac{\left|\mathbf{r}-\mathbf{r}_p\right|}{\sqrt{\frac{2}{3}}M_{s,\theta}-n_p} \qquad (3.23)$$

in which **r** is the current deviatoric stress ratio tensor. It is obvious that ζ obtains zero values at each point reversal, initiating elastic unloading, consistent with Masing rule. Parameter ζ ensures that the current stress state always lies on a loading surface described by:

$$L=\left[(\mathbf{s}-\mathbf{r}_p p):(\mathbf{s}-\mathbf{r}_p p)\right]^{1/2}-\zeta\left(\sqrt{\frac{2}{3}}M_{s,\theta}-n_p\right)p=0 \qquad (3.24)$$

Since plasticity starts practically from ζ=0, the yield surface can be derived by Eq (3.24) for ζ=0. The gradient to this failure/bounding surface is given by:

$$\boldsymbol{\Phi}_f=\frac{\partial f}{\partial \boldsymbol{\sigma}}=\mathbf{n}-\frac{1}{3}(\mathbf{n}:\mathbf{r})\mathbf{I} \qquad (3.25)$$

3.3.3 Lode Angle Dependency

The Lode angle is defined as:

$$cos(3\vartheta) = \frac{3\sqrt{3}}{2}\frac{J_3}{J_2^{3/2}} \tag{3.26}$$

where J_2 is the second deviatoric invariant J_3, the third deviatoric invariant. After using polynomial interpolation, $M_{s,\vartheta}$ can be obtained by:

$$M_{s,\vartheta} = \left(\frac{M_c + M_e}{2} - M_{ss}\right)cos^2(3\vartheta) + \left(\frac{M_c - M_e}{2}\right)cos(3\vartheta) + M_{ss} \tag{3.27}$$

in which M_c is the bounding stress ratio in compression, M_e in extension and M_s in simple shear. They are related to friction angle, φ, as:

$$M_c = \frac{6sin\varphi}{3-sin\varphi};\quad M_e = \frac{6sin\varphi}{3+sin\varphi};\quad M_{ss} = 2sin\varphi \tag{3.28}$$

Then, χ is defined:

$$\chi = \frac{M_{s,\vartheta}}{M_c} \tag{3.29}$$

3.3.4 Mapping Rule and Load Reversal Criterion

Update of the stress ratio tensor at pivot points, $\mathbf{r}_p$, in Eq. (3.16) occurs when the first order work changes sign; a feature also incorporated in the Bouc-Wen model (e.g. Gerolymos and Gazetas, 2005). The first order work is equal to the inner product of the strain rate tensor and the difference of the current stress ratio tensor from the stress ratio tensor obtained by the last pivot point:

$$dW = (\mathbf{r} - \mathbf{r}_p) : \dot{\boldsymbol{\varepsilon}} \qquad (3.30)$$

Figures 3.2 to 3.4 offer a schematic insight on how the shape of bounding surface, f=0, described by Eqs. (3.16) adapts uniquely for each stress path to the shape of the target failure surface, F=0 of Eq. (3.22).

Initially, Figure 3.2 illustrates certain snapshots of characteristic stress states in π-plane, corresponding to certain points in a stress-strain loop obtained by a cyclic simple shear test under constant mean effective stress. The resulting stress path is a straight line along $\vartheta = \pi/6$. The shapes of bounding, target failure and loading surfaces, f = 0, F = 0 and L = 0, described by Eqns. (3.16), (3.22), and (3.24) respectively, are plotted in the π-plane plots along with the current stress point (star symbol). The beginning of loading corresponds to stress point A which lies on the hydrostatic axis (ζ = 0); therefore, the loading surface (L = 0) collapses to a single line containing stress point A. From A to C-, the loading surface swells isotropically as ζ increases, until it coincides both with the target failure surface (F = 0) for ζ = 1 (point E-) and the bounding surface (f = 0), since $\mathbf{r}_p$ is yet equal to **0**. At pivot point C+, the first order work, dW, changes sign, confirming the occurrence of loading reversal and $\mathbf{r}_p$ obtains the values of point C-. At this moment, the loading surface trivializes once more to a single point (ζ = 0), while the bounding surface, though concave in general, fits perfectly to the target convex failure surface at the point opposite to the current one (namely the "image" point). The "image" point always corresponds to the point where the projection of current $\mathbf{r} - \mathbf{r}_p$, crosses the surface f = 0, as depicted in Figure 3.3.

In order to verify the unique adaptation of the bounding surface for each stress path, the same graphical illustration is adopted in Figure 3.4 for the case of a cyclic triaxial p-constant test. From points A to C-, the image is similar to that of Figure 3.2, besides the fact that the stress points lies on $\vartheta = 0$ (compression). Upon first reversal, point C+, the loading surface becomes a single point in π-plane coinciding with the stress point, while the bounding surface adapts in a way that fits the target failure at $\vartheta = \pi/3$ ("image"

point). Upon second reversal, namely point E-, the stress ratio tensor, $\mathbf{r}_p$, is updated once again, so that this time the bounding surface coincides with the target failure one at $\vartheta = 0$ (next "image" point).

Overall, Eq. (3.16) describes a uniquely adaptable bounding surface to the target surface for each specific stress path. In mathematical terms, the target surface is the geometric locus of the "image" points derived from the bounding surface. Consequently, the mapping rule is automatically incorporated in parameter ζ – since its definition is based on a reformulation of Eq. (16), and thus, in the plastic matrix $\{H\}$.

3.3.5 Flow Rule

The stress-dilatancy relationship, adopted by the model, is based on Rowe's dilatancy theory (Rowe 1962). The ratio of the plastic volumetric strain increment, $d\varepsilon_p^p$, over the plastic deviatoric strain increment, $d\varepsilon_q^p$, depends on the distance of the current stress ratio, q/p, in conventional p-q space from the phase transformation line, M_{pt}, as follows:

$$d = \frac{d\varepsilon_p^{\,p}}{d\varepsilon_q^{\,p}} = \left(M_{pt} - \frac{q}{p} \right) \qquad (3.31)$$

When $q/p > M_{pt}$, the imposed deviatoric strain increment causes $d\varepsilon_p^{\,p} < 0$ and $d < 0$ which corresponds to dilation. Respectively, when $q/p < M_{pt}$, $d\varepsilon_p^{\,p} > 0$ and $d > 0$ resulting in contraction. The dilatancy strain ratio, d, remains a scalar quantity in multiaxial stress-strain space, calculated by:

$$d = R_d \left(\sqrt{\frac{2}{3}} M_{pt}\, \chi\, \mathbf{n} - \frac{\mathbf{s}}{p} \right) : \mathbf{n} = R_d \left(\sqrt{\frac{2}{3}} M_{pt}\, \chi - \frac{\mathbf{s}}{p} : \mathbf{n} \right) \qquad (3.32)$$

where χ is the factor described by Eqn. (3.29) to account for the Lode angle effect and R_d is a parameter dependent on the current relative density (used as a state parameter) which allows to capture densification effects due to cyclic drained loading. The gradient

to the plastic potential surface, necessary for the formation of the elastoplastic matrix of Eq. (3.10), is given by:

$$\boldsymbol{\Phi}_g = \frac{\partial g}{\partial \boldsymbol{\sigma}} = \mathbf{n} + \mathbf{n}^2 d \qquad (3.33)$$

Both volumetric and deviatoric non-associativeness is applied. The increment of the plastic strain tensor can be obtained by Eq. (3.2). Due to the property of tensor **n,** described by Eq. (3.21), the plastic volumetric increment, $d\varepsilon_p^p$, is indeed equal to:

$$d\varepsilon_p^p = tr\left(d\boldsymbol{\varepsilon}^p\right) = \langle L \rangle tr\boldsymbol{\Phi}_g = \langle L \rangle dtr\mathbf{n}^2 = \langle L \rangle d \qquad (3.34)$$

It is common in literature to arbitrarily assume an isotropic distribution of the quantity, d, to the three normal plastic strain increments according to:

$$\boldsymbol{\Phi}_g = \frac{\partial g}{\partial \boldsymbol{\sigma}} = \mathbf{n} + \frac{d}{3}\mathbf{I} \qquad (3.35)$$

Herein, in an attempt to account for the effect of the loading direction on the distribution of the dilatancy, d, to the three normal plastic strain components, Eq. (3.33) is adopted. Comparison is held between Eq. (3.33) and (3.35) in order to highlight the difference in stress and strain components.

Figure 3.5 illustrates the distribution of normal strain components for a monotonic simple shear test, where only shear stress, σ_{12}, is applied. In terms of shear stress-strain curve the response is the same for both equations. Eq. (3.35) results in equal normal strains in all directions ($\varepsilon_{ii} = \varepsilon_p/3$), whereas Eq. (3.33) develops normal strains only in the directions related with the applied shear stress; ε_{11} and ε_{22}. The out of plane normal strain ε_{33} is zero, indicating that there is no tendency for contraction or dilation in the direction where no shear stress is applied.

In case of an undrained cyclic test, where no normal strain is allowed and only σ_{12} is applied, the variation of normal stresses is identical when Eq. (3.35) is adopted, resulting

in a path always lying on π/6 in π-plane plot, as depicted in Figure 3.6. Alternatively, when Eq. (3.33) is used, the out of plane normal stress, σ_{33}, decreases in a slower rate during loading, resulting in a more complicated path as plotted in a π-plane graph. Whether Eq. (3.33) or (3.35) is closer to reality is difficult to be documented, since no elaborate data exist in literature, even experimental ones.

Parameter R_d in Eq. (3.32) is given by:

$$R_d = e^{-\alpha|D_r - D_{r0}|} \qquad (3.36)$$

where D_r is the current relative density, D_{r0} is the initial relative density and α is a constant. Evidently, increase of D_r causes decrease of parameter R_d and subsequent decrease of quantity, d, resulting in densification as shown in Figure 3.7. Parameter R_d is deliberately chosen as a function of D_r, so that R_d remains unity during undrained loading. Otherwise, any decrease of R_d would hamper the occurrence of liquefaction, since densification and liquefaction are two competitive mechanisms.

The calibration of constant α for the demonstration of Figure 3.7 was based on the empirical correlations of volumetric strains with the number of cycles for 1% shear strain and D_{r0} = 45 % (Silver and Seed, 1971; Duku et al., 2008), shown in Figure 3.8.

3.3.6 Influence of Hardening Exponent n

Typical values of hardening exponent n for soils are found in the range of 0.2-0.8, as suggested by Drosos et al., 2012. In general, the monotonic response is not extremely sensitive to the evolution of hardening exponent n; thus, a satisfactory prediction can be achieved with a constant specific value within the range of 0.2-0.5, for both drained and undrained conditions, accompanied by a proper calibration of the other model parameters. However, the response under cyclic undrained loading is greatly affected by the value of n, especially in terms of number of cycles required to cause liquefaction (p =

0), as shown in Figure 3.9. Three different values of n have been used in an attempt to predict the response of a sand specimen with D_r = 70% under simple shear undrained loading. In case of n = 0.3, only 6 cycles of loading are required for liquefaction occurrence (p = 0), while large shear strains > 3% develop abruptly after the 3rd cycle. As n increases (e.g. n = 0.5), the required number of cycles also increases, until n = 0.7 for which liquefaction cannot be practically achieved within a reasonable number of cycles. However, no locking is observed, and accumulation of shear strains continues with increasing loading cycles even for large values of n.

The parameter n can be effectively calibrated to match any experimental CRR (Cyclic resistance ratio curve) curve from the literature (e.g. De Alba, 1976). Expressing n as a function of the cumulative deviatoric strain increment:

$$n = n_f + \left[n_{peak} + \left(n_0 - n_{peak} \right) e^{-\beta \sum d\varepsilon_q} - n_f \right] e^{-\gamma \left(1 - sign\left(\left| \sum d\varepsilon_p \right| \right) \right) \sum d\varepsilon_q}$$

(3.37)

was shown to provide reasonable estimates. In Eq. (3.37), n_f is the final desired value (when p tends to zero), n_0 is the initial value, n_{peak} is the potentially reached peak value, dependent on constants β and γ. The latter exponential of Eq. (3.37) depends on the function, $1 - sign\left(\left| \sum d\varepsilon_p \right| \right)$, where $\sum d\varepsilon_p$ is the accumulation of volumetric strain increments. Undrained conditions impose that $d\varepsilon_p = 0$; thus this function returns unity for undrained cylic loading. The necessity of this function will be shown in case of drained loading conditions.

The resultant prediction for undrained conditions by Eq. (3.37) is depicted in Figure 3.10. A characteristic rapid decrease of p is observed in the first two cycles (n = 0.5), followed by slower decrease (for n > 0.6) until the rate of p reduction increases again so that liquefaction is achieved (0.3 ≤ n ≤ 0.5). In terms of stress-strain loops, there is a gradual increase of shear strain amplitude for each additional cycle.

Cyclic loading under drained conditions causes densification effects, as previously described, when constant strain amplitude cycles of loading are applied. When constant stress amplitude cycles of loading are applied, densification is reflected also in stress-strain loops through decrease of the secant shear modulus. Thus, the area of the loops, which lose their symmetry, decreases during loading. This behavior can be simulated with continuous increase of the value of parameter n during loading. For this purpose, Eq. (3.37) is used, which, in case of drained loading, it is formulated as:

$$n = n_{peak} + \left(n_0 - n_{peak}\right) e^{-\beta \sum d\varepsilon_q} \qquad (3.38)$$

since $\left|\sum d\varepsilon_p\right| > 0$, so that the function $1 - \text{sign}\left(\left|\sum d\varepsilon_p\right|\right)$ becomes equal to zero. Consequently, the constant evolution of parameter n from the initial value n_0 to higher value n_{peak} is ensured. Demonstration of the impact of Eq. (3.38) on the predicted response is shown in Figure 3.11.

3.3.7 Evolution of bounding and phase transformation lines

Adopting Critical State Concept

The essence of the critical state concept is that no change in volume occurs when the current stress state reaches the critical state despite the continuous increase of shear strain. In order to achieve this kind of performance upon critical state, both the phase transformation line, M_{pt} and the bounding line (or else ultimate strength line), M_s, should gradually converge to the critical state line, M_{cs}, producing zero plastic volumetric change when the stress ratio becomes equal to $M_s = M_{pt} = M_{cs}$, according to flow rule of Eq. (3.31). Several suggestions have been made in literature for the variation of M_s and M_{pt}, based on a suitable current state material parameter relative to the critical state (Wood et al., 1994; Manzari and Dafalias,1997); one of the most recent and physically

perceptible, being proposed by Dafalias and Manzari, 2004 and adopted also by Taiebat and Dafalias, 2007:

$$M_s = M_{cs} e^{-n_b \Psi} \quad \text{and} \quad M_{pt} = M_{cs} e^{n_d \Psi} \tag{3.39}$$

in which $\Psi = e - e_c$, e_c is the void ratio given by the critical state line in e-p space described by:

$$e_c = e_0 - \lambda \left(\frac{p}{p_{at}} \right)^{\xi} \tag{3.40}$$

and n_b, n_d appropriate constants. The effectiveness of Eqs. (3.38) relies on three satisfied postulates: i) when e = e_c then $M_{pt} = M_s = M_{cs}$ and ii) for denser sands where e < e_c, then $M_{pt} < M_{cs} < M_s$ leading to dilatant response and iii) for looser sands where e > e_c, then $M_{pt} > M_{cs} > M_s$ resulting in contraction. Although the concept is flawless, at least for monotonic loading, calibration process can be challenging. The two model parameters n_b, n_d should simultaneously account for the accurate prediction of peak strength, dilatancy (developed volumetric strain) and the rate which the critical state is reached at, for all states of sand.

Moreover, the above mentioned postulates are not necessarily satisfied in case of cyclic loading. For example, in case of liquefaction it has been experimentally observed (Zhang et al.,1997; Kramer, 1996, Been and Jefferies, 2006; Elgamal et al, 1998) that cyclic loading moves the stress paths towards the critical state line which coincides with the so-called failure envelope at p = 0. However, state parameter Ψ cannot become equal to zero under cyclic strain accumulation, so that M_s converges eventually to M_{cs}. Therefore, Eqs. (3.38) lead to early stabilization at p > 0, hindering liquefaction occurrence (Dafalias and Manzari, 2004). As a result, extra features usually need to be added in a formulation, which are usually attributed to fabric-related effects (e.g. fabric-dilatancy tensor). However, this modification may only contribute to an extra decrease of p up to

liquefaction and not to a complete solution of the problem. Indeed, M_s and M_{pt} still cannot converge to M_{cs} and shear locking cannot be eventually avoided.

After meticulous observation of experimental data and careful consideration of the above, the evolution of the bounding stress ratio was chosen as a function of the cumulative deviatoric strain increments, $\Sigma|d\varepsilon_q|$:

$$M_s = M_{cs} + \left[M_{sp} + \left(M_{s0} - M_{sp} \right) e^{-c\sum d\varepsilon_q} - M_{cs} \right] e^{-c\sum d\varepsilon_q} \qquad (3.41)$$

where M_{so} is an initial value and M_{sp} is a maximum value that can be potentially reached depending on the model parameter c. For a typical value of c = 8, M_{sp} can never be reached. Instead, a lower value is reached, herein called M_{speak}. The evolution function of the bounding stress ratio M_s has the same form with Eq. (2.32) in Chapter 2. However, the present formulation uses the same coefficient, c, for both exponentials, in an attempt to minimize the number of model parameters.

The phase transformation line evolves in the same context, according to the following expression:

$$M_{pt} = M_{cs} + \left(M_{pt0} - M_{cs} \right) e^{-0.5c\sum d\varepsilon_q} \qquad (3.42)$$

where M_{pt0} is the initial value of M_{pt}. The cumulative deviatoric strain increments, $\Sigma|d\varepsilon_q|$, as the chosen hardening parameter, ensures that critical state will be reached under monotonic and cyclic loading (Tasiopoulou and Gerolymos, 2012).

Using Relative Dilatancy Index as State Parameter

The proposed set of Eqs. (3.40) and (3.41) may present a more convenient and flexible pattern, but they lack a state parameter that will provide a physical meaning. The latter

can be achieved by correlating the model parameters M_{s0}, M_{sp} and M_{pt0} with Bolton's relative dilatancy index (Bolton 1986, Ching et al., 2012):

$$I_r = D_r\left(Q - \ln(p)\right) - R \qquad (3.43)$$

where D_r is the current relative density of the sand, p is the current mean effective stress, and Q, R are constants obtaining values close to 10 and 1, respectively. Critical state occurs when $I_r = 0$, while $I_r > 0$ indicates denser states of sands and $I_r < 0$ accounts for looser contractive states. For triaxial compression the maximum friction angle is given by Bolton (1986), $\varphi_{max} - \varphi_{cs} = 3I_r$, thus:

$$M_{speak} = \frac{6\sin(\varphi_{max})}{3 - \sin(\varphi_{max})} \qquad (3.44)$$

The bounding stress ratio obtains its maximum value, M_{speak}, when:

$$\frac{\partial M_s}{\partial\left(\sum|d\varepsilon_q|\right)} = 0 \Leftrightarrow \sum|d\varepsilon_q|_{peak} = \frac{1}{c}\ln\left(\frac{M_{cs} - M_{sp}}{2\left(M_{so} - M_{sp}\right)}\right) \qquad (3.45)$$

where the initial value, M_{s0}, is chosen to be taken as:

$$M_{so} = \frac{6\sin(0.8\varphi_{cs} + 5I_{ro})}{3 - \sin(0.8\varphi_{cs} + 5I_{ro})} \qquad (3.46)$$

with I_{ro} being the initial value of the relative dilatancy index, I_r. The reason behind this selection will be extensively discussed through calibration procedure, described in Chapter 4. After calculations, M_{sp} can be obtained by:

$$M_{sp} = 2M_{speak} - M_{cs} + 0.5\sqrt{\left(2M_{cs} - 4M_{speak}\right)^2 - 16M_{so}\left(M_{speak} - M_{cs}\right) + 4M_{cs}{}^2} \qquad (3.47)$$

After statistical processing of numerous drained tests on sands, Bolton (1986) also suggested that:

$$\left[-\frac{d\varepsilon_p}{d\varepsilon_1}\right]_{\max} = 0.3I_r \qquad (3.48)$$

when the peak strength value, Mspeak, is obtained; a deduction that can be used for the calibration of the plastic flow rule and specifically the phase transformation line. Combining flow rule of Eq. (3.31) for triaxial conditions and empirical Eq.(3.48), it is shown that:

$$\left[\frac{d\varepsilon_p^p}{d\varepsilon_q^p}\right]_{max,tx} = M_{pt,peak} - M_{speak} = \frac{-3\left[-\frac{d\varepsilon_p}{d\varepsilon_1}\right]_{max}}{3+\left[-\frac{d\varepsilon_p}{d\varepsilon_1}\right]_{max}} = \frac{-3(0.3I_r)}{3+(0.3I_r)} \qquad (3.49)$$

assuming that $\left[\frac{d\varepsilon_p^p}{d\varepsilon_q^p}\right]_{max} \simeq \left[\frac{d\varepsilon_p}{d\varepsilon_q}\right]_{max}$ when maximum strength (ζ=1) has occurred. In order to satisfy the above requirement $\left(M_{pt,peak} = M_{speak} - \frac{3(0.3I_r)}{3+(0.3I_r)}\right)$, M_{pt0} is chosen:

$$M_{pt0} = M_{speak}\zeta^n - \frac{3(0.3I_r)}{3-3(0.3I_r)} \qquad (3.50)$$

Constant evolution during loading will lead to $M_{pt} \simeq M_{pt0} = M_{speak} - \frac{3(0.3I_r)}{3-3(0.3I_r)}$ at peak strength (ζ=1). In retrospect, by following the above described calibration process, the initially "physically meaningless" model parameters M_{s0}, M_{sp} and M_{pt0} are eventually expressed as functions of the fundamental soil properties φ_{cs} , D_r and current confining pressure p. It should be mentioned, that the intermediate steps behind the selections and assumptions made for formation of Eqs. (3.44) to (3.50) will be shown in detail in Chapter 4, as part of a unified calibration attempt.

3.4 MODEL PREDICTION VERSUS EXPERIMENTS

Model predictions versus experimental results have been performed for both sets of M_s and M_{pt}: Set A [Eqs. (3.40)-(3.41)] and Set B [Eqs. (3.38)] to evaluate the efficiency of the proposed set A compared to the well-established set B. Initially, simulations of drained and undrained triaxial monotonic tests for Toyoura sand were conducted. The values of the model parameters adopted in these simulations, are depicted in Table 3.1 for both set of equations. The relative density, D_r, was calculated considering e_{max}=0.977 and e_{min}=0.597 for Toyoura sand, according to Verdugo and Ishihara (1996). Figures 3.12-3.16 (a) and (b) illustrate the comparison between model predictions and experiments. The flexibility offered by the proposed set of equations for M_s and M_{pt} provides a better agreement with the experiments, especially for loose sands. In case of denser sands, the level of predictability can be considered equal for both models.

Figures 3.12-3.13 (c) and (d) offer an insight on how the new presented constitutive formulation cooperates with the two sets of equations for M_s and M_{pt} based on the evolution of state parameter I_r for set A and Ψ for set B. The required parameters for the critical state line in e-p space, λ and ξ, were obtained by Taiebat and Dafalias (2007). The differences between the two sets are mostly attributed to the initial values of M_s which in case of set A are lower than M_{cs} for both the looser and denser sand. According to these new equations, the stress ratio q/p reaches the bounding line early during loading following the shape of the bounding line up to the critical state. On the other hand, for set B, the stress ratio meets the bounding line later during loading at a higher current value of M_s and then follows the bounding line up to critical state in a much slower rate.

In the following, undrained cyclic loading was simulated and compared with experimental results, as depicted in Figure 3.17. In order to efficiently capture the number of cycles to liquefaction, Eq. (3.37) was adopted. The values of the model parameters considered in the simulations are presented in Table 3.2, for both sets of equations. Evidently, model prediction incorporating set A captures better the stress-

strain loops, whereas when set B is adopted, shear locking is observed despite the fact that early stabilization (at p>0), as previously discussed, is avoided, and liquefaction is eventually reached; a clear achievement of the proposed plasticity approach. To elucidate the differences between the two sets of equations, Figure 3.18 depicts the evolution of M_s and M_{pt} with the number of strain increments (steps). In case of set B, M_s and M_{pt}, despite the negligible fluctuations due to variation of Ψ, are practically constants throughout loading, far from their critical state value; a fact which eventually leads to shear locking. On the other hand, set A leads to a continuous variation of both M_s and M_{pt} that tend to an asymptotic oscillatory convergence to M_{cs} (due to significant variation of I_r). Overall, set A [Eqs. (3.40)-(3.41)] offers a higher degree of versatility and flexibility allowing for more consistent predictions of sand behavior under monotonic or cyclic loading.

3.5 CONCLUSIONS

A new plasticity framework for sand behavior in multiaxial stress space is developed by combining perfect plasticity with components of smooth hysteretic modeling of the Bouc-Wen type. The proposed formulation incorporates many innovations (such as new mapping and plastic flow rules) intended to provide critical state consistency not only for monotonic but also for cyclic loading and uniqueness of model parameters for a given type of sand. The comparison with experimental results reveals the capability of the model to describe complex patterns of sand behavior, such as cyclic hardening and densification, as well as its flexibility to reproduce liquefaction due to cyclic loading at very large strains (e.g. γ > 8%) without exhibiting shear locking. This very important feature is mainly attributed to a new set of evolution equations for the bounding and phase transformation lines that ensures asymptotic convergence to critical state for all types of applied loading. Implementation of the Ta-Ger sand model in a commercially

available finite element analysis program is currently under development and appears promising.

REFERENCES

Been, K. and Jefferies, M.G. (1985). A state parameter for sands. *Geotechinque* **35**, No. 2, 99-112.

Been, K. and Jefferies, M.G. (2006). *Soil liquefaction. A critical state approach*. Taylor & Francis.

Bolton, M. D. (1986). The strength and dilatancy of sands. *Geotechinque* **36**, No. 1, 65-78.

Bouc, R. (1971). Modele mathematique d' hysteresis. *Acustica* **21**, 16-25.

Boulanger, R. W. and Ziotopoulou, K. (2013). Formulation of a sand plasticity plane-strain model for earthquake engineering applications. *Soil Dynamics and Earthquake Engineering* **53**, 254-267.

Ching, J., Chen, J.R., Yeh, J.Y., and Phoon, K.K. (2012). Updating uncertainties in friction angles of clean sands. *Journal of Geotechnical and Geoenvironmental Engineering, ASC*E **138**, No. 2, 217-229.

Cubrinovski, M. and Ishihara, K. (2000). State concept and modified elastoplasticity for sand modelling, *Soils and Foundations* **40**, No. 5, 124 – 125.

Dafalias, Y.F. (1986). Bounding Surface Plasticity. I: Mathematical Foundation and Hypoplasticity. *Journal of Engineering Mechanics* **112**, No. 9, 966-987.

Dafalias, Y. F. and Manzari, M. T. (2004). Simple plasticity sand model accounting for fabric change effects. *Journal of Engineering Mechanics, ASCE* **130**, No. 6, 622-634.

De Alba, P., Seed, H. B. & Chan, C. K. (1976). Sand liquefaction in large-scale simple shear tests. *J. Soil Mech. Found. Div., ASCE* **102**, No. GT9, 909–927.

Drosos, V. A., Gerolymos, N., and Gazetas, G (2012). Constitutive model for soil amplification of ground shaking: Parameter calibration, comparisons, validation. *Soil Dynamics and Earthquake Engineering* **42**, 255-274.

Duku, P. M., Stewart, J. P., and Whang, D. H. (2008). Volumetric strains of clean sands subject to cyclic loads. *J. Geotechnical and Geoenvironmental Eng., ASCE* **134**, No. 8, 1073-1085.

Elgamal, A.W., Dobry, R., Parra, E., and Yang, Z. (1998). *Soil Dilation and Shear Deformation During Liquefaction*, *Proceedings of the 4th International Conference on Case Histories in Geotechnical Engineering*, St Louis, Missouri, March 8-15, Prakash S. (ed.): p. 22

Elgamal, A., Yang, Z., and Parra, E., (2002). Computational modeling of Cyclic Mobility and Post-Liquefaction Site Response. *Soil Dynamics and Earthquake Engineering* **22**, No. 4, 259-271.

Gerolymos, N. and Gazetas, G. (2005). Constitutive model for 1–D cyclic soil behavior applied to seismic analysis of layered deposits. *Soils and Foundations* **45**, No. 3, 147-159.

Gerolymos, N., Gazetas, G. and Vardoulakis, I. (2007). A Thermo-poro–viscoplastic shear band model for seismic triggering and evolution of catastrophic landslides. *Soils and Foundations* **47**, No 1, 11–25.

Gerolymos N. (2010). Numerical modeling of Seismic Triggering, Evolution, and deposition of Rapid Landslides: Application to Higashi Takezawa (2004). *International Journal for Numerical and Analytical Methods in Geomechanics* **34**, No 4, 383-407.

Gudehus, G. (1996). A comprehensive constitutive equation for granular materials. *Soils and Foundations* **36,** No 1**,** 1-12.

Ishihara, K. and Towhata, I. (1980). One-dimensional soil response analysis during earthquakes based on effective stress method. *Journal of the Faculty of Engineering, University of Tokyo (B)*, **35**, No. 4, 665 – 700.

Kolymbas, D. (2012). Barodesy: a new hypoplastic approach. *International Journal for Numerical and Analytical Methods in Geomechanics* **36**, No. 9, 1220-1240.

Kramer, S.L. (1996). *Geotechnical Earthquake Engineering*, Prentice Hall, Inc., Upper Saddle River, New Jersey, 653 pp.

Manzari, M. T. and Dafalias, Y. F. (1997). A two-surface critical plasticity model for sand. *Geotechnique* **47**, No. 2, 255-272.

Papadimitriou A. G., Bouckovalas G. D., Dafalias Y. F. (2001), "Plasticity model for sand under small and large cyclic strains", *Journal of Geotechnical and Geoenvironmental Engineering, ASCE* 127, No. 11, 973 – 983.

Park, S.S. and Byrne, P.M. (2004). Practical constitutive model for soil liquefaction. *Proc. of 9th Intl Sym on Numerical Models in Geomechanics*, Ottawa, Canada, 181-186.

Pastor, M., Zienkiewicz, O. C., and Chan, A. H. C. (1990). Generalized plasticity and the modelling of soil behaviour. *International Journal for Numerical and Analytical Methods in Geomechanics* **14**, No. 3, 151-190.

Prevost. J. H. (1985). A Simple Plasticity Theory for frictional Cohesionless soils. *Soil Dynamics and Earthquake Engineering* **4**, No. 1, 9-17.

Rowe, P. W. (1962). The stress-dilatancy relation for static equilibrium of an assembly of particles in contact. *Proceedings, Royal Soc. London, Ser. A,* Vol. 269, 500–527.

Sivaselvan, M.V., Reinhorn, A. M. (2000). Hysteretic models for deteriorating inelastic structures. *J. Eng. Mech.* **126**, No 6, 633–640.

Silver, M. L., and Seed, H. B. (1971). Volume changes in sand during cyclic loading. *J. Soil Mechanics and Foundations Div., ASCE* **97**, SM. 9, 1171–182.

Taborda, D.M., Zdravkovic, L., Kontoe, S., Potts, D.M. (2014). Computational study on the modification of a bounding surface plasticity model for sands. *Computers and Geotechnics* **59**, 145-160.

Taiebat, M. and Dafalias, Y. F. (2007). SANISAND: Simple anisotropic sand plasticity model. *International Journal for Numerical and Analytical Methods in Geomechanics* **32**, No. 8, 915-948.

Tasiopoulou, P. and Gerolymos, N. (2012). Development of a modified elastoplasticity model for sand. *Proceedings of the Second International Conference on Performance–Based Design in Earthquake Geotechnical Engineering, 28-30 May*, Taormina (Italy), in CD Rom.

Triantafyllou, S., Koumousis, V. (2012). An hysteretic quadrilateral plane stress element. *Archive of Applied Mechanics* **82**, 1675-1687.

Verdugo, R and Ishihara, K. (1996). The steady state of sandy soils. *Soils and Foundations* **36**, No.2, 81–91.

Wen, Y. K. (1976). Method for random vibration of hysteretic systems. *Journal of Engineering Mechanic, ASCE* **102**, 249-263.

Wood, D. M., Belkheir, K., and Liu, D. F. (1994). Strain softening and state parameter for sand modeling. *Geotechnique* **44**, No. 2, 335–339.

Zhang, J. M., Shamoto, Y. and Tokimatsu, K. (1997). Moving Critical and Phase-Transformation Stress State Lines of Saturated Sand during Undrained Cyclic Shear, *Soils and Foundations* **37**, No.2, 51-59.

Table 3.1. Model parameters and values for monotonic loading of Toyoura sand.

	SET A, Eqs (3.41)-(3.42)		**Set B, Eqs (3.39)**	
	Parameter	**Values**	**Parameter**	**Values**
Elasticity	A_o	130	A_o	130
	ν	0.15	ν	0.15
	m	0.8	m	0.8
Critical State	M_{cs}	1.25	M_{cs}	1.25
	–	–	e_0	0.934
	–	–	λ	0.019
	–	–	ξ	0.7
Bounding Surface & Dilatancy	Q	9.1	n_b	0.9
	R	0.75	n_d	0.7
	c	10	–	–
Hardening Exponent n	n	0.35	n	0.25

Table 3.2. Model parameters and values for undrained cyclic loading of Toyoura sand.

	SET A, Eqs (3.41)-(3.42)		**Set B, Eqs (3.39)**	
	Parameter	**Values**	**Parameter**	**Values**
Elasticity	A_o	130	A_o	130
	ν	0.15	ν	0.15
	m	0.8	m	0.8
Critical State	M_{cs}	1.33	M_{cs}	1.33
	–	–	e_0	0.934
	–	–	λ	0.019
	–	–	ξ	0.7
Bounding Surface & Dilatancy	Q	9.1	n_b	0.9
	R	0.77	n_d	0.7
	c	4	–	–
Hardening Exponent n	n_0	0.5	n_0	1
	n_f	0.3	n_f	0.2
	n_{peak}	8	n_{peak}	4.7
	β	3.5	β	105
	γ	30	γ	42

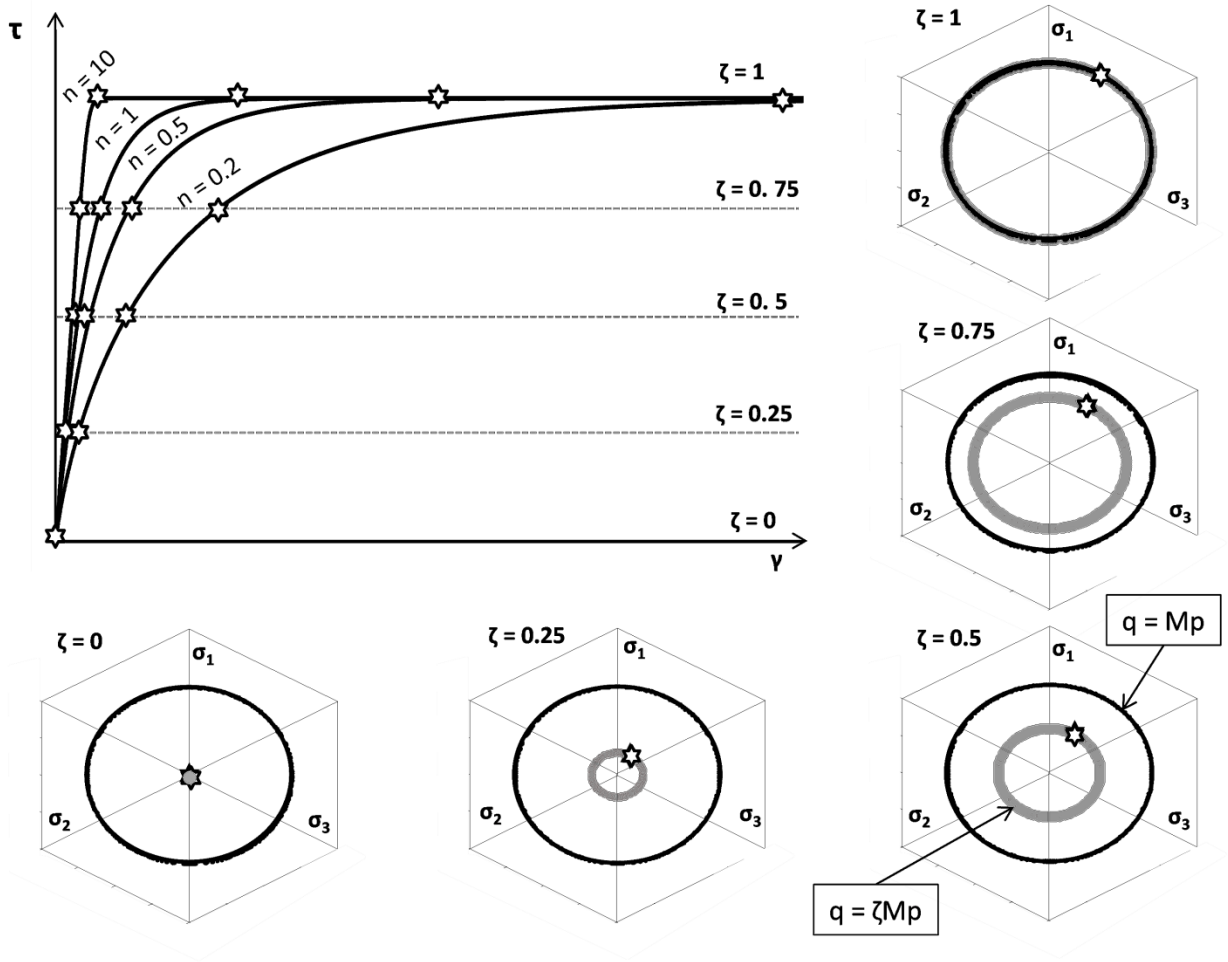

Figure 3.1. Evolution of parameter ζ during loading and influence of hardening exponent n on the predicted response, in case of a Drucker-Prager failure criterion. The star symbols characterize the current stress states.

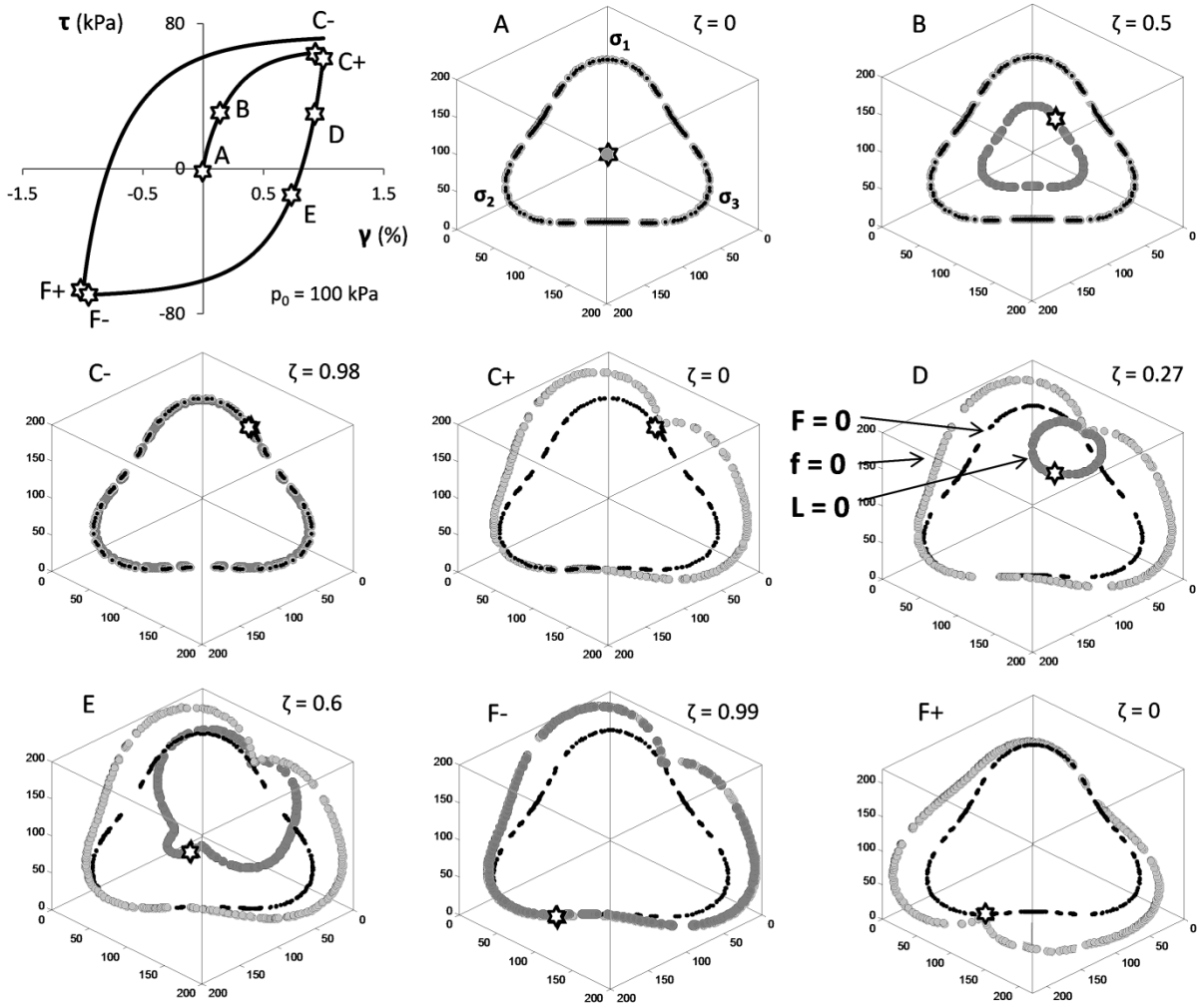

Figure 3.2. Evolution of loading, L = 0, bounding, f=0, and target failure, F=0, surface, illustrated in π-plane graphs, for a cyclic simple shear test with constant mean effective stress. The star symbols characterize the current stress states.

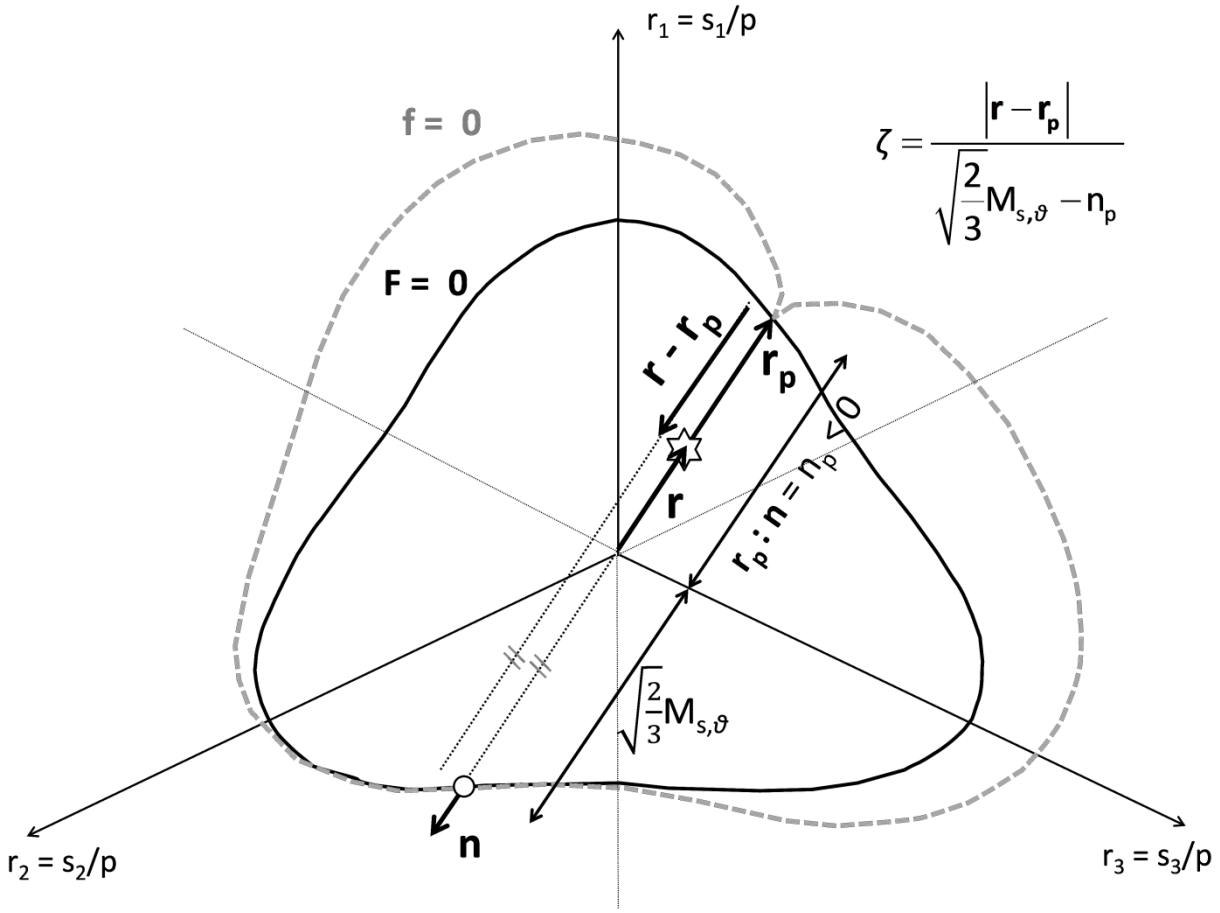

Figure 3.3. Definition of parameter ζ upon first loading reversal (point D of Figure 2) for a cyclic simple shear test with constant mean effective stress. The star symbol characterizes the current stress state, while the circle corresponds to "image" stress point.

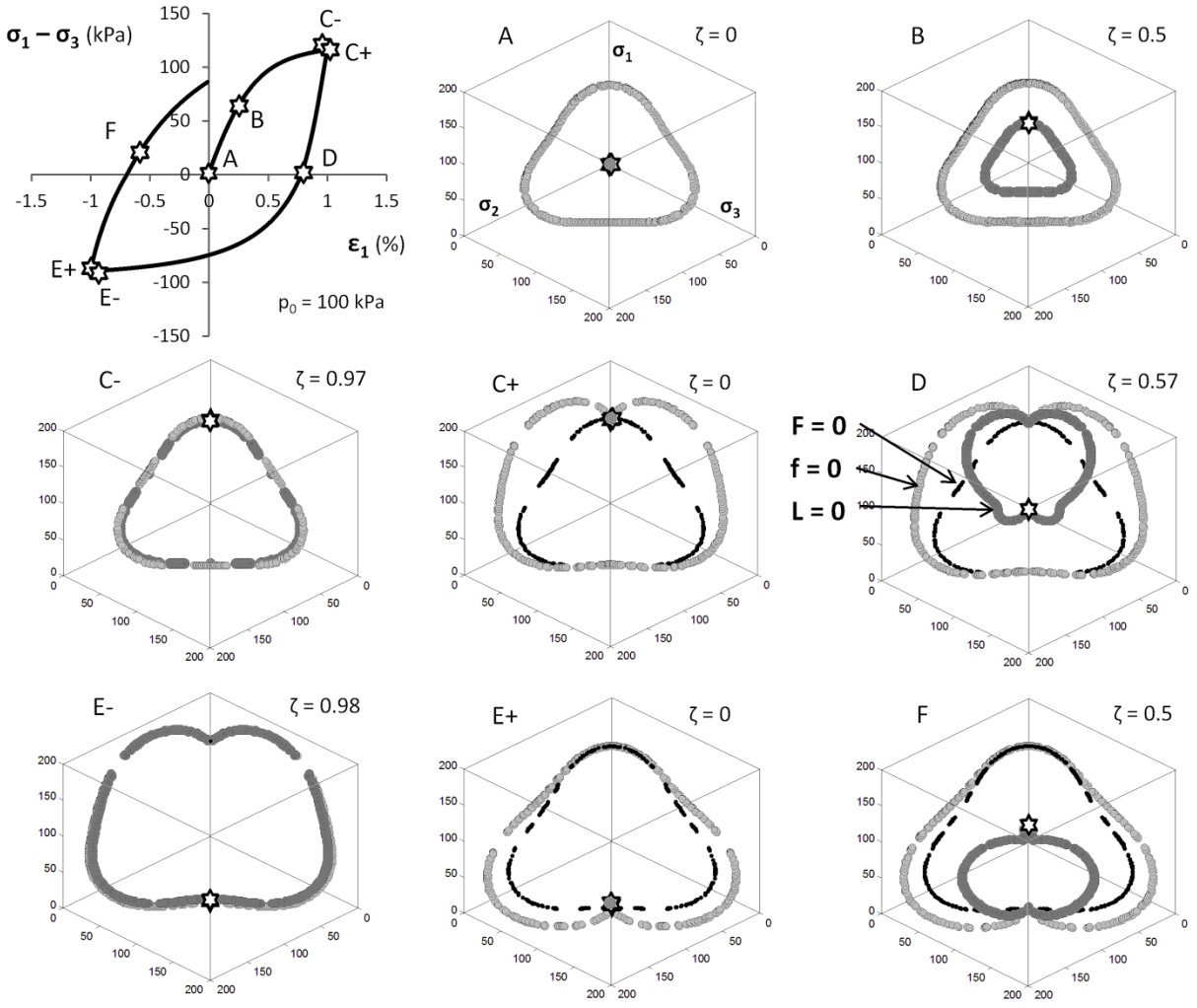

Figure 3.4. Evolution of loading, L = 0, bounding, f = 0, and target failure surface, F = 0 illustrated in π-plane graphs, for a cyclic triaxial p-constant test. The star symbols characterize the current stress states.

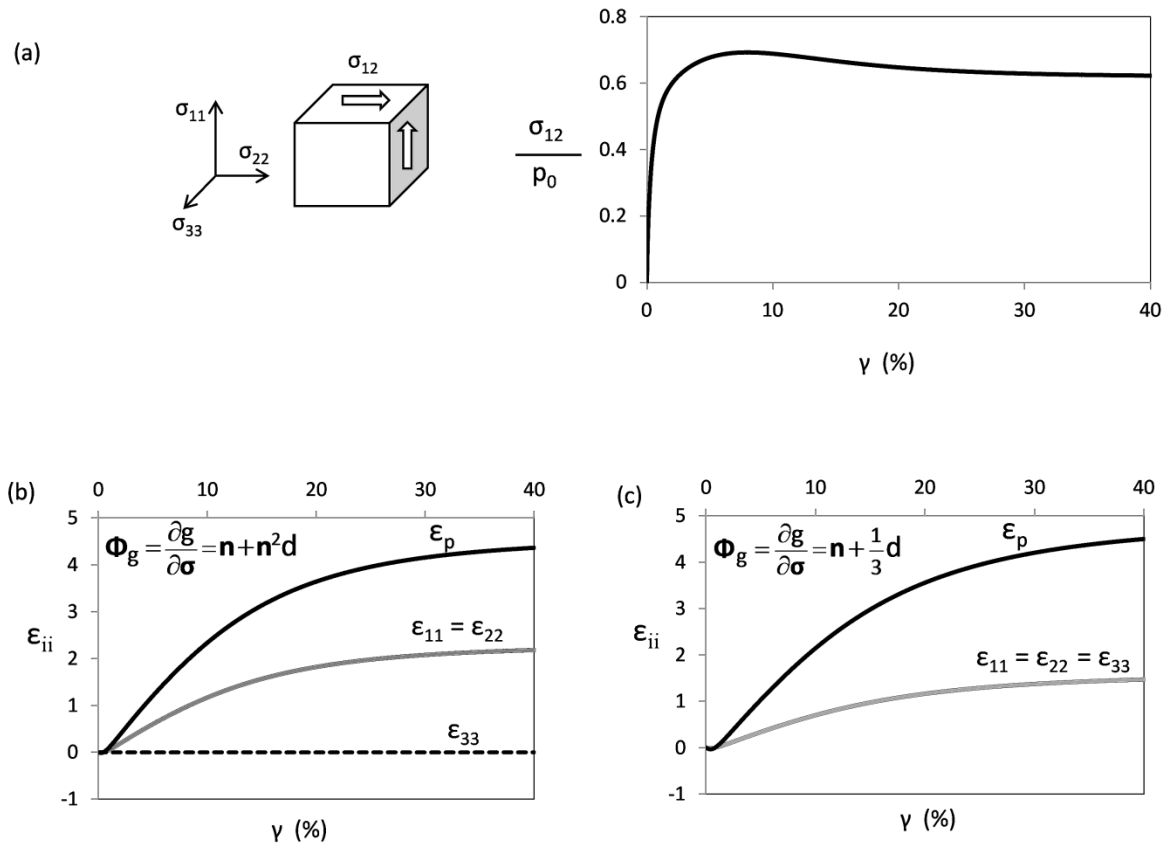

Figure 3.5. Distribution/Evolution of normal strain increments during a monotonic drained simple shear element test (a). Model prediction is held for both assumed gradients of plastic potential surface: (b) Eq.(3.33) and (c) Eq.(3.35).

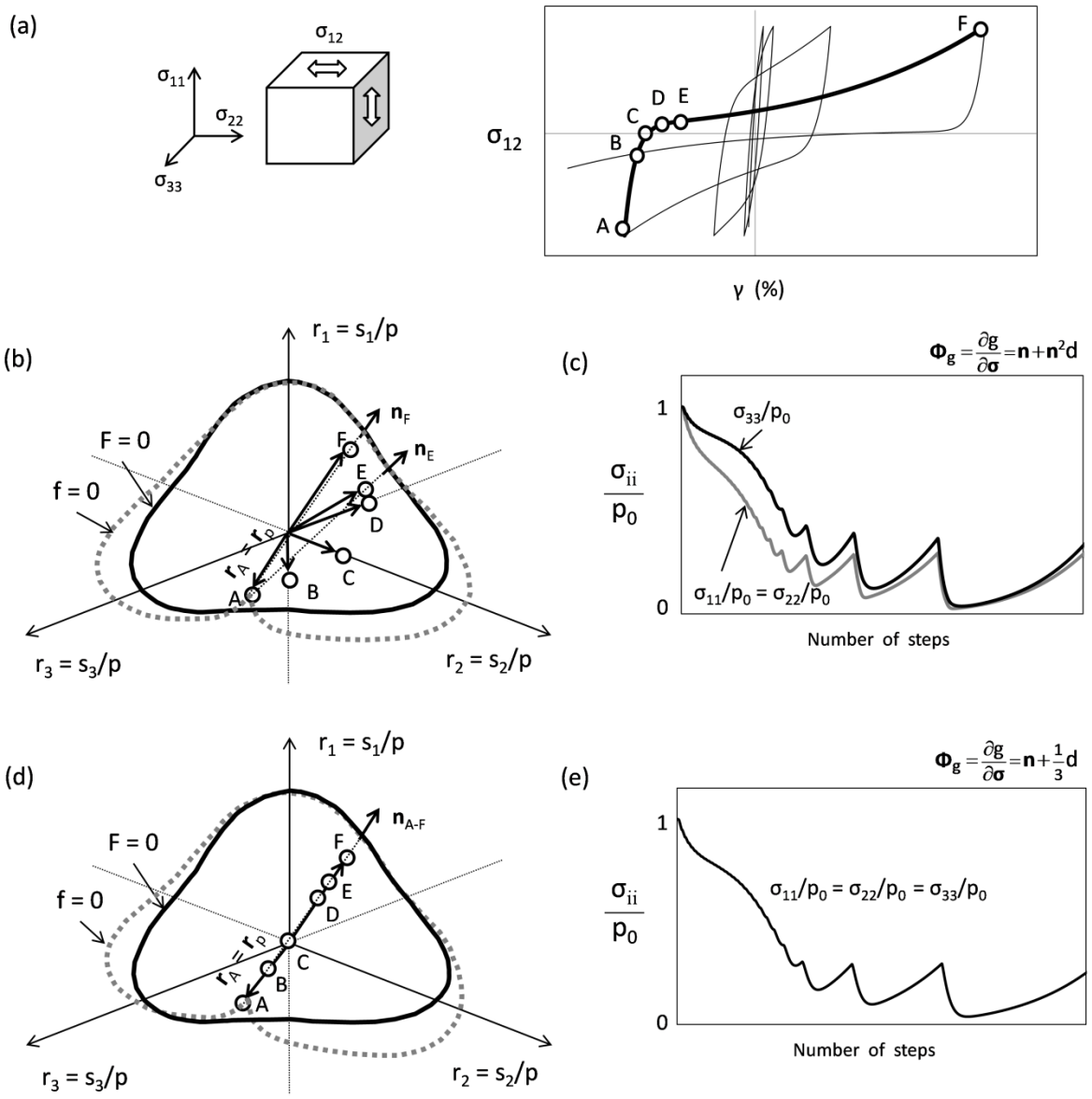

Figure 3.6. (a) Stress-strain loops under cyclic shear undrained loading. (b) Stress path in π-plane using Eq.(3.33), (c) evolution of shear stresses using Eq.(3.33), (d) Stress path in π-plane using Eq. (3.35), (c) evolution of shear stresses using Eq. (3.35).

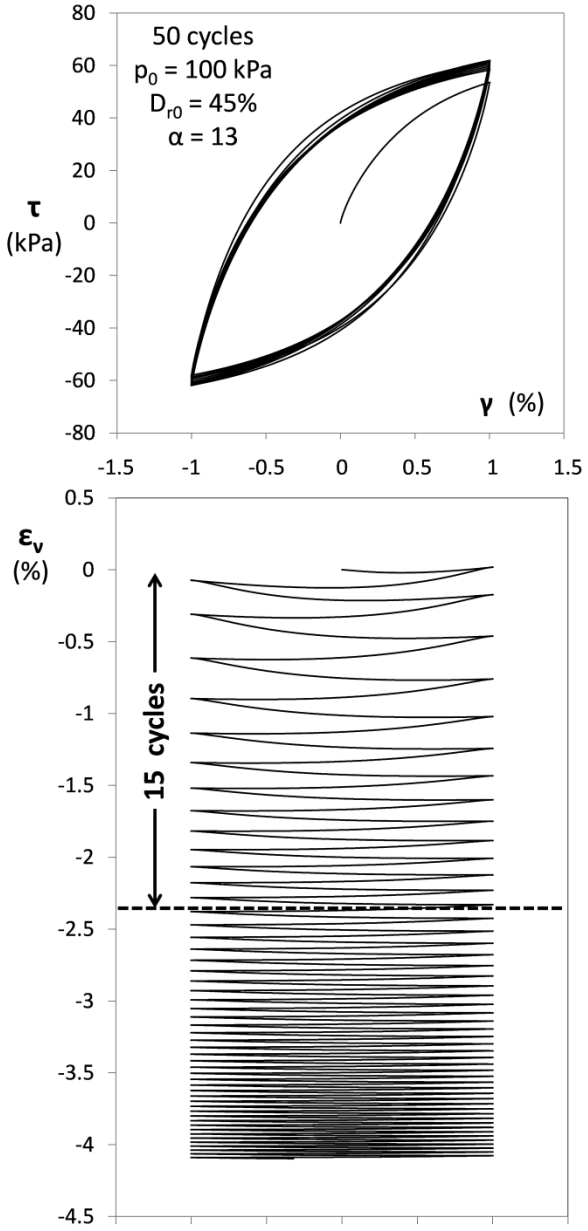

Figure 3.7. Model prediction for a cyclic simple shear test under constant shear strain amplitude, exhibiting densification.

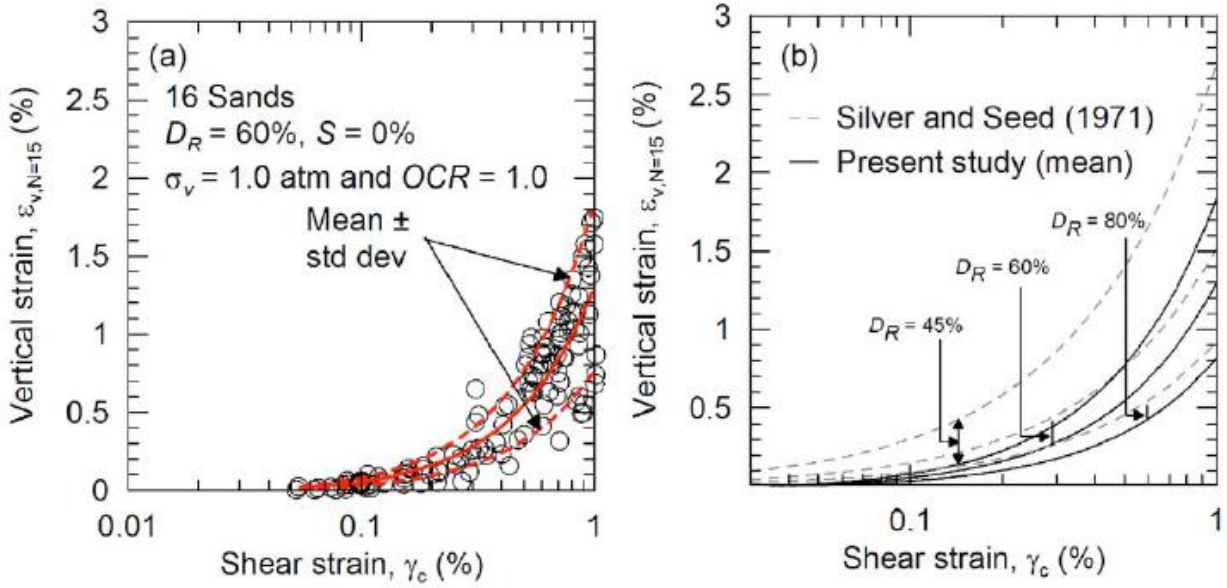

Figure 3.8. Volumetric strains in drained cyclic direct simple shear tests on clean sands (Duku et al. 2008): (a) Results from 16 sands at a relative density of about 60% with an overburden stress of 1.0 atm, and (b) Comparison of trends with earlier relationships by Silver and Seed (1971) for sands at relative densities of 45, 60, and 80%.

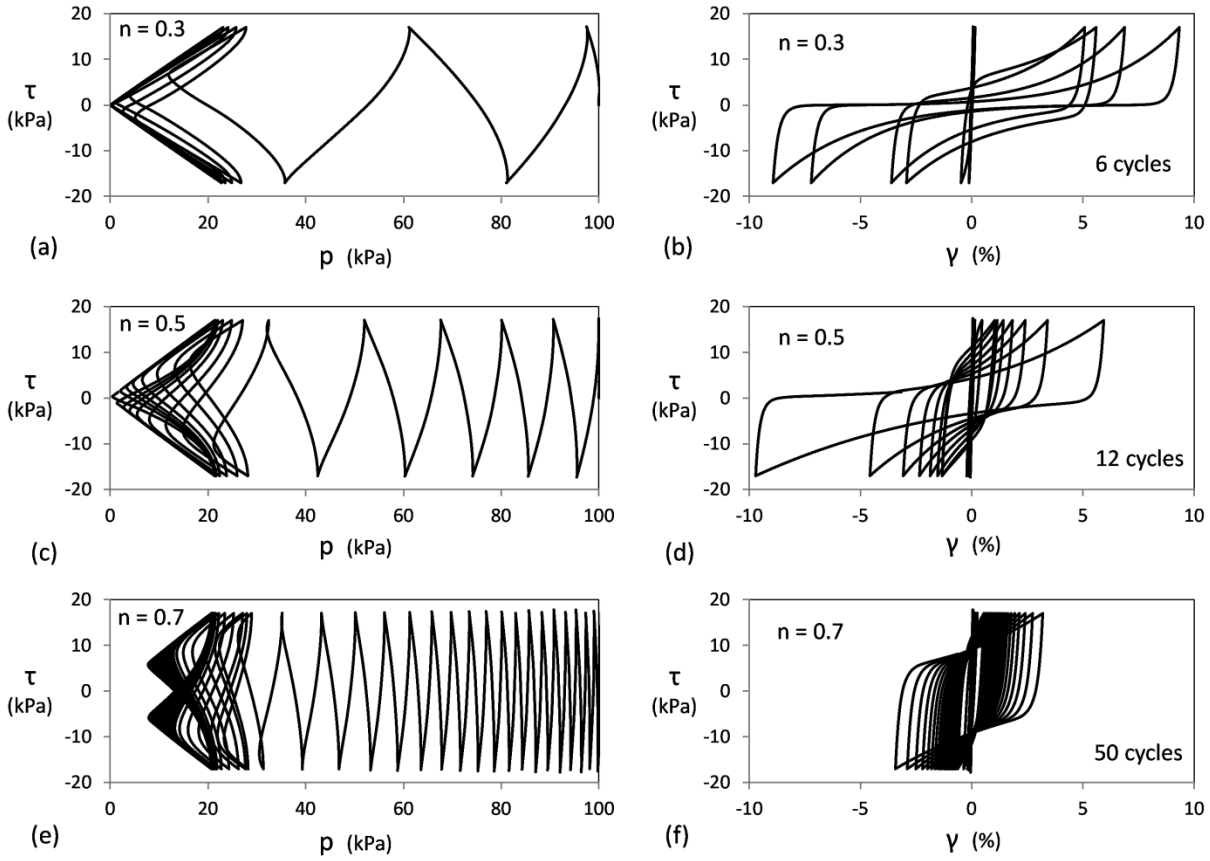

Figure 3.9. Influence of exponent hardening parameter n on the simulated cyclic undrained response of sand.

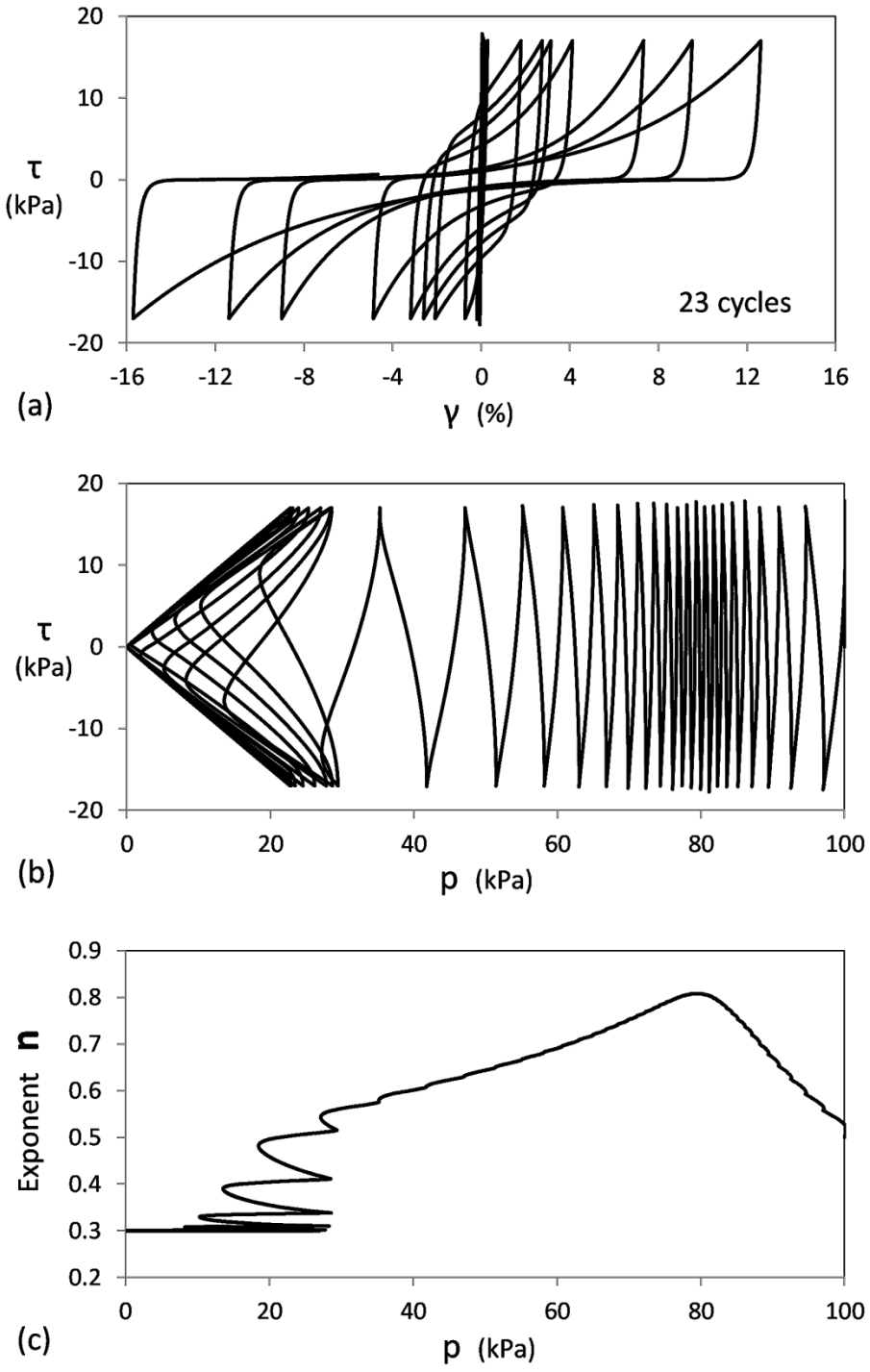

Figure 3.10. Computed cyclic simple shear undrained response of a sand specimen with D_r = 70% under constant shear stress amplitude and evolving exponent n.

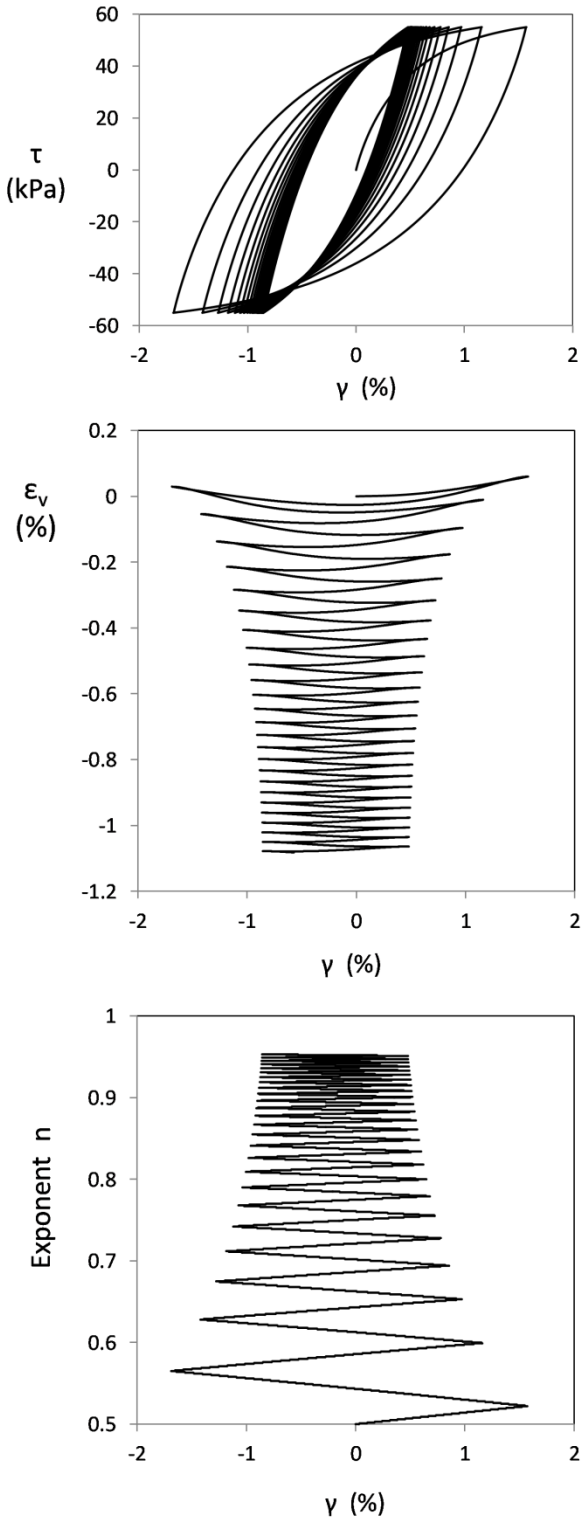

Figure 3.11. Demonstation of drained cyclic simple shear response of a sand specimen with Dr0 = 40 % under constant shear stress amplitude and evolving exponent n.

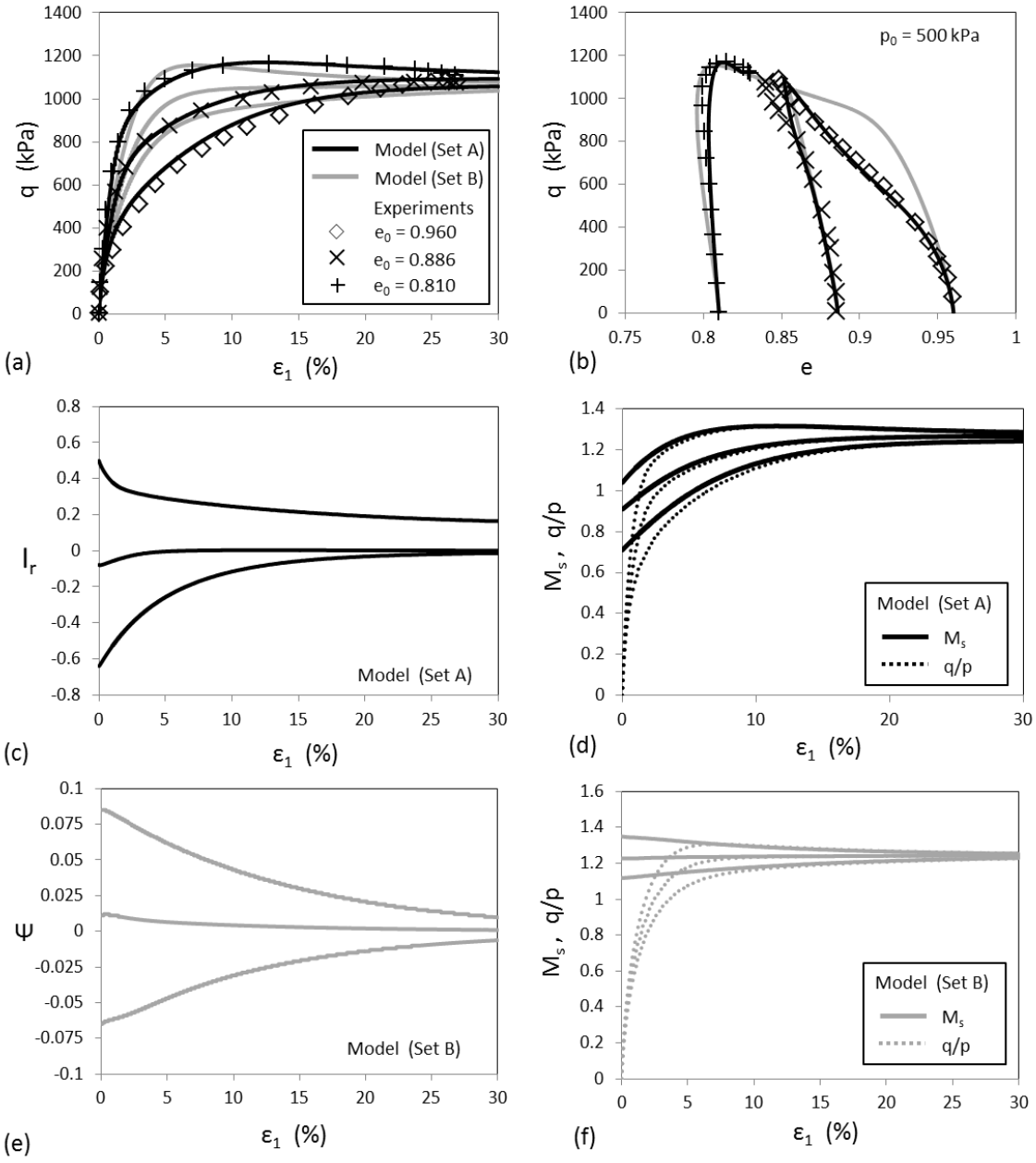

Figure 3.12. (a), (b) Comparison between experimental data from monotonic drained triaxial tests on Toyoura sand with p_0 =100 kPa (Verdugo and Ishihara, 1996) and model predictions using two different evolution rules (set of equations A proposed herein, and set B) for the bounding, M_s , and phase transformation line, M_{pt}. (c), (d) Evolution of state variable, I_r, bounding line, M_s and stress ratio, q/p, versus axial strain for set A [Eqs (3.41) -(3.42)]. (e), (f) Evolution of state variable, Ψ, bounding line, M_s and stress ratio, q/p, versus axial strain for set B [Eqs (3.39)].

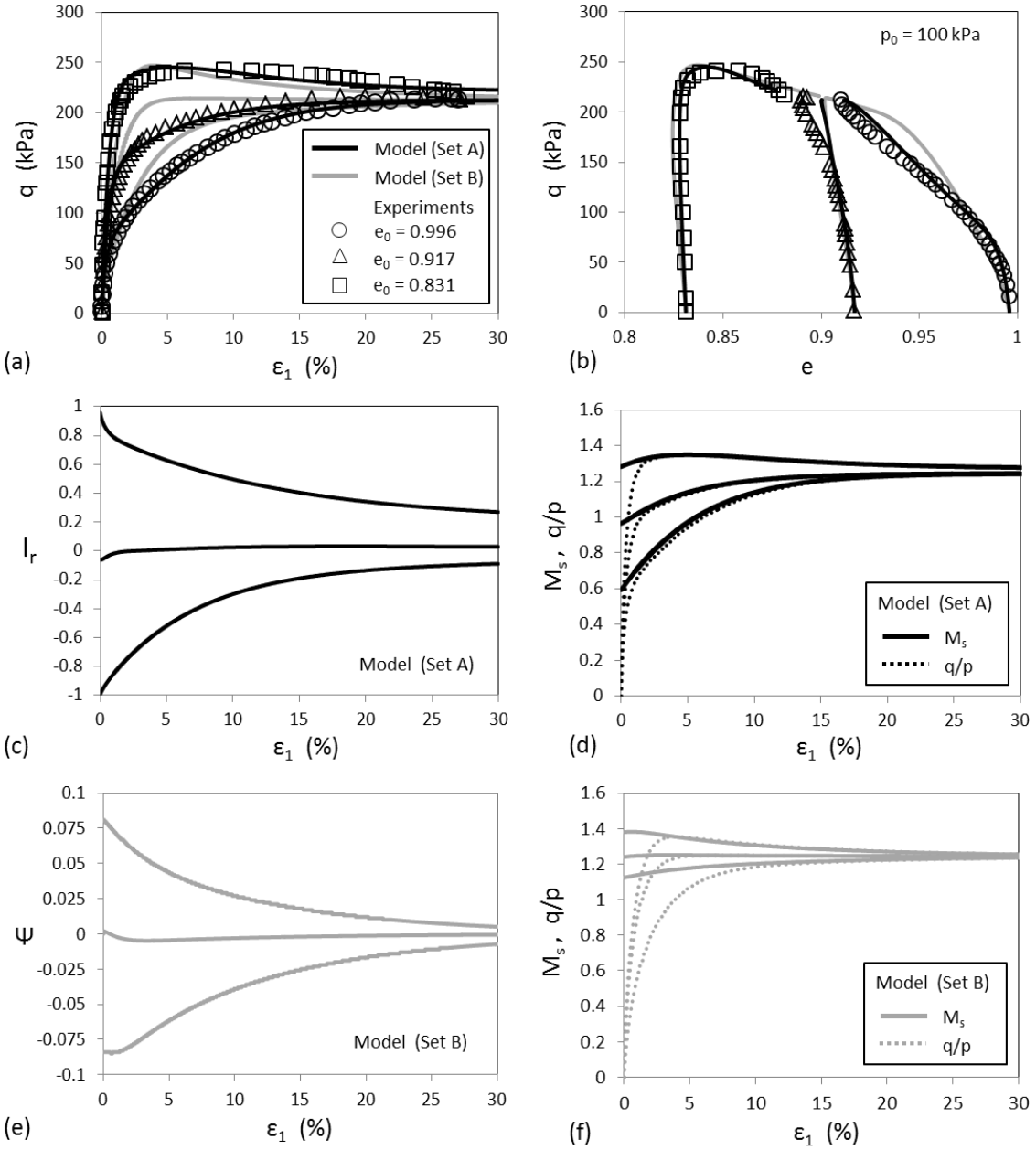

Figure 3.13. (a), (b) Comparison between experimental data from monotonic drained triaxial tests on Toyoura sand with p_0 =100 kPa (Verdugo and Ishihara, 1996) and model predictions using two different evolution rules (set of equations A proposed herein, and set B) for the bounding, M_s , and phase transformation line, M_{pt}. (c), (d) Evolution of state variable, I_r, bounding line, M_s and stress ratio, q/p, versus axial strain for set A [Eqs (3.41) -(3.42)]. (e), (f) Evolution of state variable, Ψ, bounding line, M_s and stress ratio, q/p, versus axial strain for set B [Eqs (3.39)].

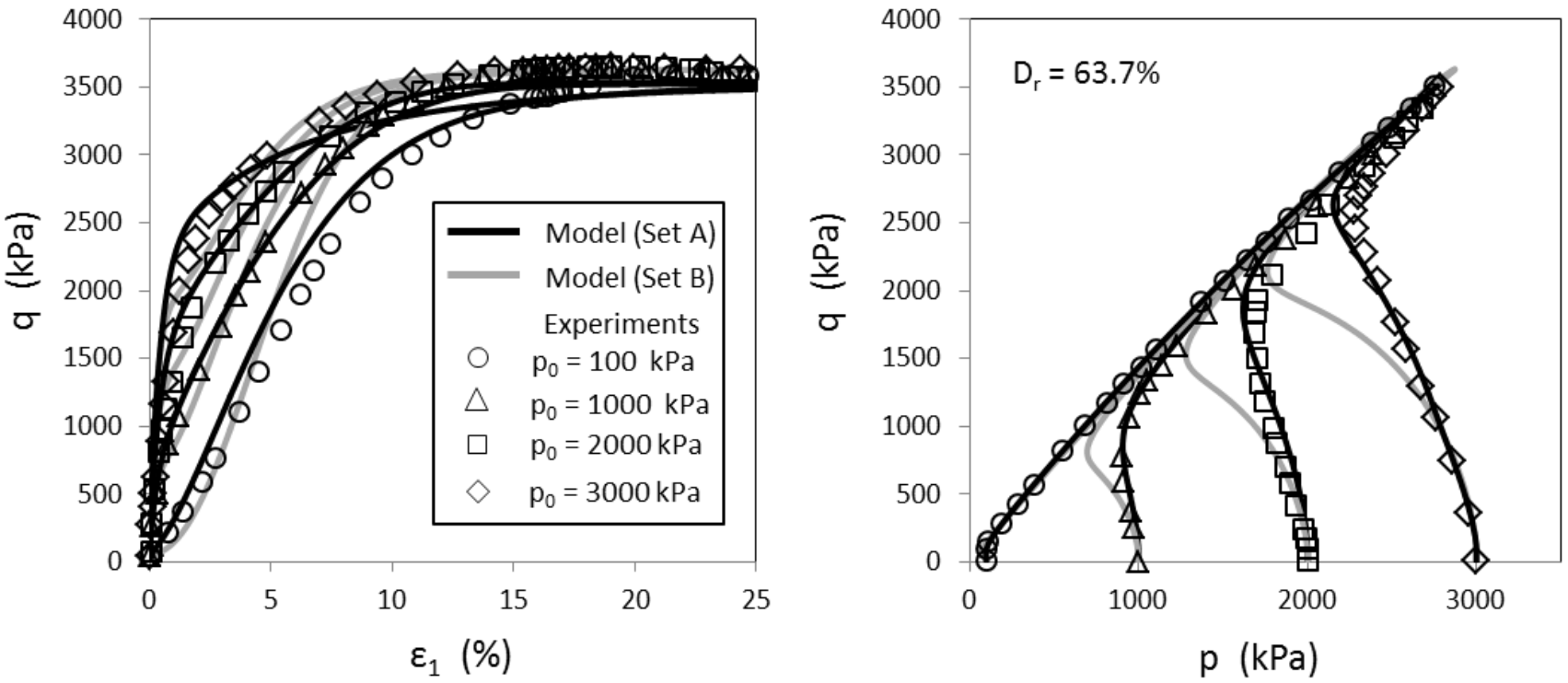

Figure 3.14. Comparison between experimental data from monotonic undrained triaxial tests on Toyoura sand (Verdugo and Ishihara, 1996) and model predictions using two different evolution rules (set of equations A proposed herein, and set B) for the bounding, M_s , and phase transformation line, M_{pt}.

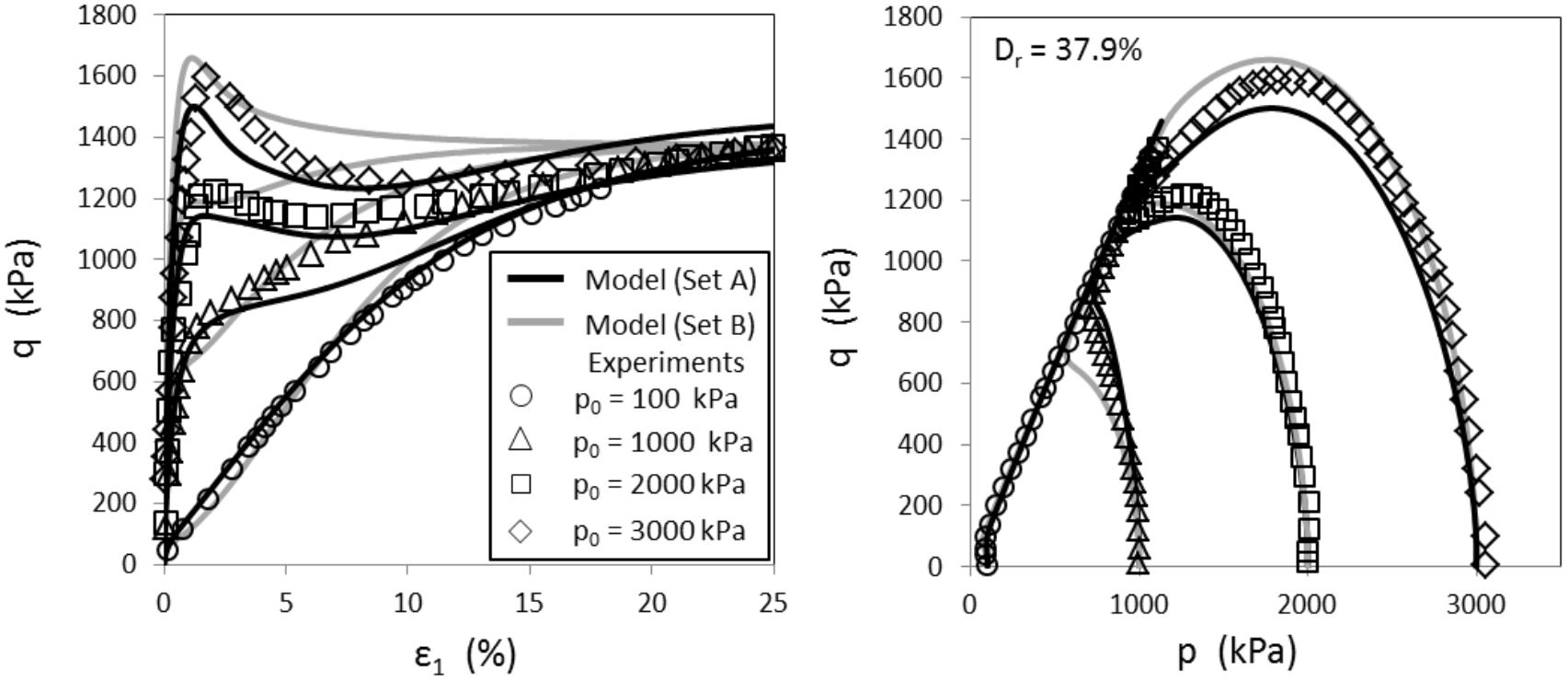

Figure 3.15. Comparison between experimental data from monotonic undrained triaxial tests on Toyoura sand (Verdugo and Ishihara, 1996) and model predictions using two different evolution rules (set of equations A proposed herein, and set B) for the bounding, M_s and phase transformation line, M_{pt}.

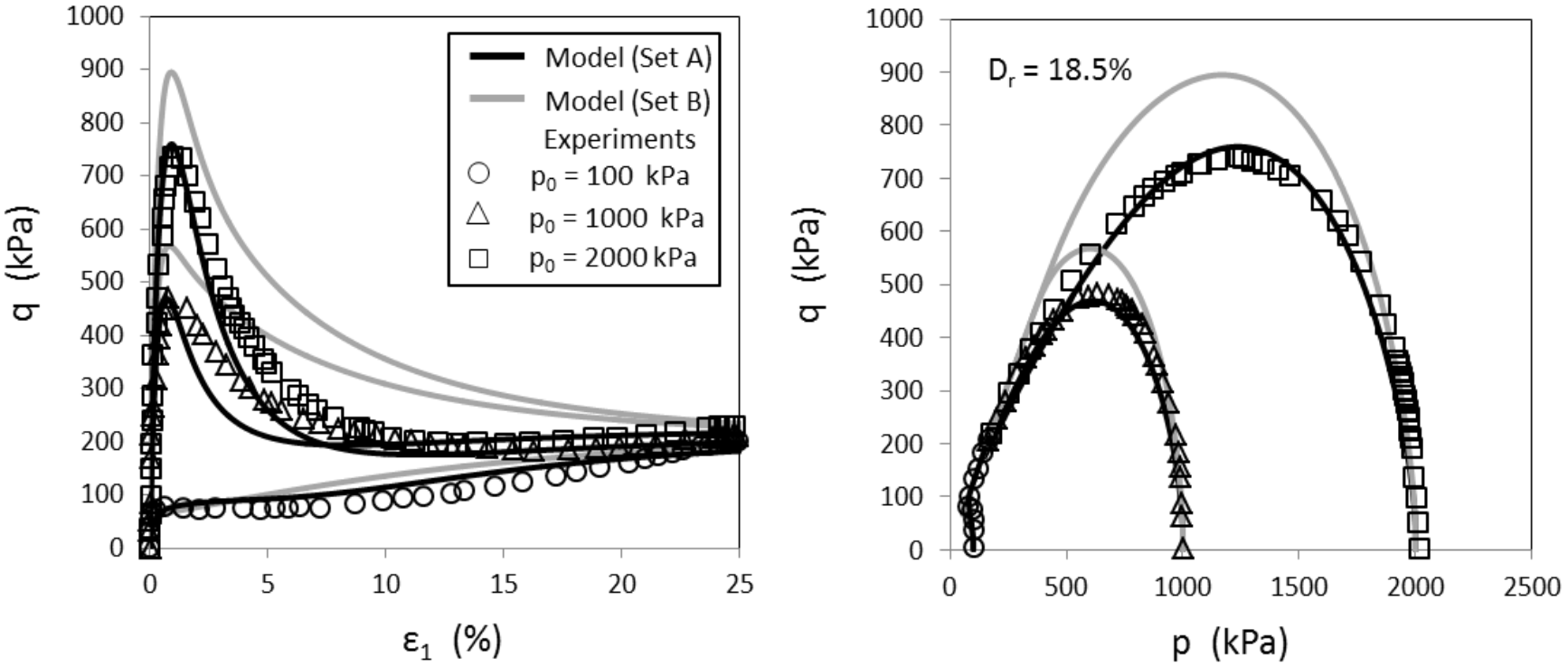

Figure 3.16. Comparison between experimental data from monotonic undrained triaxial tests on Toyoura sand (Verdugo and Ishihara, 1996) and model predictions using two different evolution rules (set of equations A proposed herein, and set B) for the bounding, M_s and phase transformation line, M_{pt}.

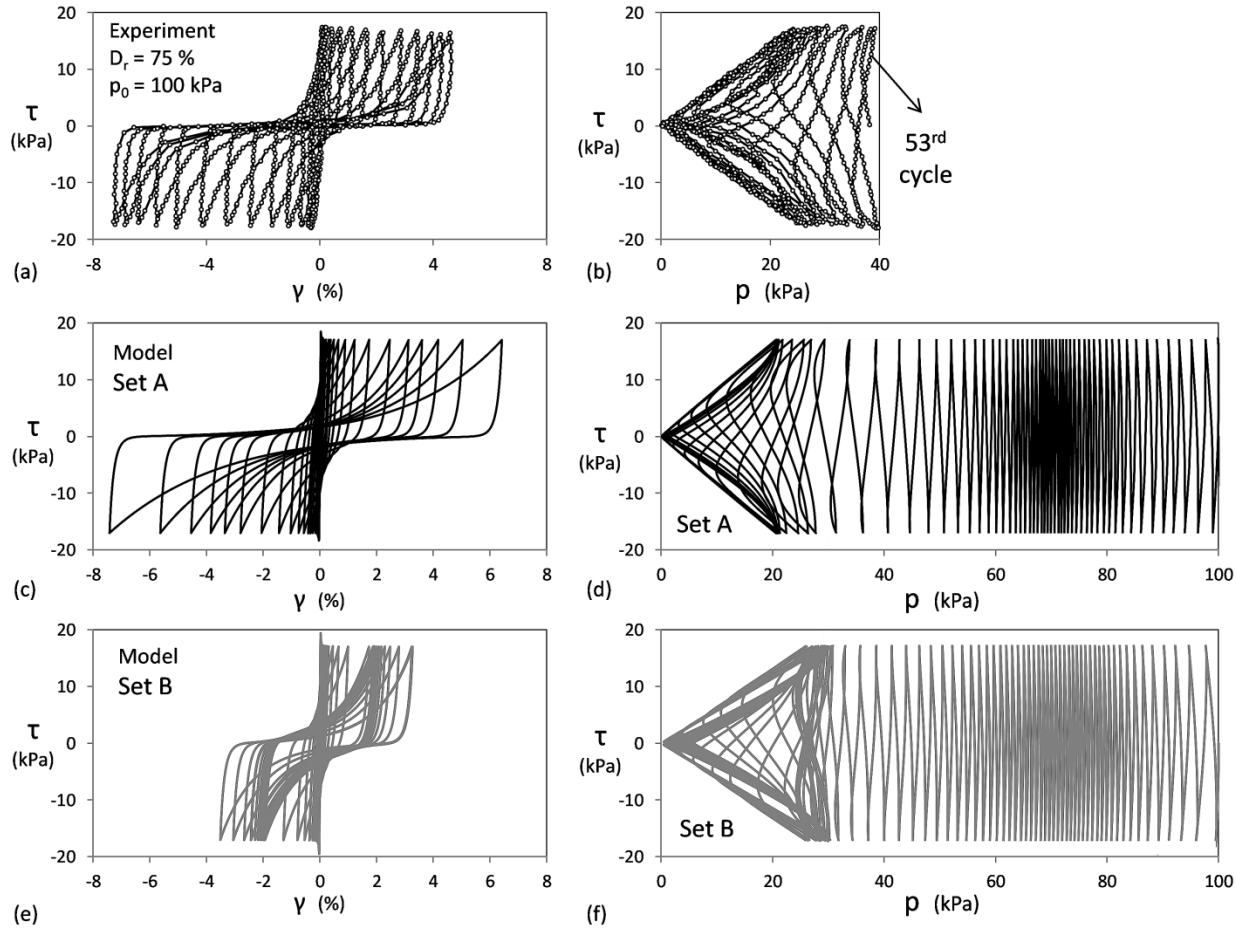

Figure 3.17. Comparison between experimental data from cyclic undrained torsional shear tests on Toyoura sand (Zhang et al., 1997) and model predictions using two different evolution rules (set of equations A proposed herein, and set B) for the bounding, M_s and phase transformation line, M_{pt}.

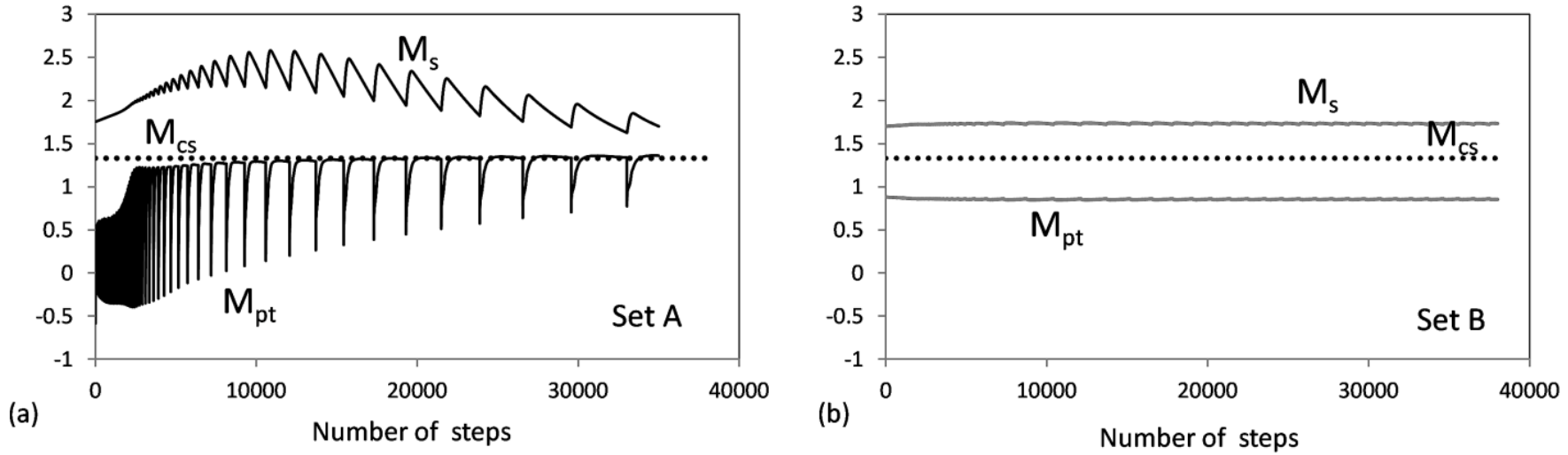

Figure 3.18. Evolution of bounding, M_s and phase transformation line, M_{pt} for model prediction of experimental data from cyclic undrained torsional shear tests on Toyoura sand (Zhang et al., 1997) of Figure 15 using two different evolution rules for the bounding and phase transformation lines: (a) set A [Eqs (3.41)-(3.42)] and (b) set B [Eqs (3.39)].

CHAPTER 4

Calibration Approach Accounting for Intrinsic and Stress-Induced Anisotropy

ABSTRACT

A practical calibration approach of a macroscopic constitutive model, based on a new plasticity framework (Tasiopoulou and Gerolymos, 2012, 2014 and 2015), is featured in this chapter. At first, the number of unknown model parameters is reduced to a minimum by incorporating Bolton's empirical relationships in model formulation. Then, calibration is performed based on data from drained and undrained triaxial compression tests for three different types of sand. At this stage, the remaining unknown parameters are expressed as a function of the initial state (relative density and pressure), while inherent fabric effects such as particle shape, size and packing on the calibration process are discussed. At last, stress-induced anisotropy is dealt by introducing a scalar-valued variable in the model, being a function of principal stress rotation angle, α and the

intermediate stress parameter, b, without affecting the number of unknown model parameters.

4.1 INTRODUCTION

Behavior of granular materials has been extensively studied in literature. After repetitive experimental observations, it has become common knowledge that sand tends to undergo shear-induced volume change until a critical state is reached, upon which shearing can no further cause any volumetric change. Whether shearing tends to develop positive (contraction) or negative (dilation) volume change depends on the initial state of the material relative to the critical state, being a function of the relative density or void ratio and the confining pressure.

Various constitutive models for sands have been proposed in literature aiming to reproduce the behavior described above by incorporating well-established theoretical frameworks such as the critical state theory and dilatancy laws (Rowe, 1962; Roscoe, 1970; Bolton, 1986). While their success in simulation is automatically ensured once a suitable plastic flow rule has been chosen and the critical state concept has been included, the real challenge arises through validation process against experiments, otherwise known as calibration. The more advanced the constitutive model is, the higher the challenge. First, the number of unknown model parameters is proportional to the level of the model complexity, which usually coincides with the level of detail in predictability. Secondarily, in these cases, it is common that most of the parameters lose their physical perceptibility and thus, they cannot be related to measurable properties.

Calibration process is considered successful when realistic model predictions versus experiments can be obtained for various initial states, covering a wide range of relative densities and pressures. However, while the set of values assigned to model parameters after the calibration process, works well for the particular sand under study, it is proven

to be unsuitable for another sand and recalibration is needed in a "case-specific" manner for each sand type. The fact that granular materials exhibit variations in their response, attributed to differences on their particle shape, size and packing, is long known (Cho et al., 2006; Santamarina and Cho, 2004; Andò et al., 2012; Desrues and Viggiani, 2004; Viggiani et al., 2001; Tsomokos and Georgiannou, 2010). Figure 1 illustrates experimental data verifying how the response of three different types of sands with the same initial state and loading conditions (drained conventional triaxial compression) varies in terms of the amount of dilation and the occurrence of peak strength. Table 1 offers information on the specific geometrical traits, distribution and arrangement of sand particles constituting a particular inherent fabric for each sand type. Experimental evidence explicitly indicates that separate calibration would be required for each type of sand even for the same loading conditions due to fabric effects.

Besides the aforementioned complications, the challenge of calibration process gets even higher when stress-induced anisotropy is accounted for. It has been observed that the maximum strength and volume change tendency of a particular sand is influenced not only by the initial density and pressure but also by the type of loading; thus, the loading direction relative to deposition plane of the sample (Tatsuoka et al. (1986); Yoshimine et al., 1998; Nakata et al., 1998) as shown in Figure 2. The differences among the three types of loading are associated with the angle formed between the maximum principal stress and the vertical direction (perpendicular to the usually horizontal bedding plane which is the common fabric orientation due to gravitational forces), α value, and the effect of the intermediate stress, b value (Yoshimine et al., 1998; Nakata et al., 1998). Clearly, the values of the model parameters obtained after calibration based on triaxial compression tests would not be appropriate for simple shear or triaxial extension loading.

Evidently, the utility of a constitutive model cannot rely on a "case-specific" calibration for each type of loading especially when large scale boundary-valued problems are

studied, where stress paths cannot be predetermined. Therefore, in order to capture all the features of sand behavior described above, a constitutive model requires supplementary formulations to account for the fabric and anisotropy effects, before calibration becomes even an issue. Various approaches have been developed to address stress-induced anisotropy, such as rotation of yield surface by introducing kinematic hardening (Sekiguchi and Ohta, 1977; Anandarajah and Dafalias, 1986; Cambou and Lanier, 1988; Pestana and Whittle, 1999; Hashiguchi and Mase, 2007; Duriez and Vincens, 2015). A most complete theoretical approach has been recently developed by Li and Dafalias (2012) and Gao et al. (2014), coupling the inherent fabric anisotropy with the loading direction within the critical state framework, named as "Anisotropic Critical State Theory". However, an adoption of any of these approaches increases inevitably the number of unknown model parameters causing further complications in the calibration process and undermining the predictability of the model; a vicious circle.

In an attempt to rise to the presented challenges while keeping a balance between utility and predictability of the model, a calibration approach of a macroscopic constitutive model based on a new plasticity framework (Tasiopoulou and Gerolymos, 2012, 2014 and 2015), is featured in this chapter. At first, the number of unknown model parameters is reduced to a minimum by incorporating Bolton's empirical relationships in model formulation. Then, calibration is performed based on data from drained and undrained triaxial compression tests for three different types of sand. At this stage, the remaining unknown parameters are expressed as a function of the initial state (relative density and pressure), while inherent fabric effects such as particle shape, size and packing on the calibration process are discussed. At last, stress-induced anisotropy is dealt by introducing a scalar-valued variable in the model, being a function of principal stress rotation angle, α and the intermediate stress parameter, b, without affecting the number of unknown model parameters.

4.2 CONSTITUTIVE MODEL FOR SAND

A brief summary of the constitutive model formulation, designated as Ta-Ger sand model and extensively described by Tasiopoulou and Gerolymos (2015), is given in the following. Ta-Ger is based on a reformulation of perfect elastoplasticity by combining features of Bouc-Wen hysteresis (Bouc, 1971 and Wen, 1976) and bounding surface plasticity (Dafalias, 1986). The developed constitutive formulation consists of a non-explicitly defined plastic modulus, a vanished elastic region and a plastic flow rule, based on a Rowe's dilatancy theory (1962) to account for anisotropic distribution of the dilatancy to the normal plastic strain increments.

4.2.1 Constitutive Formulation

The elastoplastic matrix is explicitly given by:

$$\left\{E^{ep}\right\}=\left\{E^{e}\right\}\left[\{I\}-\frac{\left\{\Phi_g\right\}\left\{\Phi_f\right\}^T\left\{E^{e}\right\}\{H\}}{\left\{\Phi_f\right\}^T\left\{E^{e}\right\}\left\{\Phi_g\right\}}\right] \qquad (4.1)$$

where $\left\{\Phi_f\right\}$ and $\left\{\Phi_g\right\}$ account for the gradients of yield surface and plastic potential surface, respectively. The plastic matrix $\{H\}$ offers a gradual and smooth ("hardening-type") transition from the elastic to perfectly plastic response. Therefore, the values of its terms are strictly bounded within the range of [0,1]. The matrix $\{H\}$ acquires only diagonal terms as a function of a dimensionless variable ζ and a hardening exponent variable, n. Both of these variables are of the Bouc-Wen type (Gerolymos and Gazetas, 2005). Matrix $\{H\}$ is given as:

$$\{H\}=\zeta^n\{I\} \qquad (4.2)$$

The failure surface which has the role of bounding surface is described by the following equation:

$$f = \left[(\mathbf{r} - \mathbf{r}_p) : (\mathbf{r} - \mathbf{r}_p) \right]^{1/2} - \left(\sqrt{\frac{2}{3}} M_{s,\theta} - n_p \right) = 0 \qquad (4.3)$$

where **r** is the second order deviatoric stress ratio tensor ($\mathbf{r} = \mathbf{s}/p$) and $M_{s,\theta}$ is the bounding stress ratio, determining the ultimate strength, dependent on the Lode angle θ. It is given as a proportion of ultimate strength at triaxial compression, M_c, where θ = 0, through a factor χ accounting for Lode angle effects:

$$M_{s,\theta} = \chi M_c \qquad (4.4)$$

where M_c is related to the friction angle ϕ:

$$M_c = \frac{6 \sin\phi}{3 - \sin\phi} \qquad (4.5)$$

The stress ratio tensor, $\mathbf{r}_p$ is given by:

$$\mathbf{r}_p = \frac{\boldsymbol{\sigma}_p - p_p \mathbf{I}}{p_p} \qquad (4.6)$$

where $\boldsymbol{\sigma}_p$ is equal to the stress tensor and p_p is the mean effective stress at the pivot points, once reversal of loading occurs. Pivot point is also considered the initial point of loading. Thus, in case of initial isotropic consolidation state (K_0 = 1), $\mathbf{r}_p$ = 0 and the bounding surface, f, returns to its common Drucker-Prager form but with Lode angle dependency. Otherwise, K_0 effects are taken into account so that the bounding surface is readjusted appropriately. The scalar valued stress ratio n_p is defined as:

$$n_p = \mathbf{n} : \mathbf{r}_p \qquad (4.7)$$

in which **n** is a normalized stress ratio tensor, normal to f:

$$\mathbf{n} = \frac{\mathbf{r} - \mathbf{r}_p}{\left[(\mathbf{r} - \mathbf{r}_p) : (\mathbf{r} - \mathbf{r}_p) \right]^{1/2}} \qquad (4.8)$$

with properties: $\mathrm{tr}\mathbf{n}=0$ and $\mathrm{tr}\mathbf{n}^2=1$. Finally, parameter ζ, required to vary strictly in the range [0,1], is defined as:

$$\zeta=\frac{\left[(\mathbf{r}-\mathbf{r}_p):(\mathbf{r}-\mathbf{r}_p)\right]^{1/2}}{\sqrt{\frac{2}{3}}M_{s,\theta}-n_p} \qquad (4.9)$$

Evidently when ζ = 1, f = 0 (Eq. (4.3)). After combining Eqs. (4.3), (4.7) and (4.8) and performing a series of calculations, the failure surface can be rewritten as:

$$f=\mathbf{r}:\mathbf{n}-\sqrt{\frac{2}{3}}M_{s,\theta}=0 \qquad (4.10)$$

The gradient to the failure surface,f, is given by:

$$\boldsymbol{\Phi}_f=\frac{\partial f}{\partial \boldsymbol{\sigma}}=\mathbf{n}-\frac{1}{3}(\mathbf{n}:\mathbf{r})\mathbf{I} \qquad (4.11)$$

Dilatancy, accounting for shear-induced volume change is based on Rowe's concept (1962):

$$d=\left(\sqrt{\frac{2}{3}}M_{pt}\chi-\mathbf{r}:\mathbf{n}\right) \qquad (4.12)$$

where M_{pt} is the phase transformation surface (or dilatancy surface) and χ is the factor dependent on Lode angle, θ. It should be noted that when d obtains positive values, contractive response is expected and vice versa. The distribution of dilatancy, d, to plastic strain components, or else the gradient to the plastic potential surface is described by:

$$\boldsymbol{\Phi}_g=\frac{\partial g}{\partial \boldsymbol{\sigma}}=\mathbf{n}+\mathbf{n}^2 d \qquad (4.13)$$

so that $d\boldsymbol{\varepsilon}^p = \langle L \rangle \boldsymbol{\Phi}_g$, where L is the common scalar-valued stress-dependent multiplier, designated as the loading index. The plastic volumetric strain increment can be estimated by:

$$d\varepsilon_p{}^p = \mathrm{tr}\left(d\boldsymbol{\varepsilon}^p\right) = \langle L \rangle \mathrm{tr}\boldsymbol{\Phi}_g = \langle L \rangle \left[n_{11} + n_{22} + n_{33} + d\left(n_{11}^2 + n_{22}^2 + n_{33}^2 + 2n_{12}^2 + 2n_{23}^2 + 2n_{31}^2\right)\right] = \langle L \rangle d$$

(4.14)

while the plastic deviatoric strain increment is calculated as:

$$d\varepsilon_q^p = \langle L \rangle \sqrt{2/3}\left[\left(\Phi_{11} - \frac{d}{3}\right)^2 + \left(\Phi_{22} - \frac{d}{3}\right)^2 + \left(\Phi_{33} - \frac{d}{3}\right)^2 + 2\Phi_{12}{}^2 + 2\Phi_{23}{}^2 + 2\Phi_{31}{}^2\right]^{1/2} = \langle L \rangle \sqrt{2/3}\mu$$

(4.15)

It should be mentioned that the value μ is approximately 1 irrespectively of the stress path, so that:

$$d\varepsilon_q^p \simeq \langle L \rangle \sqrt{2/3} \qquad (4.16)$$

Thus, the non-associative plastic flow rule in terms of the ratio of the plastic volumetric strain increment to the plastic deviatoric strain increment is calculated by combining Eqs. (4.4), (4.10), (4.12), (4.14) and (4.15), when ζ = 1 indicating that current stress rate lies on bounding surface:

$$\frac{d\varepsilon_p{}^p}{d\varepsilon_q{}^p} = \frac{\langle L \rangle d}{\langle L \rangle \sqrt{\frac{2}{3}}} = \frac{\left(\sqrt{2/3}M_{pt}\chi - \mathbf{r:n}\right)}{\sqrt{\frac{2}{3}}} = \frac{\sqrt{2/3}M_{pt}\chi - \sqrt{2/3}M_{s,\theta}}{\sqrt{\frac{2}{3}}} = M_{pt}\chi - M_c\chi = \chi\left(M_{pt} - M_c\right)$$

(4.17)

4.2.2 Bounding and Phase Transformation Ratios

In order to adopt the critical state concept, both the phase transformation ratio, M_{pt} and the bounding ratio, M_s, should gradually converge to the critical state line, M_{cs}, producing zero plastic volumetric change when the stress ratio becomes equal to $M_s = M_c = M_{pt} = M_{cs}$, according to flow rule of Eq. (4.17). The evolution of the bounding stress ratio is described as a function of the cumulative deviatoric strain increment, $\sum|d\varepsilon_q|$, which ensures that critical state will be reached under monotonic and cyclic loading (Tasiopoulou and Gerolymos, 2012).:

$$M_s = M_c = M_{cs} + \left(M_{s0} - M_{sp}\right)e^{-2c\sum d\varepsilon_q} + \left(M_{sp} - M_{cs}\right)e^{-c\sum d\varepsilon_q} \qquad (4.18)$$

where M_{s0} is an initial value and M_{sp} is a maximum value that can never be practically reached, as shown in Figure 4.3. Model parameter c controls the rate of evolution towards the critical state value. Details on the particular selection and use of the current functions for bounding and phase transformation ratio can be found by Tasiopoulou and Gerolymos (2012, 2014 and 2015). The curve formed by Eq. (4.18) is shown in Figure 4.3 as the addition of two separate functions (1) and (2). The function of Eq. (4.18) resembles the trend of sand behavior under drained conditions in deviatoric stress-strain terms. It is considered convenient in use, since variable ζ tends to become rapidly equal to 1 due to the low initial value, M_{s0}, and thereafter, the current state is forced to follow the evolution of the bounding surface. That way, the response, e.g, amount and occurrence of peak strength can be more easily controlled through calibration process. The point C of peak strength, M_{speak}, occurs when the derivative of Eq. (4.18) is equal to zero, as illustrated in Figure 4.3:

$$\frac{\partial M_s}{\partial\left(\sum|d\varepsilon_q|\right)} = 0 \Leftrightarrow \sum|d\varepsilon_q|_{peak} = \frac{1}{c}\ln\left(\frac{M_{cs} - M_{sp}}{2\left(M_{s0} - M_{sp}\right)}\right) \qquad (4.19)$$

Substituting $\sum\left|d\varepsilon_q\right|_{peak}$ of Eq. (4.19) in Eq. (4.18), M_{speak} is calculated as:

$$M_{speak}=\frac{\left(M_{sp}-M_{cs}\right)^2}{4\left(M_{sp}-M_{s0}\right)}+M_{cs} \tag{4.20}$$

Thus, if M_{speak} is known or targeted, M_{sp} can be obtained by solving Eq. (4.20) with respect to M_{speak}:

$$M_{sp}=\frac{4M_{speak}-2M_{cs}+\sqrt{\Delta}}{2} \tag{4.21}$$

where Δ is the determinant:

$$\Delta=\left(2M_{cs}-4M_{speak}\right)^2-16M_{s0}\left(M_{speak}-M_{cs}\right)+4M_{cs}{}^2 \tag{4.22}$$

with the limitation, Δ>0:

$$M_{s0}\le\frac{\left(2M_{cs}-4M_{speak}\right)^2+4M_{cs}{}^2}{16\left(M_{speak}-M_{cs}\right)} \tag{4.23}$$

which is easily satisfied if $M_{s0}\le M_{cs}$. Finally, M_{sp} can be explicitly rewritten as:

$$M_{sp}=2M_{speak}-M_{cs}+0.5\sqrt{\left(2M_{cs}-4M_{speak}\right)^2-16M_{s0}\left(M_{speak}-M_{cs}\right)+4M_{cs}{}^2} \tag{4.24}$$

The phase transformation stress ratio evolves in the same context, according to the following expression:

$$M_{pt}=M_{cs}+\left(M_{pt0}-M_{cs}\right)e^{-0.5c\sum d\varepsilon_q} \tag{4.25}$$

where M_{pt0} is the initial value of M_{pt}. Figure 4.4 demonstrates how the shape of bounding and phase transformation stress ratios can be adjusted to produce either dilative (dense

sand) or contractive response (loose sand), according to plastic flow rule given by Eq. (4.12) or Eq. (4.17) after ζ = 1.

4.3 CALIBRATION APPROACH FOR TRIAXIAL COMPRESSION

Thus far, the parameters of Ta-Ger model, 8 in total (as shown in Table 4.2) may work in a convenient manner within the formulation, but some of them, such as M_{s0}, M_{speak} and M_{pt0}, lack a physical connection with sand behavior which is mostly dependent on initial relative density and confining pressure. Moreover, this situation renders the calibration process a challenging task. However, the latter can be overcome by correlating the model parameters M_{s0}, M_{sp} and M_{pt0} with Bolton's relative dilatancy index (Bolton 1986, Ching et al., 2012):

$$I_r = D_r\left(Q - \ln(p)\right) - R \qquad (4.26)$$

where D_r is the current relative density of the sand, p is the current mean effective stress, and Q, R are constants obtaining values close to 10 and 1, respectively. Critical state occurs when $I_r = 0$, while $I_r > 0$ indicates denser states of sands and $I_r < 0$ accounts for looser contractive states. The advantage of choosing I_r as a state parameter against well-established state parameters in literature, such as Ψ by Been and Jeffrees (1985) correlated to the critical state lines in e – p space, is attributed to the fact that the relative index I_r offers a unique set of correlations (Eqs. (4.29) and (4.32)) for the dilatant behavior of a wide range of sands, as showed by Bolton (1986). In plain words, a single set of Q and R is assumed to apply for all clean sands, in a sense that critical state lines for different types of sand in e-p space converge into one in D_r – p space, since differences in e_{min} and e_{max} for each sand have been absorbed in D_r values.

At this stage of the study, calibration of the model is focused on triaxial compression type of loading. The reason is two-fold: i) Bolton's empirical relationships on maximum strength and dilatancy are based mostly on triaxial compression tests and therefore, they

can be fully taken into advantage and ii) triaxial compression is the type of loading that is the least affected by stress-induced anisotropy effects such as principal stress rotation (α = 0° = constant) and intermediate stress impact (b = 0 = constant); thus, calibration variations for different types of sand only due to inherent fabric effects such as particle shape, size etc. can be better highlighted.

4.3.1 Elastic Moduli

The elastic shear modulus is obtained as:

$$G_{el} = 1000 k_{2max} p^{0.4} \qquad (4.27)$$

where p is the current mean effective stress in kPa and k_{2max} is a coefficient adapted by Seed and Idriss (1970), dependent on initial relative density, D_{r0}. In the original paper by Seed and Idriss (1970), k_{2max} is suitable for mean effective stresses in lb/ft^2 and its values are given in a table for selected values of D_{r0}. After appropriate transformation from lb/ft^2 to kPa and interpolation between the selected values of D_{r0}, k_{2max} can be estimated by:

$$k_{2max} = 0.13 D_{r0} + 3.6 \qquad (4.28)$$

where D_{r0} is the initial relative density in %. The elastic bulk modulus, K_{el} is considered to be equal to G_{el}, assuming that Poisson's ratio, ν, is equal to 0.15.

4.3.2 Peak Strength

The maximum friction angle for triaxial compression is given by Bolton (1986), in the range $0 < I_r < 4$:

$$\phi_{max} = \phi_{cs} + 3 I_r \geq \phi_{cs} \qquad (4.29)$$

Therefore, M_{speak} can be calculated as a function of the current relative dilatancy inder, I_r:

$$M_{speak} = \frac{6\sin\left(\phi_{cs} + 3I_r\right)}{3 - \sin\left(\phi_{cs} + 3I_r\right)} \tag{4.30}$$

Finally, the critical state ratio can be estimated by:

$$M_{cs} = \frac{6\sin\left(\phi_{cs}\right)}{3 - \sin\left(\phi_{cs}\right)} \tag{4.31}$$

where, ϕ_{cs} is the friction angle at critical state and its value is offered in abundance in literature for various types of sands (Bolton, 1986; Been and Jefferies, 2006).

4.3.3 Dilatancy

After statistical processing of numerous drained triaxial and plane-strain compression tests on sands, Bolton (1986) also suggested that, in the range $0 < I_r < 4$:

$$\left[-\frac{d\varepsilon_p}{d\varepsilon_1}\right]_{max} = 0.3I_r \tag{4.32}$$

when the peak strength value, M_{speak}, is obtained at $\sum\left|d\varepsilon_q\right|_{peak}$; a deduction that can be used for the calibration of the plastic flow rule and specifically the phase transformation stress ratio. For triaxial compression conditions, where $d\varepsilon_2 = d\varepsilon_3$, the ratio of total volumetric strain increment over the total deviatoric strain increment can be expressed as a function of the current relative dilatancy index, I_r, according to the following calculations:

$$\left[\frac{d\varepsilon_p^p}{d\varepsilon_q^p}\right]_{max,tx} = \frac{d\varepsilon_1 + 2d\varepsilon_3}{\frac{2}{3}\left(d\varepsilon_1 - d\varepsilon_3\right)} = \frac{\frac{3}{2}d\varepsilon_p}{\left(d\varepsilon_1 - \frac{d\varepsilon_p}{2} + \frac{d\varepsilon_1}{2}\right)} = \frac{\frac{3}{2}d\varepsilon_p}{\left(\frac{3}{2}d\varepsilon_1 - \frac{d\varepsilon_p}{2}\right)} = \frac{-3\left[-\frac{d\varepsilon_p}{d\varepsilon_1}\right]}{3 + \left[-\frac{d\varepsilon_p}{d\varepsilon_1}\right]} = \frac{-3(0.3I_r)}{3 + (0.3I_r)} \tag{4.33}$$

Combining the plastic flow rule of Eq. (4.17) and empirical relationship for triaxial compression conditions of Eq. (4.33), it is shown that:

$$\left[\frac{d\varepsilon_p^p}{d\varepsilon_q^p}\right]_{max,tx} = \left(M_{pt,peak} - M_{speak}\right)\chi = \frac{-3\left[-\frac{d\varepsilon_p}{d\varepsilon_1}\right]_{max}}{3+\left[-\frac{d\varepsilon_p}{d\varepsilon_1}\right]_{max}} = \frac{-3(0.3I_r)}{3+(0.3I_r)} \qquad (4.34)$$

under the assumption that :

$$\left[\frac{d\varepsilon_p^p}{d\varepsilon_q^p}\right]_{max} = \left[\frac{d\varepsilon_p}{d\varepsilon_q}\right]_{max} \qquad (4.35)$$

when maximum strength (ζ = 1) has occurred. $M_{pt,peak}$ is the value of the phase transformation stress ratio at peak strength occurrence, $\sum|d\varepsilon_q|_{peak}$. Of course the value of factor χ, dependent on Lode angle, is equal to 1 for triaxial compression. Therefore, the value of $M_{pt,peak}$ can be considered known, according to Eq. (4.34):

$$M_{pt,peak} = M_{speak} - \frac{3(0.3I_r)}{3+(0.3I_r)} \qquad (4.36)$$

In order to satisfy the requirement of Eq. (4.36), at peak strength occurrence, $\sum|d\varepsilon_q|_{peak}$, M_{pt0} is chosen to be a function of current stress state, instead of being a constant:

$$M_{pto} = M_{speak}\zeta^n - \frac{3(0.3I_r)}{3-3(0.3I_r)}\frac{1}{\chi} \qquad (4.37)$$

Constant evolution of current stress state towards the critical one leads to ζ being equal to 1 (usually long before peak strength, M_{speak} has been reached), I_r tending to 0 and M_{speak} tending to M_{cs} according to Eq. (4.30); thus M_{pt0} tends to M_{cs}. It is reminded that Eq. (4.37) applies for dense initial states, $I_{r0} > 0$. In case of loose states, $I_{r0} < 0$, it is assumed that:

$$\left[-\frac{d\varepsilon_p}{d\varepsilon_1}\right]_{max}=0 \qquad (4.38)$$

so that:

$$M_{pt0}=M_{speak}\zeta^n \qquad (4.39)$$

Finally, Eq. (4.25), which describes the phase transformation stress ratio in a generalized way, is now modified as:

$$\begin{aligned} M_{pt}&=M_{cs}+\left(M_{speak}\zeta^n-\frac{3(0.3I_r)}{3-3(0.3I_r)}\frac{1}{\chi}-M_{cs}\right)e^{-0.5c\sum d\varepsilon_q}, \quad \text{if} \quad I_{r0}\geq 0 \\ M_{pt}&=M_{cs}+\left(M_{speak}\zeta^n-M_{cs}\right)e^{-0.5c\sum d\varepsilon_q}, \quad \text{if} \quad I_{r0}\leq 0 \end{aligned} \qquad (4.40)$$

While Eqs. (4.37) and (4.39) could be used for the evolution of the phase transformation stress ratio instead of Eqs. (4.40), since it fits both requirements at: i) peak strength (Eq. (4.36)) and ii) critical state (M_{pt0} = M_{cs}), use of Eqs. (4.40) ensures that critical state will occur under both monotonic and cyclic loading conditions due to dependency on $\sum|d\varepsilon_q|$. It is needless to say that in case of monotonic loading, Eqs. (4.37), (4.39) when compared to Eqs. (4.40), they give practically identical curves.

4.4 MODEL SIMULATIONS VERSUS DATA FROM TRIAXIAL COMPRESSION TESTS

Hitherto, four (G_{el}, v, M_{speak}, M_{pto}) out eight model parameters (see Table 4.2) have been expressed as a function of the current or initial state (I_r, p_0 or D_{r0}) and M_{cs} can obtain values suggested in literature for various sands (Been and Jefferies, 2006). Two extra parameters, Q and R of Eq. (4.26), have been introduced in the model formulation along with the adoption of critical state concept, as stated by Bolton (1986) in D_r – p space. The

set of values assigned to Q and R by Bolton (1986) for clean sands is 10 and 1 in respect, while Salgado et al. (2000) suggests that Q is equal to 9 and R equal to 0.49. Otherwise, Q, R can be easily estimated using laboratory tests that have achieved occurrence of critical state ($I_r = 0$), and the values of D_r and p at critical state are given. The remaining three parameters, the initial value of bounding stress ratio, M_{s0}, the evolution parameter, c and the hardening exponent, n, will be calibrated to fit experimental data from drained and undrained triaxial compression tests for three different types of sands (see Table 3): i) Toyoura, ii) Sacramento River and iii) Fontainebleau.

4.4.1 Toyoura sand

After meticulous observation of the experimental behavior of Toyoura sand under drained triaxial compression loading (Figures 4.5-4.9), one can observe the impact of initial relative density and confining pressure on the volume change (dilatancy), the maximum obtained strength and its occurrence. In particular, as initial relative density increases and/or initial confining pressure decreases, thus, Ir increases, sand behavior becomes more dilative, the maximum strength, M_{speak} increases, the evolution up to the peak strength is more rapid so that M_{speak} occurs at lower strains, $\sum|d\varepsilon_q|_{peak}$. Taking into account Eq. (4.19) which indicates that $\sum|d\varepsilon_q|_{peak}$ decreases as c and M_{s0} increase, it can be safely deduced that both parameters should be a function of initial state, I_{r0}. Moreover, according to (4.12) and (4.17), when M_{s0} increases, dilatancy, d, decreases leading to a more dilative response, based on sign convention that was previously noted. In terms of undrained response (Figures 4.10-4.13), lower values of M_{s0} are expected to lead to occurrence of phase transformation or else quasi-steady state at lower mean effective stresses.

In case of hardening exponent n, previous studies (Gerolymos and Gazetas, 2005; Drosos et al., 2012; Tasiopoulou and Gerolymos, 2015) have shown that values of exponent n

varies in the range of 0.2-0.8 for soils. The lower the value of n, the greater the coupling between elastic and plastic strain increments is until ζ = 1 (Tasiopoulou and Gerolymos, 2015). Calibration process requires that even lower values are needed for simulating a more realistic response. By decreasing the value of exponent n, the failure state (ζ = 1 and q/p = M_s), occurs more rapidly and thus, the impact of parameter M_{s0} on the response becomes more predominant. For example, in case of drained stress-strain curves, the current stress ratio would be forced to follow the bounding surface in the early stages of loading, for low values of n. Therefore by controlling the value of M_{s0}, one can control the shape of the stress-strain curve from the beginning, which is very useful especially for loose sands, such as cases (c) of Figures 4.5 and 4.6. This is desirable because the burden of proper fitting is moved basically on one key-parameter, rendering the calibration less complicated. Demonstration of the impact of M_{s0}, will be shown in case of Sacramento River sand in the following.

Taking into account how each model parameter influences the response and cooperates with each other, optimization was performed in order to formulate suitable expressions for each parameter as a function of initial state conditions. In particular, M_{s0} is calculated based on initial frinction angle ϕ_{s0}, which is dependent on friction angle at critical state, ϕ_{cs} and I_{r0}:

$$\phi_{s0} = 0.9\phi_{cs} + 5I_{r0} \le \phi_{cs} \qquad (4.41)$$

$$M_{s0} = \frac{6\sin(\phi_{s0})}{3-\sin(\phi_{s0})} \qquad (4.42)$$

The limitation $\phi_{s0} \le \phi_{cs}$ is required to avoid instability issues originated by Eqs. (4.22) and (4.23). Model parameter c is expressed as:

$$c = 6 + I_{r0} \qquad (4.43)$$

Finally, hardening exponent, n, is given as a function of initial relative density, D_{r0}:

$$n = 0.4D_{r0} + 0.14 \qquad (4.44)$$

The set of values of parameters Q and R is estimated based on undrained triaxial compression loading tests up to critical state by Verdugo and Ishihara (1996), shown in Figures 4.11-4.13. The value pairs for each test consisting of initial relative density, which remains constant during loading, and mean effective stress at critical state (the final value at the end of loading), should satisfy Eq. (4.26) when I_r = 0. . Only two value pairs (two tests) are needed to solve a system of two unknowns: Q and R. After calculations, Q and R are equal to 9.15 and 0.77, respectively falling into the range of values proposed by Bolton (1976) and Salgado et al. (2000).

4.4.2 Sacramento River sand

Initially, prediction of drained triaxial compression tests on Sacramento River sand was attempted based on expressions of model parameters M_{s0}, c and n used for Toyoura sand (see Eqs. (4.41)-(4.44)). Figure 4.14 demonstrates that model predictions are not satisfying compared to experimental data, which of course was expected based on the comparison of the experimental behavior between the two types of sand in Figure 4.1(b). Model behavior is more dilative than experimental one, while the predicted stress-strain curve transcends the one obtained from laboratory tests at the early stages of loading before peak strength is reached. The latter observation indicates that lower values of M_{s0} are required. Indeed, reducing the values of ϕ_{s0} and thus, M_{s0}, leads to better model predictions both in terms of stress-strain and volumetric-vertical strain curves. In addition, increase of parameter c further improves the model simulations, moving the occurrence of peak strength at lower strains and rendering the response slightly more dilative, as indicated by Figures 4.14 and 4.15. In detail, increase of parameter, c, increases the rate of evolution of bounding surface towards critical state value; an effect which tends to provide a slight more dilative response for looser sands and a less dilative

response for denser sands. No need for change in the expression of hardening exponent, n of Eq. (4.44) arose.

In conclusion, the expressions of model parameters, ϕ_{s0} and c, used for model simulation of Sacramento River as are:

$$\phi_{s0} = 0.7\phi_{cs} + 5I_{r0} \quad (4.45)$$

$$c = 6 + 3I_{r0} \quad (4.46)$$

4.4.3 Fontainebleau sand

After similar calibration process that was followed for Sacramento River sand, the expressions of model parameters, ϕ_{s0} and c, offering the most satisfying comparison with experimental data, as shown in Figure 4.16, are found to be:

$$\phi_{s0} = 0.8\phi_{cs} + 5I_{r0} \quad (4.47)$$

$$c = 6 + 4I_{r0} \quad (4.48)$$

In terms of dilatancy, Fontainbleau sand seems to be less dilative than Toyoura sand, as illustrated in Figure 4.1(a), and overall more dilative than Sacramento River sand, when the expressions of ϕ_{s0} for the two types of sands are compared (see Eqs. (4.45) and (4.47)). Regarding the rate of evolution of bounding stress ratio towards critical state, controlled by parameter, c, Fontainebleau sand seems to exhibit the most brittle behavior with rapid occurrence of peak stress ratio accompanied by steep reduction in strength. This is the reason why higher values of parameter c were needed for better model predictions of Fontainebleau sand behavior compared to the other two types of sand (see Eqs. (4.43), (4.46) and (4.48)). Sacramento River sand seems to be an intermediate case. This kind of discrepancy in sand behavior is mostly attributed to the particle shape (Tsomokos and Georgiannou, 2010). It has been reported experimentally

that sands consisting of rounder particles tend to behave in a more brittle way. Grain roundness also leads to a thinner shear band formation (Andò et al., 2012). The shear band starts to develop just before or at the occurrence of peak strength which coincides with the steeper slope in ε_v-γ space. The thickness of shear band is related to the shear-induced volume change or else, dilatancy. The thicker the shear band is, the more dilative the behavior until critical state. Thus, angular sand particles are expected to exhibit a more dilative response than round ones.

4.4.4 Variations in calibration for different types of sand

Table 4.4 includes the ensemble of calibrated values or expressions for Ta-Ger model parameters to provide satisfying predictions for triaxial compression loading of three different types of sand. Clearly, apart from the critical friction angle, ϕ_{cs}, only two parameters, ϕ_{s0} and c require certain fine tuning within a quite narrow range in order to account for particular inherent sand characteristics, or else fabric effects (see Table 4.3).

Various studies in literature (Cho et al., 2006; Santamarina and Cho, 2004; Andò et al., 2012; Desrues and Viggiani, 2004; Viggiani et al., 2001; Tsomokos and Georgiannou, 2010) have attempted to shed light on the impact of particle size, shape, uniformity etc on sand behavior and quantify some of these characteristics through appropriate parameters. Nevertheless, a most extensive investigation still needs to be performed in order to correlate the grain characteristics with macroscopic physical properties. Such an effort would facilitate the calibration process and increase the applicability of constitutive models in a wide range of sand types. Then, for example, a unique expression for each model parameter, ϕ_{s0} and c, would be needed as a function of initial state, I_r, as well as, other properties accounting for inherent fabric effects.

4.5 CALIBRATION FOR STRESS-INDUCED ANISOTROPY

The impact of loading direction on sand behavior has been investigated experimentally by many researchers (Tatsuoka et al. (1986); Yoshimine et al., 1998; Nakata et al., 1998). Stress-induced anisotropy has been repetitively reported, as illustrated in Figure 4.2. Three specimens of Toyoura sand with the approximately the same initial state (D_{r0}, p_0) exhibit significant diversity in their response both in terms of under different loading conditions (triaxial compression, simple shear and triaxial extension). Evidently, a constitutive model, calibrated for specific loading tests, could not be able to reproduce the dependency of sand behavior on loading direction, unless model formulation has been adjusted in a way to account for stress-induced anisotropy. For example Ta-Ger model in each current state can by no means reproduce realistically sand response under any other type of loading than triaxial compression, which is what it has been calibrated for, as demonstrated in Figure 4.17. Thus far, the only differences in response captured by the model are attributed to Lode angle dependency of the bounding stress ratio, which clearly is not adequate to account for stress-induced anisotropy effects. In this line of thought, an introduction of an appropriate variable is introduced to the model, as a function of principal stress rotation and intermediate stress parameters.

4.5.1 Principal Stress Rotation and Intermediate Stress Parameters

The impact of loading direction, causing stress-induced anisotropy, can be reflected in the principal stress rotation and intermediate stress effects (Yoshimine et al., 1998; Nakata et al., 1998). The parameter accounting for principal stress rotation is defined as the angle between the direction of maximum principal stress and the vertical one:

$$\alpha = \frac{1}{2}\tan^{-1}\left(\frac{\sigma_{12}}{\sigma_{11}-\sigma_{22}}\right) \qquad (4.49)$$

The effect of intermediate stress can be represented by parameter b, defined as:

$$b = \frac{\sigma_2 - \sigma_3}{\sigma_1 - \sigma_3} \tag{4.50}$$

In case of triaxial compression, α = 0° and b = 0, whereas in triaxial extension, α = 90° and b = 1. Parameter α under shear loading and isotropic initial consolidation state (K_0 = 1) is equal to 45°, while b is approximately 0.5 but it can be reduced to 0.25 during loading depending on strain boundary conditions. A trend can be identified by experimental observations, indicating that increase in parameter α and/or b leads to a more contractive behavior.

4.5.2 Introduction of stress-induced anisotropy internal variables

It has been previously shown that, within the current constitutive framework, reducing the values of the following model parameters would lead to a less dilative behavior: ϕ_{s0} and c. In addition, decrease of hardening exponent n and increase of the phase transformation ratio would emphasize the abovementioned effect. In this line of thought, an appropriate variable in the role of reduction factor is introduced as a function of current parameter α and b:

$$a_b = 0.98^{\sin\alpha} 0.8^b \cos^{1-b}\left(0.4\alpha\right) \tag{4.51}$$

Table 4.5 presents the values of the reduction factor, a_b, for distinguished values of parameters α and b. The values of reduction factor decrease moving from left-hand to right-hand side and from top to bottom; a trend based on experimental evidence.

The reduction factor, α_b, is applied to model parameters, ϕ_{s0} (Eqs. (4.41), (4.45), (4.47)), c (Eqs. (4.43), (4.46), (4.48)), n (Eq. (4.44)) and M_{pto} (Eq. (4.37)) according to:

$$\phi_{s0,\alpha b} = a_b \phi_{s0} = a_b\left(\kappa\phi_{cs} + 5I_{r0}\right) \tag{4.52}$$

$$c_{\alpha b} = 6a_b^{\,8} + \delta I_{r0} \tag{4.53}$$

$$n = a_b^2 (0.4 D_{r0} + 0.14) \tag{4.54}$$

$$M_{pto} = M_{speak} \zeta^n - \frac{3(0.3 I_r)}{3 - 3(0.3 I_r)} \frac{\mu}{\chi} a_b \tag{4.55}$$

where, coefficients, κ and δ vary from 0.7-0.9 and 1-4, respectively, depending on the type of sand, as shown in Table 4.4. Hence, model parameters have now become a function of, not only, the initial state, but also the loading direction, accounting for stress-induced anisotropy.

Another variable is introduced in the model formulation to address some observations by Bolton (1986) regarding plane strain conditions. Bolton (1986) provides an empirical correlation for maximum friction angle based on triaxial compression tests (b = 0), described by Eq. (4.29). However, in case of plane strain compressions tests, experimental evidence suggests a higher maximum friction angle:

$$\phi_{max} = \phi_{cs} + 5 I_r \tag{4.56}$$

The difference between the triaxial ($\sigma_2 = \sigma_3 = \text{constant}; b = 0$) and plane strain ($\sigma_3 = \text{constant}; \varepsilon_2 = 0$) compression tests can only be attributed to intermediate stress effects, since parameter α is equal to 0° for both test configurations (Tatsuoka et al., 1986). In particular, under plane strain loading, parameter b is initially equal to 0 and increases to 0.4 at peak strength for K_0 = 1, as shown by DEM experiments (Sazzad and Suzuki, 2012). Ta-Ger model predictions for plane strain compression tests estimate a value of b equal to 0.5 at peak strength occurrence. In order to account for this effect, variable g_{ab} is proposed as a function of parameter b:

$$g_{\alpha b} = 3 + 2 \sin\left(b 180^\circ\right) \tag{4.57}$$

Variable g_{ab} becomes equal to 5 when b = 0.5 while it gradually returns to value of 3 when b deviates from 0.5 towards either 0 or 1:

$$3 \leq g_{\alpha b} \leq 5 \qquad (4.58)$$

Thus, the maximum friction angle is now obtained as:

$$\phi_{max} = \phi_{cs} + g_{\alpha b} I_r \qquad (4.59)$$

4.5.3 Model Simulations versus experiments on Toyoura sand

Eqs. (4.51) to (4.59) are used to predict the behavior of Touyoura sand under various monotonic drained and undrained loading paths: simple shear, triaxial extension and shear under fixed α and b values. Coefficients κ and δ of Eqs. (4.52) and (4.53), which have been previously calibrated based on triaxial compression tests, are equal to 0.9 and 1, in respect (see Table 4.4).

Simple Shear Loading

Figure 4.18 illustrates the comparison between model predictions and experimental results (Yoshimine et al., 1998) under undrained simple shear loading for various initial relative densities and isotropic initial consolidation state (K_0 = 1). All normal strain components are constrained ($d\varepsilon_{ij} = 0$) during loading. The direction of maximum principal stress, σ_1, forms a practically constant angle, α, of 45° with the vertical direction throughout loading, both in case of model and laboratory tests. The intermediate stress value, b, remains close to 0.5 in case of model tests, while experiments showed a variation of b from 0.5 at the beginning of loading to 0.25 at the end of the test.

Figure 4.19 demonstrates model and experimental behavior (Pradhan et al., 1988) under drained direct simple shear tests for various initial states (D_{r0}, p_0) and anisotropic initial consolidation state ($K_0 = 0.52e_0$). Lateral strains were not allowed during loading. Figure 4.20 shows the relationships between parameter and angle, α. Rotation angle α is equal to 0° at starting point (initial K_0 consolidation conditions) and rapidly increases to 25° at the early stages of loading where b still remains close to zero. As larger shear strains are

induced, b increases converging to a value of 0.27 approximately while angle α reaches values of 45° to 55° (smaller for looser states). The plastic flow rule adopted by Ta-Ger model (Eq. (4.13)) predicts a similar trend, but lower values of angle α (see Figure 20). However, it gives a more realistic prediction compared to the most commonly used flow rule, according to which dilatancy, d, is equally distributed among plastic normal strain components:

$$\mathbf{\Phi}_g = \frac{\partial g}{\partial \boldsymbol{\sigma}} = \mathbf{n} + \frac{1}{3} d\mathbf{I} \qquad (4.60)$$

The plastic flow rule of Eq. (4.60) predicts a relationship between parameters α and b that can be described by:

$$b = \sin^2(\alpha) \qquad (4.61)$$

Last, Figure 4.21 compares model and experimental results (Yoshimine et al., 1998) from undrained simple shear tests where $d\varepsilon_{ij} = 0$ and K_0 = 0.5. Figure 4.22 demonstrates the principal stress rotation angle, α and the evolution of intermediate stress parameter b versus deviatoric stress, as obtained by both model and laboratory tests. Comparison indicates that model can capture the right trend of α and b evolution and its dependency on the initial state (D_{r0}). Nevertheless, model predicts lower values of angle α, as it has been also observed in case of drained simple shear tests in Figure 4.20. Despite this discrepancy, model simulations and experimental data are in good agreement in stress-strain terms.

Triaxial Extension Loading

Figure 4.23 depicts the comparison between model simulations and experiments in q-γ and q-p terms, in case of undrained triaxial extension loading. Angle α is constantly equal to 90° during loading, while parameter b remains equal to 1 ($\sigma_1 = \sigma_2$). These α, b

conditions assign the lowest value to reduction factor, a_b, leading to the most contractive behavior possibly exhibited than any other type of loading.

Loading tests with fixed α, b values

Figures 4.24 and 4.25 illustrate the capability of Ta-Ger model to capture stress-induced anisotropy effects for a wide range of principal stress rotation angle, α and intermediate stress parameter b, against experimental data. In particular, Figure 4.24 depicts sand behavior under undrained loading with fixed angle α (α = 45°) for various parameters b (0–1), while Figure 4.25 demonstrates undrained loading tests with fixed b value (b = 0.5) and varying values of angle α within a range of 15° – 75°. In all cases, $K_0 = 1$ and $d\varepsilon_{ij} = 0$. Indeed, comparison indicates the satisfying performance of the reduction factor, a_b, to account for a large combination of α and b values.

4.5.4 Model Simulations versus experiments on Fontainebleau sand

Eqs. (4.51) to (4.59) are used to predict the behavior of Fontainebleau sand under various monotonic drained and undrained simple shear loading. Coefficients κ and δ of Eqs. (4.52) and (4.53), which have been previously calibrated based on triaxial compression tests, are equal to 0.8 and 4, in respect (see Table 4.4). Figures 4.26 and 4.27 indicate a good agreement between model predictions and experimental data, indicating that the reduction factor can reproduce satisfying results for other types of sand as well, without being case-specific to the calibration needs of a particular sand (e.g. Toyoura).

4.6 CONCLUSIONS

The present chapter highlights calibration issues of constitutive modeling for sands regarding their dependency on initial state (D_{r0}, p_0) relative to the critical state, grain characterization, namely inherent fabric effects, and loading direction inducing stress anisotropy. In an effort to address these issues without increasing the number of unknown parameters which would be at the expense of the utility of the constitutive model at hand, a practical calibration approach is suggested. The constitutive model used in this study, designated as Ta-Ger sand model, is based on a reformulation of perfect elastoplasticity by combining features of Bouc-Wen hysteresis (Bouc, 1971 and Wen, 1976), bounding surface plasticity (Dafalias, 1986) and a plastic flow rule, based on a Rowe's dilatancy theory (1962) to account for anisotropic distribution of the dilatancy to the normal plastic strain increments.

Initially, constitutive formulation was adjusted to Bolton's (1986) empirical correlation for maximum friction angle and ratio of total volumetric increment to maximum principal strain increment as a function of state parameter, I_r, named as relative dilatancy index, based on triaxial and plane strain compression tests on various sands. This step led to the reduction of number of unknown model parameters to three (ϕ_{s0}, c, n) besides the ones related directly to measurable physical properties, found in literature, such as critical state angle, ϕ_{cs} and elastic modulus.

In the following, calibration was performed for three different types of sand (Toyoura, Fontainebleau and Sacramento River sand) based on triaxial compression tests. The three unknown model parameters, ϕ_{s0}, c, n, were expressed as a function of initial state, Ir0 or Dr0. It was found that readjustment of coefficients, κ and δ, in the expressions of ϕ_{s0} and c, respectively, was needed for different types of sands due to different grain characteristics, such as particle size, shape, packing etc. Hitherto, the unknown model

parameters consist only of coefficients, κ and δ. However, a quite narrow range of values is suggested.

At last, two variables, a_b and g_{ab}, were introduced to account for stress-induced anisotropy. Key-variable, a_b, is expressed as a function of the angle between the direction of maximum principal stress and the vertical one, α and intermediate stress parameter b. It was incorporated in the previous expressions of ϕ_{s0}, c, n, as a reduction factor. Hence, the number of model parameters remained unchanged. Finally, validation against experimental data was performed in every step of the way for various drained and undrained loading paths in a wide range of α, b values, as well as initial states.

REFERENCES

Anandarajah, A. and Dafalias, Y.F. (1986), Bounding surface plasticity, III: Application to anisotropic cohesive soils. *Journal of Engineering Mechanics, ASCE*, **112**. No 12, 1292–131.

Andò, E., Hall, S.A., Viggiani, G., Desrues, J. and Bésuelle, P. (2012). Grain scale experimental investigation of localised deformation in sand: a discrete particle tracking approach. *Acta Geotechnica*, **7**, 1-13.

Been, K. and Jefferies, M.G. (1985). A state parameter for sands. *Geotechinque* **35**, No. 2, 99-112.

Been, K. and Jefferies, M.G. (2006). *Soil liquefaction. A critical state approach*. Taylor & Francis.

Bolton, M. D. (1986). The strength and dilatancy of sands, *Geotechinque* **36**, No. 1, 65-78.

Bouc, R. (1971). Modele mathematique d' hysteresis. *Acustica* **21**, 16-25.

Cambou, B. and Lanier, J. (1988). Induced anisotropy in cohesionless soil: experiments and modelling. *Computers and Geotechics*, **6**, No 4,291–311.

Cho, G.C., Dodds, J. and Santamarina, J.C. (2006). Particle Shape Effects on Packing Density, Stiffness, and Strength: Natural and Crushed Sands, *Journal of Geotechnical and Geoenviromental Engineering, ASCE*, **132**, No 5, 591-602.

Dafalias, Y.F. (1986). Bounding Surface Plasticity. I: Mathematical Foundation and Hypoplasticity. *Journal of Engineering Mechanics,* **112**, No. 9, 966-987.

Desrues, J. and Viggiani, G. (2004). Strain localization in sand: an overview of the experimental results obtained in Grenoble using stereophotogrammetry, *International Journal for Numerical and Analytical Methods in Geomechanics*, **28**, No. 4, 279–321.

Drosos, V. A., Gerolymos, N., and Gazetas, G (2012). Constitutive model for soil amplification of ground shaking: Parameter calibration, comparisons, validation. *Soil Dynamics and Earthquake Engineering* **42**, 255-274.

Dupla, J-C, Andria-Ntoanina, I. and Canou, J. (2010). *Caractérisation mécanique du sable de fontainebleau à l'appareil triaxial sous cisaillement monotone*. Tech rep. Report of SOLCYP project, CERMES team, Navier Laboratory (ENPC/IFSTTAR/ CNRS).

Duriez, J. and Vincens, É. (2015). Constitutive modelling of cohesionless soils and interfaces with various internal states: An elasto-plastic approach. *Computers and Geotechnics*, **63**, 33–45.

Fukushima, S. and Tatsuoka, F., (1984). Strength and deformation characteristics of saturated sand at extremely low pressure. *Soils and Foundations*, **24**, No. 4, 30-48.

Gao, Z., Zhao, J., Li, X.-S., and Dafalias, Y.F. (2014). A critical state sand plasticity model accounting for fabric evolution. *International Journal for Numerical and Analytical Methods in Geomechanics*, **38**, No 4, 370-390.

Georgiannou, V.N., Tsomokos, A. and Stavrou, K. (2008). Monotonic and cyclic behaviour of sand under torsional loading. *Geotechnique*, **58**, No 2, 113-124.

Gerolymos, N. and Gazetas, G. (2005). Constitutive model for 1–D cyclic soil behavior applied to seismic analysis of layered deposits. *Soils and Foundations* **45**, No. 3, 147-159.

Hashiguchi, K. and Mase, T. (2007). Extended yield condition of soils with tensile yield strength and rotational hardening. *International Journal of Plasticity*, **23,** 1939–1956.

Lee, K.L. and Seed, H.B. (1967). Drained strength characteristics of sands. *Journal of Soil Mechanics and Foundation Division, ASCE*, **93**, SM6, 117–41.

Li, X.S. and Dafalias, Y.F. (2012). Anisotropic critical state theory: the role of fabric. *Journal of Engineering Mechanics, ASCE*, **138**, No 3, 263–275.

Nakata, Y., Hyodo, M., Murata, H., and Yasufuku, N. (1998). Flow deformation of sands subjected to principal stress rotation. Soils and Foundoutions, 38, No 2, 115–128.

Pestana, J.M. and Whittle, A.J. (1999). Formulation of a unified constitutive model for clays and sands. *International Journal for Numerical and Analytical Methods in Geomechanics*, **23**, 1215–1243.

Pradhan, T.B.S., Tatsuoka, F. and Horri, N. (1988). Simple shear testing on sand in a torsional shear apparatus, *Soils and Foundations*, **28**, No 2, 95-112.

Roscoe. K. H. (1970). The influence of strains in soil mechanics. *Geotechnique*, **20**, No 2, 129-170.

Rowe, P. W. (1962). The stress-dilatancy relation for static equilibrium of an assembly of particles in contact. *Proceedings, Royal Soc. London, Ser. A,* Vol. 269, 500–527.

Salgado, R., Bandini, P., and Karim, A. (2000). Shear strength and stiffness of silty sand. *Journal of Geotechnical Geoenvironmental Engineering*, 126, No 5, 451–462.

Santamarina, J.C. and Cho, G. C. (2004). Soil behaviour: The role of particle shape. *Advances in geotechnical engineering: The Skempton Conference*, R. J. Jardine, D. M. Potts, and K. G. Higgins, eds., Vol. 1, Thomas Telford, London, 604–617.

Sazzad, M. and Suzuki, K. (2012). A comparison between conventional triaxial and plane-strain compression on a particulate system using 3D DEM. *Acta Geotechnica Slovenica*, **2**, 17-23.

Seed, H.B. and Idriss, I.M. (1970). *Soil Moduli and Damping Factors for Dynamic Response Analysis*, Research Report No.UCB/EERC-70/10, Depart. of Civil & Env. Engng, University of California, Berkeley.

Seed H.B., and Lee K.L. (1966). Liquefaction of saturated sands during cyclic loading. *Journal of Soil Mechanics and Foundation Division, ASCE*, 92, No 6, 105-134.

Sekiguchi, H. and Ohta, K. (1977). Induced anisotropy and time dependency in clays. In Constitutive Equations of Soils, *Proceedings of the 9th International Conference on Soil Mech. Found. Eng.*, Special Session 9, Tokyo, 1977; 229–238.

Tasiopoulou, P. and Gerolymos, N. (2012). Development of a modified elastoplasticity model for sand. *Proceedings of the Second International Conference on Performance–Based Design in Earthquake Geotechnical Engineering, 28-30 May*, Taormina (Italy), in CD Rom.

Tasiopoulou, P. and Gerolymos, G., (2014). Constitutive modeling for sand with emphasis on the evolution of bounding and phase transformation lines. *Proceedings of the 8th*

European Conference on Numerical Methods in Geotechnical Engineering (NUMGE 2014), Delft (Netherlands), in CD Rom.

Tasiopoulou, P. and Gerolymos, G., (2015). Constitutive model for sand: A new plasticity approach. *Soil Dynamics and Earthquake Engineering* (under review).

Toyota, H., Nakamura, K. and Kazama, M. (2004). Shear and liquefaction characteristics of sandy soils in triaxial tests. *Soils and Foundations*, 44, No 2, 117-126.

Tsomokos, A. and Georgiannou, V. (2010). The Effect of Grain Shape on the Response of Sand under Monotonic Torsional Loading. *Proceedings of 6th Greek Conference on Geotechnical and Environmental Engineering,* 29 September - 1 October, Volos, Greece (in Greek).

Yoshimine, M., Ishihara, K., and Vargas, W. (1998). Effects of principal stress direction and intermediate principal stress on undrained shear behavior of sand. *Soils and Foundations*, **38**, No 3, 179–188.

Verdugo, R and Ishihara, K. (1996). The steady state of sandy soils. *Soils and Foundations* **36**, No.2, 81–91.

Viggiani, G., Kuntz, M. and Desrues, J. (2001). An experimental investigation of the relationship between grain size distribution and shear banding in granular materials. *In Continuous and Discontinuous Modelling of Cohesive Frictional Materials*, Vermeer PA et al. (eds), *Lecture Notes in Physics.* Springer: Berlin, 111–127.

Wen, Y. K. (1976). Method for random vibration of hysteretic systems. *Journal of Engineering Mechanic, ASCE,* **102**, 249-263.

Table 4.1. Properties of sands used for drained triaxial compression tests, shown in Figure 4.1.

Type of sand	Particle Shape	C_u	D_{50}	e_{min}	e_{max}	Packing e_{min}-e_{max}	References
Toyoura	angular	1.46	0.16	0.605	0.977	0.372	Fukushima and Tatsuoka (1984)
Fontainebleau	sub-rounded	1.49	0.21	0.51	0.882	0.372	Dupla et al. (2010)
Sacramento River	sub-angular	1.4	0.2	0.61	1.03	0.42	Lee and Seed (1967) Seed and Lee (1966)

Table 4.2. Model parameters.

	Model Parameters
Elasticity	G_0
	ν
Critical State	M_{cs}
Hardening Exponent	n
Bounding Surface	M_{s0}
	c
	M_{speak}
Phase Transformation Surface	M_{pto}

Table 4.3. Properties of sands used in triaxiax compression tests, which calibration was based on.

Type of sand	Particle Shape	C_u	D_{50}	e_{min}	e_{max}	Packing e_{min}-e_{max}	References
Toyoura	sub-angular to angular	1.46 N/A 1.46 1.7 1.55	0.16 0.17 0.16 0.17 0.17	0.605 0.597 0.605 0.597 0.597	0.977 0.977 0.977 0.977 0.99	0.372 0.38 0.372 0.38 0.393	Fukushima and Tatsuoka (1984) Yoshimine et al. (1998) Pradhan et al. (1988) Verdugo and Ishihara (1996) Toyota et al. (2004)
Fontainebleau	rounded to sub-rounded	1.49 1.55	0.21 0.22	0.51 0.54	0.882 0.865	0.372 0.325	Dupla et al. (2010) Georgiannou et al. (2008)
Sacramento River	sub-angular	1.4	0.2	0.61	1.03	0.42	Lee and Seed (1967) Seed and Lee (1966)

Table 4.4. Model parameters used for model prediction of laboratory tests shown in Figures 4.5-4.16.

	Model Parameters	Toyoura sand	Fontainebleau sand	Sacramento River sand
Elasticity	G_0	$1000\ k_{2max}\ p^{0.4}$ (Eq. (4.27))		
	v	0.15		
Critical State	Q	9.15		
	R	0.77		
	ϕ_{cs}	32° (33°*)	32°	34°
Hardening Exponent	n	$0.4D_{r0} + 0.14$		
Bounding Surface	ϕ_{s0}	$0.9\phi_{cs} + 5I_{r0}$	$0.8\phi_{cs} + 5I_{r0}$	$0.7\phi_{cs} + 5I_{r0}$
	c	$6 + I_{r0}$	$6 + 4I_{r0}$	$6 + 3I_{r0}$

* for experiments by Fukushima and Tatsuoka (1984)

Table 4.5. Values of internal variable a_b, accounting for stress-induced anisotropy, for specific α, b conditions.

	α = 0°	α = 15°	α = 30°	α = 45°	α = 60°	α = 75°	α = 90°
b = 0	1.000	0.989	0.968	0.938	0.898	0.849	0.793
b = 0.25	0.946	0.937	0.921	0.898	0.868	0.833	0.791
b = 0.5	0.894	0.887	0.876	0.860	0.840	0.816	0.788
b = 0.75	0.846	0.840	0.833	0.824	0.813	0.800	0.786
b = 1	0.800	0.796	0.792	0.789	0.786	0.785	0.784

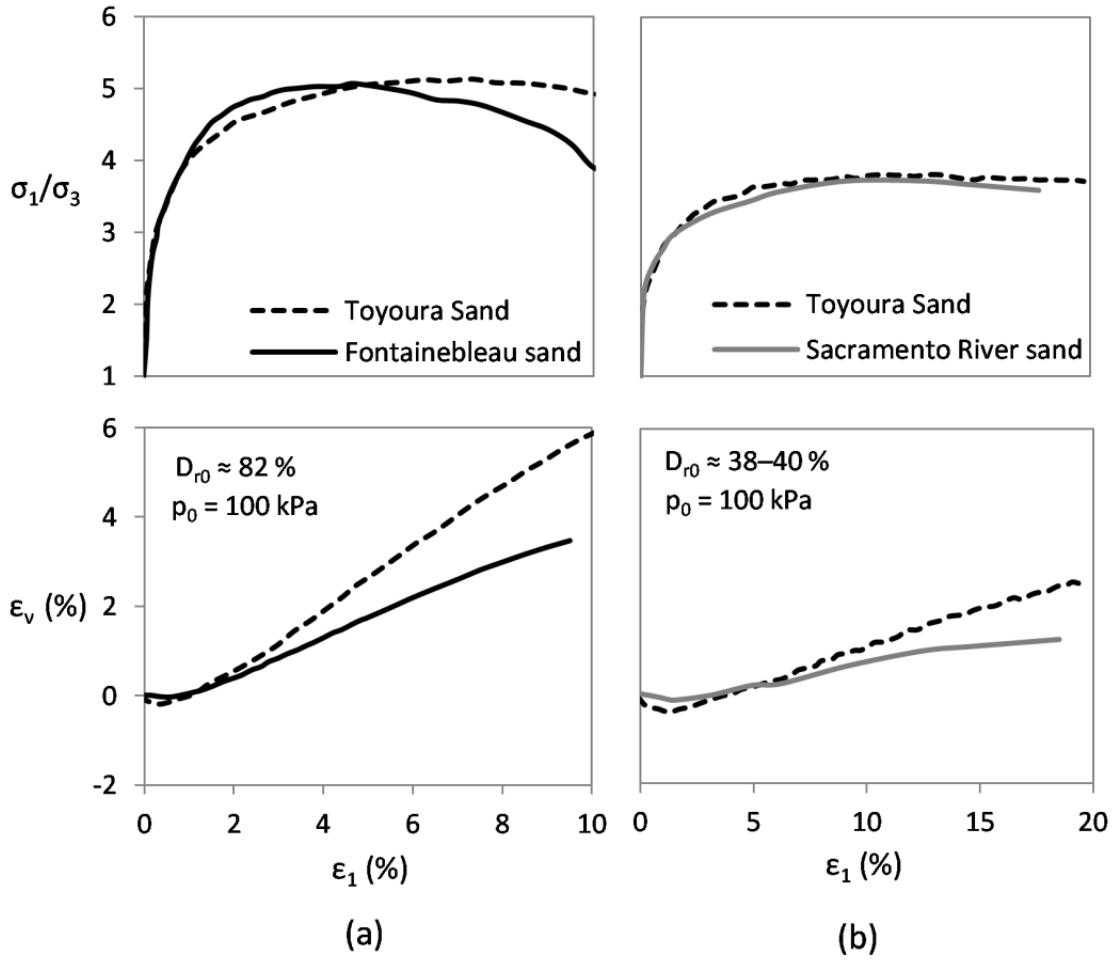

Figure 4.1. Experimental data of drained behavior of different sands under triaxial compression. Comparison under the same initial relative density and mean effective stress between: a) Toyoura (Fukushima and Tatsuoka, 1984) and Fontainebleau sand (Dupla et al., 2010) and b) Toyoura (Fukushima and Tatsuoka, 1984) and Sacramento River sand (Lee and Seed, 1967).

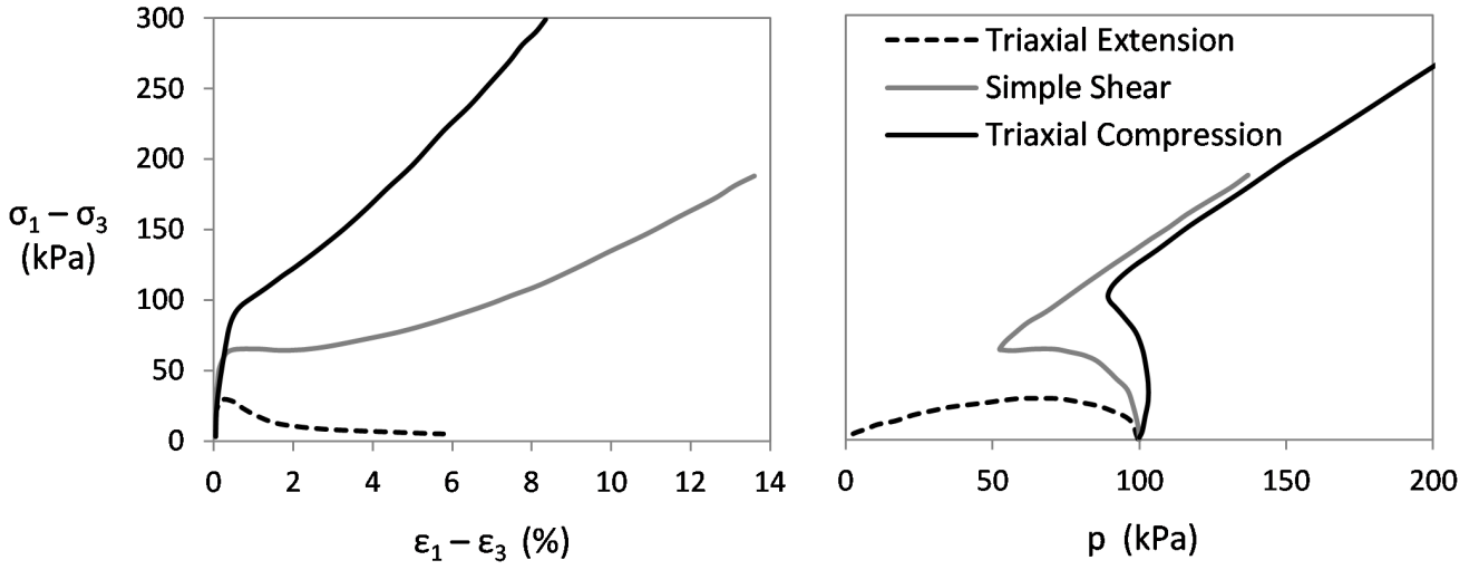

Figure 4.2. Experimental data by Yoshimine et al. (1998) showing the anisotropic behavior of Toyoura sand with initial density, D_{r0} = 33-36 %, in undrained triaxial compression, extension and simple shear.

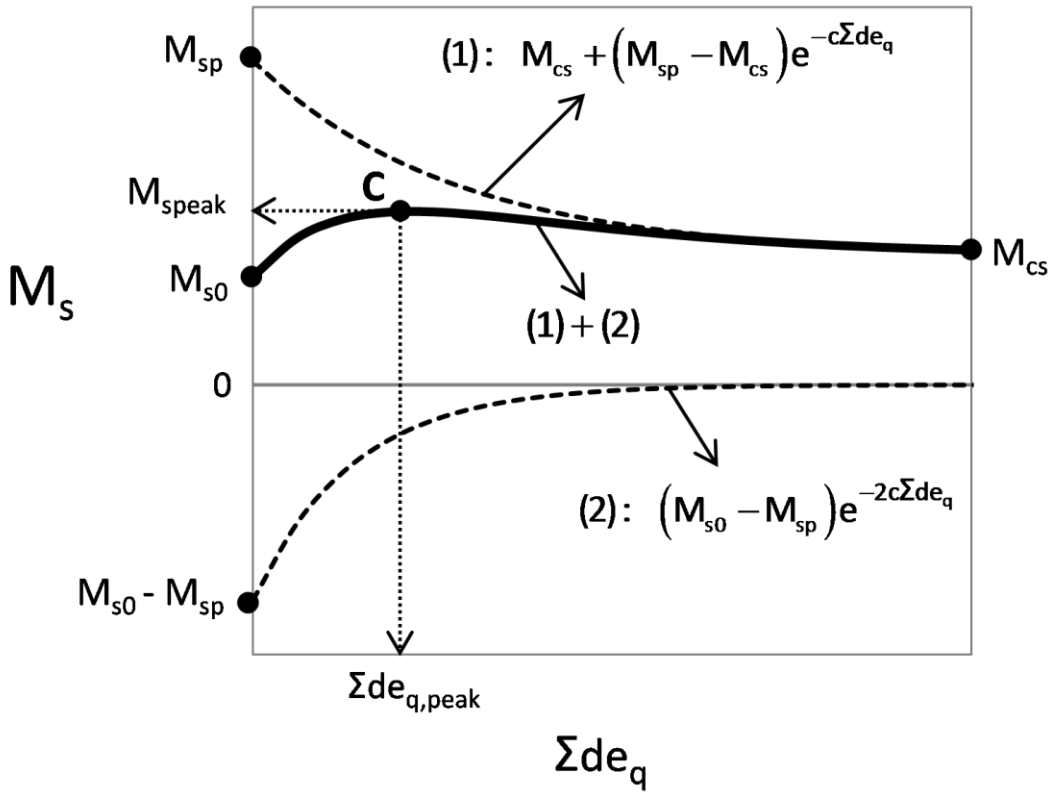

Figure 4.3. Illustration of the evolution of bounding stress ratio Ms with cumulative deviatoric strain increment $\sum\left|d\varepsilon_q\right|$, described by Eq. (4.18).

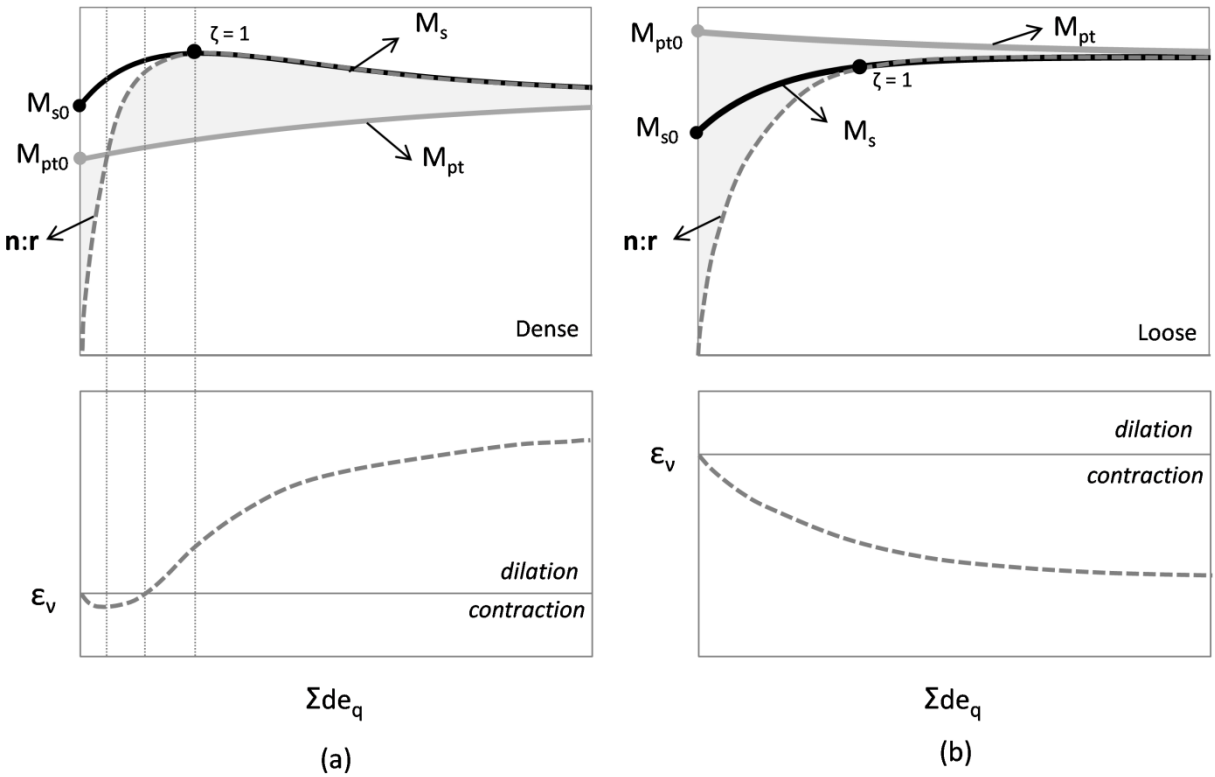

Figure 4.4. Illustration of the evolution of bounding, M_s and phase transformation, M_{pt}, stress ratios, with cumulative deviatoric strain increment, $\sum\left|d\varepsilon_q\right|$, described by Eqs. (4.18) and (4.25), in case of: (a) dense and (b) loose sand.

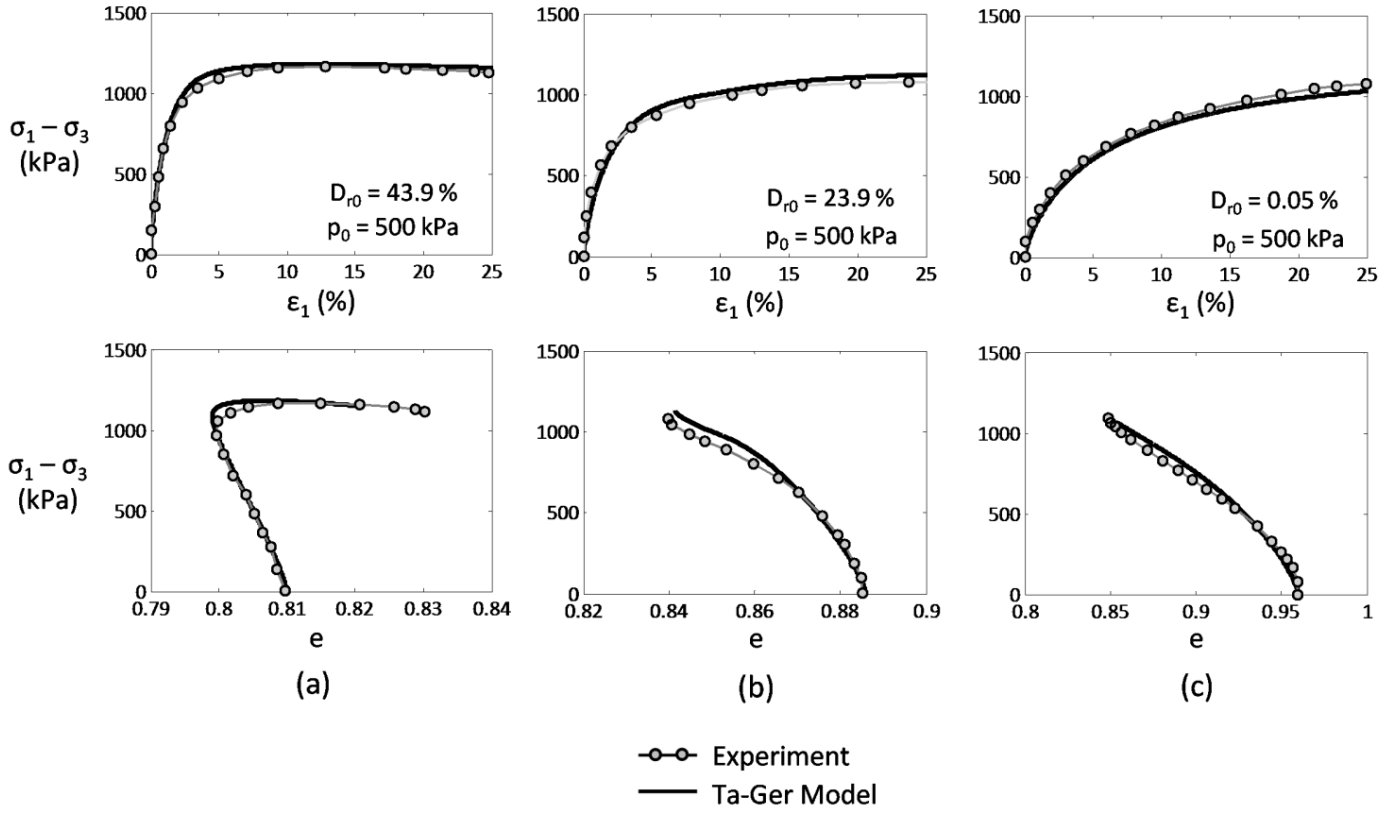

Figure 4.5. Model predictions versus experimental data from drained conventional triaxial compression tests on Toyoura sand at p_0 = 500 kPa by Verdugo and Ishihara (1996): (a) e_0 = 0.81, (b) e_0 = 0.886 and (c) e_0 = 0.96.

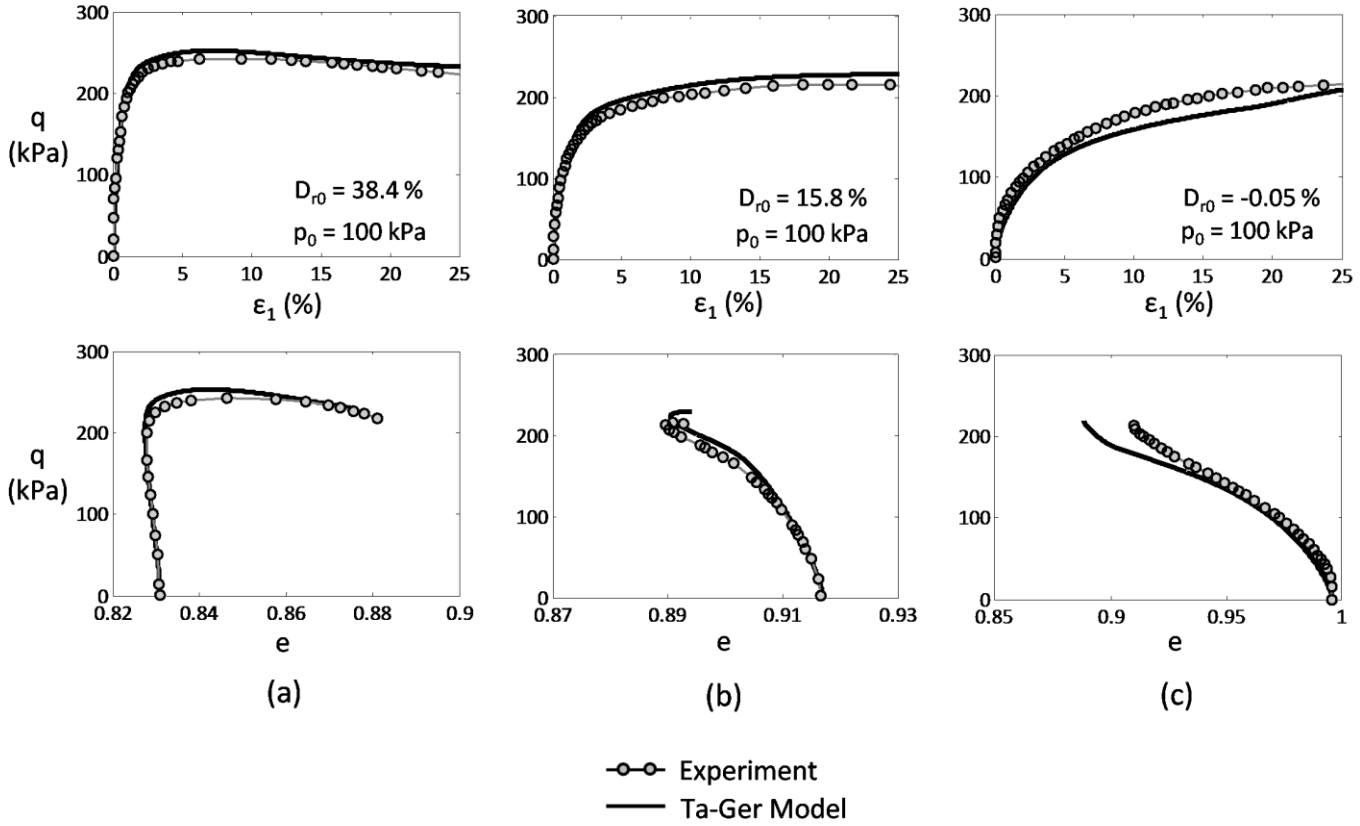

Figure 4.6. Model predictions versus experimental data from drained conventional triaxial compression tests on Toyoura sand at p_0 = 100 kPa by Verdugo and Ishihara (1996): (a) e_0 = 0.831, (b) e_0 = 0.917 and (c) e_0 = 0.996.

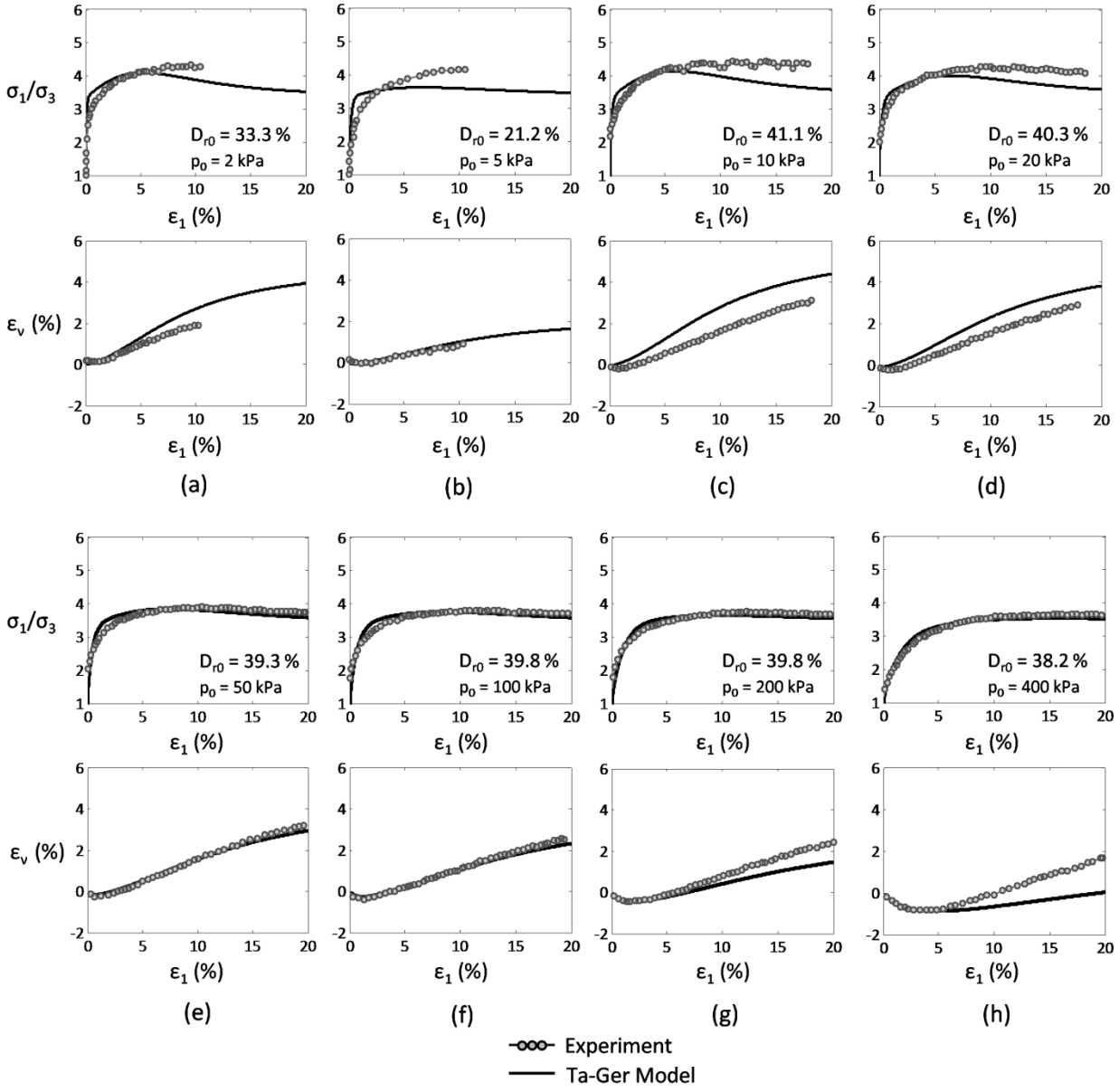

Figure 4.7. Model predictions versus experimental data from drained conventional triaxial compression tests on loose Toyoura sand specimens (D_{r0} = 21.2 – 40.3 %) at a wide range of confining pressures (p_0 = 2–400 kPa) by Fukushima and Tatsuoka (1984).

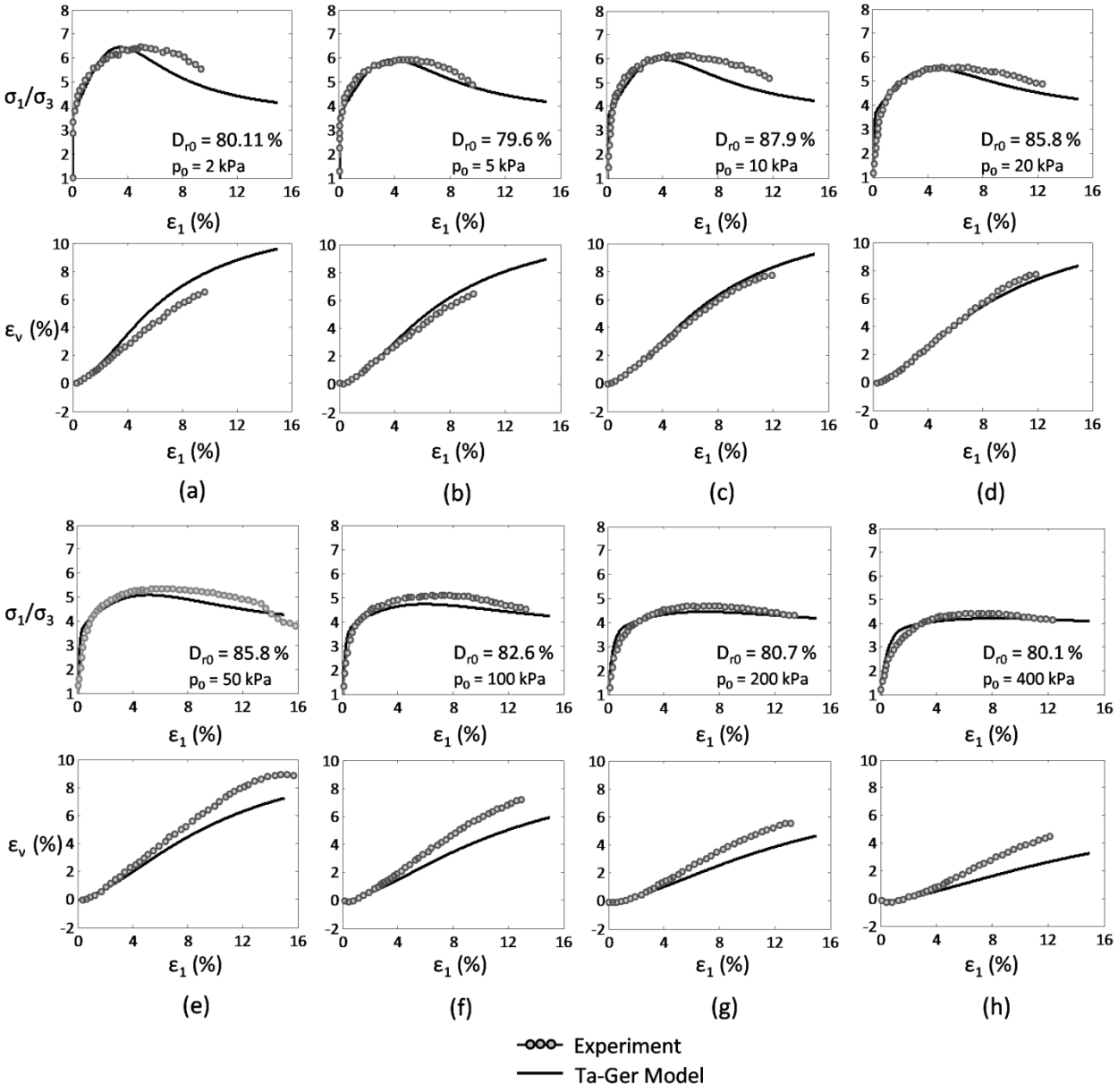

Figure 4.8. Model predictions versus experimental data from drained conventional triaxial compression tests on dense Toyoura sand specimens (D_{r0} = 79.6 - 87.9 %) at a wide range of confining pressures (p_0 = 2 – 400 kPa) by Fukushima and Tatsuoka (1984).

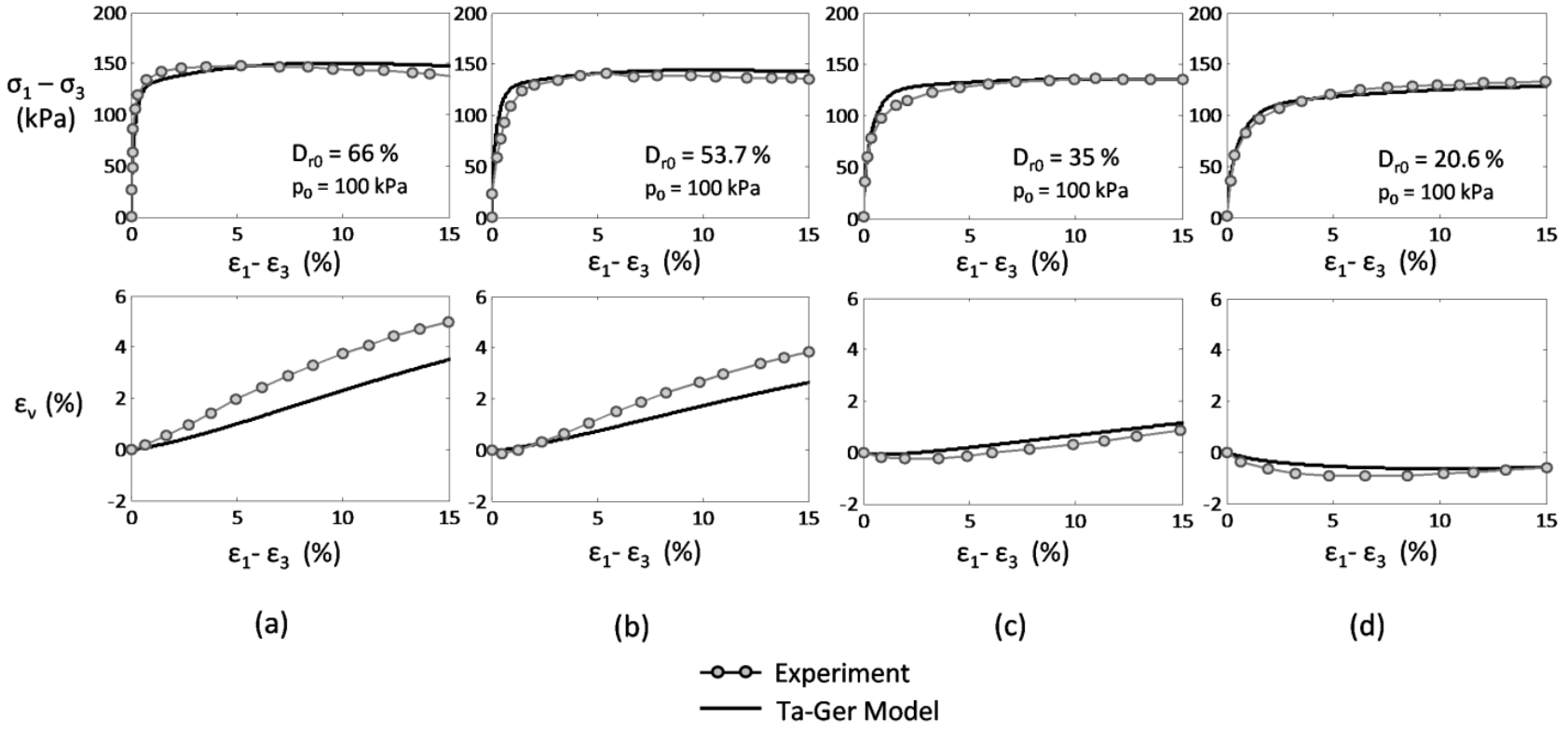

Figure 4.9. Model predictions versus experimental data from drained triaxial compression tests (p constant) on Toyoura sand at p_0 = 100 kPa by Toyota et al. (2004).

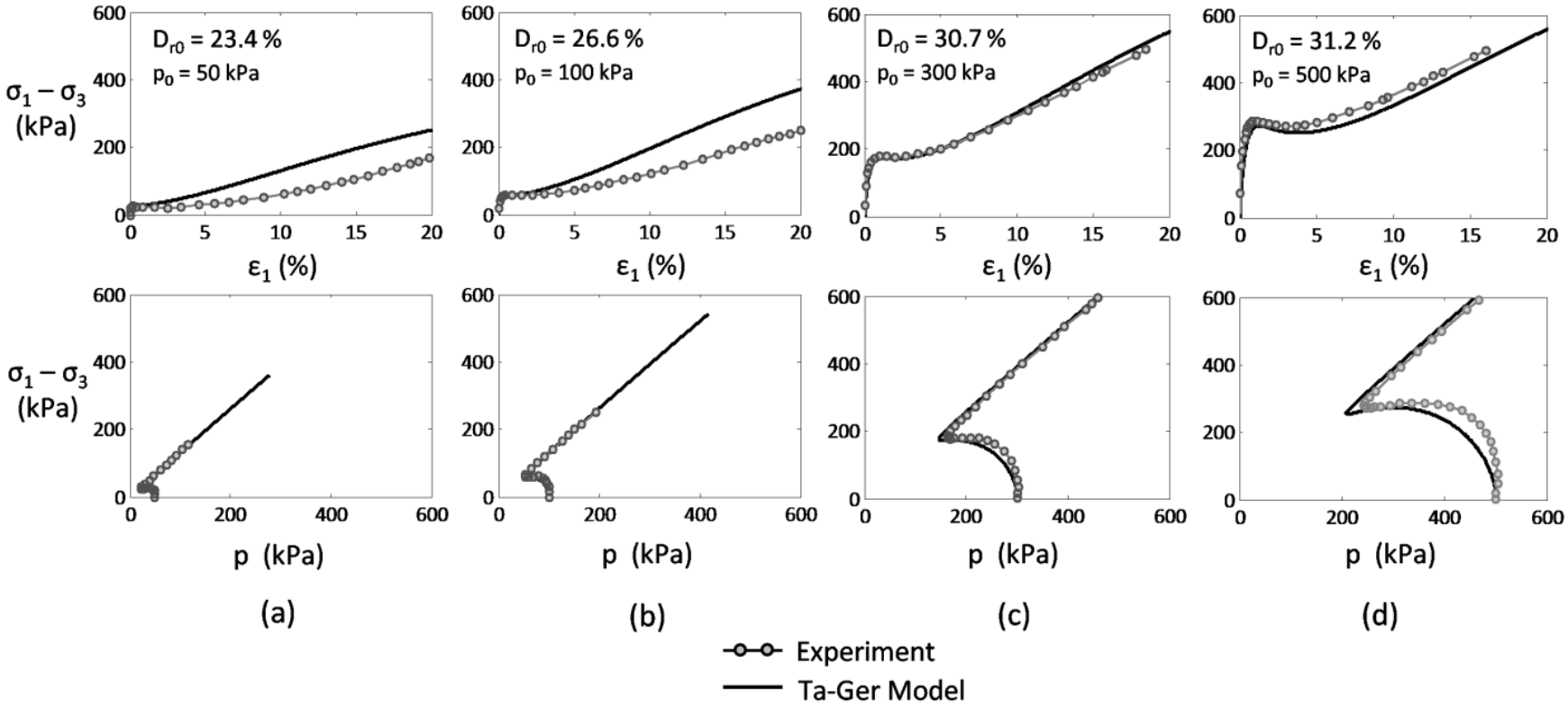

Figure 4.10. Model predictions versus experimental data from undrained conventional triaxial compression tests on Toyoura sand by Yoshimine et al. (1998).

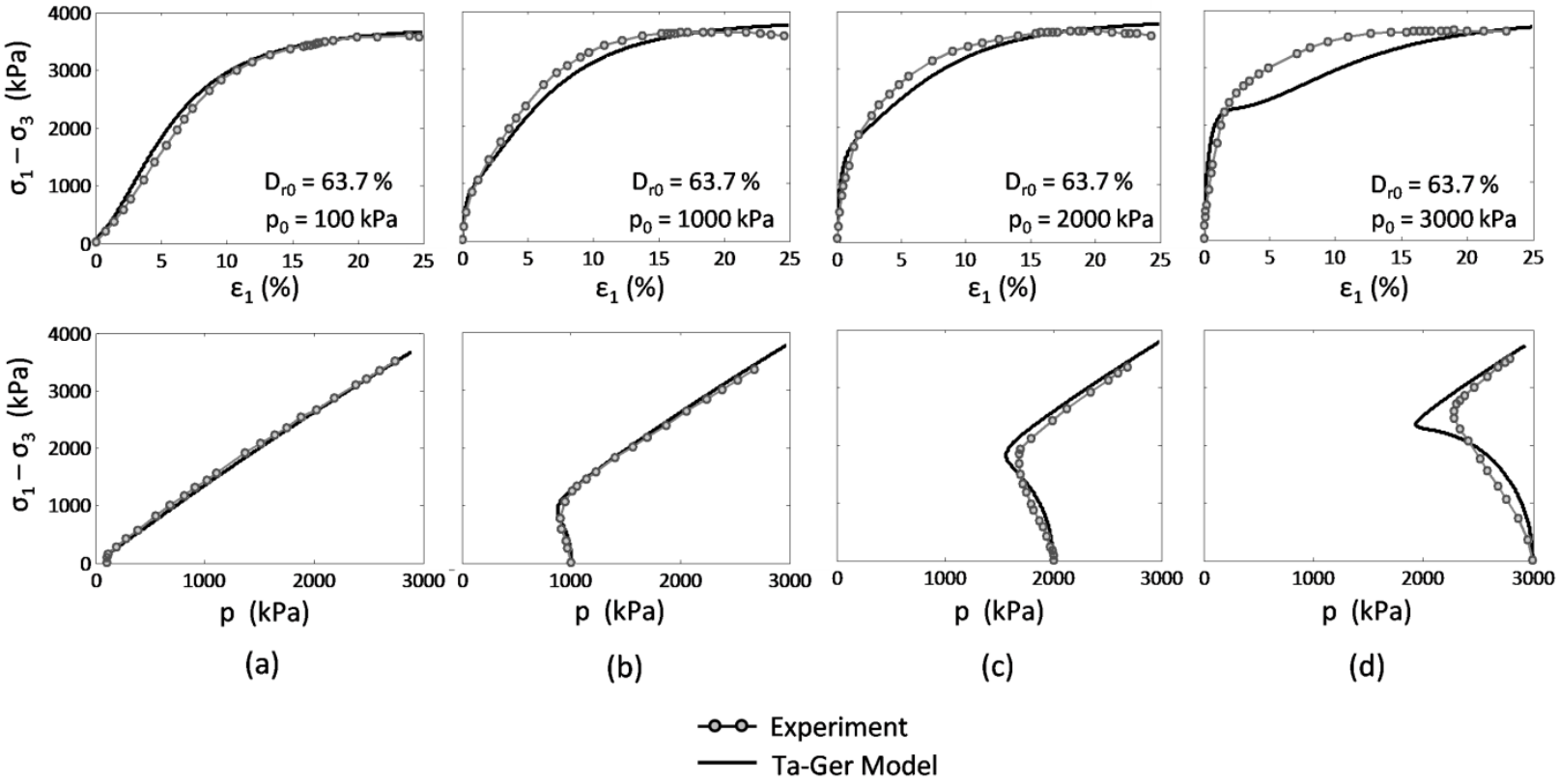

Figure 4.11. Model predictions versus experimental data from undrained conventional triaxial compression tests on Toyoura sand by Verdugo and Ishihara (1996).

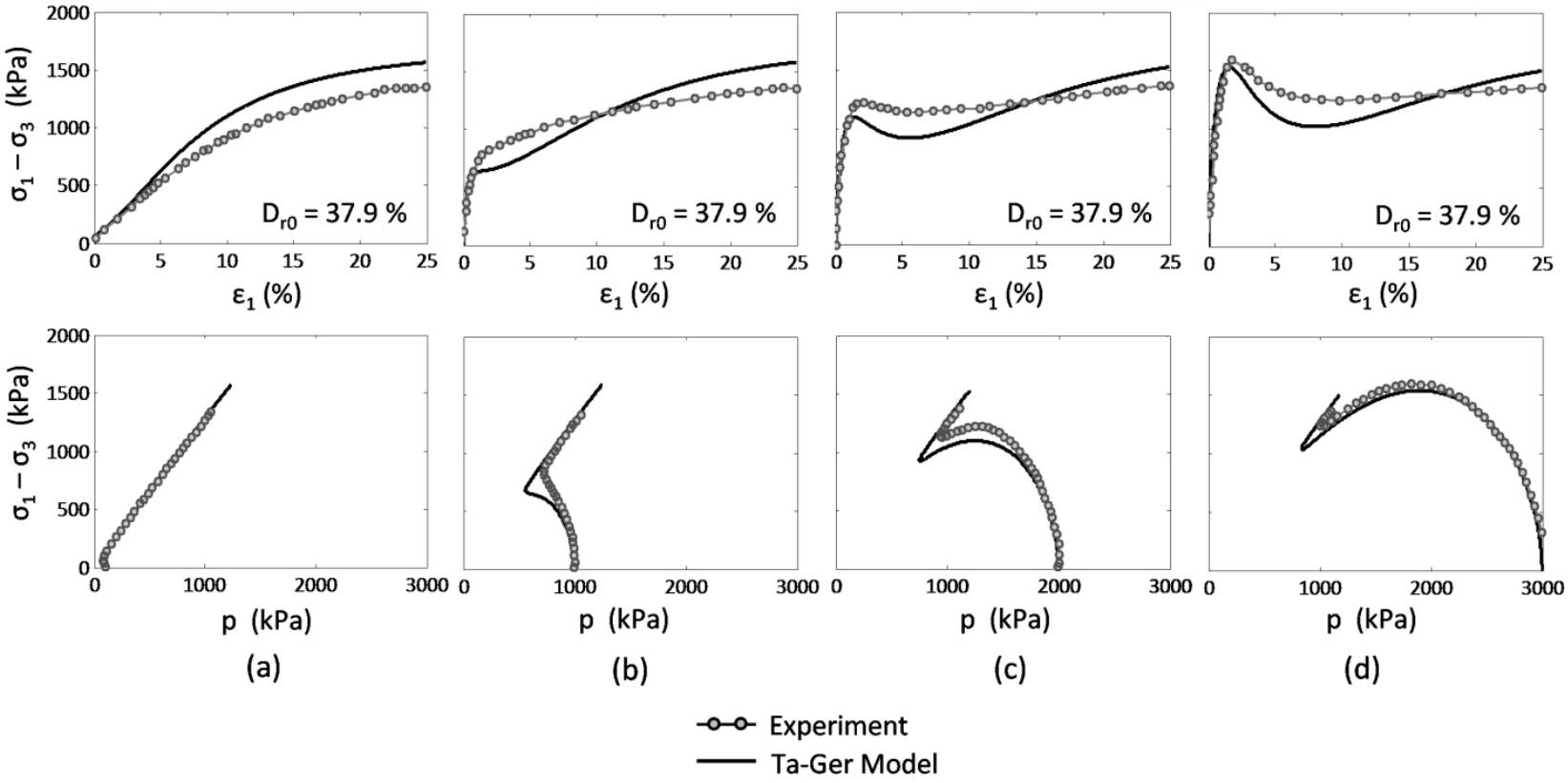

Figure 4.12. Model predictions versus experimental data from undrained conventional triaxial compression tests on Toyoura sand by Verdugo and Ishihara (1996).

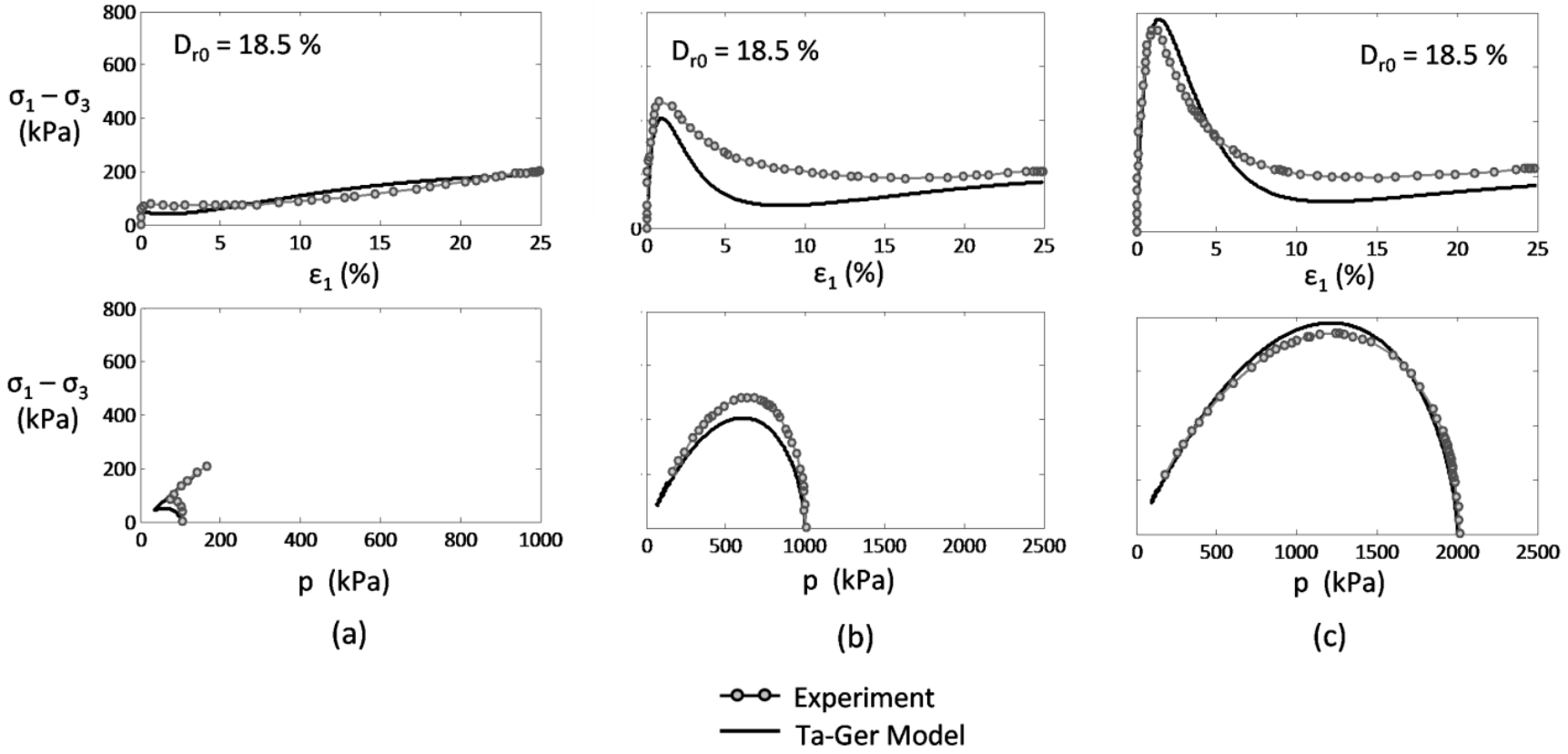

Figure 4.13. Model predictions versus experimental data from undrained conventional triaxial compression tests on Toyoura sand by Verdugo and Ishihara (1996).

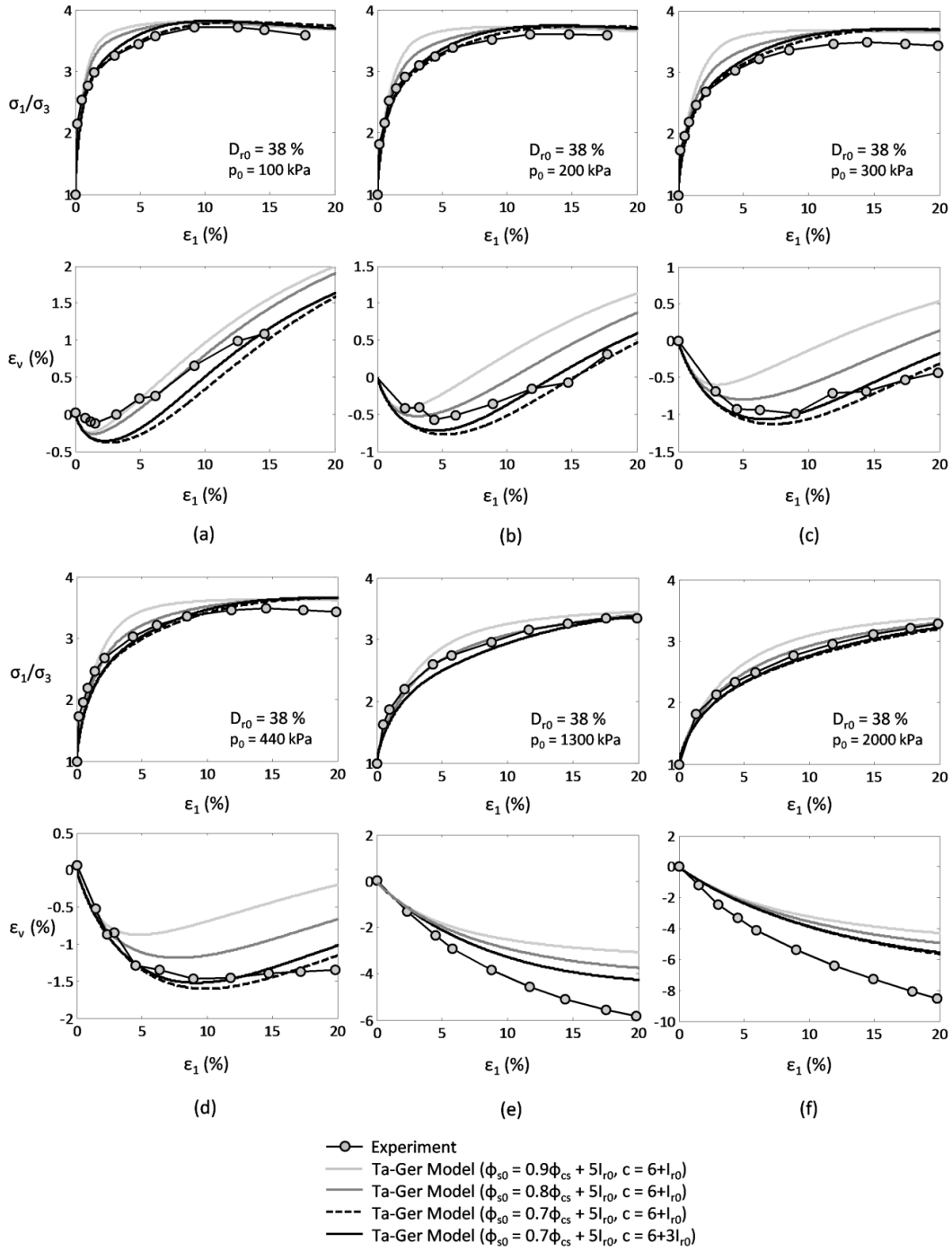

Figure 4.14. Model predictions versus experimental data from drained triaxial compression tests on loose Sacramento River sand (K_0 = 1) by Lee and Seed (1967).

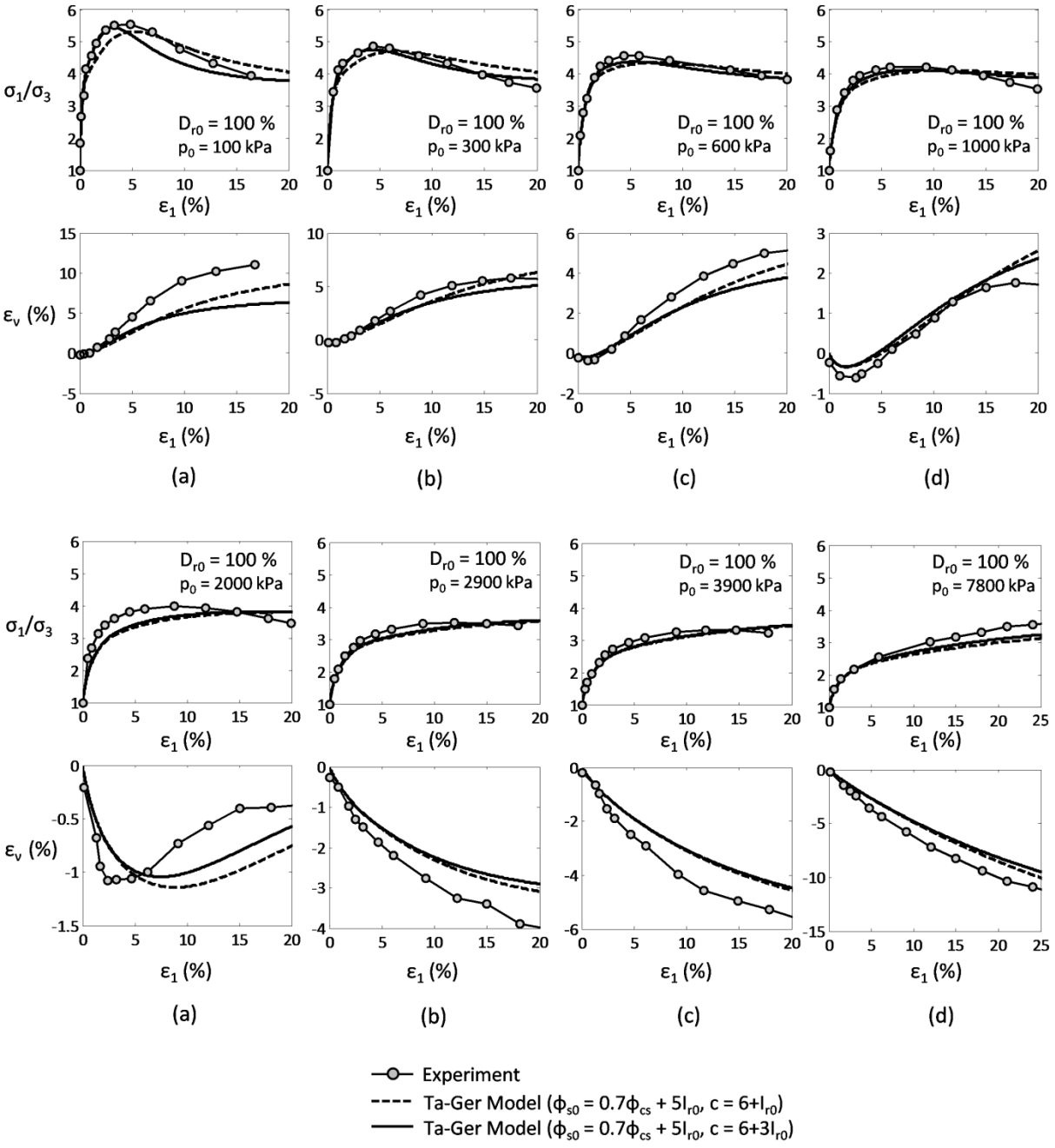

Figure 4.15. Model predictions versus experimental data from drained triaxial compression tests on dense Sacramento River sand (K_0 =1) by Lee and Seed (1967).

sand particles are expected to exhibit a more dilative response than round ones.

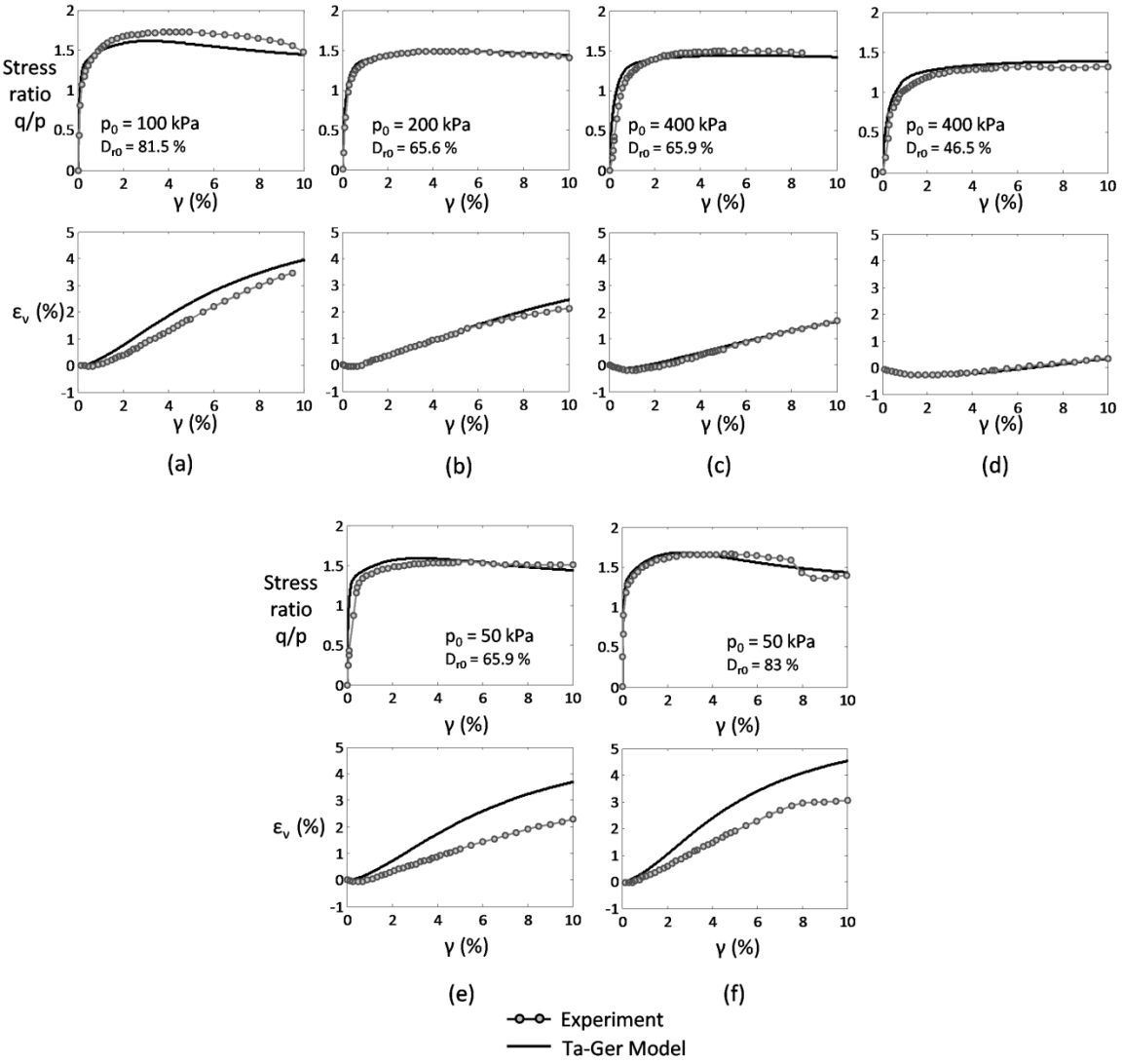

Figure 4.16. Model predictions versus experimental data from drained triaxial compression tests on Fontainebleau sand (K_0 =1) by Dupla et al. (2010): (a) p_0= 100 kPa and D_r = 81.5 %, (b) p_0= 200 kPa and D_r = 65.6 %, (c) p_0= 400 kPa and D_r = 65.9 % and (d) p_0= 400 kPa and D_r = 46.5 %.

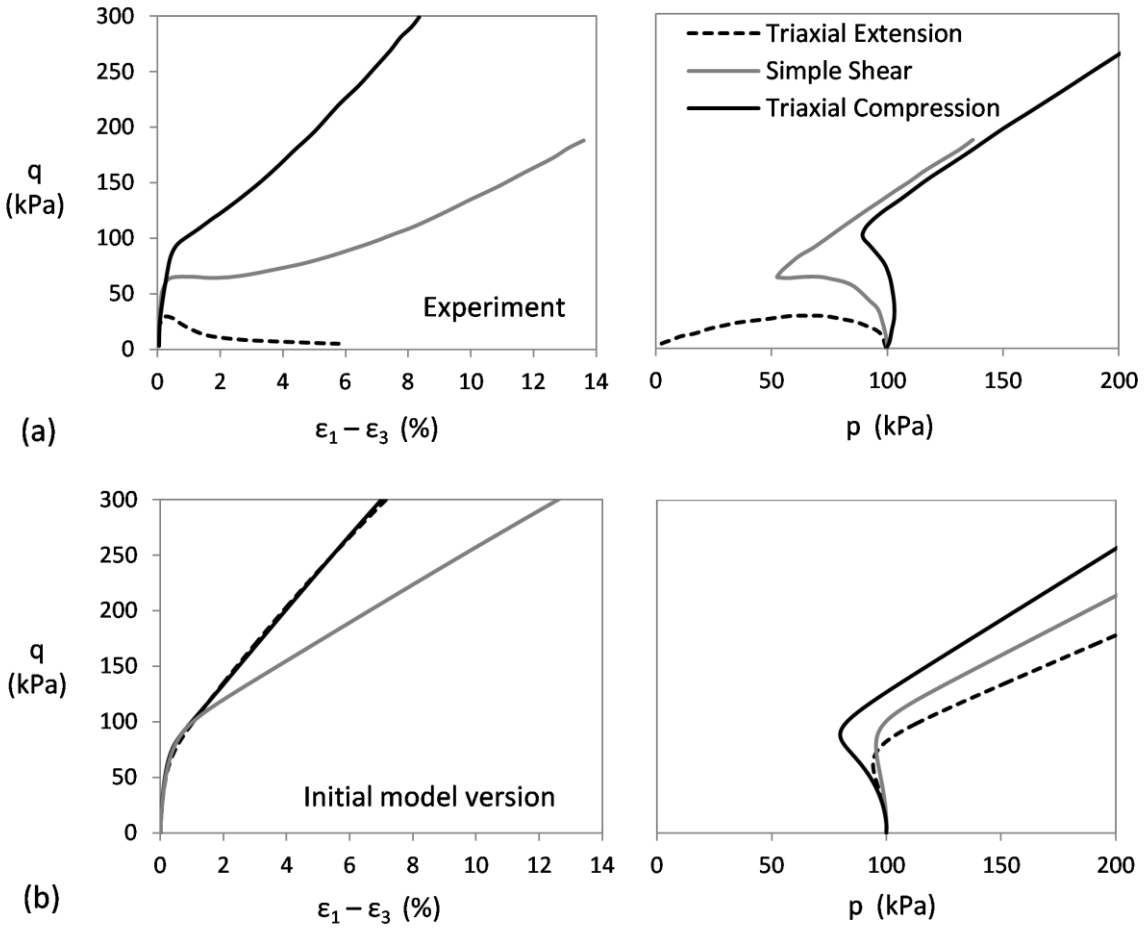

Figure 4.17. Comparison between: (a) experiments and (b) predictions performed with the initial version of the model based on triaxial compression tests (Table 4), which does not account for stress-induced anisotropy.

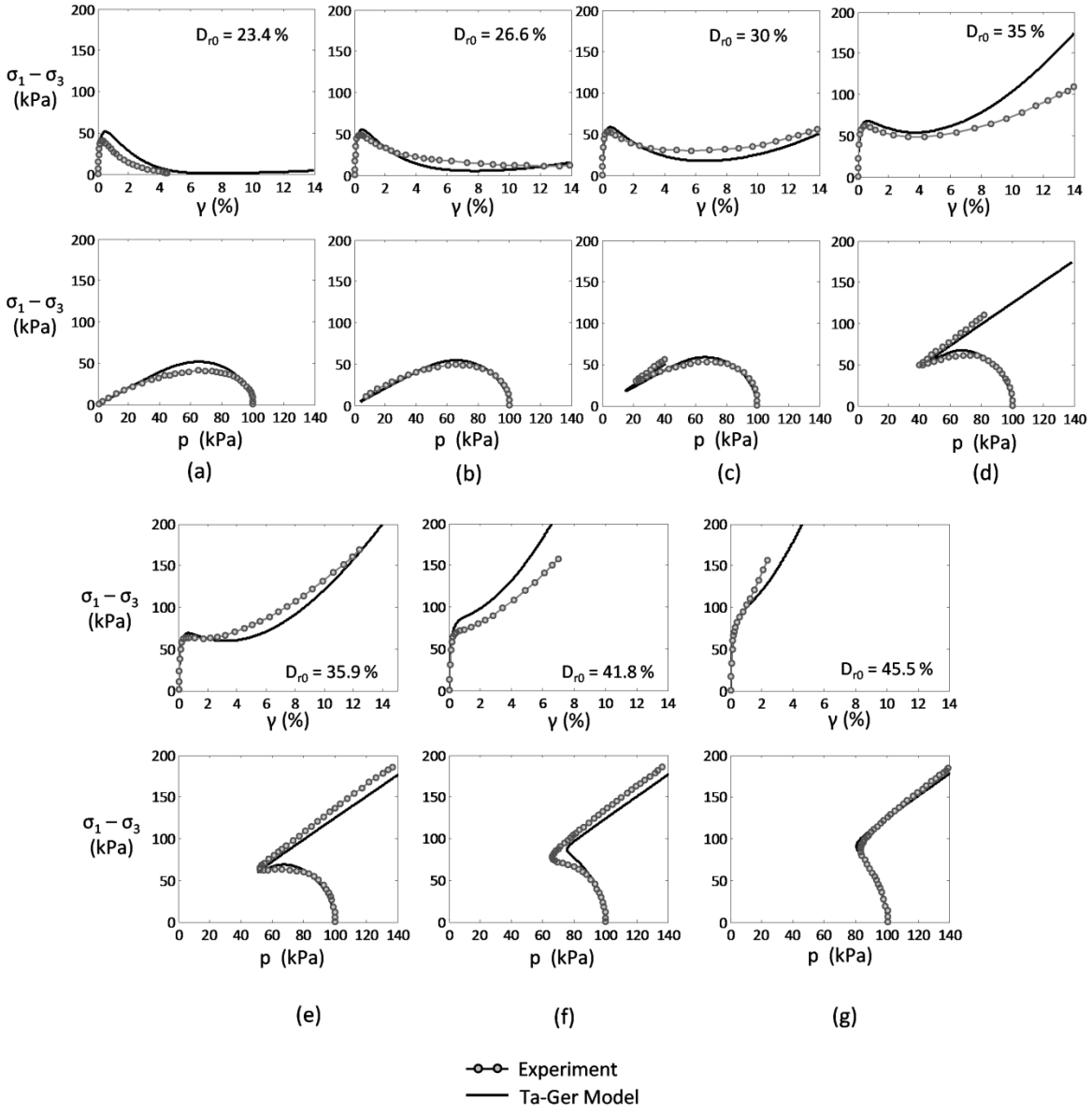

Figure 4.18. Model predictions versus experimental data from undrained simple shear tests on Toyoura sand with isotropic consolidation state, K_0 = 1, by Yoshimine et al. (1998) for p_0= 100 kPa.

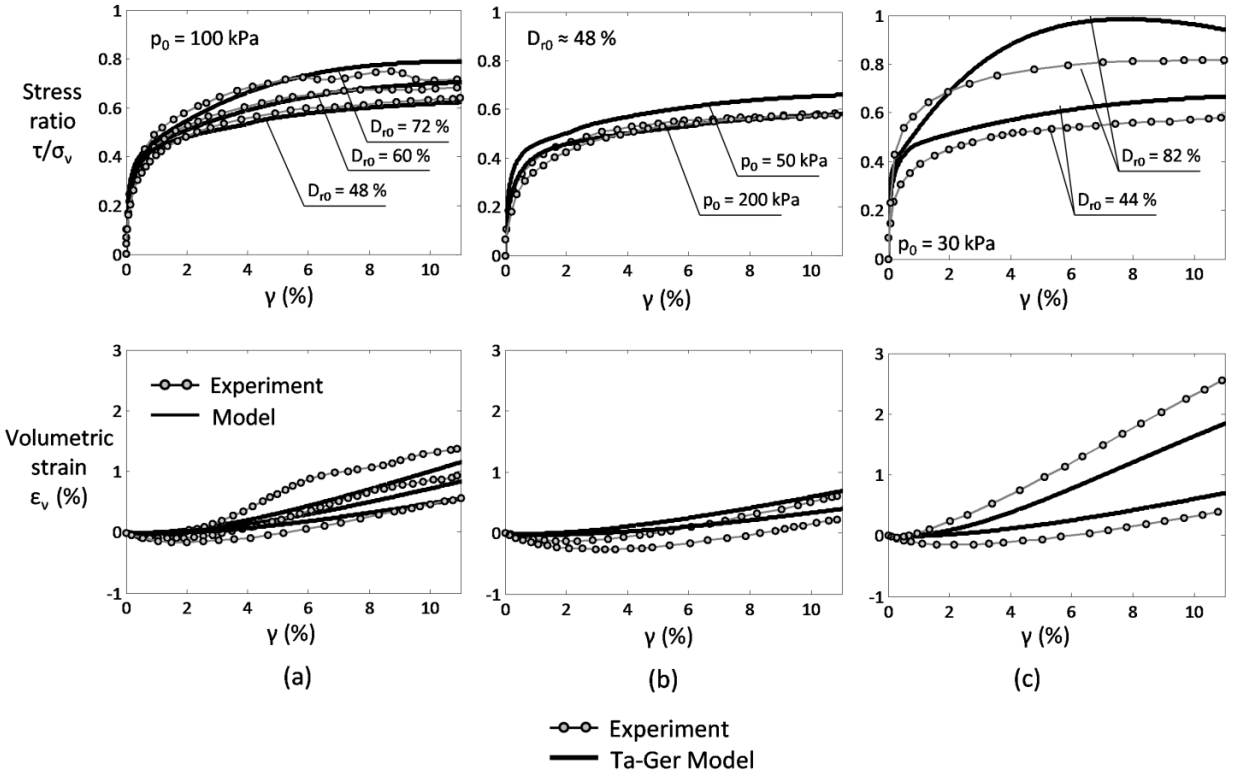

Figure 4.19. Model predictions versus experimental data from drained torsional simple shear tests (lateral strains equal to zero) on Toyoura sand with $K_0 = 0.52e_0$ by Pradhan et al. (1988): (a) $p_0 = 100$ kPa for various D_{r0} , (b) $D_{r0} \approx 48$ % for various p_0 and (c) $p_0 = 30$ kPa for various D_{r0}.

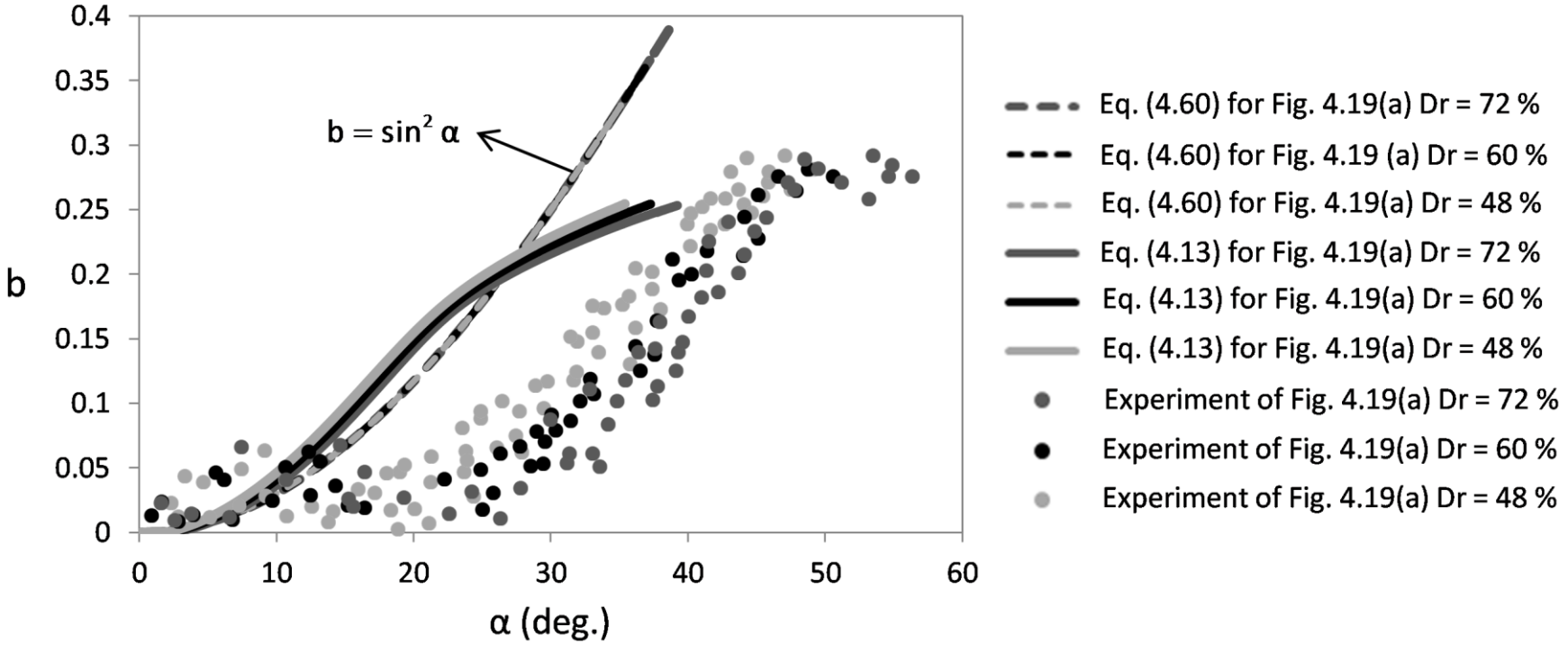

Figure 4.20. Relationship between α and b parameters during a drained direct simple shear tests with $K_0 = 0.52e_0$ by Pradhan et al. (1988): Comparison of new plastic flow rule of Eq. (4.13) and commonly used in literature flow rule of Eq. (4.60) against experimental data.

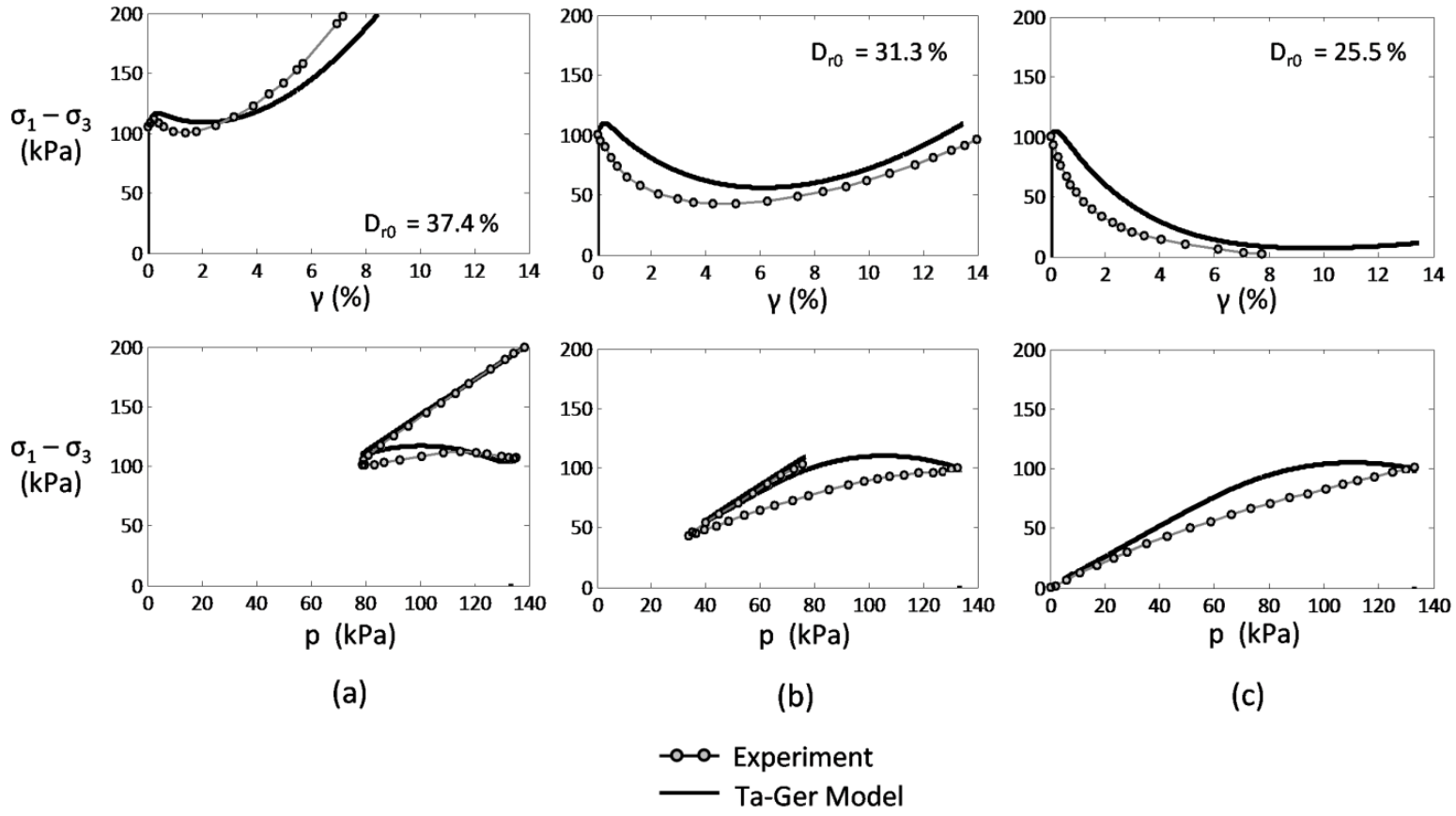

Figure 4.21. Model predictions versus experimental data from undrained simple shear tests on Toyoura sand with anisotropic consolidation state (K_0 = 0.5) by Yoshimine et al. (1998) for p_0= 133.3 kPa: (a) D_r = 37.4 %, (b) D_r = 31.3% and (c) D_r = 25.5 %.

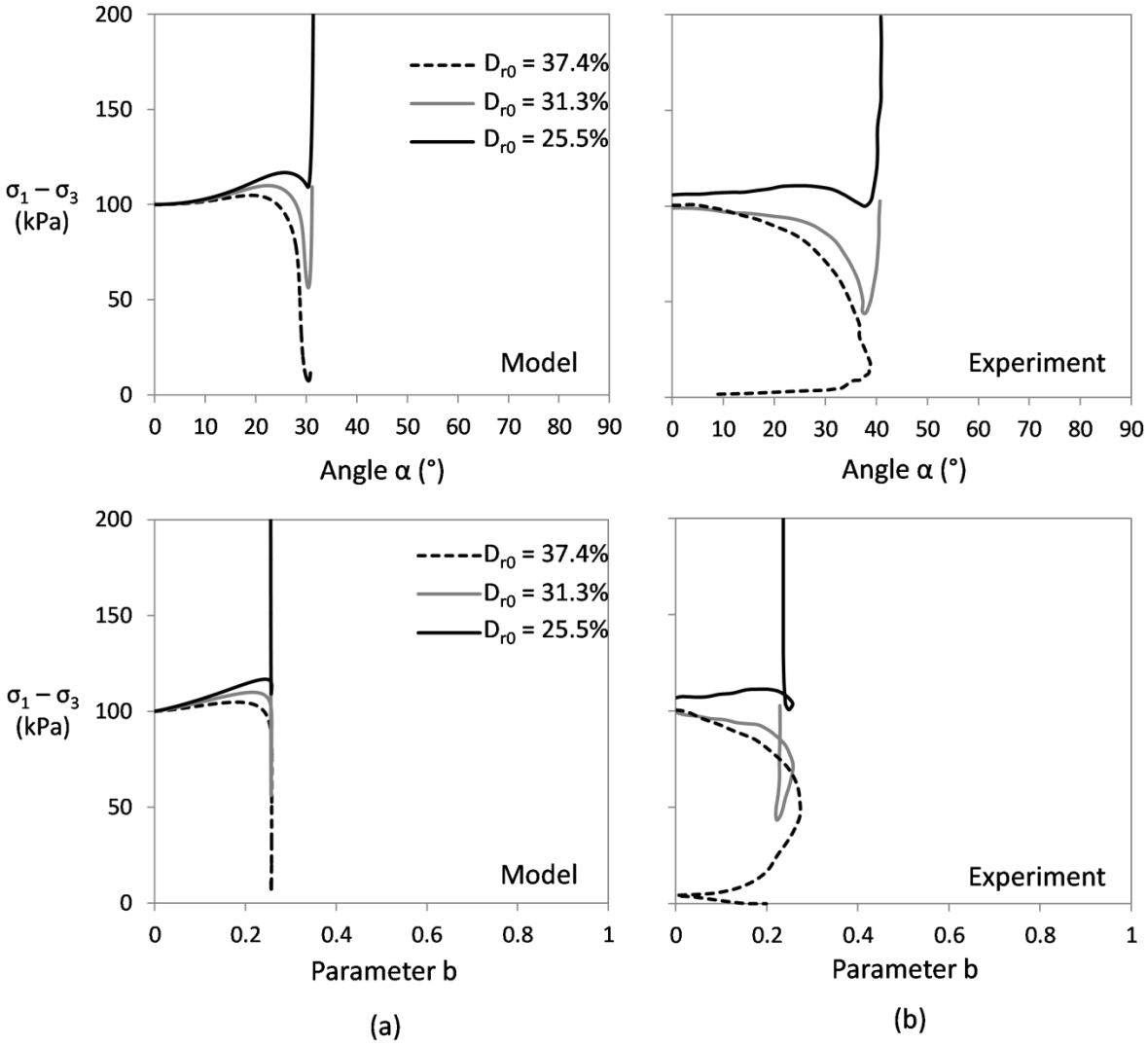

Figure 4.22. Evolution of parameters α and b versus deviatoric stress, $\sigma_1 - \sigma_3$, for undrained simple shear tests with K_0 = 0.5 by Yoshimine (1998) of Figure 20: Model predictions versus experimental data.

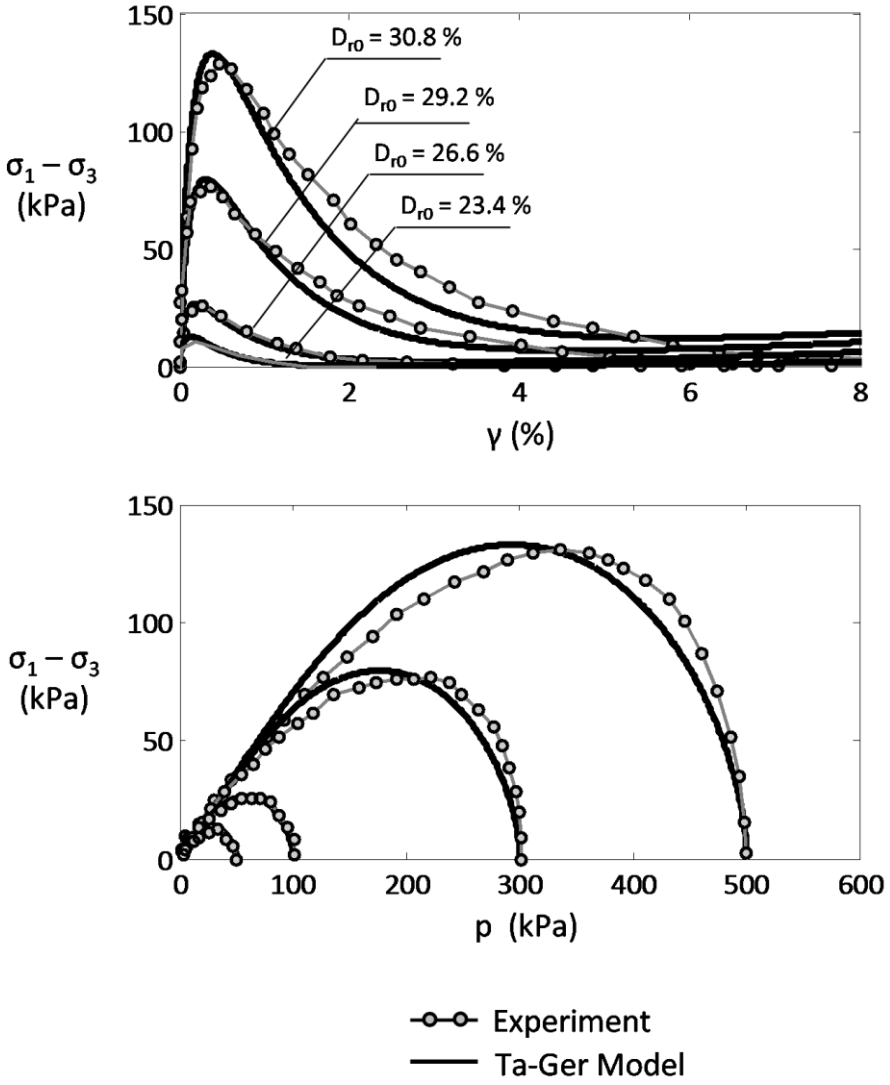

Figure 4.23. Model predictions versus experimental data from undrained triaxial extension tests on Toyoura sand with isotropic consolidation state (K_0 = 1) by Yoshimine et al. (1998) for various values of initial relative density, D_{r0} and mean effective stress, p_0.

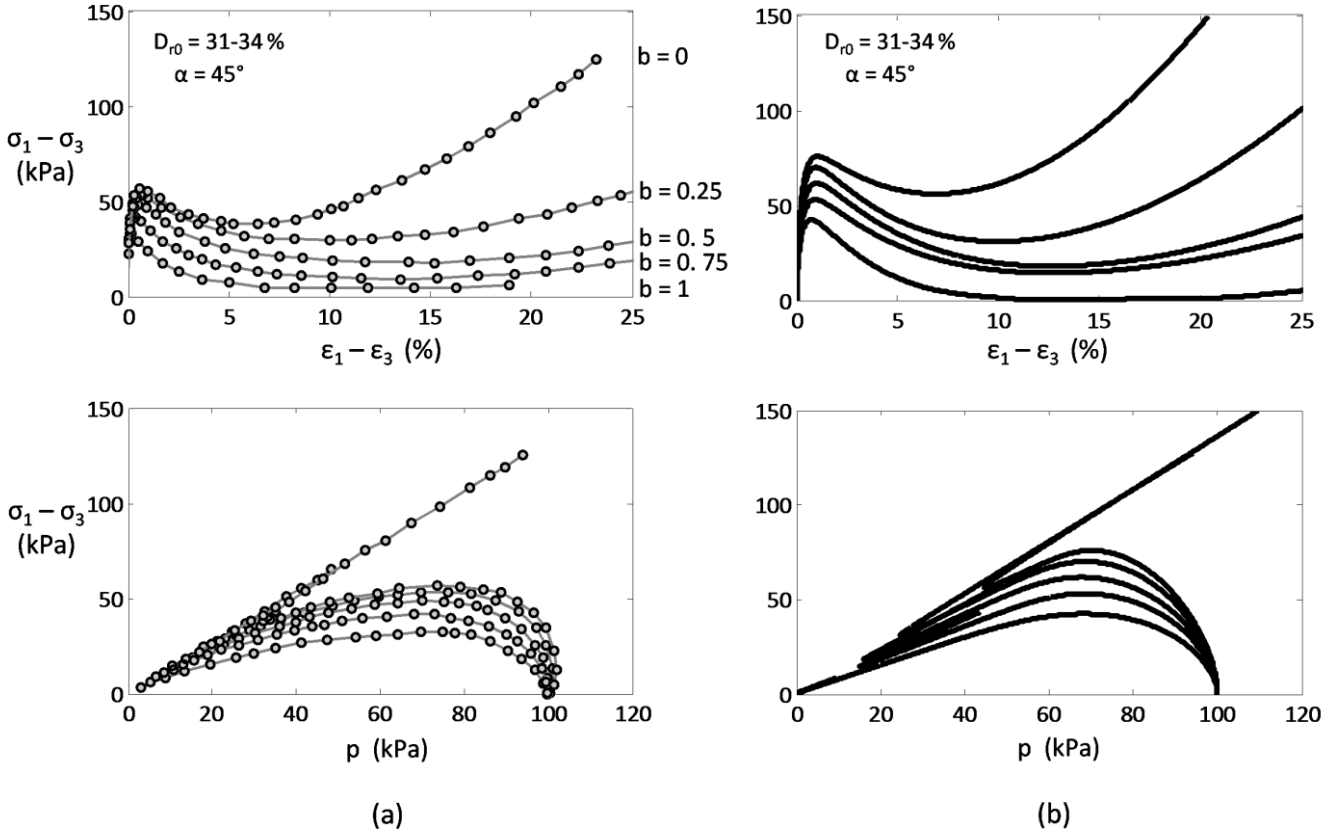

Figure 4.24. Model predictions versus experimental data from undrained tests on Toyoura sand with variation of b by Yoshimine et al. (1998) for p_0= 100 kPa and D_{r0} = 31-34 %: (a) experiments and (b) model predictions.

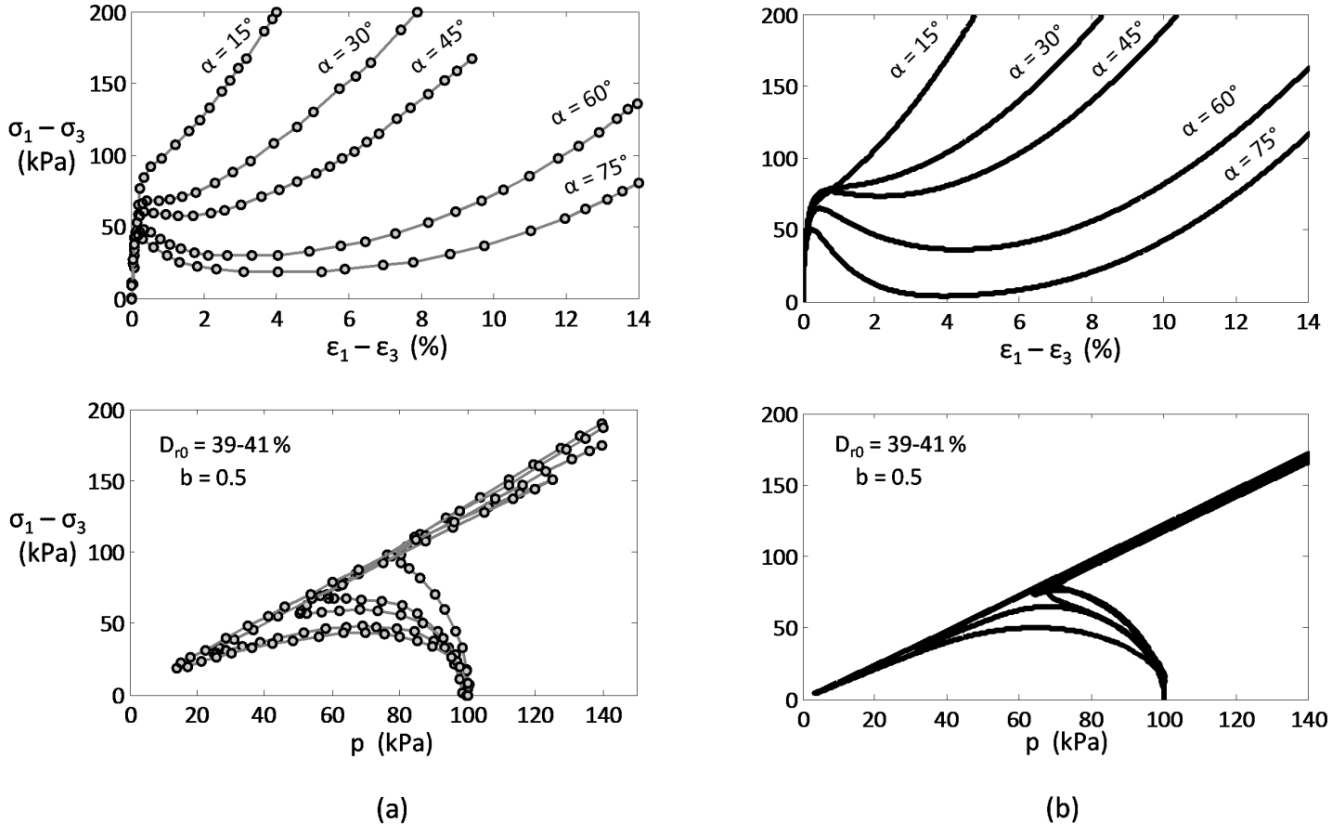

Figure 4.25. Model predictions versus experimental data from undrained tests on Toyoura sand with variation of rotation angle α by Yoshimine et al. (1998) for p_0= 100 kPa and D_{r0} = 39-41 %: (a) experiments and (b) model predictions.

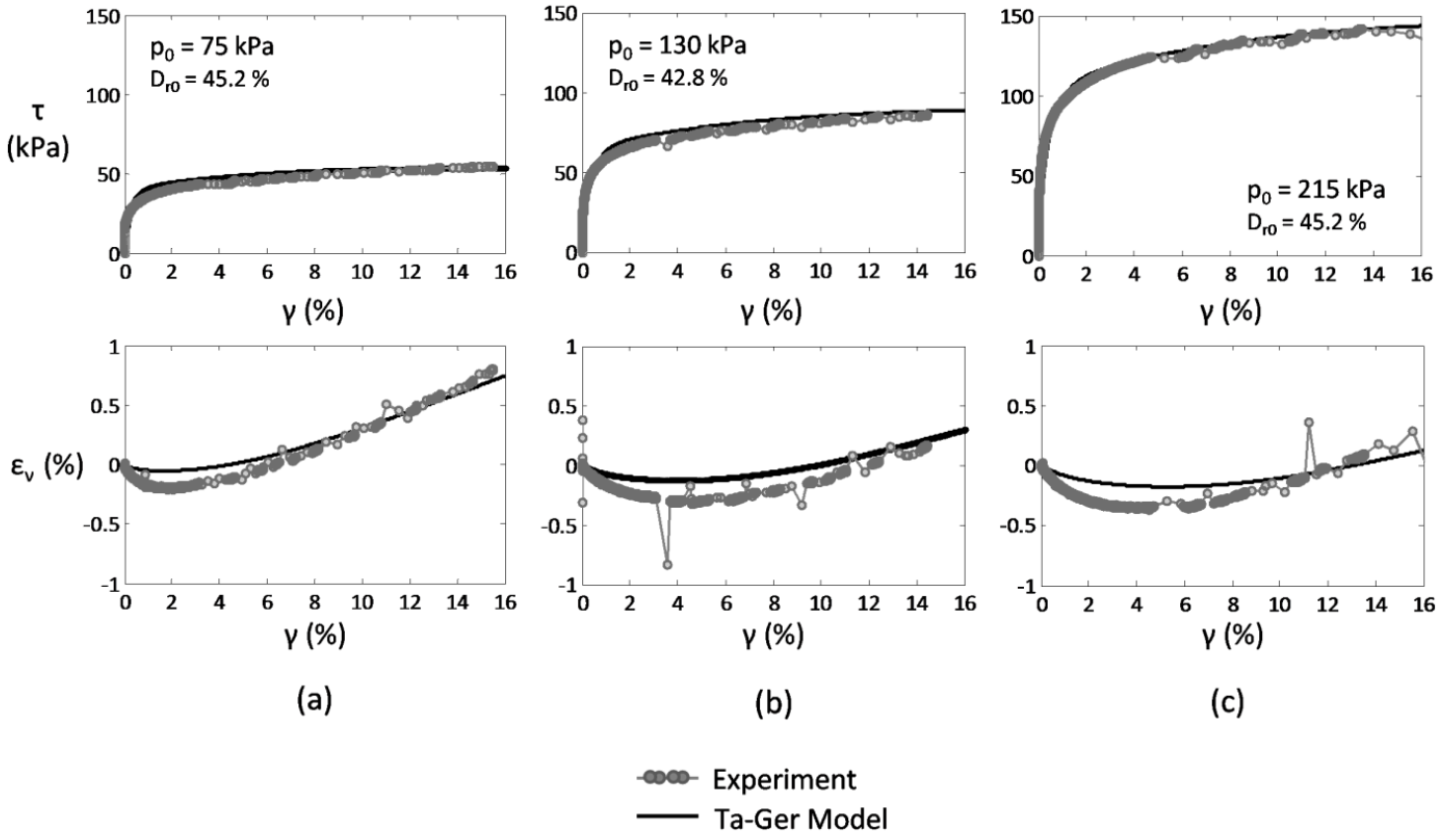

Figure 4.26. Model predictions versus experimental data from drained torsional tests on Fontainebleau sand (K_0 =1) by Georgiannou et al. (2008) : (a) p_0= 75 kPa and D_r = 45.2 %, (b) p_0= 130 kPa and D_r = 42.8 % and (c) p_0= 215 kPa and D_r = 45.2 %.

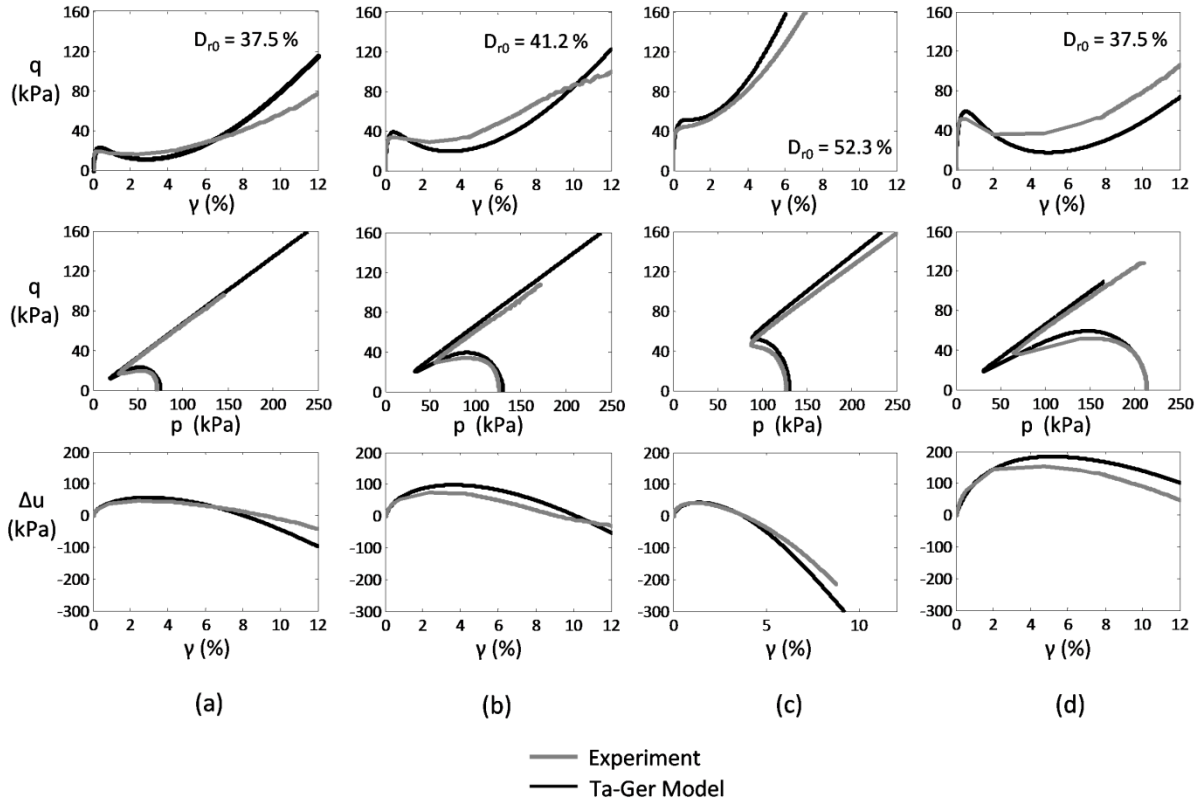

Figure 4.27. Model predictions versus experimental data from undrained torsional tests on Fontainebleau sand (K_0 =1) by Georgiannou et al. (2008) : (a) p_0= 75 kPa and D_r = 37.5 %, (b) p_0= 130 kPa and D_r = 41.2 %, (c) p_0= 130 kPa and D_r = 52.3 % and (d) p_0= 215 kPa and D_r = 37.5 %.

CHAPTER 5

Conclusions

In retrospect, a complete novel constitutive model for sand has been proposed as an alternative plasticity formulation that exhibits critical state consistency for both monotonic and cyclic loading and uniqueness of its parameters for a given type of sand, irrespective of loading conditions. The model, designated as Ta-Ger sand model is based on a reformulation of perfect elastoplasticity by introducing a hardening law inspired from Bouc-Wen hysteresis. The proposed formulation incorporates many innovations intended to provide critical state consistency not only for monotonic but also for cyclic loading and uniqueness of model parameters for a given type of sand:

- a new plastic flow rule based on a revision of Rowe dilatancy theory (1962), accounting for anisotropic distribution of dilatancy to the normal plastic strain increments, as well as densification due to cyclic loading,
- a mapping rule and load reversal criterion based on the first order work, inspired from Bouc-Wen hysteresis
- a new formulation for the evolution of the bounding and phase transformation surfaces as a function of the cumulative deviatoric strain increment, ensuring critical state consistency not only for monotonic but also for cyclic loading.

The developed constitutive formulation can be regarded as a bounding single-surface model with vanished elastic region and the distinguished characteristic of an explicitly formulated plastic matrix instead of a plastic modulus. The explicitly formulated plastic matrix plays a triple role:

- it offers a gradual and smooth ("hardening-type") transition from the elastic to perfectly plastic response in order to capture pre-failure nonlinearity and the coupling between elastic and plastic counterparts composing the total strain increment,
- it provides an appropriate loading/unloading/reloading mapping rule by tracking the distance from the ultimate perfectly plastic state as defined by the failure surface, which herein, serves as a bounding surface, and
- its terms attain values that are strictly bounded within the range of [0,1].

An extensive calibration procedure has been developed aiming at:

- increasing model predictability,
- minimizing the number of unknown model parameters,
- addressing intrinsic and stress-induced anisotropy.

Constitutive formulation was adjusted to Bolton's (1986) empirical correlations for dilatancy, given as a function of relative dilatancy index, I_r; the latter works as a state parameter in the constitutive framework. This step reduced the number of unknown model parameters to three, besides the ones related directly to measurable physical properties, such as critical state friction angle and elastic modulus. At this stage, the remaining three unknown parameters were expressed as functions of the initial state (relative density and pressure), while inherent fabric effects (such as particle shape, size and packing) on the calibration process are considered. At last, stress-induced anisotropy was dealt with introducing a scalar-valued variable in the model, a function of principal

stress rotation angle, α, and the intermediate stress parameter, b, without affecting the number of unknown model parameters.

Validation against experimental data was performed in every step for various drained and undrained loading paths in a wide range of α, b values, as well as initial states, for three different types of sand (Toyoura, Fontainebleau, Sacramento–River). Comparison with experiments reveals the capability of the model to describe complex patterns of sand behavior, such as densification, cyclic hardening, as well as liquefaction due to cyclic loading at very large strains (e.g. $\gamma > 8\%$) without exhibiting shear locking.

APPENDIX

Elasticity matrix:

$$\mathbf{E}^{e} = \begin{bmatrix} E_1 & E_2 & E_2 & 0 & 0 & 0 \\ E_2 & E_1 & E_2 & 0 & 0 & 0 \\ E_2 & E_2 & E_1 & 0 & 0 & 0 \\ 0 & 0 & 0 & 2G & 0 & 0 \\ 0 & 0 & 0 & 0 & 2G & 0 \\ 0 & 0 & 0 & 0 & 0 & 2G \end{bmatrix} \qquad (5.1)$$

where:

$$E_1 = K + \frac{4G}{3} \qquad (5.2)$$

and

$$E_2 = K - \frac{2G}{3} \qquad (5.3)$$

in which, *G* and *K* are the elastic shear and bulk moduli, in respect.

Deviatoric Stress:

$$q = \sqrt{J_2} \qquad (5.4)$$

where J_2 is the second deviatoric stress invariant:

$$J_2 = \frac{1}{2}\mathbf{s}:\mathbf{s} = \frac{1}{2}s_{ij}s_{ij} = \frac{1}{2}(s_{11}^2 + s_{22}^2 + s_{33}^2 + 2s_{12}^2 + 2s_{23}^2 + 2s_{31}^2) \qquad (5.5)$$

where $\mathbf{s} = \boldsymbol{\sigma} - p\mathbf{I}$ is the deviatoric stress tensor and $p = \frac{\sigma_{11} + \sigma_{22} + \sigma_{33}}{3}$ is the mean effective stress.

The second deviatoric invariant can be also defined (after calculations) as:

$$J_2 = \frac{1}{6}\left[(\sigma_{11} - \sigma_{22})^2 + (\sigma_{22} - \sigma_{33})^2 + (\sigma_{33} - \sigma_{11})^2\right] + \sigma_{12}^2 + \sigma_{23}^2 + \sigma_{31}^2 \qquad (5.6)$$

Thus, the deviatoric stress *q*, can be written according to Eqn. (5.5) as:

$$q = \sqrt{\frac{3}{2}}(\mathbf{s}:\mathbf{s})^{1/2} = \sqrt{\frac{3}{2}}(s_{11}^2 + s_{22}^2 + s_{33}^2 + 2s_{12}^2 + 2s_{23}^2 + 2s_{31}^2)^{1/2} \qquad (5.7)$$

and according to Eqn. (5.6) as:

$$q = \sqrt{\frac{1}{2}}\left[(\sigma_{11} - \sigma_{22})^2 + (\sigma_{22} - \sigma_{33})^2 + (\sigma_{33} - \sigma_{11})^2 + 6\sigma_{12}^2 + 6\sigma_{23}^2 + 6\sigma_{31}^2\right]^{1/2} \qquad (5.8)$$

Deviatoric Strain (equivalent strain)

$$\varepsilon_q = \sqrt{2/3}\,(\mathbf{e}:\mathbf{e})^{1/2} = \sqrt{2/3}\left[\left(\varepsilon_{11} - \frac{\varepsilon_p}{3}\right)^2 + \left(\varepsilon_{22} - \frac{\varepsilon_p}{3}\right)^2 + \left(\varepsilon_{33} - \frac{\varepsilon_p}{3}\right)^2 + 2\varepsilon_{12}{}^2 + 2\varepsilon_{23}{}^2 + 2\varepsilon_{31}{}^2\right]^{1/2}$$

(5.9)

where $\varepsilon_p = \varepsilon_{11} + \varepsilon_{22} + \varepsilon_{33}$ and $\mathbf{e} = \boldsymbol{\varepsilon} - \frac{\varepsilon_p}{3}\mathbf{I}$

or (after calculations)

$$\varepsilon_q = \frac{1}{3}\left[2\left(\varepsilon_{11}-\varepsilon_{22}\right)^2 + 2\left(\varepsilon_{22}-\varepsilon_{33}\right)^2 + 2\left(\varepsilon_{33}-\varepsilon_{11}\right)^2 + 12\varepsilon_{12}{}^2 + 12\varepsilon_{23}{}^2 + 12\varepsilon_{31}{}^2\right]^{1/2} \quad (5.10)$$

or, considering that $\varepsilon_{ij} = e_{ij} = \frac{\gamma_{ij}}{2}$ when $i \neq j$

$$\varepsilon_q = \frac{1}{3}\left[2\left(\varepsilon_{11}-\varepsilon_{22}\right)^2 + 2\left(\varepsilon_{22}-\varepsilon_{33}\right)^2 + 2\left(\varepsilon_{33}-\varepsilon_{22}\right)^2 + 3\gamma_{12}{}^2 + 3\gamma_{23}{}^2 + 3\gamma_{31}{}^2\right]^{1/2} \quad (5.11)$$

Principal stresses

$$\sigma_1 = \frac{I_1}{3} + \frac{2}{3}\left(\sqrt{I_1^2 - 3I_2}\right)\cos\phi_\theta \quad (5.12)$$

$$\sigma_2 = \frac{I_1}{3} + \frac{2}{3}\left(\sqrt{I_1^2 - 3I_2}\right)\cos\left(\phi_\theta + \frac{2\pi}{3}\right) \quad (5.13)$$

$$\sigma_3 = \frac{I_1}{3} + \frac{2}{3}\left(\sqrt{I_1^2 - 3I_2}\right)\cos\left(\phi_\theta + \frac{4\pi}{3}\right) \quad (5.14)$$

where

$$\phi_\theta = \frac{1}{3}\cos^{-1}\left(\frac{2I_1^3 - 9I_1I_2 + 27I_3}{2\left(I_1^2 - 3I_2\right)^{3/2}}\right) \quad (5.15)$$

$$I_1 = \sigma_{11} + \sigma_{22} + \sigma_{33} \quad (5.16)$$

$$I_2 = \sigma_{11}\sigma_{22} + \sigma_{22}\sigma_{33} + \sigma_{33}\sigma_{11} - \sigma_{12}^2 - \sigma_{23}^2 - \sigma_{31}^2 \quad (5.17)$$

$$I_3 = \sigma_{11}\sigma_{22}\sigma_{33} - \sigma_{11}\sigma_{23}^2 - \sigma_{22}\sigma_{31}^2 - \sigma_{33}\sigma_{12}^2 + 2\sigma_{12}\sigma_{23}\sigma_{31} \quad (5.18)$$

The quanties I_1, I_2, I_3 are stress invariants.

Failure/Bounding Surface

$$\left[\left(\mathbf{s}-\mathbf{r}_{\mathrm{p}}p\right):\left(\mathbf{s}-\mathbf{r}_{\mathrm{p}}p\right)\right]^{1/2}+\left(\mathbf{n}:\mathbf{r}_{\mathrm{p}}\right)p-\sqrt{\frac{2}{3}}M_{s,\theta}p=0\Leftrightarrow$$

$$\left(\mathbf{s}-\mathbf{r}_{\mathrm{p}}p\right):\left(\mathbf{s}-\mathbf{r}_{\mathrm{p}}p\right)+\left(\mathbf{n}:\mathbf{r}_{\mathrm{p}}\right)p\left[\left(\mathbf{s}-\mathbf{r}_{\mathrm{p}}p\right):\left(\mathbf{s}-\mathbf{r}_{\mathrm{p}}p\right)\right]^{1/2}$$

$$-\sqrt{\frac{2}{3}}M_{s,\theta}p\left[\left(\mathbf{s}-\mathbf{r}_{\mathrm{p}}p\right):\left(\mathbf{s}-\mathbf{r}_{\mathrm{p}}p\right)\right]^{1/2}=0\Leftrightarrow$$

$$\left(\mathbf{s}-\mathbf{r}_{\mathrm{p}}p\right):\left(\mathbf{s}-\mathbf{r}_{\mathrm{p}}p\right)+\left(\mathbf{s}-\mathbf{r}_{\mathrm{p}}p\right):\mathbf{r}_{\mathrm{p}}p-\sqrt{\frac{2}{3}}M_{s,\theta}p\left[\left(\mathbf{s}-\mathbf{r}_{\mathrm{p}}p\right):\left(\mathbf{s}-\mathbf{r}_{\mathrm{p}}p\right)\right]^{1/2}=0\Leftrightarrow$$

$$\left(\mathbf{s}-\mathbf{r}_{\mathrm{p}}p\right):\left(\mathbf{s}-\mathbf{r}_{\mathrm{p}}p+\mathbf{r}_{\mathrm{p}}p\right)-\sqrt{\frac{2}{3}}M_{s,\theta}p\left[\left(\mathbf{s}-\mathbf{r}_{\mathrm{p}}p\right):\left(\mathbf{s}-\mathbf{r}_{\mathrm{p}}p\right)\right]^{1/2}=0\Leftrightarrow$$

$$\frac{\left(\mathbf{s}-\mathbf{r}_{\mathrm{p}}p\right):\mathbf{s}}{\left[\left(\mathbf{s}-\mathbf{r}_{\mathrm{p}}p\right):\left(\mathbf{s}-\mathbf{r}_{\mathrm{p}}p\right)\right]^{1/2}}-\sqrt{\frac{2}{3}}M_{s,\theta}p=0\Leftrightarrow$$

$$\mathbf{s}:\mathbf{n}-\sqrt{\frac{2}{3}}M_{s,\theta}p=0\Leftrightarrow\frac{\mathbf{s}}{p}:\mathbf{n}-\sqrt{\frac{2}{3}}M_{s,\theta}=0\Leftrightarrow\mathbf{r}:\mathbf{n}-\sqrt{\frac{2}{3}}M_{s,\theta}=0 \qquad (5.19)$$

where

$$\mathbf{n}=\frac{\left(\mathbf{s}-\mathbf{r}_{\mathrm{p}}p\right)}{\left[\left(\mathbf{s}-\mathbf{r}_{\mathrm{p}}p\right):\left(\mathbf{s}-\mathbf{r}_{\mathrm{p}}p\right)\right]^{1/2}}=\frac{\left(\mathbf{s}-\mathbf{r}_{\mathrm{p}}p\right)}{q_{\mathrm{p}}} \qquad (5.20)$$

where

$$q_{\mathrm{p}}=\left[\left(\mathbf{s}-\mathbf{r}_{\mathrm{p}}p\right):\left(\mathbf{s}-\mathbf{r}_{\mathrm{p}}p\right)\right]^{1/2}\Leftrightarrow$$

$$q_{\mathrm{p}}=\left[\begin{array}{l}\left(\sigma_{11}-p-\frac{\sigma_{11,\mathrm{p}}-p_{\mathrm{p}}}{p_{\mathrm{p}}}p\right)^2+\left(\sigma_{22}-p-\frac{\sigma_{22,\mathrm{p}}-p_{\mathrm{p}}}{p_{\mathrm{p}}}p\right)^2+\left(\sigma_{33}-p-\frac{\sigma_{33,\mathrm{p}}-p_{\mathrm{p}}}{p_{\mathrm{p}}}p\right)^2\\+2\left(\sigma_{12}-\frac{\sigma_{12,\mathrm{p}}}{p_{\mathrm{p}}}p\right)^2+2\left(\sigma_{23}-\frac{\sigma_{23,\mathrm{p}}}{p_{\mathrm{p}}}p\right)^2+2\left(\sigma_{31}-\frac{\sigma_{31,\mathrm{p}}}{p_{\mathrm{p}}}p\right)^2\end{array}\right]^{0.5} \qquad (5.21)$$

Properties of tensor n

$$\begin{aligned}
&\mathrm{tr}\mathbf{n} = n_{11} + n_{22} + n_{33} = \\
&= \frac{1}{q_p}\left[\sigma_{11} - p - \frac{\sigma_{11,p} - p_p}{p_p}p + \sigma_{22} - p - \frac{\sigma_{22,p} - p_p}{p_p}p + \sigma_{33} - p - \frac{\sigma_{33,p} - p_p}{p_p}p\right] = \textit{(5.22)} \\
&= \frac{1}{q_p}\left[\sigma_{11} + \sigma_{22} + \sigma_{33} - 3p - \left(\sigma_{11,p} + \sigma_{22,p} + \sigma_{33,p} - 3p_p\right)\frac{p}{p_p}\right] = 0
\end{aligned}$$

$$\begin{aligned}
&\mathrm{tr}\mathbf{n}^2 = \mathbf{n}:\mathbf{n} = n_{11}^2 + n_{22}^2 + n_{33}^2 + 2n_{12}^2 + 2n_{23}^2 + 2n_{31}^2 = \\
&= \frac{1}{q_p^2}\left[\begin{array}{l}\left(\sigma_{11} - p - \dfrac{\sigma_{11,p} - p_p}{p_p}p\right)^2 + \left(\sigma_{22} - p - \dfrac{\sigma_{22,p} - p_p}{p_p}p\right)^2 + \left(\sigma_{33} - p - \dfrac{\sigma_{33,p} - p_p}{p_p}p\right)^2 + \\ +2\left(\sigma_{12} - \dfrac{\sigma_{12,p}}{p_p}p\right)^2 + 2\left(\sigma_{23} - \dfrac{\sigma_{23,p}}{p_p}p\right)^2 + 2\left(\sigma_{31} - \dfrac{\sigma_{31,p}}{p_p}p\right)^2\end{array}\right] \\
&= \frac{q_p^2}{q_p^2} = 1
\end{aligned}$$

(5.23)

***Gradient of the failure/bounding surface of Eq.* (5.19)**

The volumetric parts:

$$\Phi_{f,11}=\frac{\partial f}{\partial\sigma_{11}}=\frac{1}{2q_p}2\left(\sigma_{11}-p-\frac{\sigma_{11,p}-p_p}{p_p}p\right)\left(1-\frac{1}{3}-\frac{1}{3}\frac{\sigma_{11,p}-p_p}{p_p}\right)+$$
$$+\frac{1}{2q_p}2\left(\sigma_{22}-p-\frac{\sigma_{22,p}-p_p}{p_p}p\right)\left(-\frac{1}{3}-\frac{1}{3}\frac{\sigma_{22,p}-p_p}{p_p}\right)+$$
$$+\frac{1}{2q_p}2\left(\sigma_{33}-p-\frac{\sigma_{33,p}-p_p}{p_p}p\right)\left(-\frac{1}{3}-\frac{1}{3}\frac{\sigma_{33,p}-p_p}{p_p}\right)+$$
$$+\frac{2}{2q_p}2\left(\sigma_{12}-\frac{\sigma_{12,p}}{p_p}p\right)\left(-\frac{1}{3}\frac{\sigma_{12,p}}{p_p}\right)+\frac{2}{2q_p}2\left(\sigma_{23}-\frac{\sigma_{23,p}}{p_p}p\right)\left(-\frac{1}{3}\frac{\sigma_{23,p}}{p_p}\right)+$$
$$+\frac{2}{2q_p}2\left(\sigma_{31}-\frac{\sigma_{31,p}}{p_p}p\right)\left(-\frac{1}{3}\frac{\sigma_{31,p}}{p_p}\right)-\frac{1}{3}\sqrt{\frac{2}{3}}M_{s,\theta}+\frac{1}{3}n_p=$$
$$=\frac{\sigma_{11}-p-\frac{\sigma_{11,p}-p_p}{p_p}p}{q_p}-\frac{1}{3q_p}\left[\sigma_{11}+\sigma_{22}+\sigma_{33}-3p-\frac{p}{p_p}\left(\sigma_{11,p}+\sigma_{22,p}+\sigma_{33,p}-3p_p\right)\right]-$$
$$-\frac{1}{3q_p}\left[\begin{array}{l}\left(\sigma_{11}-p-\frac{\sigma_{11,p}-p_p}{p_p}p\right)\left(\frac{\sigma_{11,p}-p_p}{p_p}\right)+\left(\sigma_{22}-p-\frac{\sigma_{22,p}-p_p}{p_p}p\right)\left(\frac{\sigma_{22,p}-p_p}{p_p}\right)+\\ \left(\sigma_{33}-p-\frac{\sigma_{33,p}-p_p}{p_p}p\right)\left(\frac{\sigma_{33,p}-p_p}{p_p}\right)+2\left(\sigma_{12}-\frac{\sigma_{12,p}}{p_p}p\right)\left(\frac{\sigma_{12,p}}{p_p}\right)+\\ 2\left(\sigma_{23}-\frac{\sigma_{23,p}}{p_p}p\right)\left(\frac{\sigma_{23,p}}{p_p}\right)+2\left(\sigma_{31}-\frac{\sigma_{12,p}}{p_p}p\right)\left(\frac{\sigma_{31,p}}{p_p}\right)\end{array}\right]-$$
$$-\frac{1}{3}\sqrt{\frac{2}{3}}M_{s,\theta}+\frac{1}{3}n_p=\frac{\sigma_{11}-p-\frac{\sigma_{11,p}-p_p}{p_p}p}{q_p}-\frac{1}{3}n_p-\frac{1}{3}\sqrt{\frac{2}{3}}M_{s,\theta}+\frac{1}{3}n_p=$$
$$=\frac{\sigma_{11}-p-\frac{\sigma_{11,p}-p_p}{p_p}p}{q_p}-\frac{1}{3}\sqrt{\frac{2}{3}}M_{s,\theta}=n_{11}-\frac{1}{3}\sqrt{\frac{2}{3}}M_{s,\theta}$$

(5.24)

Combining Eqs. (5.19) and (5.24):

$$\Phi_{f,11}=n_{11}-\frac{1}{3}\mathbf{r}:\mathbf{n} \qquad (5.25)$$

where

$$\mathbf{r}:\mathbf{n}=\frac{1}{q_p}\left[\begin{array}{l}\left(\sigma_{11}-p-\frac{\sigma_{11,p}-p_p}{p_p}p\right)\left(\frac{\sigma_{11}-p}{p}\right)+\left(\sigma_{22}-p-\frac{\sigma_{22,p}-p_p}{p_p}p\right)\left(\frac{\sigma_{22}-p}{p}\right)\\+\left(\sigma_{33}-p-\frac{\sigma_{33,p}-p_p}{p_p}p\right)\left(\frac{\sigma_{33}-p}{p}\right)+2\left(\sigma_{12}-\frac{\sigma_{12,p}}{p_p}p\right)\left(\frac{\sigma_{12}}{p}\right)\\+2\left(\sigma_{23}-\frac{\sigma_{23,p}}{p_p}p\right)\left(\frac{\sigma_{23}}{p}\right)+2\left(\sigma_{31}-\frac{\sigma_{31,p}}{p_p}p\right)\left(\frac{\sigma_{31}}{p}\right)\end{array}\right] \qquad (5.26)$$

In the same logic,

$$\Phi_{f,22}=n_{22}-\frac{1}{3}\mathbf{r}:\mathbf{n} \qquad (5.27)$$

$$\Phi_{f,33}=n_{33}-\frac{1}{3}\mathbf{r}:\mathbf{n} \qquad (5.28)$$

The deviatoric parts:

$$\Phi_{f,12}=\frac{\partial f}{\partial\sigma_{12}}=\frac{2}{2q_p}2\left(\sigma_{12}-\frac{\sigma_{12,p}}{p_p}p\right)=\frac{2\left(\sigma_{12}-\frac{\sigma_{12,p}}{p_p}p\right)}{q_p}=2n_{12} \qquad (5.29)$$

$$\Phi_{f,23}=\frac{\partial f}{\partial\sigma_{23}}=\frac{2\left(\sigma_{23}-\frac{\sigma_{23,p}}{p_p}p\right)}{q_p}=2n_{23} \qquad (5.30)$$

$$\Phi_{f,31}=\frac{\partial f}{\partial\sigma_{31}}=\frac{2\left(\sigma_{31}-\frac{\sigma_{31,p}}{p_p}p\right)}{q_p}=2n_{31} \qquad (5.31)$$

Gradient of the plastic potential surface

The volumetric parts:

$$\Phi_{g,11} = \frac{\partial g}{\partial \sigma_{11}} = n_{11} + \left(n_{11}^2 + n_{12}^2 + n_{13}^2\right) d$$
$$\Phi_{g,22} = \frac{\partial g}{\partial \sigma_{22}} = n_{22} + \left(n_{22}^2 + n_{12}^2 + n_{23}^2\right) d \qquad (5.32)$$
$$\Phi_{g,33} = \frac{\partial g}{\partial \sigma_{33}} = n_{33} + \left(n_{33}^2 + n_{13}^2 + n_{23}^2\right) d$$

The deviatoric parts:

$$\Phi_{g,12} = \frac{\partial g}{\partial \sigma_{12}} = 2n_{12} + \left(n_{11}n_{12} + n_{22}n_{12} + n_{31}n_{23}\right) d$$
$$\Phi_{g,23} = \frac{\partial g}{\partial \sigma_{23}} = 2n_{23} + \left(n_{12}n_{31} + n_{22}n_{23} + n_{23}n_{33}\right) d \qquad (5.33)$$
$$\Phi_{g,31} = \frac{\partial g}{\partial \sigma_{31}} = 2n_{31} + \left(n_{11}n_{31} + n_{12}n_{23} + n_{31}n_{33}\right) d$$

Elasto-plastic Matrix $\mathbf{E}_h^{ep}$

$$\mathbf{E}_h^{ep} = \begin{bmatrix} A_1 & A_2 & A_3 & A_4 & A_5 & A_6 \\ B_1 & B_2 & B_3 & B_4 & B_5 & B_6 \\ C_1 & C_2 & C_3 & C_4 & C_5 & C_6 \\ D_1 & D_2 & D_3 & D_4 & D_5 & D_6 \\ E_1 & E_2 & E_3 & E_4 & E_5 & E_6 \\ F_1 & F_2 & F_3 & F_4 & F_5 & F_6 \end{bmatrix} \qquad (5.34)$$

$$\begin{bmatrix} d\sigma_{11} \\ d\sigma_{22} \\ d\sigma_{33} \\ d\sigma_{12} \\ d\sigma_{23} \\ d\sigma_{31} \end{bmatrix} = \begin{bmatrix} A_1 & A_2 & A_3 & A_4 & A_5 & A_6 \\ B_1 & B_2 & B_3 & B_4 & B_5 & B_6 \\ C_1 & C_2 & C_3 & C_4 & C_5 & C_6 \\ D_1 & D_2 & D_3 & D_4 & D_5 & D_6 \\ L_1 & L_2 & L_3 & L_4 & L_5 & L_6 \\ F_1 & F_2 & F_3 & F_4 & F_5 & F_6 \end{bmatrix} \begin{bmatrix} d\varepsilon_{11} \\ d\varepsilon_{22} \\ d\varepsilon_{33} \\ d\varepsilon_{12} \\ d\varepsilon_{23} \\ d\varepsilon_{31} \end{bmatrix} \qquad (5.35)$$

The components of the elastoplastic matrix are given by:

$$\begin{aligned}
A_1 &= E_1 - \frac{\zeta^n}{S}\left(\Phi_{f,11}E_1 + \Phi_{f,22}E_2 + \Phi_{f,33}E_2\right)\left(\Phi_{g,11}E_1 + \Phi_{g,22}E_2 + \Phi_{g,33}E_2\right) \\
A_2 &= E_2 - \frac{\zeta^n}{S}\left(\Phi_{f,11}E_2 + \Phi_{f,22}E_1 + \Phi_{f,33}E_2\right)\left(\Phi_{g,11}E_1 + \Phi_{g,22}E_2 + \Phi_{g,33}E_2\right) \\
A_3 &= E_2 - \frac{\zeta^n}{S}\left(\Phi_{f,11}E_2 + \Phi_{f,22}E_2 + \Phi_{f,33}E_1\right)\left(\Phi_{g,11}E_1 + \Phi_{g,22}E_2 + \Phi_{g,33}E_2\right) \\
A_4 &= -\frac{2G\zeta^n}{S}\left(\Phi_{g,11}E_1 + \Phi_{g,22}E_2 + \Phi_{g,33}E_2\right)\Phi_{f,12} \\
A_5 &= -\frac{2G\zeta^n}{S}\left(\Phi_{g,11}E_1 + \Phi_{g,22}E_2 + \Phi_{g,33}E_2\right)\Phi_{f,23} \\
A_6 &= -\frac{2G\zeta^n}{S}\left(\Phi_{g,11}E_1 + \Phi_{g,22}E_2 + \Phi_{g,33}E_2\right)\Phi_{f,31}
\end{aligned} \qquad (5.36)$$

$$\begin{aligned}
B_1 &= E_2 - \frac{\zeta^n}{S}\left(\Phi_{f,11}E_1 + \Phi_{f,22}E_2 + \Phi_{f,33}E_2\right)\left(\Phi_{g,11}E_2 + \Phi_{g,22}E_1 + \Phi_{g,33}E_2\right) \\
B_2 &= E_2 - \frac{\zeta^n}{S}\left(\Phi_{f,11}E_2 + \Phi_{f,22}E_1 + \Phi_{f,33}E_2\right)\left(\Phi_{g,11}E_2 + \Phi_{g,22}E_1 + \Phi_{g,33}E_2\right) \\
B_3 &= E_2 - \frac{\zeta^n}{S}\left(\Phi_{f,11}E_2 + \Phi_{f,22}E_2 + \Phi_{f,33}E_1\right)\left(\Phi_{g,11}E_2 + \Phi_{g,22}E_1 + \Phi_{g,33}E_2\right) \\
B_4 &= -\frac{2G\zeta^n}{S}\left(\Phi_{g,11}E_2 + \Phi_{g,22}E_1 + \Phi_{g,33}E_2\right)\Phi_{f,12} \\
B_5 &= -\frac{2G\zeta^n}{S}\left(\Phi_{g,11}E_2 + \Phi_{g,22}E_1 + \Phi_{g,33}E_2\right)\Phi_{f,23} \\
B_6 &= -\frac{2G\zeta^n}{S}\left(\Phi_{g,11}E_2 + \Phi_{g,22}E_1 + \Phi_{g,33}E_2\right)\Phi_{f,31}
\end{aligned} \qquad (5.37)$$

$$
\begin{aligned}
C_1 &= E_2 - \frac{\zeta^n}{S}\left(\Phi_{f,11}E_1 + \Phi_{f,22}E_2 + \Phi_{f,33}E_2\right)\left(\Phi_{g,11}E_2 + \Phi_{g,22}E_2 + \Phi_{g,33}E_1\right)\\
C_2 &= E_2 - \frac{\zeta^n}{S}\left(\Phi_{f,11}E_2 + \Phi_{f,22}E_1 + \Phi_{f,33}E_2\right)\left(\Phi_{g,11}E_2 + \Phi_{g,22}E_2 + \Phi_{g,33}E_1\right)\\
C_3 &= E_2 - \frac{\zeta^n}{S}\left(\Phi_{f,11}E_2 + \Phi_{f,22}E_2 + \Phi_{f,33}E_1\right)\left(\Phi_{g,11}E_2 + \Phi_{g,22}E_2 + \Phi_{g,33}E_1\right)\\
C_4 &= -\frac{2G\zeta^n}{S}\left(\Phi_{g,11}E_2 + \Phi_{g,22}E_2 + \Phi_{g,33}E_1\right)\Phi_{f,12}\\
C_5 &= -\frac{2G\zeta^n}{S}\left(\Phi_{g,11}E_2 + \Phi_{g,22}E_2 + \Phi_{g,33}E_1\right)\Phi_{f,23}\\
C_6 &= -\frac{2G\zeta^n}{S}\left(\Phi_{g,11}E_2 + \Phi_{g,22}E_2 + \Phi_{g,33}E_1\right)\Phi_{f,31}
\end{aligned}
\qquad (5.38)
$$

$$
\begin{aligned}
D_1 &= -\frac{2G\zeta^n}{S}\left(\Phi_{f,11}E_1 + \Phi_{f,22}E_2 + \Phi_{f,33}E_2\right)\Phi_{g,12}\\
D_2 &= -\frac{2G\zeta^n}{S}\left(\Phi_{f,11}E_2 + \Phi_{f,22}E_1 + \Phi_{f,33}E_2\right)\Phi_{g,12}\\
D_3 &= -\frac{2G\zeta^n}{S}\left(\Phi_{f,11}E_2 + \Phi_{f,22}E_2 + \Phi_{f,33}E_1\right)\Phi_{g,12}\\
D_4 &= 2G\left(1 - \frac{2G\zeta^n}{S}\Phi_{f,12}\Phi_{g,12}\right)\\
D_5 &= -\frac{4G^2\zeta^n}{S}\Phi_{f,12}\Phi_{g,23}\\
D_6 &= -\frac{4G^2\zeta^n}{S}\Phi_{f,12}\Phi_{g,31}
\end{aligned}
\qquad (5.39)
$$

$$
\begin{aligned}
L_1 &= -\frac{2G\zeta^n}{S}\left(\Phi_{f,11}E_1 + \Phi_{f,22}E_2 + \Phi_{f,33}E_2\right)\Phi_{g,23} \\
L_2 &= -\frac{2G\zeta^n}{S}\left(\Phi_{f,11}E_2 + \Phi_{f,22}E_1 + \Phi_{f,33}E_2\right)\Phi_{g,23} \\
L_3 &= -\frac{2G\zeta^n}{S}\left(\Phi_{f,11}E_2 + \Phi_{f,22}E_2 + \Phi_{f,33}E_1\right)\Phi_{g,23} \\
L_4 &= -\frac{4G^2\zeta^n}{S}\Phi_{f,23}\Phi_{g,12} \\
L_5 &= 2G\left(1 - \frac{2G\zeta^n}{S}\Phi_{f,23}\Phi_{g,23}\right) \\
L_6 &= -\frac{4G^2\zeta^n}{S}\Phi_{f,23}\Phi_{g,31}
\end{aligned}
\qquad (5.40)
$$

$$
\begin{aligned}
F_1 &= -\frac{2G\zeta^n}{S}\left(\Phi_{f,11}E_1 + \Phi_{f,22}E_2 + \Phi_{f,33}E_2\right)\Phi_{g,31} \\
F_2 &= -\frac{2G\zeta^n}{S}\left(\Phi_{f,11}E_2 + \Phi_{f,22}E_1 + \Phi_{f,33}E_2\right)\Phi_{g,31} \\
F_3 &= -\frac{2G\zeta^n}{S}\left(\Phi_{f,11}E_2 + \Phi_{f,22}E_2 + \Phi_{f,33}E_1\right)\Phi_{g,31} \\
F_4 &= -\frac{4G^2\zeta^n}{S}\Phi_{f,31}\Phi_{g,12} \\
F_5 &= -\frac{4G^2\zeta^n}{S}\Phi_{f,31}\Phi_{g,23} \\
F_6 &= 2G\left(1 - \frac{2G\zeta^n}{S}\Phi_{f,31}\Phi_{g,31}\right)
\end{aligned}
\qquad (5.41)
$$

where:

$$
\begin{aligned}
S = {} & \Phi_{g,11}\left(E_1\Phi_{f,11} + E_2\Phi_{f,22} + E_2\Phi_{f,33}\right) + \Phi_{g,22}\left(E_2\Phi_{f,11} + E_1\Phi_{f,22} + E_2\Phi_{f,33}\right) \\
& + \Phi_{g,33}\left(E_2\Phi_{f,11} + E_2\Phi_{f,22} + E_1\Phi_{f,33}\right) + \\
& + 2G\left(\Phi_{g,12}\Phi_{f,12}\right) + 2G\left(\Phi_{g,23}\Phi_{f,23}\right) + 2G\left(\Phi_{g,31}\Phi_{f,31}\right)
\end{aligned}
\qquad (5.42)
$$

Boundary and Loading conditions of Element Tests

All the calculations for model predictions of various experimental tests were based on solution of Eq. (5.35). For each test six known variables (stress or strain increments) were needed for the solution. In the following, the boundary and loading conditions of each type of test are given:

- ***Conventional Drained Triaxial Test***

(1): $d\varepsilon_{22} = d\varepsilon_{33}$

(2): $d\sigma_{22} = d\sigma_{33} = 0$

(3): $d\varepsilon_{11}$ known (imposed)

(4): $d\sigma_{12} = 0 \;\; d\varepsilon_{12} = 0$

(5): $d\sigma_{23} = 0 \;\; d\varepsilon_{23} = 0$

(6): $d\sigma_{31} = 0 \;\; d\varepsilon_{31} = 0$

- ***Conventional UNDrained Triaxial Test***

(1): $d\varepsilon_{22} = d\varepsilon_{33}$

(1): $d\varepsilon_{11}$ known (imposed)

(3): $d\varepsilon_{11} + d\varepsilon_{22} + d\varepsilon_{33} = d\varepsilon_{11} + 2d\varepsilon_{22} = 0 \Rightarrow d\varepsilon_{22} = -\dfrac{d\varepsilon_{11}}{2}$

(4): $d\sigma_{12} = 0 \;\; d\varepsilon_{12} = 0$

(5): $d\sigma_{23} = 0 \;\; d\varepsilon_{23} = 0$

(6): $d\sigma_{31} = 0 \;\; d\varepsilon_{31} = 0$

- ***P-constant Drained Triaxial Test***

(1): $d\varepsilon_{22} = d\varepsilon_{33}$

(2): $d\sigma_{11} + d\sigma_{22} + d\sigma_{33} = 0 \Rightarrow d\sigma_{11} + 2d\sigma_{22} = 0 \Rightarrow d\sigma_{22} = -\frac{d\sigma_{11}}{2}$

(3): $d\varepsilon_{11}$ known (imposed)

(4): $d\sigma_{12} = 0 \;\; d\varepsilon_{12} = 0$

(5): $d\sigma_{23} = 0 \;\; d\varepsilon_{23} = 0$

(6): $d\sigma_{31} = 0 \;\; d\varepsilon_{31} = 0$

- ***Drained Direct Simple Shear test***

(1): $d\varepsilon_{22} = 0$

(2): $d\varepsilon_{33} = 0$

(2): $d\sigma_{11} = 0$

(3): $d\varepsilon_{12}$ known (imposed)

(5): $d\sigma_{23} = 0 \;\; d\varepsilon_{23} = 0$

(6): $d\sigma_{31} = 0 \;\; d\varepsilon_{31} = 0$

- ***Undrained Direct Simple Shear test***

(1): $d\varepsilon_{11} = 0$

(2): $d\varepsilon_{22} = 0$

(3): $d\varepsilon_{33} = 0$

(4): $d\varepsilon_{12}$ known (imposed)

(5): $d\sigma_{23} = 0 \;\; d\varepsilon_{23} = 0$

(6): $d\sigma_{31} = 0 \;\; d\varepsilon_{31} = 0$

- ***Drained Simple Shear test (p constant)***

(1): $d\sigma_{11} = 0$

(2): $d\sigma_{22} = 0$

(3): $d\sigma_{33} = 0$

(4): $d\varepsilon_{12}$ known (imposed)

(5): $d\sigma_{23} = 0 \;\; d\varepsilon_{23} = 0$

(6): $d\sigma_{31} = 0 \;\; d\varepsilon_{31} = 0$

- ***Undrained* Simple Shear test with fixed α, b values**

(1): $d\varepsilon_{11} + d\varepsilon_{22} + d\varepsilon_{33} = 0$

(2): $d\varepsilon_{12}$ known (imposed)

(3): α known→

$$\alpha = \frac{1}{2}\tan^{-1}\left(\frac{2\sigma_{12}}{\sigma_{22} - \sigma_{11}}\right) \Leftrightarrow \tan(2\alpha) = \frac{2\sigma_{12}}{\sigma_{22} - \sigma_{11}}$$

$$\Rightarrow \mathrm{d}\sigma_{22} - \mathrm{d}\sigma_{11} = \frac{2\mathrm{d}\sigma_{12}}{\tan(2\alpha)}$$

(4): b known →

$$b=\frac{\sigma_2-\sigma_3}{\sigma_1-\sigma_3}=\frac{1}{2}\left(\frac{\sigma_{33}-(\sigma_{11}+\sigma_{22})/2}{\sqrt{\left(\frac{\sigma_{22}-\sigma_{11}}{2}\right)^2+(\sigma_{12})^2}}+1\right)\Leftrightarrow$$

$$(2b-1)\sqrt{\left(\frac{\sigma_{12}}{\tan(2\alpha)}\right)^2+(\sigma_{12})^2}=\sigma_{33}-\frac{\sigma_{11}+\sigma_{22}}{2}\Rightarrow$$

$$d\sigma_{33}-\frac{d\sigma_{11}}{2}-\frac{d\sigma_{22}}{2}=(2b-1)\frac{\sigma_{12}\left(\frac{1}{\tan(2\alpha)}+1\right)}{\sqrt{\left(\frac{\sigma_{12}}{\tan(2\alpha)}\right)^2+(\sigma_{12})^2}}d\sigma_{12}$$

(5): $d\sigma_{23}=0 \;\; d\varepsilon_{23}=0$

(6): $d\sigma_{31}=0 \;\; d\varepsilon_{31}=0$